

**Studies of Hadronic Spin Structure
in Hard Scattering Processes
at the Next-to-Leading Order of QCD**

Dissertation
zur Erlangung des
Doktorgrades der Naturwissenschaften
(Dr. rer. nat.)
der Naturwissenschaftlichen Fakultät II – Physik
der Universität Regensburg

vorgelegt von
Barbara Jäger

Regensburg, April 2004

Promotionsgesuch eingereicht am: 20. 4. 2004

Die Arbeit wurde angeleitet von: Prof. Dr. A. Schäfer

Prüfungsausschuß: Prof. Dr. W. Wegscheider
 Prof. Dr. A. Schäfer
 Prof. Dr. U. Rößler
 Prof. Dr. V. Braun

*Die Physik erklärt die Geheimnisse der Natur nicht,
sie führt sie auf tieferliegende Geheimnisse zurück.*

Carl Friedrich von Weizsäcker

Contents

1	Introduction	1
I	Concepts and Techniques	7
2	Basic Concepts of Perturbative QCD	8
2.1	The Lagrangian of QCD	8
2.2	Regularization	12
2.3	Renormalization	14
2.3.1	Example: Quark Selfenergy	16
2.4	Factorization	18
2.5	Parton Distributions and Fragmentation Functions	20
3	Technical Issues	26
3.1	Born Cross Sections	28
3.2	Virtual Contributions	35
3.2.1	Vertex and Selfenergy Corrections	36
3.2.2	Box Contributions	38
3.3	Helicity Method	39
3.4	Real Contributions	41
3.4.1	Three-Body Phase Space	42
3.4.2	Phase Space Integration	45
3.5	Cancellation of Singularities	48
II	Phenomenological Applications and Results	53
4	High-p_T Hadron Production in pp-Collisions	54
4.1	Setting the Stage	55
4.2	First Numerical Results and Discussion	61
4.3	The Double-Spin Asymmetry	66
4.4	Summary	79

5	Single-Inclusive Jet Production in pp-Collisions	81
5.1	Jet Definition	81
5.2	Analytical Calculation of Jet Cross Sections	83
5.2.1	The One-Parton-to-Jet Cross Section $d\Delta\hat{\sigma}_{j(k)}$	86
5.2.2	The Two-Parton-to-Jet Cross Section $d\Delta\hat{\sigma}_{jk}$	89
5.2.3	Cancellation of Final State Singularities	92
5.3	Numerical Results and Discussion	95
5.4	Summary and Conclusions	102
6	Photoproduction of Inclusive Hadrons	104
6.1	The Parton Structure of the Photon	105
6.2	Some Technicalities	107
6.3	Numerical Results	114
6.3.1	Pionproduction at an Electron-Proton Collider	114
6.3.2	Pionproduction in Fixed-Target Experiments	122
6.4	Summary and Conclusions	131
7	Summary and Conclusions	135
A	Feynman Rules	137
B	Leading Order $2 \rightarrow 2$ Scattering Cross Sections	140
C	Passarino-Veltman Decomposition	143
D	Parametrization of Momenta	145
E	Lorentz Boosts	148
	Acknowledgements	150
	Bibliography	151

Chapter 1

Introduction

One of the longest standing and still not satisfactorily answered questions of mankind is which fundamental entities constitute the world we are living in. The very concept of a microscopic structure underlying all matter first occurred in ancient Greek philosophy, when Demokrit suggested that everything consists of small objects, so-called atoms. It was not before the end of the 19th century, however, that science had developed a first picture of atomic physics, which could be thoroughly understood only with the advent of quantum mechanics in the early 20th century. At the same time Rutherford's scattering experiments revealed that atoms are not fundamental, but have a substructure themselves, which eventually was traced back to nuclei consisting of nucleons – protons and neutrons – surrounded by electrons. Continuous efforts in the following decades established the basic ideas of nuclear physics, but remained limited to a phenomenological description of interactions among nuclei. Only when it was realized that nucleons themselves have an inner structure and consist of even smaller particles, quarks and gluons, a fundamental theory of the force driving the interaction of the smallest building blocks could be developed. Our present knowledge of the basic entities and forces in nature is summarized in the Standard Model of elementary particle physics, based on the assumption that all matter consists of fundamental particles – quarks and leptons – which interact via the exchange of gauge bosons. Although the gross features of this model are well-established and experimentally verified by now, our understanding of elementary particle dynamics is still incomplete in many aspects, including the issues of a possible existence of additional elementary particles and a yet smaller substructure underlying all quarks and leptons. It therefore needs to be improved by ongoing experimental and theoretical efforts.

In this thesis we are focusing on the theory of the strong interaction, Quantum Chromodynamics (QCD), the sector of the Standard Model which at present is believed to be the fundamental theory of hadronic structure and interactions. QCD is a non-Abelian quantum field theory which describes the interaction of spin-1/2 quarks and spin-1 gluons. Due to the non-Abelian character of the gauge fields, self-interactions of the gluons occur – quite in contrast to Quantum Electrodynamics (QED) where the gauge bosons, the photons, are electrically neutral and couple therefore only to charged fermions. Similar to this electric charge, quarks and gluons are ascribed a “color-charge”. In nature, however, the

colored quarks and gluons cannot be observed as free particles, but only in color-neutral combinations – hadrons, highly non-trivial bound states such as, e.g., the proton. The formation of hadrons is due to a central feature of QCD: *confinement*. The complexity of hadronic systems makes the theoretical description of strongly interacting particles an intricate task, which only becomes feasible through another fundamental characteristic of QCD: *asymptotic freedom* [1]. The strength of the strong interaction depends significantly on the kinematic domain of the reaction. Contrary to the electromagnetic force, which becomes stronger with decreasing separation of the interacting particles, the strong coupling α_s diminishes the smaller the distances become. This feature makes QCD at high energies amenable to perturbative methods.

The basic observation underlying any such approach is manifested in *factorization theorems* [2]. They state that in certain kinematic domains strong interactions can be described as a combination of universal “soft” functions, parametrizing the distribution of quarks and gluons inside hadrons independently of the reaction they are involved in, and “hard” partonic quantities, which account for the interaction of quasi-free quarks and gluons emerging from the hadrons which are involved in a specific process. In the framework of perturbative QCD (pQCD) these latter pieces are calculated as a series in α_s . The definition and convergence of a perturbative expansion in quantum field theories is an intricate task, far beyond the scope of this thesis. These issues are intimately related to profound physics, such as a non-trivial, non-perturbative structure of the vacuum and its excitations [3]. Nonetheless, the results of a perturbative calculation very often give good approximations for physical observables. This remarkable feature, tested in a multitude of reactions, makes pQCD an indispensable tool for a better understanding of hard scattering processes. In the past, calculations have mostly been restricted to the leading order (LO) in the strong coupling. Thereby, however, only qualitative aspects can be addressed. Quantitative predictions, free of large theoretical uncertainties, require an extension of the perturbative expansion to, at least, the next-to-leading order (NLO). The internal structure of hadrons is a long-distance phenomenon, which cannot be calculated perturbatively, but has to be extracted from experiment or addressed by non-perturbative methods. At present, the parton distributions of the unpolarized nucleon are well-established [4-7] from the analysis of a wealth of hard scattering data. The verification of their universality has given some confidence in the validity of the factorization theorems mentioned above and thereby put the framework of pQCD on a solid footing. Altogether, the description of *spin-averaged* reactions with perturbative methods has been a success story.

However, one of the most fundamental properties of elementary particles crucial for a complete understanding of the internal structure and the dynamics driving the interaction of hadrons and therefore of QCD itself – but not entirely accessible in experiments without polarization – is their *spin*. A key issue for a better comprehension of spin is the question of how the spin of the proton, S_z^p , is built up from its constituents. This is expressed by the spin sum rule,

$$S_z^p = \frac{1}{2} = \frac{1}{2}\Delta\Sigma + \Delta G + L_z^q + L_z^g, \quad (1.1)$$

stating that S_z^p , which is well-known to be 1/2, is determined by the sum of the orbital angular momenta $L_z^{q,g}(Q)$ of the quarks and gluons in the nucleon, the total gluon

polarization, $\Delta G(Q) = \int_0^1 dx \Delta g(x, Q)$ ¹, and the total quark polarization, $\Delta\Sigma(Q) = \int_0^1 dx [\Delta u + \Delta\bar{u} + \Delta d + \Delta\bar{d} + \Delta s + \Delta\bar{s}](x, Q)$. The spin-dependent parton distribution functions Δq and $\Delta\bar{q}$ for quarks and antiquarks of any flavor ($q = u, d, s$) in a longitudinally polarized proton can be accessed, for instance, via the polarized deep-inelastic scattering (DIS) of leptons off nucleons [8], parametrized by the spin-dependent inelastic structure function

$$g_1(x, Q) = \frac{1}{2} \sum_{q=u,d,s} e_q^2 [\Delta q(x, Q) + \Delta\bar{q}(x, Q)] + \mathcal{O}(\alpha_s). \quad (1.2)$$

Here, the “resolution scale” Q determines the length scale $R \sim 1/Q$ probed in DIS, and x denotes the fraction of the nucleon’s momentum carried by the respective parton. The special interest of particle physicists has been aroused by the unexpected result of the European Muon Collaboration (EMC) [9] for the first moment of the structure function (1.2) for a proton target, $\int_0^1 dx g_1^p(x, Q)$, which could be translated into a surprisingly small value for $\Delta\Sigma \simeq 0.1 \div 0.2$. This finding was in complete contradiction to the naive expectation that the spin of the proton is carried mainly by its quark constituents, i.e., $\Delta\Sigma \simeq 1$. From the spin sum rule (1.1) it follows then that the main contributions to the proton spin have to come from the gluon polarization and/or the orbital angular momenta $L_z^{q,g}$.

So far, very little is known about orbital angular momenta. On the theoretical side, attempts are underway which aim to define $L_z^{q,g}$ consistently [10, 11] and access it by QCD sum rules [12] or in processes such as deeply-virtual Compton scattering [13], thereby providing the basis for a future extraction from experiment. Complementary to the analytical approach, first results have been obtained in numerical lattice simulations [14-16], which will help to constrain the orbital angular momenta as well.

Considerable efforts are now also taken to constrain the gluon polarization in the nucleon. The standard process for studying nucleon structure, deep inelastic scattering, is suitable only for a first determination of the quark distributions, as the virtual photon does not couple to a gluon directly. The structure function g_1 in Eq. (1.2) therefore depends on the gluon polarization only indirectly via scale evolution of the parton densities and through contributions of higher order in perturbation theory, both making an extraction of Δg from polarized DIS data difficult if not impracticable [17-21]. In addition, the separation of contributions from quarks and antiquarks of different flavors is impossible from a measurement of DIS structure functions. One thus has to resort to different reactions if definite information on the spin-dependent parton distributions of the proton is wanted. An observable suitable for the extraction of parton densities should be free of large experimental errors and theoretically under good control. Gluonic contributions should enter at the lowest order of pQCD already, and a clear separation of channels with quarks and antiquarks of different flavor is desirable. Resorting to reactions at high momentum transfer allows to neglect unwanted, so-called “higher-twist” contributions, suppressed by inverse powers of the hard scale specific to the reaction.

¹Here, $\Delta g(x, Q)$ denotes the spin-dependent parton distribution of a gluon in a longitudinally polarized proton, in analogy to the quark and antiquark distributions $\Delta q(x, Q)$ and $\Delta\bar{q}(x, Q)$. A detailed definition of these quantities is not required here, but will be given in Chap. 2.

New, unequalled possibilities have opened up with the advent of the Relativistic Heavy-Ion Collider (RHIC) at Brookhaven National Laboratory (BNL) in 2000 [22], the first collider facility which is able to run in a mode with polarized protons at high energies up to 250 GeV. The prime goal of the RHIC spin program is constraining the so far largely unknown gluon polarization in the nucleon. On the long run, at RHIC Δg can be studied in a variety of channels, for instance, the production of prompt photons and heavy flavors – reactions which have been calculated up to the next-to-leading order (NLO) of pQCD already [23-26]. Of most immediate relevance for the determination of Δg , however, are single-inclusive hadron and jet production processes, as these measurements require only a modest performance of RHIC. It is the main aim of this thesis to provide pQCD calculations for these reactions at NLO and to show how they can serve for a theoretical interpretation of RHIC measurements in the near future. The largely analytical results we thereby obtain are indispensable for an extraction of the spin-dependent parton distributions of the nucleon from data in a fast, efficient, and reliable way and will therefore help to clarify the still unsettled proton spin puzzle related to (1.1).

Further information on the spin-structure of hadrons could be provided by current fixed-target experiments like COMPASS at CERN [27] or a future polarized lepton-proton collider such as the planned eRHIC facility at BNL [28]. In addition to an alternative measurement of the gluon polarization in the nucleon, the latter would address the so far completely unknown parton content of the polarized photon. In this work we provide the theoretical framework necessary for an analysis of photoproduction data in fixed-target and collider experiments at NLO QCD, which on the long run will help to further deepen our understanding of hadronic structure gained from hadron-hadron collisions at RHIC.

Before going into the details of the respective processes we give a short outline of fundamental concepts of perturbative QCD in Chap. 2. We start by introducing the Lagrangian of QCD, and then show how to make predictions for processes involving strongly interacting particles at high energy with perturbative methods. We discuss the subtleties associated with dimensional regularization in polarized calculations and principal aspects of renormalization. We briefly sketch the concept of factorization in a formal way without going into calculational details at this point. Afterwards we summarize our present knowledge of parton distribution and fragmentation functions.

In Chap. 3 we focus on the technical issues of a next-to-leading order pQCD calculation. Basic perturbative methods, in particular the correct implementation of polarization sums and the phase space integration of a two-particle final state, are discussed on the basis of the concise, but instructive Born cross sections. We then turn to the explicit calculation of $2 \rightarrow 2$ scattering diagrams, including virtual loop corrections, using different techniques, and the treatment of $2 \rightarrow 3$ matrix elements with special emphasis on their phase space integration. Thereafter we show how factorization works in practice.

In the following two chapters we apply the methods developed before in thorough analyses of hadronic reactions which turn out to be particularly sensitive to the gluon polarization of the nucleon and will soon be studied experimentally at RHIC. Chapter 4 addresses single-inclusive hadron production in longitudinally polarized proton-proton collisions beyond the leading order. After giving some technical details we present the outcome of a numerical study to clarify the remaining theoretical uncertainties associated

with the NLO calculation. We then critically examine possible implications of first, preliminary data from the PHENIX collaboration at RHIC [29] on the gluon polarization of the nucleon.

Chapter 5 deals with single-inclusive jet production at RHIC in the context of the so-called “small-cone approximation”. Jet observables are supposed to be a particularly clean tool for the extraction of information on the spin structure of the nucleon, since they are free of any dependence on final state hadronization effects. We show how to compute the parton-to-jet cross sections on a fully analytical level. These results will greatly facilitate the analysis of upcoming data on polarized jet production in terms of the gluon polarization in the nucleon. Then we present our numerical predictions for the relevant spin asymmetry within the small cone approximation and compare them with results obtained in a Monte-Carlo approach which can take the finite cone size fully into account at the expense of a high numerical complexity.

In Chap. 6 we turn to longitudinally polarized lepton-photon interactions and study the photoproduction of inclusive hadrons. In particular, the sensitivity of this reaction to the spin-dependent parton distributions of the photon and the nucleon is of interest. We perform our numerical analysis in the two kinematic domains relevant for the conceivable eRHIC project at BNL and the COMPASS experiment, respectively. We critically discuss that the application of perturbative methods in the low-energy range solely accessible with fixed target experiments is not unproblematic.

Major parts of the results presented in this thesis have been published before in Physical Review D [30, 31], Physical Review Letters [32], and in [33]. The particular aim of this work, however, is to give a detailed outline of the methods used in an NLO pQCD calculation and to show how they can serve to provide a reliable theoretical framework for processes of special interest. Technicalities are omitted in the publications, but are useful for forthcoming calculations as they apply in general. They will therefore be discussed rather explicitly in Part I of this work. The reader familiar with perturbative methods can easily skip the corresponding sections and immediately turn to Part II with the chapters focusing on the presentation of our phenomenological results relevant for the RHIC spin program, COMPASS, and a possible future eRHIC facility.

Part I

Concepts and Techniques

Chapter 2

Basic Concepts of Perturbative Quantum Chromodynamics

In this chapter we introduce the Lagrangian of QCD which serves as starting point for the derivation of the Feynman rules needed in the calculation of physical observables for strongly interacting elementary particles. The underlying theoretical framework is well-known and discussed in any textbook of pQCD, e.g., Refs. [34-36]. Next, we focus on perturbative methods for the description of high-energy reactions in the context of the QCD-improved parton model, which inevitably lead to artificial divergencies beyond the lowest order approximation, thereby requiring the development of sophisticated techniques for their proper treatment [37, 38]. In particular, we will demonstrate how to isolate singularities in intermediate steps of a calculation and give them a well-defined meaning by *regularization*. We will show the removal or *renormalization* of divergencies stemming from the region where unobserved loop momenta go to infinity and demonstrate how to do this in an explicit example. Singularities arising from the emission of collinear massless particles from external legs are treated by means of an appropriate *factorization* procedure. Finally, we give a short overview on the status of the parton distribution and fragmentation functions relevant for the computation of hadronic observables.

This chapter is intended to give a general picture of the fundamental concepts of pQCD without resorting to the technical details associated with a NLO calculation. These will be discussed in Chap. 3.

2.1 The Lagrangian of QCD

The theory of strong interactions is based on the Lagrangian density

$$\mathcal{L}_{QCD} = \mathcal{L}_{classical} + \mathcal{L}_{gauge-fixing} + \mathcal{L}_{ghost} . \quad (2.1)$$

The “classical” Lagrangian is given by

$$\mathcal{L}_{classical} = -\frac{1}{4}F^{a,\mu\nu}F_{\mu\nu}^a + \sum_{f=1}^{N_f} \bar{\psi}_{f,i} (i\gamma_\mu D_{ij}^\mu - m_f \delta_{ij}) \psi_{f,j} . \quad (2.2)$$

Here and in the following summation over repeated indices is implicitly understood. $\mathcal{L}_{\text{classical}}$ describes the interaction of the gauge bosons of the theory, the massless spin-1 gluons, with the fermionic quark fields $\psi_{f,i}$ of flavor f , mass m_f , and color i . All fields depend on the four-dimensional space-time, x , but we do not indicate the argument explicitly. Since the quarks belong to the fundamental representation of an $SU(N = 3)$ gauge theory, i runs from 1 to $N = 3$. In QCD, N denotes the number of colors. We adopt the convention of Bjorken and Drell [39] with $g^{\mu\nu} = \text{diag}(1, -1, -1, -1)$ and set $c = \hbar = 1$.

In four dimensions, the Dirac matrices γ_μ satisfy the anti-commutation relation

$$\{\gamma_\mu, \gamma_\nu\} = 2 g_{\mu\nu} . \quad (2.3)$$

We will often use the symbolic notation $\not{D} = a_\mu \gamma^\mu$. The D_{ij}^μ in Eq. (2.2) is the covariant derivative,

$$D_{ij}^\mu = \partial^\mu \delta_{ij} - i g_s T_{ij}^a A^{a,\mu} , \quad (2.4)$$

with the strong coupling g_s . The gluonic fields A_a^μ have color indices a running from 1 to $(N^2 - 1) = 8$. The T^a are the generators of the gauge group and obey

$$[T^a, T^b] = i f^{abc} T^c . \quad (2.5)$$

The f^{abc} are the structure constants characterizing the algebra of the group. $F_{\mu\nu}^a$ in Eq. (2.2) is the field strength tensor built up from the gauge fields A_μ^a ,

$$F_{\mu\nu}^a = \partial_\mu A_\nu^a - \partial_\nu A_\mu^a + g_s f^{abc} A_\mu^b A_\nu^c . \quad (2.6)$$

The striking difference between QCD and an Abelian gauge field theory such as Quantum Electrodynamics (QED) resides in the non-Abelian term of the field strength tensor, $g_s f^{abc} A_\mu^b A_\nu^c$. It accounts for self-interactions amongst the “color-charged” gluons, in contrast to the neutral gauge bosons of QED, the photons, which couple only to the electrically charged fermions of the theory.

The quantization of QCD requires an additional gauge-fixing condition for the gluon fields. For our purposes it is useful to adopt a manifestly covariant gauge and choose $\partial^\mu A_\mu^a = 0$. Implementing this condition in the QCD Lagrangian yields an additional term,

$$\mathcal{L}_{\text{gauge-fixing}} = -\frac{1}{2\eta} (\partial^\mu A_\mu^a)^2 . \quad (2.7)$$

Since all physical observables which can be derived from \mathcal{L}_{QCD} must be independent of the choice of gauge, η can in principle take any arbitrary value. The choice $\eta = 1$ (Feynman gauge) is frequently used and will be adopted throughout this work. In covariant gauges, $\mathcal{L}_{\text{gauge-fixing}}$ must be supplemented by a ghost Lagrangian [40],

$$\mathcal{L}_{\text{ghost}} = (\partial^\mu \chi^{a*}) D_\mu^{ab} \chi^b , \quad (2.8)$$

with the scalar, anti-commuting Faddeev-Popov ghost fields χ^a and the covariant derivative in the adjoint representation,

$$D_\mu^{ab} = \partial_\mu \delta^{ab} - g_s f^{abc} A_\mu^c . \quad (2.9)$$

The ghost term in the Lagrangian is necessary to remove unphysical polarization degrees of freedom in the gluon fields, emerging in covariant gauges. Alternatively, the condition (2.7) could be replaced by a non-covariant gauge, e.g., an axial gauge with $A_3^a = 0$, which a priori excludes unphysical gluon polarizations and therefore does not require the introduction of ghost fields.

In a covariant gauge the complete Lagrangian of QCD then takes the form

$$\begin{aligned} \mathcal{L}_{QCD} = & -\frac{1}{4}F^{a,\mu\nu}F_{\mu\nu}^a + \sum_{f=1}^{N_f} \bar{\psi}_{f,i}(i\gamma_\mu D_{ij}^\mu - m_f\delta_{ij})\psi_{f,j} \\ & -\frac{1}{2\eta}(\partial^\mu A_\mu^a)^2 + (\partial^\mu \chi^{a*})D_\mu^{ab}\chi^b, \end{aligned} \quad (2.10)$$

which is invariant under local gauge transformations. The actual calculation of physical observables in the framework of QCD is cumbersome due to the non-Abelian character of \mathcal{L}_{QCD} . Depending on the energy-range relevant for the calculation different methods have been proposed to cope with the complexity of the strong interaction.

In the low-energy regime, on the one hand numerical methods are used, which rely on a discretization of the continuous four-dimensional space-time on a lattice. This approach turned out to successfully describe aspects of hadronic structure, such as the baryon mass spectrum or hadronic corrections to weak matrix elements, and the strong running coupling [41], and has the advantage of being conceptually consistent. However, it suffers from a high numerical intricateness, requiring very time-consuming computations. Above these technical difficulties lattice calculations are so far restricted to rather small volumes in space-time, and the extrapolation from the lattice to the continuum is not unproblematic. Another method applied at low energies is chiral perturbation theory [42], constructed as an expansion in the momenta and masses of the physical particles, which are considered to be small. The parameters of this effective field theory have to be determined from experiment. More heuristic approaches rely on phenomenologically inspired models. A large variety of methods has been proposed, starting from bag models [43] via Goldstone boson exchange mechanisms [44], diquark potentials [45], chiral quark solitons [46], and instanton models [47], up to all kinds of attempts to simply fit data from current experiments. Although such models are indispensable for a first qualitative description of measurements, they certainly cannot account for a thorough test of QCD itself and fall behind other methods, if precision calculations are required.

One therefore resorts to yet another approach, perturbative Quantum Chromodynamics, which is, however, applicable solely in the high momentum-transfer regime of the strong interaction. The basic observation underlying pQCD is the decrease of the strong running coupling α_s , related to the coupling constant g_s entering \mathcal{L}_{QCD} via $\alpha_s = g_s^2/4\pi$. This feature of the strong interaction, referred to as “asymptotic freedom” [1], allows treating hard interactions between quasi-free quarks and gluons at high energies as only small perturbations, which can be accounted for by a series expansion in the coupling constant α_s . This approach has the advantage that the Feynman rules, which are used to calculate physical observables describing the interaction of quarks and gluons, can be derived from \mathcal{L}_{QCD} directly without any model assumptions or restrictions on space-time as

in lattice gauge theories. We have listed the Feynman rules of QED and QCD in App. A.

The coefficients of a perturbation series in QCD exhibit factorial growth, i.e., they diverge [48]. It is one of the basic assumptions of pQCD that such an expansion, despite being divergent, is *asymptotic* [49]. The perturbative description of a physical, i.e., experimentally observable quantity Γ by a series $\sum_{n=0}^{\infty} \alpha_s^n \Gamma^{(n)}$ in the limit $\alpha_s \rightarrow 0$ does not necessarily uniquely define Γ , even if summed to all orders. However, if

$$\left| \Gamma - \sum_{n=0}^N \alpha_s^n \Gamma^{(n)} \right| \leq C_{N+1} \alpha_s^{N+1} \quad (2.11)$$

for all positive integer N , the series is said to be asymptotic to Γ and may reproduce the observable to a good approximation, even though the coefficients C_N do not converge. The divergent behavior of the perturbation series often indicates non-perturbative effects [3] and will not concern us in this thesis, as it has been shown in a multitude of reactions that perturbation theory indeed works well in matters of practical relevance.

The qualitative behavior of a physical observable can often be estimated by a leading order (LO) analysis where the perturbative expansion is truncated at the first non-vanishing order in α_s . A reliable quantitative understanding, however, requires the inclusion of higher order corrections although the computation of such contributions can be cumbersome in practice. Higher order corrections to an observable can be large, as was found, e.g., for prompt photon production [50]. Above that, theoretical predictions exhibit a dependence on unphysical scales, if the perturbation series is truncated at some finite order in α_s . For instance, a physical quantity Γ which is a priori independent of the arbitrary scale μ ,

$$\mu \frac{d}{d\mu} \Gamma = \mu \frac{d}{d\mu} \sum_{n=0}^{\infty} \alpha_s^n \Gamma^{(n)} = 0, \quad (2.12)$$

acquires in an N -th order perturbative calculation via renormalization and factorization procedures a residual scale dependence of order α_s^{N+1} :

$$\mu \frac{d}{d\mu} \sum_{n=0}^N \alpha_s^n \Gamma^{(n)} = -\mu \frac{d}{d\mu} \sum_{n=N+1}^{\infty} \alpha_s^n \Gamma^{(n)}. \quad (2.13)$$

Taking into account as many orders as possible in the perturbative expansion therefore reduces the artificial scale dependence and thus the uncertainty of a theoretical prediction to a minimum amount, provided pQCD is applicable. The reduction of scale dependence when extending a perturbative calculation to higher orders is then a “measure” for the reliability of the perturbative expansion.

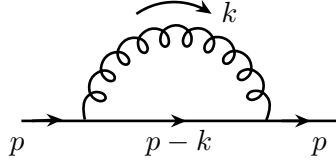
The calculation of higher order QCD contributions is furthermore called for by the ongoing hunt for signatures of “new physics”, i.e., physics beyond the Standard Model. The large systematic uncertainties of a lowest order pQCD analysis do not allow to disentangle presumably tiny effects of so far unobserved mechanisms from the omni-present QCD background. Only a thorough understanding of QCD opens up ways to a search for such phenomena.

2.2 Regularization

Let us now turn to the introduction of theoretical methods for the handling of divergencies emerging in a higher order perturbative calculation.

The interaction of any set of quarks and gluons is described by the invariant matrix element $\mathcal{M}_{i \rightarrow f}$. In perturbation theory, $\mathcal{M}_{i \rightarrow f}$ is computed via a series expansion in α_s with the Feynman rules given in App. A. In a LO calculation one needs not deal with singularities. If not only the qualitative behavior of a physical observable is to be estimated but precision results are required, the perturbation series has to be extended beyond the leading order. As soon as higher orders in α_s are considered, divergencies emerge in the intermediate steps of the calculation, although the final result describing a physically measurable quantity has to be finite. If the masses of the quarks involved in the reaction are neglected, there are basically three sources for singularities:

- Ultraviolet (UV) divergencies emerge when virtual, i.e., loop corrections to LO diagrams are considered. Since the momentum involved in an internal loop is not observed, it can take any arbitrary value and therefore has to be integrated over. As the upper integration limit approaches large momenta the integral becomes singular. An example for the appearance of UV divergencies are integrals \mathcal{I} of the general form



$$\mathcal{I} = \int \frac{d^4k}{(2\pi)^4} \frac{f(k)}{k^2(k-p)^2}, \quad (2.14)$$

arising, e.g., in the calculation of the selfenergy of a massless quark with momentum p . Naive power counting indicates already that \mathcal{I} diverges as $k \rightarrow \infty$. This finding is confirmed by an explicit calculation, see Sec. 2.3.1.

- When the momentum of an emitted parton approaches zero, one encounters infrared (IR) or soft singularities. In our previous example such a type of divergence is encountered if the quark goes on-shell.
- Yet another source of singularities are collinear configurations. They arise when a parton is emitted collinearly and propagates in the same direction as its “parent”.

UV divergencies are removed by an appropriate renormalization procedure as will be discussed in the following section. Singularities arising from the emission of partons collinear to either in- or outgoing external legs are factorized into the bare parton distribution or fragmentation functions of the hadrons associated with the respective quarks and gluons. Contributions which are simultaneously softly and collinearly divergent and simple IR singularities cancel in the sum of all contributions in a suitably defined observable. In the massless limit a physically meaningful, i.e., “infrared safe” quantity is then free of singularities [51, 52].

However, to finally remove the singularities by renormalization, factorization, or an appropriate combination of intermediate results, all divergencies *first* have to be isolated and quantified. This procedure of making all singularities manifest is called *regularization*. A proper regularization procedure should respect Lorentz invariance and unitarity and preserve the gauge symmetry of the theory. The only consistent procedure in the context of perturbative calculations fulfilling all these requirements [53, 54] is dimensional regularization. This method was developed in the early seventies [53, 55] and relies basically on an extension of space-time from four to $n = 4 - 2\varepsilon$ dimensions, with an a priori arbitrary, but small parameter ε . In this way UV and IR singularities can be regularized simultaneously, giving rise to $1/\varepsilon$ terms for simple poles and to $1/\varepsilon^2$ divergencies for contributions which are simultaneously IR and collinearly divergent. Only after a careful cancelation of all poles the limit $\varepsilon \rightarrow 0$ can be taken and, thereby, the physically relevant result restored.

The actual calculation of partonic matrix elements in the framework of dimensional regularization requires an extension of the Dirac algebra to n dimensions. Whereas this is a rather straightforward procedure if only unpolarized particles are involved, special care has to be taken if polarized observables are to be computed. This is mainly due to the fact that γ_5 and the Levi-Civita tensor $\epsilon^{\mu\nu\rho\sigma}$, which show up in any projection onto helicities [cf. (A.1)–(A.3)], are genuinely four-dimensional quantities and hence do not have a natural extension to $4 - 2\varepsilon$ dimensions. Algebraic inconsistencies stemming from an ill-defined treatment of these quantities may yield non-vanishing artificial contributions to polarized quantities at NLO. A fully consistent way to treat γ_5 and $\epsilon^{\mu\nu\rho\sigma}$ in n dimensions is the so-called HVBM scheme [53, 56]. It mainly consists of splitting the n -dimensional metric tensor $g_{\mu\nu}$ into a four- and an $(n - 4)$ -dimensional one. The Levi-Civita tensor is then *defined* by having components in the four-dimensional subspace only. As usual, γ_5 anti-commutes with γ_μ in four dimensions, but commutes in the other $(n - 4)$ dimensions.

In addition, all vectors, such as momenta, polarization vectors, etc., are defined in n rather than four dimensions, the $(n - 4)$ additional components of an arbitrary vector a_μ , the so-called “hat-momenta”, genuinely denoted by \hat{a}_μ . They have to be retained carefully throughout a calculation as they may give finite contributions when combined with $1/\varepsilon$ -poles. A massless spin-1 boson in n dimensions has $n - 2 = 2(1 + \varepsilon)$ spin degrees of freedom. This has to be taken into account whenever the polarizations of a gauge boson are summed over and averaged, e.g., in the computation of unpolarized matrix elements. Above that, demanding that the action \mathcal{S}_{QCD} , related to the QCD Lagrangian via

$$\mathcal{S}_{QCD} = \int d^n x \mathcal{L}_{QCD}(x) , \quad (2.15)$$

remains a dimensionless quantity, regardless of the dimension of space-time, requires the replacement of the dimensionless coupling constant g_s of the original four-dimensional theory by the dimensional \tilde{g}_s [34, 38],

$$g_s \rightarrow \tilde{g}_s = \mu_d^\varepsilon g_s , \quad (2.16)$$

where μ_d is an arbitrary mass scale. The advantage of introducing this scale is that the dimensionless g_s can be retained also in n dimensions. These prescriptions, in particular

the treatment of γ_5 and $\epsilon^{\mu\nu\rho\sigma}$, lead to a higher complexity in all steps of the n -dimensional calculation as compared to an ordinary four-dimensional one, starting from the algebraic evaluation of Feynman diagrams up to the computation of phase space integrals, as will be discussed later. However, algebraic computer programs such as TRACER exist [57], which handle the split-up of space-time into a four- and an $(n - 4)$ -dimensional part, including γ_5 and the Levi-Civita tensor, correctly. TRACER is extremely useful in the analytical computation of traces of Dirac matrices and contraction of Lorentz indices in n dimensions and has been used extensively for our calculations which we have performed in the HVBM-scheme throughout.

2.3 Renormalization

It has been mentioned above that in the calculation of virtual corrections to LO diagrams UV divergencies are encountered. These are associated with the large-momentum limit of the emerging loop integrals. In a renormalizable quantum field theory like QCD, such divergencies can be removed at any order in the perturbative expansion by adding a finite number of terms to the original, unrenormalized Lagrangian. This amounts to a redefinition of the gluon, ghost, and quark fields, and the parameters of the theory, i.e., the coupling g_s , quark masses (if appropriate), and gauge-fixing parameter η in \mathcal{L}_{QCD} :

$$\begin{aligned} A_\mu^a &\rightarrow Z_3^{1/2} A_{r\mu}^a, \\ \chi^a &\rightarrow \tilde{Z}_3^{1/2} \chi_r^a, \\ \psi &\rightarrow Z_2^{1/2} \psi_r, \\ g_s &\rightarrow Z_g g_{S,r}, \\ m &\rightarrow Z_m m_r, \\ \eta &\rightarrow Z_3 \eta_r, \end{aligned} \tag{2.17}$$

where $Z_3, \tilde{Z}_3, Z_2, Z_g, Z_m$ are the gluon-, ghost-, and quark-field, coupling-constant, and mass renormalization constants. The subscript r labels the renormalized fields and parameters. Color and flavor indices have been suppressed for simplicity. The gauge-fixing parameter η is associated with the same renormalization constant Z_3 as the gluon fields in order to preserve the form of the gauge-fixing term in \mathcal{L}_{QCD} . Also the other renormalization constants are related to each other via so-called Slavnov-Taylor identities [58, 59] reflecting the gauge-symmetry of the Lagrangian.

So far we have only renamed the fields and parameters entering the Lagrangian. The ultimate goal of this procedure, however, is to obtain a priori unrenormalized – so-called bare – Greens functions G_b , e.g., two-point functions such as quark or gluon propagators, from the rewritten \mathcal{L}_{QCD} in a form that all UV singularities can be reshuffled into the multiplicative renormalization constants Z_i ,

$$G_b = Z_i G_r. \tag{2.18}$$

The remaining – UV finite – pieces G_r are then interpreted as the “physical” Greens functions of the renormalized fields. If it is possible to follow this procedure, the Lagrangian is said to be renormalizable. In a fixed order perturbative calculation a multiplicative renormalization of the form (2.18) amounts to a subtraction of divergencies. For instance, considering the Greens function of Eq. (2.18) at $\mathcal{O}(\alpha_s)$, we find after writing Z_i and G_b as series in α_s

$$G_r = Z_i^{-1} G_b \simeq (1 - \alpha_s C_i) (G_{b,0} + \alpha_s G_{b,1}) , \quad (2.19)$$

with coefficients C_i and $G_{b,1}$ which still contain singularities, while the lowest-order contribution $G_{b,0}$ is finite. Expanding Eq. (2.19) and disregarding terms of $\mathcal{O}(\alpha_s^2)$ we obtain

$$G_r = G_{b,0} + \alpha_s [G_{b,1} - C_i G_{b,0}] + \mathcal{O}(\alpha_s^2) . \quad (2.20)$$

The C_i in the $\mathcal{O}(\alpha_s)$ contribution of Eq. (2.20) serves to cancel the pole terms of $G_{b,1}$. It is therefore often referred to as “counter term”. We will illustrate the concept sketched here by an explicit example in Sec. 2.3.1

The renormalization procedure contains a certain amount of arbitrariness. In order to obtain finite and therewith physically meaningful quantities, clearly all divergencies have to be removed. However, there exists no physical constraint restricting the subtractions to infinities only. Any number of finite terms can be subtracted along with the UV poles as well. Therefore, a certain prescription has to be chosen for the calculation of renormalized quantities. Depending on this rule one encounters different renormalization schemes. Applying dimensional regularization for isolating any kind of singularities suggests to simply subtract any UV poles of the form $1/\varepsilon$ from the unrenormalized Greens functions and reshuffle them into the associated renormalization constants. This method is known as Minimal Subtraction (MS) and was developed by ’t Hooft in the early seventies [60]. On the other hand, any poles in ε usually show up in the combination

$$\frac{1}{\varepsilon} + \ln 4\pi - \gamma_E , \quad (2.21)$$

where γ_E is the Euler-Mascheroni constant. Thus, it is more natural to subtract this expression rather than simply the $1/\varepsilon$ poles. In practice, this is done by a replacement of the regularization scale,

$$\mu_d^2 \rightarrow \tilde{\mu}_d^2 = \mu_d^2 \frac{e^{\gamma_E}}{4\pi} , \quad (2.22)$$

and the subtraction of $1/\varepsilon$ -poles only rather than the full expression (2.21). It can be easily seen that performing a series expansion for the factor $(\tilde{\mu}_d^2)^\varepsilon$, which always enters along with the dimensionless coupling, produces exactly the terms of Eq. (2.21) as $\varepsilon \rightarrow 0$. This renormalization prescription, the so-called Modified Minimal Subtraction ($\overline{\text{MS}}$) scheme [61] is the most commonly used in pQCD and will be applied throughout this work.

In practice, the renormalization of the sum of all virtual corrections to a massless cross section can also be achieved by the replacement of the bare coupling α_s^b according to

$$\frac{\alpha_s^b}{4\pi} = \frac{\alpha_s(\mu_r)}{4\pi} \left[1 - \frac{\alpha_s(\mu_r)}{4\pi} \frac{\beta_0}{\varepsilon} S_\varepsilon \left(\frac{\mu_r^2}{\mu_d^2} \right)^{-\varepsilon} \right] , \quad (2.23)$$

see, e.g., [62], with

$$S_\varepsilon = \exp \{ \varepsilon [\ln 4\pi - \gamma_E] \} \quad \text{and} \quad \beta_0 = \frac{11}{3}C_A - \frac{2}{3}N_f, \quad (2.24)$$

where $C_A = 3$ and μ_r is an arbitrary scale introduced via the renormalization procedure.

Observables computed at different scales are related to each other via renormalization group equations [60, 63]. These are based on the physical requirement that any observable must be independent of unphysical scales, which are only an artifact of the renormalization procedure as discussed in (2.12). If the behavior of a quantity under the renormalization group equations is known its variation in a change of the scale from an initial value μ_0 to any other value μ is determined up to terms beyond the order in α_s considered.

E.g., at NLO the running of the strong coupling $\alpha_s(\mu^2)$ is controlled by the renormalization group equation

$$\mu \frac{\partial \alpha_s}{\partial \mu} = -\frac{\beta_0}{2\pi} \alpha_s^2 - \frac{\beta_1}{4\pi^2} \alpha_s^3 + \mathcal{O}(\alpha_s^4), \quad (2.25)$$

where $\beta_1 = 51 - 19N_f/3$ and N_f is the number of flavors. Solving this equation one obtains [64]

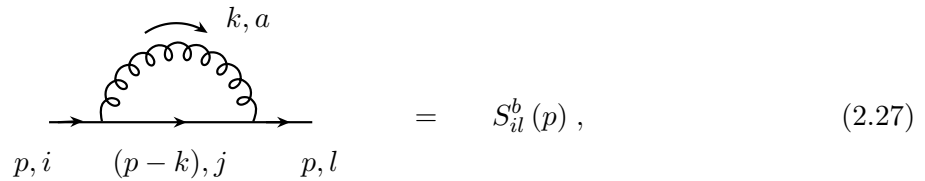
$$\alpha_s(\mu) \simeq \frac{4\pi}{\beta_0 \ln(\mu^2/\Lambda^2)} \left[1 - \frac{2\beta_1}{\beta_0^2} \frac{\ln[\ln(\mu^2/\Lambda^2)]}{\ln(\mu^2/\Lambda^2)} \right]. \quad (2.26)$$

Here the mass parameter Λ encodes the constant of integration in a convenient way. It is a fundamental parameter of QCD and has to be determined from experiment. Λ also depends on the choice of renormalization scheme. Of course, results obtained in one specific renormalization scheme can be transformed to another one by performing an additional finite renormalization.

2.3.1 Example: Quark Selfenergy

To illustrate the concepts and methods introduced so far by an instructive example let us calculate the selfenergy $S(p)$ of a quark at $\mathcal{O}(\alpha_s)$ in n dimensions and renormalize it in the $\overline{\text{MS}}$ scheme. A generalization of the methods encountered in this simple task to more complicated cases will be presented in Chap. 3.

The bare or unrenormalized selfenergy $S_{il}^b(p)$ of a quark with momentum p , a loop momentum k , and color indices i, l ,



$$= S_{il}^b(p), \quad (2.27)$$

is calculated with the help of the Feynman rules of App. A. For the computation of the color factor we use the identity

$$\sum_{a,j} T_{ij}^a T_{jl}^a = C_F \delta_{il} , \quad (2.28)$$

with $C_F = 4/3$. The dimensionless coupling constant g_s is replaced according to Eq. (2.16) by $\tilde{g}_s = g_s \tilde{\mu}_d^\varepsilon$. Doing so we obtain

$$S_{il}^b(p) = -\tilde{g}_s^2 C_F \delta_{il} \int \frac{d^n k}{(2\pi)^n} \frac{\gamma_\mu (\not{p} - \not{k}) \gamma^\mu}{k^2 (k-p)^2} , \quad (2.29)$$

with a loop integration that diverges in four dimensions as $k \rightarrow \infty$. In $n < 4$ dimensions, however, it has a well-defined meaning and can be calculated in a straightforward manner. With a projection onto the scalar integral

$$\tilde{B}_0 = \frac{1}{i} \int \frac{d^n k}{(2\pi)^n} \frac{1}{k^2 (k-p)^2} = \frac{1}{16\pi^2} \left(\frac{-p^2}{4\pi} \right)^{-\varepsilon} \Gamma(1+\varepsilon) \left(2 + \frac{1}{\varepsilon} \right) , \quad (2.30)$$

both integrals, resulting from a decomposition of the integrand in (2.29), can be calculated. Making furthermore use of the expansion

$$\Gamma(1+\varepsilon) \sim e^{-\gamma_E \varepsilon} \quad (2.31)$$

we obtain

$$S_{il}^b(p) = i \not{p} C_F \delta_{il} \frac{\tilde{g}_s^2}{16\pi^2} \left(\frac{-p^2}{4\pi} \right)^{-\varepsilon} e^{-\varepsilon \gamma_E} \left(1 + \frac{1}{\varepsilon} \right) \quad (2.32)$$

$$= -i \not{p} C_F \delta_{il} \Sigma_b(p^2) . \quad (2.33)$$

After rewriting $\tilde{g}_s = \tilde{\mu}_d^\varepsilon g_s = [\mu_d (e^{\gamma_E}/4\pi)]^\varepsilon g_s$ and inserting $\alpha_s = g_s^2/4\pi$ any dependence on $(e^{\gamma_E}/4\pi)$ cancels out and we arrive at

$$\Sigma_b(p^2) = -\frac{\alpha_s}{4\pi} \left(\frac{\mu_d^2}{-p^2} \right)^\varepsilon \left(1 + \frac{1}{\varepsilon} \right) . \quad (2.34)$$

This unrenormalized expression for the quark selfenergy obviously diverges as $\varepsilon \rightarrow 0$. To get a physically sensible, renormalized result $\Sigma(p^2)$, we have to subtract solely the singular term,

$$\Sigma(p^2) = -\frac{\alpha_s}{4\pi} \left[\left(\frac{\mu_d^2}{-p^2} \right)^\varepsilon \left(1 + \frac{1}{\varepsilon} \right) - \frac{1}{\varepsilon} \right] , \quad (2.35)$$

which yields for off-shell quarks after an expansion of the $(-p^2/\mu_d^2)^{-\varepsilon}$ factor

$$\Sigma(p^2 \neq 0) = -\frac{\alpha_s}{4\pi} \left[1 + \ln \left(\frac{\mu_d^2}{-p^2} \right) \right] , \quad (2.36)$$

where ε is positive and $p^2 \neq 0$.

This renormalization prescription has to be slightly modified for external on-shell quarks. Starting from the unrenormalized selfenergy (2.34), only a counter term $1/2\varepsilon$ rather than $1/\varepsilon$ is subtracted for external legs since these lines are renormalized with the square root of the respective renormalization constant, $\sqrt{Z_i}$, rather than Z_i as internal propagators, cf. Eqs. (2.19) and (2.20),

$$\Sigma(p^2) = -\frac{\alpha_s}{4\pi} \left[\left(\frac{\mu_d^2}{-p^2} \right)^\varepsilon \left(1 + \frac{1}{\varepsilon} \right) - \frac{1}{2\varepsilon} \right]. \quad (2.37)$$

Then, ε is analytically continued to negative values, $\varepsilon \rightarrow \tilde{\varepsilon} = -\varepsilon$, giving

$$\Sigma(p^2) = -\frac{\alpha_s}{4\pi} \left[\left(\frac{-p^2}{\mu_d^2} \right)^\varepsilon \left(1 - \frac{1}{\varepsilon} \right) + \frac{1}{2\varepsilon} \right]. \quad (2.38)$$

Now the quark can safely be put onto the mass-shell. Setting $p^2 = 0$ we obtain

$$\Sigma(p^2 = 0) = -\frac{\alpha_s}{4\pi} \frac{1}{2\varepsilon}. \quad (2.39)$$

The UV divergence has transformed into an IR pole by the renormalization procedure. As mentioned above, such singularities cancel if all contributions to a physically well-defined observable are added.

2.4 Factorization

By the renormalization procedure discussed above all UV singularities emerging in a higher order calculation can be removed. Soft divergencies cancel if all matrix elements squared contributing to an observable are added. Still, we have to specify how to deal with singularities stemming from the collinear emission of massless partons from external legs. Such divergencies are removed by factorizing them into the bare parton distribution or fragmentation functions of the hadrons the respective partons are associated with [2]. Thereby, for instance, a singularity arising from the collinear emission of a gluon by an external quark emerging from an incoming proton is subtracted from the partonic cross section and shifted into the bare quark density in the proton.

Formally, this rearrangement proceeds as follows: A generic hadronic cross section $d\sigma$, evaluated at a hard momentum scale Q , which allows for a factorized picture, can be written as a convolution \otimes of a partonic cross section $d\hat{\sigma}_b$ and some soft functions, f_b and D_b , which contain the bare parton distribution and fragmentation functions of the hadrons participating in the reaction, respectively,

$$d\sigma(Q) = f_b \otimes d\hat{\sigma}_b(Q/\mu_d, \varepsilon) \otimes D_b. \quad (2.40)$$

The partonic cross section depends on the arbitrary mass scale μ_d , introduced by dimensional regularization, and exhibits divergencies, indicated by the ε in the argument, while $d\sigma$ is finite. All arguments not relevant for this discussion are omitted here and in the following. Let us assume that all UV and IR singularities have already been removed

from $d\hat{\sigma}_b$. Then, poles can arise solely from collinear divergencies in the partonic cross section. The aim of the factorization procedure is to shift all singularities from $d\hat{\sigma}_b$ to the bare parton distribution and fragmentation functions, thereby giving rise to the renormalized, but scale-dependent quantities f and D . To this end, one first has to separate those parts of the partonic cross section which contain singularities stemming from collinear parton emission in the initial and final state, $d\hat{\sigma}_{coll}$ and $d\hat{\sigma}'_{coll}$, respectively, from the finite piece, $d\hat{\sigma}$. This is done at the factorization scales μ_f and μ'_f , which are of the order of the hard scale, but not further specified by theory,

$$\begin{aligned} d\sigma(Q, \mu_f, \mu'_f) &= f_b \otimes d\hat{\sigma}_{coll}(\mu_f/\mu_d, \varepsilon) \\ &\otimes d\hat{\sigma}(Q/\mu_f, \mu_f/\mu'_f, Q/\mu'_f) \otimes d\hat{\sigma}'_{coll}(\mu'_f/\mu_d, \varepsilon) \otimes D_b. \end{aligned} \quad (2.41)$$

Similar to the subtraction of UV-singularities by a renormalization procedure, discussed in Sec. 2.3, the factorization of divergencies is ambiguous. Different schemes separate a different amount of finite pieces along with the poles, thereby yielding scheme dependent expressions for each part of the partonic cross section, the $d\hat{\sigma}_{coll}$, $d\hat{\sigma}'_{coll}$, and $d\hat{\sigma}$. In this thesis we will mostly employ the $\overline{\text{MS}}$ factorization scheme, where, similar to the $\overline{\text{MS}}$ renormalization procedure, $1/\varepsilon$ -poles are subtracted along with the accompanying $(\ln 4\pi - \gamma_E)$ terms [cf. Eq. (2.21)].

In an all-orders calculation the hadronic cross section $d\sigma$ is free of the unphysical scales μ_f and μ'_f , as stated in Eq. (2.12). However, the truncation of the perturbative expansion at a finite order of α_s inhibits a complete cancelation of terms depending on μ_f and μ'_f beyond that order and gives rise to a residual scale dependence of $d\sigma$ in Eq. (2.41).

After the isolation of divergencies by the reshuffling sketched in Eq. (2.41) all singularities are absorbed in the bare parton densities and fragmentation functions, which thereby become scale dependent,

$$\begin{aligned} f(\mu_f) &= f_b \otimes d\hat{\sigma}_{coll}(\mu_f/\mu_d, \varepsilon), \\ D(\mu'_f) &= D_b \otimes d\hat{\sigma}'_{coll}(\mu'_f/\mu_d, \varepsilon). \end{aligned} \quad (2.42)$$

With this rearrangement we end up with completely finite expressions for the physical parton distributions f and fragmentation functions D . Above that, we have removed all divergencies from $d\hat{\sigma}_b$ and obtained a finite partonic cross section $d\hat{\sigma}$. The mass scale μ_d has canceled in both, soft and hard contributions to $d\sigma$ after the convolution of the collinear contributions with the bare parton densities. The hadronic cross section finally reads schematically

$$d\sigma(Q, \mu_f, \mu'_f) = f(\mu_f) \otimes d\hat{\sigma}(Q/\mu_f, \mu_f/\mu'_f, Q/\mu'_f) \otimes D(\mu'_f). \quad (2.43)$$

This expression is free of all singularities and serves as starting point for any analysis of physical observables in pQCD. The actual choice of the factorization scales present in $d\sigma$ indicates how much of the QCD radiation emitted in a hadronic reaction is attributed to the evolution of the parton distributions and fragmentation functions and what is left in the hard scattering.

2.5 Parton Distributions and Fragmentation Functions

In the applications of Eq. (2.43) most relevant for this thesis the quantity f is identified with the parton distribution functions $f_i^H(x_i, \mu_f)$ of the particles scattering off each other in a hadronic reaction. In the QCD-improved parton model the $f_i^H(x_i, \mu_f)$ at the leading order in α_s give the probability for finding parton i in hadron H at a scale μ_f carrying a fraction x_i of the hadron's momentum, irrespective of its spin orientation,

$$f_i^H(x_i, \mu) \equiv f_{i+}^{H+}(x_i, \mu) + f_{i-}^{H+}(x_i, \mu) . \quad (2.44)$$

Here, the f_{i+}^{H+} and f_{i-}^{H+} stand for the distributions of a parton with its spin being aligned or anti-aligned with the hadron's longitudinal spin direction. Parity conservation implies $f_{i-}^{H-} = f_{i+}^{H+}$ and $f_{i+}^{H-} = f_{i-}^{H+}$. For spin-dependent cross sections, the main theme of this thesis, the longitudinally polarized parton densities become relevant. In contrast to the spin-averaged parton distributions, given in Eq. (2.44), these $\Delta f_i^H(x_i, \mu_f)$, being defined via

$$\Delta f_i^H(x_i, \mu) \equiv f_{i+}^{H+}(x_i, \mu) - f_{i-}^{H+}(x_i, \mu) , \quad (2.45)$$

are sensitive to the polarization of the parton inside the hadron at given x_i and μ . Their first moments, $\int_0^1 dx f_i^H(x, \mu)$, enter the spin sum rule in Eq. (1.1) and are therefore closely related to the total spin of the hadron they are associated with. Beyond the LO such a simple probabilistic interpretation of the parton distributions is no longer possible. Then, the $(\Delta) f_i^H$ are scheme-dependent, unphysical quantities which acquire a well-defined meaning only in combination with the partonic cross sections of a specific reaction, as sketched in Eq. (2.43), evaluated in the *same* factorization scheme.

Parton distribution functions cannot be calculated with perturbative methods from first principles. Since they are genuinely non-perturbative objects, describing the internal structure of hadrons, they either have to be estimated resorting to models of hadronic structure, calculated on the lattice, or determined from experiment via a fitting procedure. Once the parton densities are known at some initial scale $\mu = \mu_0$ their evolution to other values of the scale parameter is determined by the DGLAP evolution equations [65, 66],

$$\mu \frac{d}{d\mu} \begin{pmatrix} \Delta f_q^H(x, \mu) \\ \Delta f_g^H(x, \mu) \end{pmatrix} = \frac{\alpha_s}{2\pi} \int_x^1 \frac{dy}{y} \begin{pmatrix} \Delta P_{qq} & \Delta P_{qg} \\ \Delta P_{gq} & \Delta P_{gg} \end{pmatrix}_{(y, \alpha_s(\mu))} \cdot \begin{pmatrix} \Delta f_q^H(x/y, \mu) \\ \Delta f_g^H(x/y, \mu) \end{pmatrix} , \quad (2.46)$$

and analogously for the unpolarized case, if one replaces all spin-dependent quantities by their spin-averaged counterparts. The splitting functions $(\Delta)P_{ij}$ in Eq. (2.46) describe the transition of parton j into parton i . They are calculable in pQCD and have been determined up to NLO [67-70]. Very recently, the unpolarized splitting functions have been calculated up to three loops [71-73]. Of course, a *physical observable* calculated to all orders in perturbation theory must fulfill (2.12). This relation, however, applies only to the combination of the parton distributions with the appropriate partonic cross sections, but not to either of these pieces itself.

To extract parton densities from measurements of suitable observables one usually starts from a functional ansatz for the x -shape of the wanted distributions at a scale μ_0

with a certain set of free parameters. The trial functions are then evolved to values of the scale parameter μ relevant for a certain data point of the measured quantity. Using the thereby obtained parton densities for calculating the respective observable and comparing this theoretical prediction to experimental results, an estimate for the quality of the ansatz is obtained. Repeating this procedure again and again for all data points and different observables the ansatz can be optimized, e.g., in a χ^2 -analysis, yielding a set of parton densities that parametrize our current knowledge on the distribution of quarks and gluons in the hadron.

The presently available sets of *spin-averaged* parton distributions [4-7] are mainly based on analyses of DIS data, provided by an abundance of accurate fixed-target and also collider experiments at fairly high energies over the last couple of years at CERN, SLAC, and DESY. Figure 2.1 shows the unpolarized parton distributions of the proton as obtained by the NLO analysis of Ref. [4] at different scales. The curves demonstrate that the densities of the u and d quarks which contain both, a valence and a sea contribution, are peaked around $x \approx 0.3$ due to their valence part, as expected from the naive parton model. The sea quark distributions are largest at small values of x and die away above. The gluonic component g rises strongly towards small x , its large value indicating the importance of the gluon distribution in the proton. The lower plots in Fig. 2.1 illustrate the statistical uncertainty of the unpolarized u -quark and gluon distributions. It can be seen that $u(x, \mu)$ is fairly well-known over the entire x -range, and also $g(x, \mu)$ can be determined with some accuracy at low values of x . Only at large x , the gluon density is insufficiently constrained by present data. This issue could be addressed, e.g., in future measurements at the Tevatron at Fermilab and the Large Hadron Collider (LHC) at CERN, as discussed in [76].

The determination of the *spin-dependent* parton densities of the proton cannot be performed at the same level of precision as in the unpolarized case due to the sparse amount of data containing information on the structure of the longitudinally polarized proton stemming – so far – solely from fixed-target experiments at rather low energies. The polarized parton distributions can therefore only be estimated, if the lack of measurements is compensated by some physical considerations and assumptions. An important ingredient is the positivity condition which constrains the polarized parton distributions at LO,

$$|\Delta f(x, \mu)| \leq f(x, \mu) , \quad (2.47)$$

a feature used in many analyses. At NLO, this relation no longer strictly applies, since parton distributions are no longer objects with a probabilistic interpretation, but scheme dependent quantities with no immediate physical meaning. However, NLO corrections are not supposed to completely change LO predictions. Thus, it may make sense to apply the positivity bound also in fits beyond the leading order, keeping in mind that it must not be interpreted as a strict upper limit in that case.

To illustrate the current status of knowledge, in Figs. 2.2, taken from Ref. [18], we show a comparison of different sets of polarized parton distributions [17-19], as obtained in the $\overline{\text{MS}}$ scheme. Also indicated are the statistical errors of these fits. Further uncertainties, for instance, the freedom in choosing an ansatz for the parton distributions, increase the

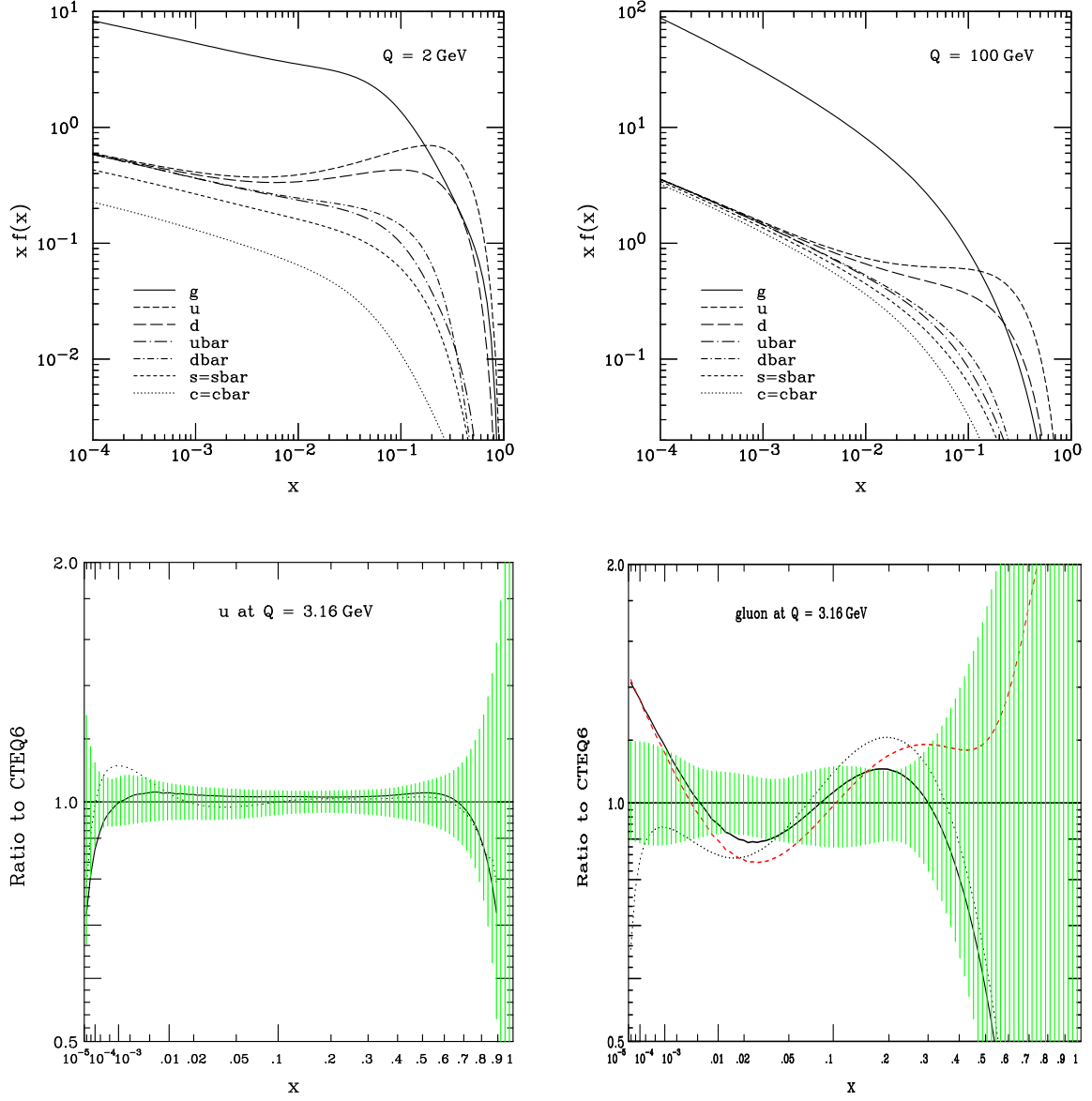


Figure 2.1: The upper plots show the parton densities $xf(x, Q)$ ($f = g, u, d, \bar{u}, \bar{d}, s, c$) in the CTEQ6 NLO parametrization [4] at a scale $\mu = Q = 2 \text{ GeV}$ (l.h.s.) and $Q = 100 \text{ GeV}$ (r.h.s.), respectively. In the lower plots the shaded areas represent the uncertainty bands for the u -quark and the gluon distribution functions, together with the ratios of the corresponding CTEQ5 [74] (solid and dashed lines) and MRST2001 [75] (dotted lines) distributions to the CTEQ6 results at a scale $Q = \sqrt{10} \text{ GeV}$. The figures are taken from Ref. [4].

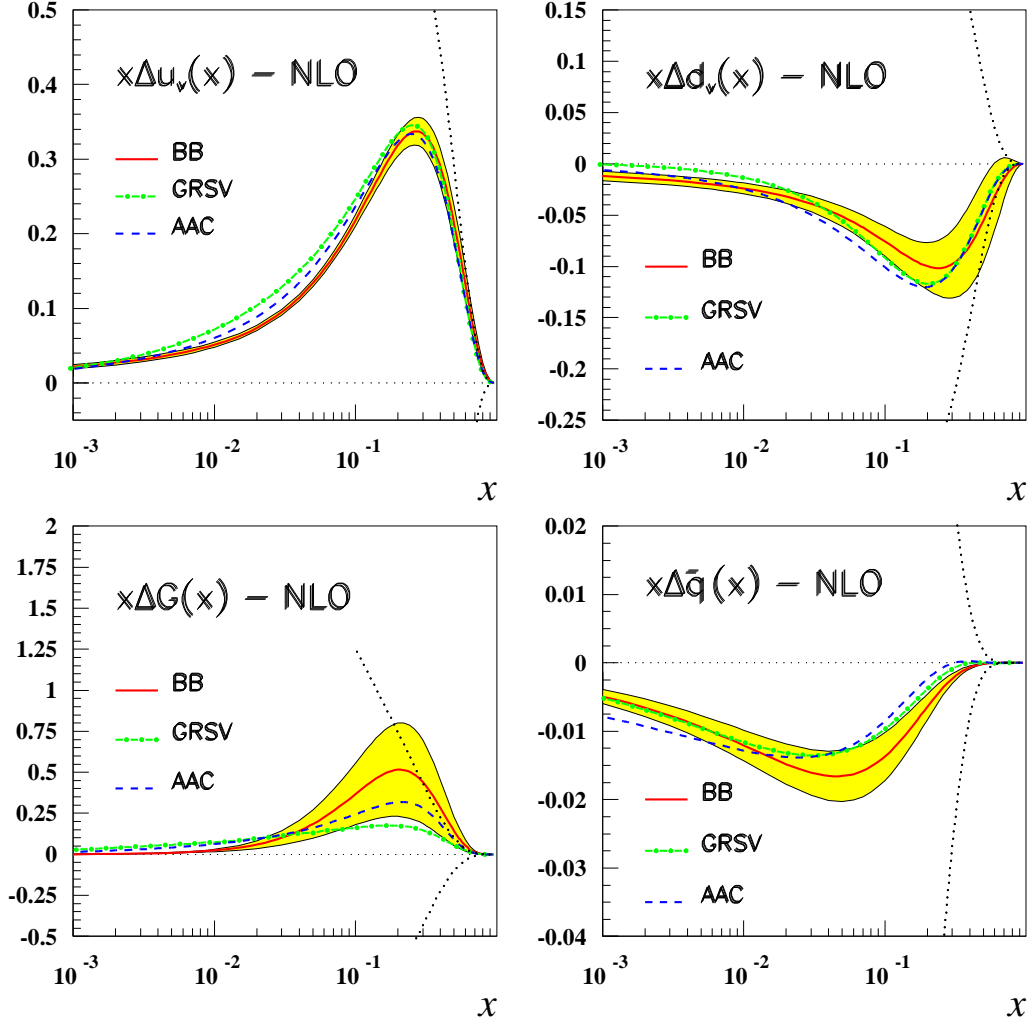


Figure 2.2: Comparison of different sets of polarized parton distributions at NLO at a scale $\mu = 2$ GeV. The curves correspond to the parametrizations of Blümlein and Böttcher [18] (solid lines), GRSV [17] (dashed-dotted lines), and AAC [19] (dashed lines). The dotted lines indicate the positivity bounds (2.47) corresponding to the unpolarized distributions of Ref. [77]. The shaded areas represent the statistical uncertainties in the respective parton densities. The figure is taken from Ref. [18].

errors, especially for Δg . In particular, the valence quark distribution Δu_v is fairly well constrained by the data used for the analysis, yielding similar results in all parametrizations. From inclusive DIS data on g_1^p alone it is impossible to separate quark and antiquark distributions [cf. Eq (1.2)]. Due to the resulting uncertainty in the flavor decomposition of the proton sea, the errors are more pronounced for $\Delta \bar{q} = \Delta \bar{u} = \Delta \bar{d} = \Delta \bar{s} = \Delta s$, assuming an SU(3) symmetric sea. The most striking point, however, is the completely unsatisfactory constraint of Δg . Entirely different ansätze for the polarized gluon distribution are equally well capable of reproducing all available DIS data. Since this problem can only be solved by new experiments yielding information from other reactions in addition to existing DIS data, any set of spin-dependent parton distributions can merely suggest a reasonable form for Δg , but not really constrain it. The spin program at the BNL-RHIC collider is exactly intended to cure this shortcoming. It will yield indispensable information from various reactions sensitive to the gluon polarization of the nucleon and thereby allow for a first determination of $\Delta g(x, \mu)$ in the range $10^{-2} \lesssim x \lesssim 0.3$. This thesis will provide the necessary theoretical framework to analyze upcoming data for inclusive hadron and jet production at RHIC.

Similarly to parton distributions the fragmentation functions $(\Delta)D_i^H(z_i, \mu'_f)$, in the factorized cross section formula, Eq. (2.43), generically denoted by D , describe the fragmentation of parton i into a (polarized) hadron H at a scale μ'_f , now z_i being the fraction of the parton momentum taken by the hadron. Since free quarks and gluons cannot be observed in nature, each parton in the final state of a hard scattering process is supposed to ultimately fragment into a hadron, giving rise to the relation

$$\int_0^1 dz z \sum_H D_i^H(z, \mu) = 1, \quad (2.48)$$

where the sum is to be taken over hadrons H of any type. Again, once the unpolarized fragmentation functions are known at an initial scale μ_0 their evolution is determined by Altarelli-Parisi-type evolution equations,

$$\mu \frac{d}{d\mu} \begin{pmatrix} D_q^H(z, \mu) \\ D_g^H(z, \mu) \end{pmatrix} = \frac{\alpha_s}{2\pi} \int_z^1 \frac{dy}{y} \begin{pmatrix} P_{qq} & P_{qg} \\ P_{gq} & P_{gg} \end{pmatrix}_{(y, \alpha_s(\mu))} \cdot \begin{pmatrix} D_q^H(z/y, \mu) \\ D_g^H(z/y, \mu) \end{pmatrix}, \quad (2.49)$$

with the $P_{ij}(z, \mu)$ now denoting the time-like splitting functions rather than the spacelike ones in Eq. (2.46). They are known up to NLO [68, 78, 79]. An analogous equation describes the evolution of fragmentation functions $\Delta D_i^H(z, \mu)$ for polarized hadrons when the P_{ij} in Eq. (2.49) are replaced by the respective ΔP_{ij} [80]. Processes with polarized hadrons in the final state are not considered in this thesis. In principle, they can be described with the theoretical framework developed here and are also accessible in experiment, for instance via self-analyzing decay channels [81] in the case of polarized Λ baryons.

The explicit form of the $(\Delta)D_i^H$ again has to be determined from experiment in a fitting procedure analogous to the extraction of parton densities described above. Particularly useful for this purpose are experiments at e^+e^- colliders, since they are not obscured

by uncertainties associated with hadrons in the initial state like measurements at hadron colliders and fixed-target experiments. However, presently available sets of fragmentation functions, e.g., for pions and kaons [82, 83], and Λ -baryons [84], obtained from analyses of data on e^+e^- annihilation into hadrons mainly at the Z -boson resonance, suffer from poor constraints on D_g^H and the separation of D_{u+d+s}^H into contributions from individual flavors, D_u^H , D_d^H , and D_s^H . These deficiencies can only be cured by an inclusion of further data from reactions other than e^+e^- annihilation. Future data on inclusive hadron production from RHIC, discussed in Chap. 4, might be of particular use here.

Chapter 3

Technical Issues of a Next-to-Leading Order pQCD Calculation

In this chapter we will describe the methods required for the computation of differential cross sections for hadronic reactions in the framework of pQCD. To this end, we resort to single-inclusive hadron production at high transverse momenta keeping, however, in mind that the techniques illustrated by that example can be applied – after an appropriate modification – in any perturbative calculation of hadronic observables. In particular, we will concentrate on the reaction

$$A(P_A) + B(P_B) \rightarrow C(P_C) + X , \quad (3.1)$$

where two incoming hadrons, A and B , produce another hadron C and arbitrary, unobserved by-products X . Here and in the following P_H denotes the momentum of a hadron H ($H = A, B, C$). The reaction (3.1) is usually referred to as “*single-inclusive*”, since just one of the particles in the final state is detected. In this feature it differs from fully inclusive observables where the final state is not specified at all, as well as from exclusive processes where all participating particles are observed. Single-inclusive processes exhibit considerably larger cross sections than comparable exclusive reactions, and the theoretical framework needed for their description is less complex. On the other hand, they yield information on aspects of hadronic structure which are not accessible in fully inclusive measurements like, for instance, Δg .

In the presence of a hard scale, single-inclusive reactions are accessible with perturbative methods. Such a scale is provided, e.g., by the transverse momentum p_T of the observed final state hadron, provided it is large ($p_T \gtrsim 2$ GeV). From now on we will focus on high- p_T scattering processes. In this case, hadronic cross sections are determined according to Eq. (2.43) [2] as a convolution of perturbatively calculable partonic cross sections describing the hard scattering of the hadronic constituents and parton distribution and fragmentation functions, which parametrize the bound-state dynamics of the

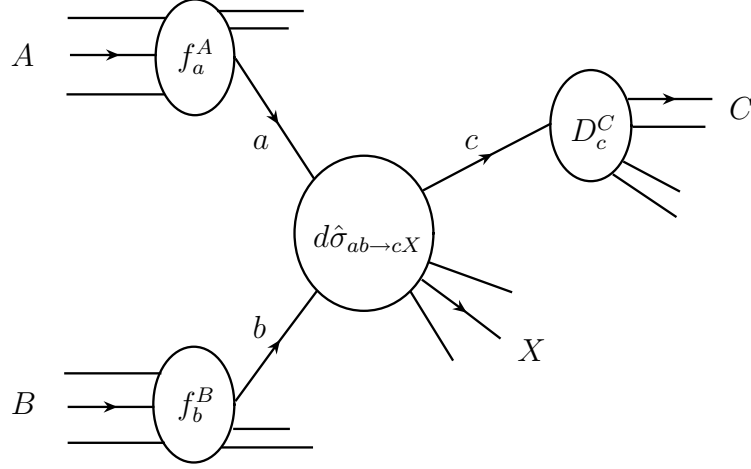


Figure 3.1: Sketch for the factorization of the hadronic cross section $d\sigma$ for the reaction $AB \rightarrow CX$ according to Eq. (3.2) into the parton distributions f_a^A and f_b^B , the fragmentation function D_c^C , and the partonic cross section $d\hat{\sigma}_{ab \rightarrow cX}$ for the underlying hard scattering $ab \rightarrow cX$.

experimentally observable hadrons as discussed in some detail in Sec. 2.5,

$$d(\Delta)\sigma = \sum_{a,b,c} \int dx_a dx_b dz_c (\Delta) f_a^A(x_a, \mu_f)(\Delta) f_b^B(x_b, \mu_f)(\Delta) D_c^C(z_c, \mu_f') \times d(\Delta) \hat{\sigma}_{ab \rightarrow cX}(x_a P_A, x_b P_B, P_C/z_c, \mu_r, \mu_f, \mu_f'). \quad (3.2)$$

We have sketched the factorization of the reaction $AB \rightarrow CX$ into its various components in Fig. 3.1. The sum in Eq. (3.2) is to be taken over all partonic channels $ab \rightarrow cX$ which contribute to the process under consideration. The x_a and x_b are the fractions of P_A and P_B taken by partons a and b , respectively. Parton c carries a momentum of P_C/z_c . The unpolarized and polarized hadronic cross sections in Eq. (3.2) are defined via

$$d\sigma \equiv \frac{1}{2} [d\sigma^{++} + d\sigma^{+-}] , \quad (3.3)$$

$$d\Delta\sigma \equiv \frac{1}{2} [d\sigma^{++} - d\sigma^{+-}] , \quad (3.4)$$

where the superscripts denote the helicities of hadrons A and B , and where we have used that parity conservation implies $d\sigma^{++} = d\sigma^{--}$ and $d\sigma^{-+} = d\sigma^{+-}$. In complete analogy, the partonic cross sections are given by

$$\begin{aligned} d\hat{\sigma}_{ab \rightarrow cX} &\equiv \frac{1}{2} [(d\hat{\sigma}_{ab \rightarrow cX})^{++} + (d\hat{\sigma}_{ab \rightarrow cX})^{+-}] , \\ d\Delta\hat{\sigma}_{ab \rightarrow cX} &\equiv \frac{1}{2} [(d\hat{\sigma}_{ab \rightarrow cX})^{++} - (d\hat{\sigma}_{ab \rightarrow cX})^{+-}] , \end{aligned} \quad (3.5)$$

with the superscripts now referring to partonic rather than hadronic helicities.

We wish to emphasize, however, that Eq. (3.2) does not apply any longer in the absence of a hard scale. If p_T acquires only low values and is not replaced by another large quantity serving as a hard scale, such as, e.g., the heavy quark mass in open charm production, the framework of pQCD breaks down. In the following we discuss the computation of partonic cross sections in some detail up to NLO, i.e., $\mathcal{O}(\alpha_s^3)$, at high p_T , where any contributions coming with inverse powers of p_T , so-called power or higher-twist corrections, can safely be neglected.

3.1 Born Cross Sections

By introducing dimensional regularization and the concepts of renormalization and factorization in Chap. 2 we have outlined the framework of a perturbative calculation in QCD. We are now in principle in a position to compute partonic scattering cross sections beyond the leading order approximation. Still, there are some subtleties we would like to emphasize by discussing the calculation of cross sections at Born level, i.e., $\mathcal{O}(\alpha_s^2)$, rather than immediately turn to the more involved evaluation of NLO corrections.

Within the scope of dimensional regularization, the n -dimensional differential partonic cross section $d(\Delta)\hat{\sigma}_{ab\rightarrow cd}$ for the scattering of two partons,

$$a(p_1) + b(p_2) \rightarrow c(p_3) + d(p_4) , \quad (3.6)$$

with the p_i denoting the momenta of the respective particles, at a partonic center of mass (c.m.s) energy \sqrt{s} is given by

$$\begin{aligned} d(\Delta)\hat{\sigma}_{ab\rightarrow cd} &= \frac{1}{2s} \frac{d^n p_3}{(2\pi)^{n-1}} \frac{d^n p_4}{(2\pi)^{n-1}} (2\pi)^n \overline{\sum_{\text{color, spin}}} |\mathcal{M}|_{ab\rightarrow cd}^2 \\ &\quad \times \delta^{(n)}(p_1 + p_2 - p_3 - p_4) \delta(p_3^2) \delta(p_4^2) . \end{aligned} \quad (3.7)$$

Here, $1/2s$ stems from the flux factor, which provides the proper mass dimension of the scattering cross section. The $d^n p_i/(2\pi)^{n-1}$ are the phase space factors for the outgoing particles. Unobserved momenta are usually integrated over. The first delta function accounts for momentum conservation in n dimensions, whereas the other two ensure that the on-shell condition for massless particles, $p_i^2 = 0$, is fulfilled. Depending on the polarization of the scattering partons, $\overline{\sum}$ denotes an appropriate sum over unobserved spin and color degrees of freedom for outgoing and average for incoming particles. Each quark in the initial state is ascribed a color average of $1/C_A$. Gluons receive a factor $1/(C_A^2 - 1)$. Since a fermion has two spin degrees of freedom, an additional factor of $1/2$ has to be included for unpolarized quarks. Special care has to be taken in the spin average of unpolarized gluons, since $2(1 + \epsilon)$ different polarization states are possible for a massless gauge boson in n dimensions as discussed in Sec. 2.2. Polarized partons are in a clearly defined spin state and thus do not receive a spin-averaging factor. The actual information on the hard scattering is contained in the partonic matrix elements $\mathcal{M}_{ab\rightarrow cd}$, which are computed up to a fixed order in α_s using the Feynman rules of App. A.

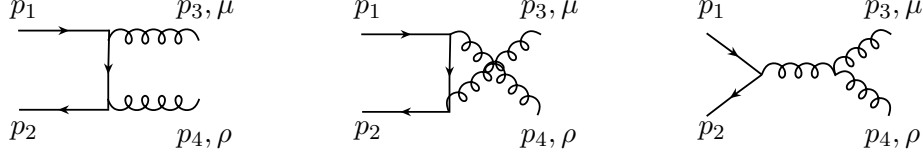


Figure 3.2: Feynman diagrams contributing to $q(p_1) \bar{q}(p_2) \rightarrow g(p_3) g(p_4)$ at tree-level.

In the following we will focus on processes with two polarized particles in the initial state. It will be convenient to explicitly decompose the matrix element squared $|\mathcal{M}|^2$ for the scattering of two partons with helicity h_1 and h_2 , respectively, into two parts,

$$\begin{aligned} |\overline{\mathcal{M}}|^2 &= \frac{1}{2} [|\mathcal{M}|^2(+, +) + |\mathcal{M}|^2(+, -)] , \\ \Delta|\mathcal{M}|^2 &= \frac{1}{2} [|\mathcal{M}|^2(+, +) - |\mathcal{M}|^2(+, -)] , \end{aligned} \quad (3.8)$$

with the arguments denoting the helicity of the incoming particles which can acquire the values ± 1 . The two components of \mathcal{M} do not mix,

$$|\mathcal{M}|^2(h_1, h_2) = |\overline{\mathcal{M}}|^2 + h_1 h_2 \Delta|\mathcal{M}|^2 , \quad (3.9)$$

and their squares can be identified with the unpolarized and the spin-dependent parts of the reaction, respectively, in a straightforward way. From now on we will label the helicity of parton i by h_i for fermions and λ_i for gauge bosons for clarity.

As an example, let us compute $\sum |\mathcal{M}|^2$ in n dimensions at LO for the process

$$q(p_1, h_1) + \bar{q}(p_2, h_2) \rightarrow g(p_3) + g(p_4) , \quad (3.10)$$

with initial state particles of definite helicities, whereas the produced gluons are unpolarized. All quarks and gluons are assumed to be massless, $p_i^2 = m_i^2 = 0$. It will turn out to be convenient to express all results in terms of quantities which are Lorentz-invariant like the scalar products of momenta – so-called Mandelstam variables, defined by

$$s = (p_1 + p_2)^2, \quad t = (p_1 - p_3)^2, \quad u = (p_2 - p_3)^2 . \quad (3.11)$$

Due to momentum conservation these variables are not independent of each other and obey

$$s + t + u = 0 . \quad (3.12)$$

The three contributions to $\mathcal{M}_{q\bar{q} \rightarrow gg}$ at tree level are depicted in Fig. 3.2. Using App. A we obtain for the first diagram

$$\mathcal{M}_1 = c_1 g_s^2 \sum_{\lambda_3, \lambda_4} \epsilon_\mu^*(p_3, \lambda_3) \epsilon_\rho^*(p_4, \lambda_4) \bar{v}(p_2, h_2) \gamma^\rho \frac{(\not{p}_1 - \not{p}_3)}{(-2p_1 \cdot p_3)} \gamma^\mu u(p_1, h_1) , \quad (3.13)$$

with a color factor c_1 to be determined below. Since the polarization states of the outgoing gluons, λ_3 and λ_4 , are not specified they have to be summed over. With a similar expression for the complex conjugate amplitude \mathcal{M}_1^* , we get after contracting repeated indices and rewriting the projection operators for the quarks according to Eq. (A.1)

$$\begin{aligned} \mathcal{M}_1 \mathcal{M}_1^* &= |\mathcal{M}_1|^2 \\ &= |c_1|^2 \frac{g_s^4}{t^2} \sum_{\lambda_3, \lambda_4} \epsilon_\mu(p_3, \lambda_3) \epsilon_\nu^*(p_3, \lambda_3) \epsilon_\rho(p_4, \lambda_4) \epsilon_\sigma^*(p_4, \lambda_4) \\ &\quad \times \text{Tr} [\not{p}_1 (1 - h_1 \gamma_5) \gamma^\nu (\not{p}_1 - \not{p}_3) \gamma^\sigma \not{p}_2 (1 + h_2 \gamma_5) \gamma^\rho (\not{p}_1 - \not{p}_3) \gamma^\mu] , \end{aligned} \quad (3.14)$$

where the trace $\text{Tr}[\dots]$ still has to be evaluated in n -dimensional Dirac space. This can be done, e.g., with the help of the algebraic computer package TRACER [57] in MATHEMATICA [85], which handles γ_5 and the Levi-Civita tensor $\epsilon^{\mu\nu\rho\sigma}$ in n dimensions correctly in the HVBM scheme. Note that $|\mathcal{M}_1|^2$ in Eq. (3.14) is indeed of the form (3.9), i.e., $|\mathcal{M}_1|^2 = \overline{|\mathcal{M}_1|^2} + h_1 h_2 \Delta |\mathcal{M}_1|^2$. Contributions proportional to h_1 or h_2 alone vanish due to the symmetry properties of the Lorentz structure. A separate calculation of the color factor yields

$$|c_1|^2 = \text{Tr}_c [T^a T^b T^b T^a] = C_A C_F^2 . \quad (3.15)$$

Here the trace is to be taken in color space as indicated by the subscript. As usual, repeated indices are summed over. Complicated color factors can be conveniently simplified by FEYN CALC [86], another tool for the evaluation of Feynman diagrams in MATHEMATICA. Expressions similar to Eq. (3.14) for $|\mathcal{M}_1|^2$ are obtained for the matrix elements squared $|\mathcal{M}_2|^2$ and $|\mathcal{M}_3|^2$ of the other diagrams contributing to $q\bar{q} \rightarrow gg$ at tree level as depicted in Fig. 3.2, and for the interference terms $\mathcal{M}_i \mathcal{M}_j^*$ needed for the computation of the sum

$$|\mathcal{M}_1 + \mathcal{M}_2 + \mathcal{M}_3|^2 . \quad (3.16)$$

The further evaluation of (3.16) requires the contraction of all Lorentz indices. Although this procedure is rather straightforward at leading order it will be crucial to organize it economically in more complex higher order calculations to restrict the computing time needed by the algebraic programs we use to a tolerable amount. In the unpolarized case, the summation over all gluonic helicity degrees of freedom in the final state has to be performed. Frequently this is done by using

$$\sum_{\lambda} \epsilon_\mu(p, \lambda) \epsilon_\nu^*(p, \lambda) = -g_{\mu\nu} . \quad (3.17)$$

This approach has the advantage that all gluonic polarization sums are replaced solely by the respective metric tensors. Further contractions of Lorentz indices in the $\mathcal{M}_i \mathcal{M}_j^*$ can then be carried out easily. However, the sum in Eq. (3.17) includes unphysical polarization degrees of freedom for external, physical gluons. The contributions resulting from such configurations have to be removed by including additional Feynman diagrams, where external gluons are replaced by ghosts. These diagrams are depicted in Fig. 3.3 for our

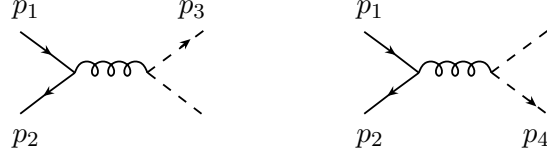


Figure 3.3: Ghost diagrams contributing to the reaction $q\bar{q} \rightarrow gg$ at tree-level.

sample process $q\bar{q} \rightarrow gg$. The full matrix element squared for this reaction then reads

$$|\mathcal{M}|^2 = |\mathcal{M}_1 + \mathcal{M}_2 + \mathcal{M}_3|^2 - |\mathcal{M}_4|^2 - |\mathcal{M}_5|^2, \quad (3.18)$$

where we have used that only ghost diagrams with equal flow of momentum can interfere with each other. In the reaction $q\bar{q} \rightarrow gg$ therefore only $|\mathcal{M}_4|^2$ and $|\mathcal{M}_5|^2$, but no interference terms of the type $\mathcal{M}_4\mathcal{M}_5^*$, or of \mathcal{M}_4 and \mathcal{M}_5 with one of the gluonic matrix elements \mathcal{M}_1 , \mathcal{M}_2 , and \mathcal{M}_3 contribute. As ghosts obey Fermionic statistics despite being scalar particles [40], the corresponding diagrams are added with opposite sign to the gluonic contributions and thereby subtract terms associated with unphysical polarization states.

An alternative approach avoids the introduction of external ghosts and thus significantly reduces the number of diagrams one has to evaluate. This is particularly useful in the computation of matrix elements beyond the leading order for processes including several external gluons, such as, e.g., the NLO reaction $gg \rightarrow ggg$. Instead of Eq. (3.17) the polarization sum now is replaced by the more complicated expression

$$\sum_{\lambda} \epsilon_{\mu}(p, \lambda) \epsilon_{\nu}^*(p, \lambda) = \left[-g_{\mu\nu} + \frac{p_{\mu}r_{\nu} + p_{\nu}r_{\mu}}{p \cdot r} \right], \quad (3.19)$$

where r_{μ} is an arbitrary vector fulfilling $r^2 = 0$ and $p \cdot r \neq 0$. Since r_{μ} has no physical meaning whatsoever it has to cancel in the final result. For processes involving a number m of external gluons it is sufficient to employ the full polarization tensor, Eq. (3.19), for $(m - 1)$ gluons. For the remaining polarization sum the simpler expression Eq. (3.17) can be used. This approach has the advantage of intrinsically taking into account only physical gluon polarizations. The introduction of external ghosts is no longer necessary. The drawback is the complexity of the polarization sum (3.19). In particular for processes involving several external gluons, the number of additional terms in intermediate steps of the Lorentz-index contraction in the respective matrix elements may become enormous and thus difficult to handle. In the end, certainly both methods of dealing with gluonic polarization sums must yield the same results.

Having summed over the unobserved polarization states of the external gluons it remains a simple task to perform the remaining contractions in the various contributions

to $q\bar{q} \rightarrow gg$. Finally we obtain

$$\begin{aligned} |\overline{\mathcal{M}}|^2 &= 8 g_s^4 C_F \left\{ (1-\varepsilon) \varepsilon - C_A^2 (1-\varepsilon) \frac{(t^2 + u^2)}{s^2} - C_A C_F (1-\varepsilon)^2 \frac{(t^2 + u^2)}{tu} \right\} , \\ \Delta |\mathcal{M}|^2 &= 8 g_s^4 C_F \left\{ (3+\varepsilon) \varepsilon + C_A^2 (1-\varepsilon) \frac{(t^2 + u^2)}{s^2} - C_A C_F (1+\varepsilon)^2 \frac{(t^2 + u^2)}{tu} \right\} . \end{aligned} \quad (3.20)$$

All hat-momenta – in principle present in calculations performed in the framework of dimensional regularization, as discussed in Sec. 2.2 – have been removed from these matrix elements, since such contributions are excluded by the kinematics of a $2 \rightarrow 2$ scattering process where at least one particle in the final state is observed. We wish to mention that the transition from n to four dimensions, which implies disregarding all terms proportional to ε or ε^2 , must not be performed at the level of matrix elements squared already. Such contributions can combine, for instance when used in the factorization of collinear singularities, to be discussed in Sec. 3.5, with inverse powers of ε to give finite contributions in the partonic cross sections. Therefore they must be retained throughout all intermediate steps of the analytical calculation. We can set $\varepsilon \rightarrow 0$ only in the very end. It can be easily seen that the result (3.20) remains invariant under the transformation $t \leftrightarrow u$. This symmetry corresponds to an exchange of the two indistinguishable gluons in the final state, $p_3 \leftrightarrow p_4$. We will encounter similar identities, so-called “crossing” relations, in the context of more complex matrix elements beyond the leading order and use them as important check for our calculations repeatedly.

In the unpolarized case, the matrix elements for all $2 \rightarrow 2$ QCD scatterings can be obtained by crossing from the generic reactions $q\bar{q}' \rightarrow q\bar{q}'$, $q\bar{q} \rightarrow q\bar{q}$, $qg \rightarrow qg$, and $g\bar{g} \rightarrow g\bar{g}$. We have depicted the relevant LO diagrams in Fig. 3.4. For spin-dependent processes this method does not work any longer in the diagrammatic approach we have used, since we have retained the helicities of two particles only. For example, the matrix element squared for a generic reaction with two polarized particles in the initial state, $\vec{a}\vec{b} \rightarrow cd$, does not contain information about a process where parton c or d is polarized, which we therefore have to calculate separately. Alternatively, the matrix elements squared for all $2 \rightarrow 2$ processes could be calculated by means of the helicity method which will be discussed in Sec. 3.3. In this approach the polarization of each scattering parton is retained. The helicity amplitudes for the generic processes specified above then serve as a tool to obtain matrix elements squared for all partonic processes involving polarized partons.

Having evaluated $|\mathcal{M}|^2$ we are now in a position to compute the unpolarized and polarized parts of the differential cross section, defined in Eq. (3.7). In experiment often the angle and transverse momentum of the produced particles, but no further degrees of freedom, are measured. Theoretically, such a cross section can be obtained by integrating the matrix elements squared, $|\mathcal{M}|^2$, for a specific reaction over the components of all momenta which are not observed. This is done by means of a phase space integration. The invariant differential phase space in n dimensions entering the definition of the differential cross section $d\hat{\sigma}_{i \rightarrow f}$ (3.7) for the scattering of i initial state to f final state massless partons

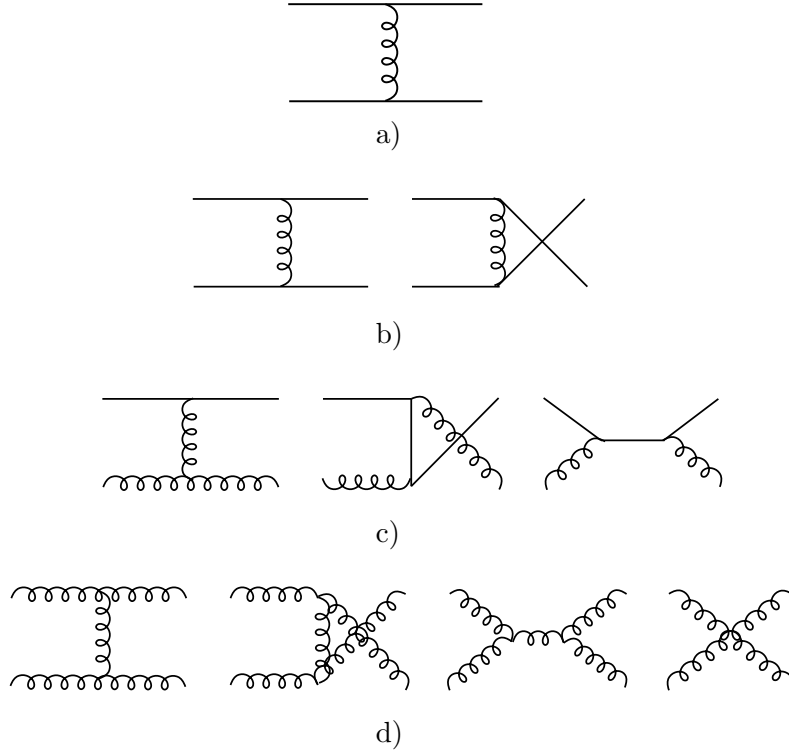


Figure 3.4: Leading order Feynman diagrams contributing to the generic $2 \rightarrow 2$ processes:
 a) $qq' \rightarrow qq'$, b) $qq \rightarrow qq$, c) $gg \rightarrow gg$, d) $gg \rightarrow gg$.

is given by

$$dPS_f = \left(\prod_f \frac{d^n p_f}{(2\pi)^{n-1}} \delta(p_f^2) \right) (2\pi)^n \delta^{(n)} \left(\sum_i p_i - \sum_f p_f \right). \quad (3.21)$$

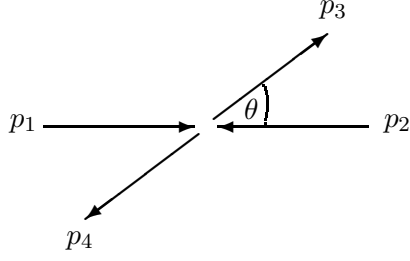
Let us first consider the differential phase space dPS_2 for the process investigated above with two partons in the initial and final states, respectively, and assume that p_4 is entirely unobserved, whereas the scattering angle θ of the third particle is measured. We can thus integrate over p_4 and the components of p_3 we are not interested in,

$$dPS_2 = \int \frac{d^n p_3}{(2\pi)^{n-1}} \int \frac{d^n p_4}{(2\pi)^{n-1}} (2\pi)^n \delta^{(n)}(p_1 + p_2 - p_3 - p_4) \delta(p_3^2) \delta(p_4^2). \quad (3.22)$$

The n -dimensional delta function can be used to perform the p_4 -integration, and we obtain

$$dPS_2 = (2\pi)^{2-n} \int d^n p_3 \delta(p_3^2) \delta([p_1 + p_2 - p_3]^2). \quad (3.23)$$

The further evaluation of dPS_2 is most easily performed in the c.m.s. frame of the incoming particles, where



$$\begin{aligned}\vec{p}_1 + \vec{p}_2 &= 0, \\ (p_1 + p_2)^2 &= (p_1^0 + p_2^0)^2 = s, \end{aligned} \quad (3.24)$$

and the zero components of the momenta denote their energy, for example p_1^0 stands for E_1 . In this particular frame, the argument of the second delta-function in (3.23), $[2p_1 \cdot p_2 - 2(p_1 + p_2) \cdot p_3]$, can be rewritten as $s - 2\sqrt{s}p_3^0$. After decomposing the n -dimensional p_3 -integration into an energy and $(n-1)$ momentum components, $d^n p_3 = dp_3^0 d^{n-1} \vec{p}_3$, the p_3^0 -integration can be performed and gives

$$dPS_2 = \frac{(2\pi)^{2-n}}{2\sqrt{s}} \int d^{n-1} \vec{p}_3 \delta\left(\frac{s}{4} - \vec{p}_3^2\right). \quad (3.25)$$

The spatial part \vec{p}_3 of the n -dimensional vector p_3 can be parametrized by its magnitude $|\vec{p}_3|$ and $n-2$ angles $\theta_1, \dots, \theta_{n-2}$. The components $p_3^1, p_3^2, \dots, p_3^{n-1}$ of \vec{p}_3 are given by

$$\begin{aligned} p_3^1 &= |\vec{p}_3| \cos \theta_1, \\ p_3^2 &= |\vec{p}_3| \sin \theta_1 \cos \theta_2, \\ &\vdots \\ p_3^{n-2} &= |\vec{p}_3| \sin \theta_1 \sin \theta_2 \dots \cos \theta_{n-2}, \\ p_3^{n-1} &= |\vec{p}_3| \sin \theta_1 \sin \theta_2 \dots \sin \theta_{n-2}, \end{aligned} \quad (3.26)$$

where $0 \leq \theta_i \leq \pi$ for $i = 1, \dots, n-3$, and $0 \leq \theta_{n-2} \leq 2\pi$. Identifying the angle θ_1 with the scattering angle θ the volume element in $(n-1)$ dimensions takes the form

$$d^{n-1} \vec{p}_3 = d|\vec{p}_3| |\vec{p}_3|^{n-2} (\sin \theta)^{n-4} d\cos \theta d\Omega_{(n-1)}, \quad (3.27)$$

with

$$d\Omega_{(n-1)} = (\sin \theta_2)^{n-4} (\sin \theta_3)^{n-5} \dots (\sin \theta_{n-2})^0 d\theta_2 d\theta_3 \dots d\theta_{n-2}. \quad (3.28)$$

Since only the scattering angle θ of particle 3 is observed, we can integrate over all other components. With the volume of angular phase space,

$$V(n) \equiv \int d\Omega_{(n)} = \frac{2\pi^{(n-1)/2}}{\Gamma\left(\frac{n-1}{2}\right)}, \quad (3.29)$$

we obtain

$$dPS_2 = \frac{(2\pi)^{2-n}}{4\sqrt{s}} V(n-1) \left(\frac{\sqrt{s}}{2}\right)^{n-3} d\cos \theta [1 - \cos^2 \theta]^{\frac{n-4}{2}}. \quad (3.30)$$

It is customary to re-express any dependence on $\cos\theta$ in terms of the frame independent Mandelstams s, t, u , which are related to the c.m.s. scattering angle via

$$t = -\frac{s}{2}(1 - \cos\theta) \ , \quad u = -\frac{s}{2}(1 + \cos\theta) \ . \quad (3.31)$$

The final expression for the two-particle phase space in $n = (4 - 2\varepsilon)$ dimensions, differential in t and u , is then

$$dPS_2 = \frac{1}{\Gamma(1 - \varepsilon)} \left(\frac{1}{4\pi} \right)^{1 - \varepsilon} \frac{1}{2s} \left[\frac{tu}{s} \right]^{-\varepsilon} \delta(s + t + u) du dt \ . \quad (3.32)$$

Having collected all the necessary building blocks we are now in a position to compute the (un)polarized partonic cross sections differential in t and u at $\mathcal{O}(\alpha_s^2)$. Taking into account that still appropriate prefactors for the spin ($A_{spin}, \tilde{A}_{spin}$) and color (A_{col}) average have to be included, we arrive at the final result

$$\begin{aligned} \frac{d\hat{\sigma}_{ab \rightarrow cX}}{du dt} &= \frac{1}{2s} \frac{dPS_2}{du dt} A_{col} A_{spin} \overline{|\mathcal{M}|}_{ab \rightarrow cd}^2 \ , \\ \frac{d\Delta\hat{\sigma}_{ab \rightarrow cX}}{du dt} &= \frac{1}{2s} \frac{dPS_2}{du dt} A_{col} \tilde{A}_{spin} \Delta|\mathcal{M}|_{ab \rightarrow cd}^2 \ . \end{aligned} \quad (3.33)$$

The partonic cross sections at LO are known for all possible $2 \rightarrow 2$ reactions in QCD, see, for example, Ref. [87] for the 4-dimensional case. The n -dimensional results are listed for the processes relevant in this thesis in App. B. We will turn to the more interesting case of NLO contributions in the following.

3.2 Virtual Contributions

Corrections to the Born cross sections discussed above arise if additional unobserved – virtual – particles are emitted and re-absorbed as the scattering happens. Since each such interaction brings in an extra factor of g_s in the corresponding matrix elements, a $2 \rightarrow 2$ diagram with one virtual emission is altogether of $\mathcal{O}(g_s^4)$. Therefore, at $\mathcal{O}(\alpha_s^3)$ only the interference of these diagrams with matrix elements at Born level can contribute to the relevant partonic cross sections. Interferences of $\mathcal{O}(g_s^4)$ diagrams among themselves, as well as reactions with more than one virtual emission, are already of higher order in the perturbative expansion and will not be considered here. They will become relevant, of course, in a next-to-next-to-leading order computation.

The corrections to LO diagrams we have to consider are then selfenergies of internal or external parton legs, vertex corrections, and box diagrams, as sketched in Fig. 3.5. The latter are UV finite and therefore not subject to renormalization. On the other hand, selfenergies and vertex corrections exhibit IR as well as UV divergencies and thus have to be renormalized properly. Although this procedure is straightforward and can in principle be performed as described in Sec. 2.3, it requires some efforts to subtract the poles for all UV-divergent diagrams in practice. However, the $\overline{\text{MS}}$ -renormalized building blocks needed for the computation of such contributions have been published, e.g., in

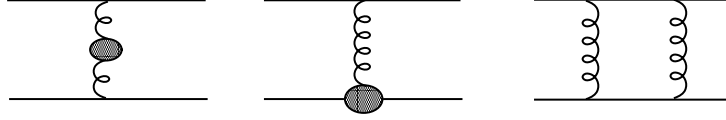
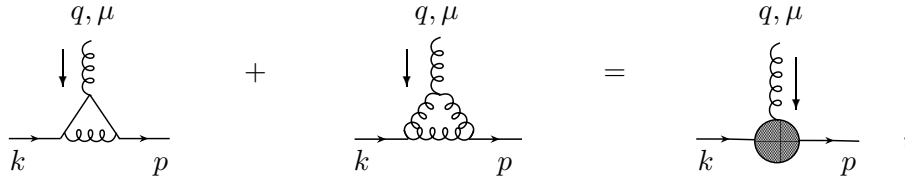


Figure 3.5: Schematically depicted NLO corrections to the process $qq' \rightarrow qq'$.

Ref. [88] in Feynman gauge. These expressions allow us to calculate diagrams including selfenergy or vertex corrections in the $\overline{\text{MS}}$ scheme without actually renormalizing each UV divergence ourselves. The most complicated, UV-finite box diagrams cannot be found in the literature and have to be calculated from scratch. For the computation of diagrams with virtual emissions we use that each $2 \rightarrow 2$ scattering is characterized by the same kinematics (3.11), (3.12) and phase space (3.32) as the Born diagrams.

3.2.1 Vertex and Selfenergy Corrections

The emission and reabsorption of an additional gluon at any of the quark-gluon vertices, symbolically depicted as



requires the calculation of vertex corrections. Here and in the following we will use “blobs” ($\text{---}\bullet\text{---}$) to generically sketch these $\mathcal{O}(\alpha_s)$ corrections. Rather than explicitly renormalizing such contributions, the results of Ref. [88] allow us to simply replace the Feynman rule for an ordinary quark-gluon vertex by the exact expression for the $\overline{\text{MS}}$ -renormalized vertex,

$$-ig_s \gamma^\mu \rightarrow -ig_s \frac{\alpha_s}{4\pi} \Lambda^\mu, \quad (3.34)$$

where Λ_μ is a function of the momenta entering the vertex, q , k , and p , and the renormalization scale. The renormalized expressions still contain IR poles. We will take care of these later. A replacement similar to (3.34) is possible for the ghost-gluon vertex,

$$g_s f^{abc} p^\mu \rightarrow g_s \frac{\alpha_s}{4\pi} f^{abc} H^\mu. \quad (3.35)$$

The explicit form of the Λ^μ and H^μ depends on which parton at the vertex goes on-shell. Since these expressions are rather lengthy we refrain from quoting them here explicitly and refer the interested reader to Table B.II of Ref. [88]. For the three-gluon vertex at NLO we have to insert

$$= -g_s \frac{\alpha_s}{4\pi} f^{abc} G^{\mu\nu\lambda}(q, k, p) , \quad (3.36)$$

with a , b , and c denoting the color indices of the gluons, as usual, and $p^2 = k^2 = 0$, but $q^2 \neq 0$. Contrary to the three-gluon vertex at LO, $G^{\mu\nu\lambda}$ is not symmetric in q , k , and p , which requires some care in the practical implementation of this effective Feynman rule. The explicit form of $G^{\mu\nu\lambda}$ is given in Table B.III of Ref. [88].

Similar to the vertex corrections, insertions for selfenergies of quarks, ghosts, and gluons are tabulated:

$$= -i \not{p} C_F \frac{\alpha_s}{4\pi} \Sigma(p^2) , \quad (3.37)$$

$$= -i p^2 C_A \frac{\alpha_s}{4\pi} D(p^2) , \quad (3.38)$$

$$= i \frac{\alpha_s}{4\pi} \Pi^{\mu\nu}(p) . \quad (3.39)$$

The expressions for the $\Sigma(p^2)$, $D(p^2)$, and $\Pi(p)$, which differ for on-shell and off-shell lines, $p^2 = 0$ and $p^2 \neq 0$, respectively, as explicitly discussed for the quark selfenergy in Sec. 2.3.1, can be found in Table B.I of Ref. [88].

The procedure of calculating selfenergy corrections to Born diagrams is rather straightforward as long as internal lines are concerned. E.g., considering the selfenergy of the virtual gluon in $q(p_1) q'(p_2) \rightarrow q(p_3) q'(p_4)$ scattering,

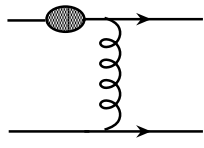
$$\Rightarrow ,$$

yields the $\mathcal{O}(\alpha_s^2)$ matrix element

$$i\mathcal{M}_s = c_{born} \bar{u}(p_3)(-ig_s\gamma_\mu)u(p_1) \frac{(-i)}{(p_3 - p_1)^2} \times \left[i \frac{\alpha_s}{4\pi} \Pi^{\mu\nu}(p_3 - p_1) \right] \frac{(-i)}{(p_3 - p_1)^2} \bar{u}(p_4)(-ig_s\gamma_\nu)u(p_2), \quad (3.40)$$

with the same color factor c_{born} as for the corresponding LO diagram. The interference $\mathcal{M}_s\mathcal{M}_{born}^*$ can now easily be calculated with the techniques introduced in Sec. 3.1. Diagrams with internal quark- and ghost selfenergies are treated likewise.

Care has to be taken in the calculation of virtual corrections to external legs, as already mentioned in Sec. 2.3.1. If, for instance, in the afore-mentioned process a virtual gluon is emitted from the external quark line we obtain the matrix element

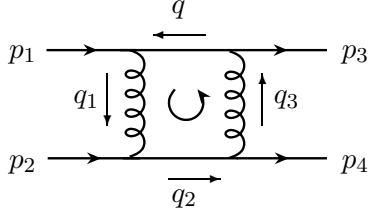


$$i\mathcal{M}_e = c_{born} \bar{u}(p_4)(-ig_s\gamma_\mu)u(p_2) \frac{(-i)}{t} \times \bar{u}(p_3)(-ig_s\gamma^\mu) \frac{i\not{p}_1}{p_1^2} \left[-i\not{p}_1 C_F \frac{1}{2} \frac{\alpha_s}{4\pi} \Sigma(p_1^2) \right] u(p_1), \quad (3.41)$$

where we have included the extra factor of $1/2$ required for the computation of selfenergy corrections for external legs as discussed in Sec. 2.3.1. Since $p_1^2 = 0$ for the on-shell quark, \mathcal{M}_e seems to be ill-defined due to the internal quark propagator which brings a factor of $1/p_1^2$. However, if the numerator of this propagator, \not{p}_1 , is combined with the extra \not{p}_1 in the expression for the quark selfenergy, it exactly cancels the apparent singularity. Afterwards the limit $p_1 \rightarrow 0$, including the replacement $\Sigma(p_1) \rightarrow \Sigma(0)$, can safely be taken. The evaluation of $\mathcal{M}_e\mathcal{M}_{born}^*$ is then a simple task. Generally, the computation of diagrams with selfenergy corrections for external partons with momentum q is performed by explicitly putting them off the mass-shell, $q^2 \neq 0$, and retaining any terms proportional to q^2 . In the course of the calculation any denominators of the form $1/q^2$ will cancel out. At the end one can safely set $q^2 = 0$. The expressions for selfenergies of external parton legs, $\Sigma(0)$, $D(0)$, and $\Pi(0)$, cannot be obtained from those for off-shell partons but are tabulated separately. Like $\Sigma(0)$, explicitly calculated in Sec. 2.3.1, also the selfenergies of on-shell ghosts and gluons exhibit poles, reflecting the IR-sensitivity of these contributions.

3.2.2 Box Contributions

As mentioned above, diagrams including boxes have to be calculated from scratch, since for such contributions no precalculated building blocks are available like those for the vertex and selfenergy corrections discussed in the previous section. Because of the closed loops in each of these graphs n -dimensional integrals over the loop momentum have to be evaluated, as illustrated for a box contribution \mathcal{M}_b to the process $q q' \rightarrow q q'$,



$$\begin{aligned}
q_1 &= q + p_1, \\
q_2 &= q + p_1 + p_2, \\
q_3 &= q + p_1 + p_2 - p_4.
\end{aligned} \tag{3.42}$$

Here, q is the loop momentum which is unobserved and can take any value. Therefore it has to be integrated over. The momenta of the remaining internal lines, q_1 , q_2 , and q_3 , are determined by imposing momentum conservation at each vertex. One then arrives at

$$\begin{aligned}
i\mathcal{M}_b &= c_{box} \int \frac{d^n q}{(2\pi)^n} \bar{u}(p_3) (-ig_s \gamma_\mu) \frac{(-i \not{q})}{q^2} (-ig_s \gamma_\nu) u(p_1) \\
&\quad \times \frac{(-i)}{q_1^2} \frac{(-i)}{q_3^2} \bar{u}(p_4) (-ig_s \gamma^\mu) \frac{i \not{q}_2}{q_2^2} (-ig_s \gamma^\nu) u(p_2).
\end{aligned} \tag{3.43}$$

with the appropriate color factor c_{box} . The further evaluation of this matrix element requires the computation of the integral

$$\int \frac{d^n q}{(2\pi)^n} \frac{q^\rho q_2^\sigma}{q^2 q_1^2 q_2^2 q_3^2} = (p_1 + p_2)^\sigma \int \frac{d^n q}{(2\pi)^n} \frac{q^\rho}{q^2 q_1^2 q_2^2 q_3^2} + \int \frac{d^n q}{(2\pi)^n} \frac{q^\rho q^\sigma}{q^2 q_1^2 q_2^2 q_3^2}, \tag{3.44}$$

which can be reduced by means of a Passarino-Veltman decomposition [89] into a set of calculable scalar integrals, as outlined in App. C. Applying this procedure, one ends up with an expression for $i\mathcal{M}_b$ which no longer depends on the loop momentum q . Then $\mathcal{M}_b \mathcal{M}_{box}^*$ can be calculated as usual by evaluating traces and contracting all Lorentz indices in n dimensions. Since box diagrams are UV finite they need not be renormalized. IR divergencies show up as poles in ε in the matrix elements and have to be retained carefully. Their cancelation will be discussed later.

3.3 Helicity Method

Although the procedure of calculating partonic matrix elements diagram by diagram is quite straightforward, it takes some efforts to actually evaluate all relevant contributions to a certain reaction, in particular beyond the leading order. We therefore briefly discuss an alternative method, which not only systematizes the computation of $2 \rightarrow 2$ partonic cross sections, but also provides us with an important tool to double-check the results for the virtual corrections obtained in the afore described, conventional manner.

The basic idea of this “helicity method” [90, 91] is to make as much use as possible of the color and helicity structure of partonic scattering amplitudes to reduce the number and complexity of the expressions showing up in intermediate steps of a calculation to a minimum amount. One starts with the calculation of individual, so-called “helicity amplitudes”, which describe the scattering of partons with definite helicities and – after squaring – enter the relevant partonic cross sections. Only in the end of the calculation

helicity and color of the respective partons are fixed. A summation over the appropriate degrees of freedom will then yield the wanted unpolarized or polarized matrix elements squared for the reaction. The strength of this approach is that it exploits symmetry relations and conservation laws extensively, thereby ruling out many, in principle contributing, amplitudes from the very beginning which significantly simplifies further steps of the calculation. In contrast to that, symmetry principles are rarely implemented in the conventional “diagram by diagram” technique, where they manifest themselves often only in the end of a lengthy calculation. A minor drawback of the helicity method is that it does not a priori yield partonic matrix elements in the HVBM regularization scheme we employ throughout this work. Due to the genuine singularity structure of a generic virtual contribution \mathcal{V} to a $2 \rightarrow 2$ scattering process it is, however, possible to unambiguously transform results from a given to another regularization scheme. In the following we will label the regularization scheme specific to the helicity method as “helicity scheme”.

In Ref. [92], NLO corrections to the basic $2 \rightarrow 2$ reactions $qq' \rightarrow qq'$, $qq \rightarrow qq$, $gg \rightarrow q\bar{q}$, and $gg \rightarrow gg$ have been calculated within the helicity scheme. From these results virtual corrections to all QCD tree-level diagrams can be obtained by simple crossing relations, since the polarizations of all scattering partons are kept in the corresponding helicity amplitudes. For example, $qq \rightarrow qq$ emerges from $gg \rightarrow q\bar{q}$ after exchanging the gluon in the initial state with the outgoing antiquark. In terms of Mandelstam variables this amounts to an exchange of s and t , whereas u remains unaffected. Transforming the antiquark into a quark requires an additional overall factor of (-1) , thus yielding $|\mathcal{M}|_{qq \rightarrow qq}^2(s, t, u) = -|\mathcal{M}|_{gg \rightarrow q\bar{q}}^2(t, s, u)$. It has been shown that each of the resulting NLO contributions is of the form

$$\begin{aligned} \mathcal{V}^{(h)}(s, t, u) = & \mathcal{B}^{(h)}(s, t, u) \left\{ -\frac{1}{\varepsilon^2} \sum_n C(a_n) - \frac{1}{\varepsilon} \sum_n \gamma(a_n) \right\} \\ & + \frac{1}{\varepsilon} \sum_{m < n} \ln \left(\frac{2p_n \cdot p_m}{s} \right) \tilde{\mathcal{B}}_{mn}^{(h)}(s, t, u) + \tilde{\mathcal{V}}^{(h)}(s, t, u) , \end{aligned} \quad (3.45)$$

where the sums run over all external legs ($m, n = 1 \dots 4$), and the p_i denote the external parton momenta. $C(a)$ is the color charge of parton a , with a being either a gluon (g) or a quark (q),

$$C(g) = C_A , \quad C(q) = C_F , \quad (3.46)$$

and the $\gamma(a)$ are defined via the behavior of the Altarelli-Parisi kernel $P_{aa}(\zeta)$ near $\zeta = 1$,

$$\int_z^1 d\zeta P_{aa}(\zeta) = 2C(a) \ln(1-z) + \gamma(a) + \mathcal{O}(1-z) , \quad (3.47)$$

yielding

$$\gamma(g) = \frac{\beta_0}{2} , \quad \gamma(q) = \frac{3C_F}{2} . \quad (3.48)$$

The $\mathcal{B}^{(h)}$ denotes the four dimensional Born cross section for the reaction under consideration, whereas the $\tilde{\mathcal{B}}_{mn}^{(h)}$ stand for the “color-linked” matrix elements squared in the helicity scheme. The latter can be obtained from the tree-level diagrams for the respective $2 \rightarrow 2$

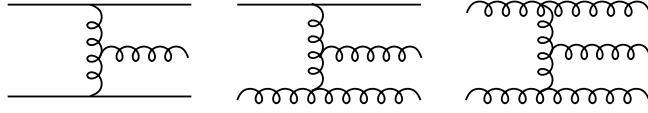


Figure 3.6: Contributions to the generic $2 \rightarrow 3$ processes: $qq \rightarrow qqg$, $qg \rightarrow qgg$, $gg \rightarrow ggg$.

process by an appropriate modification of color factors and are listed in Ref. [93]. The finite remainder is contained in $\tilde{\mathcal{V}}^{(h)}$. To establish the relationship between the helicity scheme result $\mathcal{V}^{(h)}$ and the corresponding quantity $\mathcal{V}^{(dr)}$ in conventional dimensional regularization, it is important to note that any dependence on the regularization scheme resides in the coefficients of the poles, $\mathcal{B}^{(h)}$ and $\tilde{\mathcal{B}}_{mn}^{(h)}$. Whereas in the helicity scheme they are genuinely four-dimensional, the respective quantities in conventional dimensional regularization are calculated in n dimensions making use of the HVBM scheme. The finite expressions $\tilde{\mathcal{V}}^{(h)} = \tilde{\mathcal{V}}^{(dr)}$ are not affected by any such scheme convention. Thus, simply replacing the $\mathcal{B}^{(h)}$ and $\tilde{\mathcal{B}}_{mn}^{(h)}$ by their n -dimensional counterparts calculated in the HVBM scheme transforms $\mathcal{V}^{(h)}$ into $\mathcal{V}^{(dr)}$, the virtual correction to a $2 \rightarrow 2$ cross section in conventional dimensional regularization.

With this transformation prescription for virtual cross sections in different regularization schemes in mind we are in a position to use the results of Ref. [93] as starting point for getting all unpolarized and polarized $2 \rightarrow 2$ cross sections at NLO in conventional dimensional regularization. We find that the results for the virtual corrections of the basic QCD cross sections obtained by means of this helicity method are – after the appropriate scheme transformation – in perfect agreement with those computed in the “standard way” diagram by diagram.

3.4 Real Contributions

In addition to the virtual corrections to the Born cross sections discussed above, a full NLO calculation includes contributions from processes where an extra (real) parton is emitted,

$$a(p_1) + b(p_2) \rightarrow c(p_3) + d(p_4) + e(p_5) . \quad (3.49)$$

Again, partonic cross sections of $\mathcal{O}(\alpha_s^3)$ arise. In analogy to the $2 \rightarrow 2$ reactions discussed in the previous sections, all $2 \rightarrow 3$ processes can be derived from the basic scatterings $qq' \rightarrow qq'g$, $qq \rightarrow qqg$, $qg \rightarrow qgg$, and $gg \rightarrow ggg$ after an appropriate crossing procedure in the unpolarized case. We have sketched some examples for these reactions in Fig. 3.6. Rather than using crossing relations for the computation of matrix elements we will calculate the cross sections for all partonic $2 \rightarrow 3$ processes from scratch and employ crossing as a valuable check for our results. This is anyway required in the polarized case as outlined in Sec. 3.1.

The actual computation of the relevant matrix elements proceeds along the same lines as for a LO calculation, but requires the evaluation of a significantly larger number of diagrams. Due to the additional parton leg in the final state the calculation of $2 \rightarrow 3$ scattering diagrams can be rather time consuming. In particular, the evaluation of traces with many Dirac matrices, which arise from diagrams including several quarks, and of expressions involving the Levi-Civita tensor, which emerges whenever polarized gauge bosons are to be considered, makes the analytical evaluation of Feynman diagrams at NLO – though straightforward – a tedious task.

Above that, the “unphysical” hat components of n -dimensional momenta can no longer be disregarded in a calculation involving more than one unobserved parton in the final state. It has been mentioned in Sec. 2.2 that in principle within the framework of dimensional regularization any momentum k_μ is defined in $n = 4 - 2\varepsilon$ dimensions, the $(n - 4)$ -dimensional components being denoted by \hat{k}_μ . However, measuring the momenta of three particles and imposing momentum conservation in a $2 \rightarrow 2$ process ensures that the cross section for such a reaction is free of contributions from hat momenta. This is no longer the case for a $2 \rightarrow 3$ scattering, where only the sum of hat momenta of all unobserved particles is fixed by kinematics. Assuming that partons a , b , and c are observed in experiment, the hat momenta of partons d and e in (3.49), \hat{p}_4 and \hat{p}_5 are equal, but opposite. They can acquire any arbitrary value as long as their sum vanishes, i.e., $\hat{p}_4 + \hat{p}_5 = 0$. This will be used for the parametrization of momenta presented in App. D. Once we set $\hat{p}_4 = -\hat{p}_5$ we have to retain all terms including any dependence on \hat{p}_4 throughout our calculation and take them carefully into account in the phase space integration.

3.4.1 Three-Body Phase Space

The calculation of the phase space for a $2 \rightarrow 3$ scattering with two unobserved particles in the final state differs considerably from the $2 \rightarrow 2$ case where the momentum components of only one particle have to be integrated out completely. As a first step, we introduce a set of ten Mandelstam variables to express all possible scalar products in terms of invariants,

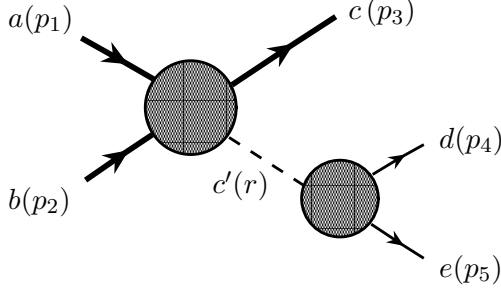
$$\begin{aligned} s &= (p_1 + p_2)^2, & t &= (p_1 - p_3)^2, & u &= (p_2 - p_3)^2, \\ s_{12} &= (p_3 + p_4)^2, & t_2 &= (p_1 - p_4)^2, & u_2 &= (p_2 - p_4)^2, \\ s_{13} &= (p_3 + p_5)^2, & t_3 &= (p_1 - p_5)^2, & u_3 &= (p_2 - p_5)^2. \\ s_{23} &= (p_4 + p_5)^2, \end{aligned} \quad (3.50)$$

This set is by no means unique, but suitable for our purposes. Due to momentum conservation the variables are related to each other via

$$\begin{aligned} u_3 &= -s - u - u_2, \\ t_3 &= -s - t - t_2, \\ s_{23} &= s + t + u, \\ s_{13} &= s + t_2 + u_2, \\ s_{12} &= -s - t - t_2 - u - u_2. \end{aligned} \quad (3.51)$$

We will make extensive use of these relations in the phase space integration of partonic matrix elements squared to be discussed in the following section.

Now we have to deal with the actual three-body phase space. A convenient way for handling this type of kinematics is to split up of the full $2 \rightarrow 3$ phase space into a $2 \rightarrow 2$ scattering, followed by a $1 \rightarrow 2$ decay:



Here, we introduce the auxiliary variable

$$r = p_4 + p_5, \quad (3.52)$$

for the momentum of the intermediate state c' which subsequently decays into the two unobserved partons d and e .

From the general expression for the Lorentz invariant phase space in n dimensions, Eq. (3.21), we obtain the required three-particle differential phase space,

$$dPS_3 = \int \frac{d^n p_3}{(2\pi)^{n-1}} \int \frac{d^n p_4}{(2\pi)^{n-1}} \int \frac{d^n p_5}{(2\pi)^{n-1}} \times (2\pi)^n \delta^{(n)}(p_1 + p_2 - p_3 - p_4 - p_5) \delta(p_3^2) \delta(p_4^2) \delta(p_5^2), \quad (3.53)$$

which can then be rewritten as

$$dPS_3 = (2\pi)^{(3-2n)} \int ds_{23} \overbrace{\int d^n p_3 d^n r \delta^{(n)}(p_1 + p_2 - p_3 - r) \delta(p_3^2) \delta(r^2 - s_{23})}^I \times \underbrace{\int d^n p_4 d^n p_5 \delta^{(n)}(r - p_4 - p_5) \delta(p_4^2) \delta(p_5^2)}_{II}. \quad (3.54)$$

Apart from some constant prefactors, contribution I in Eq. (3.54) resembles the usual two-particle phase space [cf. Eq. (3.22)] for the massless parton c and the (unobserved) state c' with an effective mass $r^2 = s_{23}$. Proceeding in the same way as for the ordinary $2 \rightarrow 2$ phase space we obtain

$$I = \frac{\pi^{\frac{n-2}{2}}}{\Gamma(\frac{n-2}{2})} d\cos\theta \left[\frac{(s - s_{23})^2}{4s} \right]^{\frac{n-3}{2}} (\sin\theta)^{n-4} \frac{1}{2\sqrt{s}}, \quad (3.55)$$

with θ denoting the scattering angle of parton c with respect to \vec{p}_1 .

The $1 \rightarrow 2$ phase space II in Eq. (3.54) is most easily evaluated in the rest frame of the auxiliary state c' where $r = (r_0, \vec{0})$. The p_3 -integration is performed by using the n -dimensional delta function. For the remaining integrals we have to keep in mind that

the hat momentum \hat{p}_4 does not necessarily vanish in a $2 \rightarrow 3$ scattering process including polarized partons. We thus have to carefully split the volume element into a four- and an $(n-4)$ -dimensional part,

$$d^n p_4 = d^4 p_4 d^{n-4} \hat{p}_4 . \quad (3.56)$$

Since the matrix elements we are considering depend only on the magnitude of \hat{p}_4 the integration over its angular components can be done using

$$d^{n-4} \hat{p}_4 = d|\hat{p}_4| |\hat{p}_4|^{n-5} d\Omega_{(n-3)} = \frac{1}{2} d(\hat{p}_4^2) (\hat{p}_4^2)^{\frac{n-6}{2}} d\Omega_{(n-3)} . \quad (3.57)$$

The spatial components of $d^4 p_4$ in Eq. (3.56) are then parametrized according to Eq. (D.2) in App. D in terms of the angles θ_1 , and θ_2 , with $p_4^0 = \sqrt{s_{23}}/2$ and p_4^y arbitrary. Rewriting the delta functions in terms of the relevant variables and performing the p_4^0 and p_4^y integrations one ends up with

$$II = \frac{\pi^{\frac{n-4}{2}}}{\Gamma\left(\frac{n-4}{2}\right)} \frac{\sqrt{s_{23}}}{8} \int d\theta_1 d\theta_2 \sin^2 \theta_1 \sin \theta_2 d(\hat{p}_4^2) (\hat{p}_4^2)^{\frac{n-6}{2}} \frac{1}{\sqrt{\frac{s_{23}}{4} \sin^2 \theta_1 \sin^2 \theta_2 - \hat{p}_4^2}} . \quad (3.58)$$

Now I and II can be combined to give

$$\begin{aligned} dPS_3 &= \frac{(4\pi)^{-n}}{\Gamma\left(\frac{n-2}{2}\right) \Gamma\left(\frac{n-4}{2}\right)} \frac{1}{2\sqrt{s}} \int ds_{23} \sqrt{s_{23}} d\cos \theta (\sin \theta)^{n-4} \left[\frac{(s - s_{23})^2}{4s} \right]^{\frac{n-3}{2}} \\ &\times \int d\theta_1 d\theta_2 \sin^2 \theta_1 \sin \theta_2 d(\hat{p}_4^2) (\hat{p}_4^2)^{\frac{n-6}{2}} \frac{1}{\sqrt{\frac{s_{23}}{4} \sin^2 \theta_1 \sin^2 \theta_2 - \hat{p}_4^2}} . \end{aligned} \quad (3.59)$$

Keeping in mind that $s_{23} = s + t + u$, $t = (p_1 - p_3)^2$, and $u = (p_2 - p_3)^2$ we can easily express the integration variables s_{23} and $\cos \theta$ in terms of the more familiar Mandelstam variables s , t , and u ,

$$\cos \theta = \frac{u - t}{u + t} , \quad ds_{23} d\cos \theta = -\frac{2}{t + u} du dt . \quad (3.60)$$

Demanding a real value for the square root $\sqrt{\frac{s_{23}}{4} \sin^2 \theta_1 \sin^2 \theta_2 - \hat{p}_4^2}$ sets an upper bound for the \hat{p}_4^2 integration:

$$\hat{p}_{4,max}^2 = \frac{s_{23}}{4} \sin^2 \theta_1 \sin^2 \theta_2 . \quad (3.61)$$

It is then convenient to introduce a dimensionless integration variable,

$$x = \frac{\hat{p}_4^2}{\hat{p}_{4,max}^2} . \quad (3.62)$$

The emerging integral,

$$\int_0^1 dx \frac{x^{\frac{n-6}{2}}}{\sqrt{1-x}} = B\left(\frac{1}{2}, \frac{n-4}{2}\right) , \quad (3.63)$$

with the Euler Beta function $B(x, y)$, is normalized such that it gives unity, if the matrix element which is to be phase space integrated is free of any dependence on hat momenta as, e.g., in the unpolarized case. Finally, we obtain for the three-particle phase space differential in u and t

$$\begin{aligned} \frac{dPS_3}{dtdu} &= \frac{1}{(4\pi)^n} \frac{1}{\Gamma(n-3)} \frac{1}{s} (s_{23})^{\frac{n-4}{2}} \left[\frac{tu}{s} \right]^{\frac{n-4}{2}} \\ &\times \int d\theta_1 d\theta_2 (\sin \theta_1)^{n-3} (\sin \theta_2)^{n-4} \frac{1}{B\left(\frac{1}{2}, \frac{n-4}{2}\right)} \int_0^1 dx \frac{x^{\frac{n-6}{2}}}{\sqrt{1-x}}. \end{aligned} \quad (3.64)$$

Sometimes it is useful to express all Mandelstams in terms of the dimensionless variables

$$v = 1 + \frac{t}{s} \quad \text{and} \quad w = \frac{-u}{s+t}. \quad (3.65)$$

The corresponding phase space then takes the form [24]

$$\begin{aligned} \frac{dPS_3}{dvdw} &= \frac{s}{(4\pi)^4 \Gamma(1-2\varepsilon)} \left[\frac{4\pi}{s} \right]^{2\varepsilon} v^{1-2\varepsilon} (1-v)^{-\varepsilon} [w(1-w)]^{-\varepsilon} \\ &\times \int d\theta_1 d\theta_2 (\sin \theta_1)^{1-2\varepsilon} (\sin \theta_2)^{-2\varepsilon} \frac{1}{B\left(\frac{1}{2}, -\varepsilon\right)} \int_0^1 dx \frac{x^{-1-\varepsilon}}{\sqrt{1-x}}. \end{aligned} \quad (3.66)$$

3.4.2 Phase Space Integration

Contributions to differential cross sections are calculated analogously to the LO case (3.33) by integrating the respective matrix elements squared over the entire phase space of the unobserved partons, attaching the flux factor, and by appropriately averaging over spin and color degrees of freedom:

$$\begin{aligned} \frac{d\hat{\sigma}_{ab \rightarrow cX}}{dv dw} &= \frac{1}{2s} \frac{dPS_3}{dv dw} A_{col} A_{spin} |\overline{\mathcal{M}}|_{ab \rightarrow cde}^2, \\ \frac{d\Delta\hat{\sigma}_{ab \rightarrow cX}}{dv dw} &= \frac{1}{2s} \frac{dPS_3}{dv dw} A_{col} \tilde{A}_{spin} \Delta |\mathcal{M}|_{ab \rightarrow cde}^2. \end{aligned} \quad (3.67)$$

As mentioned above, the x -integration gives unity for terms independent of hat momenta and

$$\frac{1}{B\left(\frac{1}{2}, -\varepsilon\right)} \int_0^1 dx \frac{x^{-(1+\varepsilon)}}{\sqrt{1-x}} \hat{p}_4^2 = -\frac{2\varepsilon}{1-2\varepsilon} \frac{s_{23}}{4} \sin^2 \theta_1 \sin^2 \theta_2 \quad (3.68)$$

for terms being proportional to \hat{p}_4^2 , which is related to x as specified in Eq. (3.62). No other functional dependence on \hat{p}_4 arises in the matrix elements squared for a $2 \rightarrow 3$ partonic scattering reaction at $\mathcal{O}(\alpha_s^3)$. Note that according to Eq. (3.68) all integrals containing hat momenta acquire an overall factor of ε and thus contribute in the limit $\varepsilon \rightarrow 0$ only in combination with $1/\varepsilon$ -poles as we will see below.

To evaluate the angular integrals one parametrizes each expression of Mandelstam variables in the matrix elements squared in the rest frame of $p_4 + p_5$ with the help of one of the three “sets” for the momenta p_1 , p_2 , and p_3 given in App. D. The use of the appropriate set is crucial, since all integrals have to be cast into the standard form [94]

$$\begin{aligned} I^{(j,l)} &= \int_0^\pi d\theta_1 \sin^{1-2\varepsilon} \theta_1 \int_0^\pi d\theta_2 \sin^{-2\varepsilon} \theta_2 \frac{1}{(1 - \cos \theta_1)^j (1 - \cos \theta_1 \cos \chi - \sin \theta_1 \cos \theta_2 \sin \chi)^l} \\ &= 2\pi \frac{\Gamma(1-2\varepsilon)}{\Gamma(1-\varepsilon)} 2^{-j-l} \frac{B(1-\varepsilon-j, 1-\varepsilon-l)}{\Gamma(1-\varepsilon)} {}_2F_1(j, l, 1-\varepsilon; \cos^2 \frac{\chi}{2}) , \end{aligned} \quad (3.69)$$

to become amenable to an analytical integration. Here, ${}_2F_1(a, b, c; z)$ denotes the hypergeometric function and χ stands for ψ , ψ' , ψ'' , or an appropriately shifted “angle” (e.g., $\psi + \pi$) introduced by the parametrization of the Mandelstam variables in Eqs. (D.3), (D.4), and (D.5).

In practice, not all terms in a matrix element squared a priori exhibit the form (3.69). Often, before parametrizing the momenta extensive partial fractioning has to be performed to finally obtain expressions that can be integrated by employing the master formula Eq. (3.69). Let us illustrate this by a brief example [95]: A contribution proportional to $1/u_3 t_3 s_{12}$, for instance, cannot be brought into the form (3.69) by any of the parametrizations given in App. D, since it contains a product of three Mandelstam variables in the denominator. To evaluate the needed integral nonetheless, it is therefore rewritten with the help of Eqs. (3.51) as

$$\frac{1}{u_3 t_3 s_{12}} = \frac{1}{s} \left[-\frac{1}{u_3 s_{12}} - \frac{1}{t_3 s_{12}} + \frac{1}{t_3 u_3} \right] . \quad (3.70)$$

Now, each term on the right-hand-side can be cast into the form of Eq. (3.69), since the prefactor $1/s$ is independent of the integration variables θ_1 and θ_2 . E.g., $1/u_3 s_{12}$ can be parametrized either in set 2 or in set 3 corresponding to Eqs. (D.9) and (D.10), respectively. Set 1 (D.8) is not suitable as it yields expressions different from the standard form (3.69), which cannot be integrated with the given master formula. A similar partial fractioning as the one sketched in Eq. (3.70) can be performed for each term in the matrix elements squared relevant for our purposes.

In general, only the case $j \leq 1, l \leq 1$ in Eq. (3.69) occurs. For j or $l < 0$ the series expansion for ${}_2F_1(a, b, c; z)$ terminates, yielding a simple result for the $I^{(j,l)}$. Making use of the identities

$$\begin{aligned} \Gamma(x+1) &= x \Gamma(x) , \\ B(x, y) &= \frac{\Gamma(x) \Gamma(y)}{\Gamma(x+y)} , \\ {}_2F_1(0, 0, c; z) &= {}_2F_1(0, 1, c; z) = {}_2F_1(1, 0, c; z) = 1 , \end{aligned} \quad (3.71)$$

integrand	integral	integrand	integral
$\frac{1}{1-\cos\theta_1}$	$-\frac{(1-2\varepsilon)}{2\varepsilon} I^{(0,0)}$	$\frac{\cos\theta_1}{1-\cos\theta_1}$	$-\frac{1}{2\varepsilon} I^{(0,0)}$
$\frac{\cos^2\theta_1}{1-\cos\theta_1}$	$-\frac{1}{2\varepsilon} I^{(0,0)}$	$\frac{\sin^2\theta_1 \cos^2\theta_1}{1-\cos\theta_1}$	$\frac{1}{2(1-\varepsilon)} I^{(0,0)}$
$\cos^2\theta_1$	$\frac{1}{3-2\varepsilon} I^{(0,0)}$	$\frac{\cos^2\theta_1}{1-\cos\theta_1}$	$-\frac{1}{2\varepsilon} I^{(0,0)}$
$\frac{\cos^3\theta_1}{1-\cos\theta_1}$	$-\frac{3}{2\varepsilon} \frac{1}{(3-2\varepsilon)} I^{(0,0)}$	$\frac{\sin^2\theta_1 \cos\theta_1 \cos^2\theta_2}{1-\cos\theta_1}$	$\frac{1}{2(1-\varepsilon)(3-2\varepsilon)} I^{(0,0)}$

Table 3.1: Phase space integrals for terms emerging in $2 \rightarrow 3$ matrix elements.

we obtain

$$I^{(0,0)} = \int_0^\pi d\theta_1 \sin^{1-2\varepsilon} \theta_1 \int_0^\pi d\theta_2 \sin^{-2\varepsilon} \theta_2 = \frac{2\pi}{1-2\varepsilon} . \quad (3.72)$$

The results for other phase space integrals with $l = 0$ are listed in Tab. 3.1. The case $j = l = 1$ is a little bit more involved, as

$${}_2F_1(1, 1, 1 - \varepsilon; \cos^2 \frac{\chi}{2}) \approx \left(\sin^2 \frac{\chi}{2} \right)^{-1-\varepsilon} \left[1 + \varepsilon^2 \text{Li}_2 \left(\cos^2 \frac{\chi}{2} \right) \right] , \quad (3.73)$$

where Li_2 is the dilogarithm function. After expressing χ in terms of v and w , see Eq. (3.65), according to Eq. (D.7), the factor $(\sin^2 \frac{\chi}{2})^{-1-\varepsilon}$ produces a pole as $w \rightarrow 1$. Combined with the prefactor $(1-w)^{-\varepsilon}$ from the phase space integral (3.66) this singularity is handled by the identity

$$(1-w)^{-1-\varepsilon} = \frac{1}{\varepsilon} \delta(1-w) + \frac{1}{(1-w)_+} - \varepsilon \left(\frac{\ln(1-w)}{1-w} \right)_+ + \mathcal{O}(\varepsilon^2) , \quad (3.74)$$

where $[g(z)]_+$ denotes a so-called “+”-distribution, defined via an arbitrary test function $f(z)$ by

$$\int_0^1 dz f(z) [g(z)]_+ \equiv \int_0^1 dz [f(z) - f(1)] g(z) . \quad (3.75)$$

Eq. (3.74) can easily be verified by integrating both sides over a test function according to Eq. (3.75).

For all terms including hat momenta an additional factor of $\sin^2 \theta_1 \sin^2 \theta_2$ emerges from the x -integration, see Eq. (3.68) . This amounts to a simple shift $\varepsilon \rightarrow \varepsilon' = \varepsilon - 1$ in the

angular integral $\hat{I}^{(j,l)}$, Eq. (3.69), thereby yielding

$$\begin{aligned} \hat{I}^{(j,l)} &= \int_0^\pi d\theta_1 \sin^{1-2\varepsilon} \theta_1 \int_0^\pi d\theta_2 \sin^{-2\varepsilon} \theta_2 \left[-\frac{2\varepsilon}{1-2\varepsilon} \frac{s_{23}}{4} \sin^2 \theta_1 \sin^2 \theta_2 \right] \\ &\quad \times \frac{1}{(1 - \cos \theta_1)^j (1 - \cos \theta_1 \cos \chi - \sin \theta_1 \cos \theta_2 \sin \chi)^l} \\ &= \left[-\frac{2\varepsilon}{1-2\varepsilon} \frac{s_{23}}{4} \right] 2\pi \frac{\Gamma(1-2\varepsilon')}{\Gamma(1-\varepsilon')} 2^{-j-l} \frac{B(1-\varepsilon'-j, 1-\varepsilon'-l)}{\Gamma(1-\varepsilon')} {}_2F_1(j, l, 1-\varepsilon'; \cos^2 \frac{\chi}{2}) . \end{aligned} \quad (3.76)$$

Thus we obtain

$$\hat{I}^{(0,0)} = \left[-\frac{2\varepsilon}{1-2\varepsilon} \frac{s_{23}}{4} \right] \frac{2\pi}{3-2\varepsilon} \quad \text{and} \quad \hat{I}^{(2,0)} = \left[-\frac{2\varepsilon}{1-2\varepsilon} \frac{s_{23}}{4} \right] \left(-\frac{\pi}{\varepsilon} \right) . \quad (3.77)$$

For the computation of

$$\hat{I}^{(2,1)} = \left[-\frac{2\varepsilon}{1-2\varepsilon} \frac{s_{23}}{4} \right] \left(-\frac{\pi}{2\varepsilon} \right) \frac{1-2\varepsilon}{1-\varepsilon} {}_2F_1(2, 1, 2-\varepsilon; \cos^2 \frac{\chi}{2}) \quad (3.78)$$

we use

$${}_2F_1(a, b, c; -z) = {}_2F_1(b, a, c; -z) \quad \text{and} \quad {}_2F_1(-n, b, b; -z) = (1+z)^n \quad (3.79)$$

and perform a series expansion for ${}_2F_1(1, 2, 2-\varepsilon; \cos^2 \frac{\chi}{2})$ in ε , which gives up to $\mathcal{O}(\varepsilon)$

$$\hat{I}^{(2,1)} = \left[-\frac{2\varepsilon}{1-2\varepsilon} \frac{s_{23}}{4} \right] \left(-\frac{\pi}{2\varepsilon} \right) \frac{1-2\varepsilon}{1-\varepsilon} \frac{1}{\sin^2 \frac{\chi}{2}} . \quad (3.80)$$

Finally, $\hat{I}^{(2,2)} = \hat{I}^{(2,1)}$. Terms proportional to $\hat{I}^{(j,l)}$ with j or $l \leq 2$ vanish in the limit $\varepsilon \rightarrow 0$ because of the overall ε stemming from the x -integration [cf. Eq. (3.68)], unless this factor is canceled by an additional pole. Such poles can only arise from terms proportional to \hat{p}_4^2/s_{23}^2 , where $s_{23} \sim (1-w)$. Combined with the s_{23} -prefactor from the hat integration such terms still diverge as $w \rightarrow 1$ and give rise to distributions of the form Eq. (3.74) when the prefactor $(1-w)^{-\varepsilon}$ from the phase space integral is included. For $\varepsilon \rightarrow 0$ only their $\delta(1-w)$ part survives in the final result.

3.5 Cancellation of Singularities

Having computed all partonic matrix elements and integrated them over the entire phase space of all unobserved partons, we are now in a position to add them and take care of the singularities which have not been removed by the renormalization of virtual diagrams. As mentioned in Chap. 2, infrared $1/\varepsilon$ poles and coinciding IR and collinear $1/\varepsilon^2$ singularities cancel for each process if an appropriate sum of real and virtual contributions is taken [51]. Still, we are left with divergencies caused by collinear emissions from external parton legs. However, for hadronic reactions only the convolution of the hard partonic cross sections

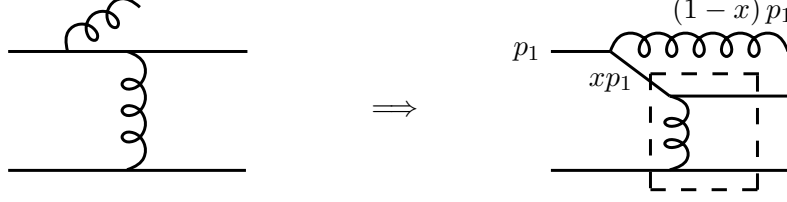


Figure 3.7: Generic structure of the singularity arising when a gluon is emitted collinearly by the incoming quark in the reaction $qq \rightarrow qgg$. The box indicates the left over Born cross section following the collinear quark-gluon splitting.

with the soft parton distribution and fragmentation functions of the participating hadrons is a physically meaningful quantity by virtue of the factorization theorem discussed in Sec. 2.4. This offers the freedom to shift singularities from one building block to the other. Only the complete result including both hard and soft parts has to be free of divergencies. We therefore aim to remove collinear singularities from the partonic cross sections by factorizing them into the bare parton distribution or fragmentation functions, depending on whether they stem from the initial or final state. This subtraction is performed at a scale μ_f for incoming and μ'_f for outgoing partons and gives rise to dressed functions $(\Delta)f_a^A(x, \mu_f)$, $(\Delta)f_b^B(x, \mu_f)$, and $(\Delta)D_c^C(z, \mu'_f)$. Since most of the currently available sets of parton distribution and fragmentation functions are given in the $\overline{\text{MS}}$ factorization scheme we adopt this prescription in removing collinear singularities from the partonic cross sections throughout. Similar to the $\overline{\text{MS}}$ renormalization procedure $1/\varepsilon$ poles are subtracted along with accompanying γ_E and $\ln 4\pi$ terms.

In practice, the factorization is performed by adding an appropriate counter term to each partonic cross section which serves to cancel the poles. To this end one makes use of the simple structure of the singularities that arise in the collinear limit of any $2 \rightarrow 3$ cross section, sketched in Fig. 3.7. The appropriate subtraction can always be written as a convolution of an n -dimensional Born cross section and a divergent term of the form

$$(\Delta)H_{ij}(x, \mu) \equiv \left(-\frac{1}{\varepsilon} + \gamma_E - \ln 4\pi \right) (\Delta)P_{ij}^{(4)}(x) \left(\frac{s}{\mu^2} \right)^\varepsilon + (\Delta)h_{ij}(x), \quad (3.81)$$

with the four-dimensional LO splitting function $(\Delta)P_{ij}^{(4)}(x)$ [65]. The actual form of the functions $(\Delta)h_{ij}(x)$ depends on the factorization scheme used. In the $\overline{\text{MS}}$ scheme $h_{ij}(x) = 0$. However, some care has to be taken in the polarized case. In the framework of the HVBm regularization procedure [53, 56] the definition of γ_5 results in helicity non-conservation at the quark-gluon vertex in n dimensions [24, 96, 97]. This causes the polarized n -dimensional quark-to-quark splitting function at LO to deviate from the corresponding unpolarized quantity,

$$\Delta P_{qq}(x) - P_{qq}(x) = 4C_F \varepsilon (1-x), \quad (3.82)$$

whereas in a theory respecting helicity conservation P_{qq} and ΔP_{qq} must coincide. As a consequence, the first moment of the flavor non-singlet anomalous dimension at NLO, which governs the evolution of a particular combination of polarized quark densities, would not vanish and thereby violate conservation of flavor non-singlet axial currents [96-98]. Above that, beyond the NLO naive $\overline{\text{MS}}$ factorization leads to inconsistencies in the renormalization of the axial current, no longer allowing for a cancelation of all singularities [99]. It is thus mandatory to slightly deviate from the literal $\overline{\text{MS}}$ prescription in the spin-dependent case and to carefully restore helicity conservation by choosing [96, 97]

$$\Delta h_{qq}(x) = -4C_F(1-x) . \quad (3.83)$$

All other Δh_{ij} are set to zero. Since the HVBM-“ γ_5 effect” is an artifact of the regularization procedure, it is customary to remove it by the above choice for Δh_{qq} and refer to the thereby obtained factorization scheme as the “genuine” $\overline{\text{MS}}$ prescription. The sets of NLO ($\overline{\text{MS}}$) spin-dependent parton densities we are going to use [17] make use of this convention.

To illustrate the actual implementation of the factorization prescription let us resort to the specific example of the process $qq \rightarrow qX$ with two polarized quarks in the initial state. At NLO, we have to consider contributions from virtual corrections to the $2 \rightarrow 2$ reaction $qq \rightarrow qq$ and from the $2 \rightarrow 3$ process $qq \rightarrow qqg$. The UV divergencies in the virtual contributions have already been removed by an $\overline{\text{MS}}$ renormalization of vertex and selfenergy corrections. All IR as well as coinciding IR and collinear singularities cancel in the sum of the phase space integrated contributions from $qq \rightarrow qq$ and $qq \rightarrow qqg$. The remaining poles arise from configurations where one of the unobserved particles in the $2 \rightarrow 3$ scattering is emitted collinearly from an external parton leg, e.g., as depicted in Fig 3.7. There, x denotes the fraction of the incoming quark’s momentum which is taken by the splitting quark, whereas the remaining part, $(1-x)p_1$, is carried by the quasi-collinear gluon. The variable x can in principle take any value in the range $0 \leq x \leq 1$. The entire contribution can be viewed as a collinear quark-quark splitting with a subsequent $2 \rightarrow 2$ scattering. However, in contrast to the kinematics of a genuine Born cross section $d\Delta\hat{\sigma}(s, t, u, \varepsilon)$, describing a $2 \rightarrow 2$ scattering without an accompanying collinear splitting, the arguments of the cross section emerging in a collinear $2 \rightarrow 3$ configuration are shifted. Rather than s , t , and u we now have

$$s' = (xp_1 + p_2)^2 = xs , \quad t' = (xp_1 - p_3)^2 = xt , \quad u' = u , \quad (3.84)$$

which can straightforwardly be expressed in terms of v and w ,

$$v' = 1 + \frac{t'}{s'} = v , \quad w' = \frac{-u'}{s' + t'} = \frac{w}{x} , \quad (3.85)$$

and obey the relation

$$s' + t' + u' = x(s + t) + u = 0 . \quad (3.86)$$

To remove the pole associated with this collinear configuration, we have to add a counter term of the form

$$-\frac{\alpha_s}{2\pi} \int_0^1 dx \Delta H_{qq}(x, \mu_f) \frac{d\Delta\hat{\sigma}_{qq \rightarrow qq}}{dv}(s', t', u', \varepsilon) \delta(s' + t' + u') \quad (3.87)$$

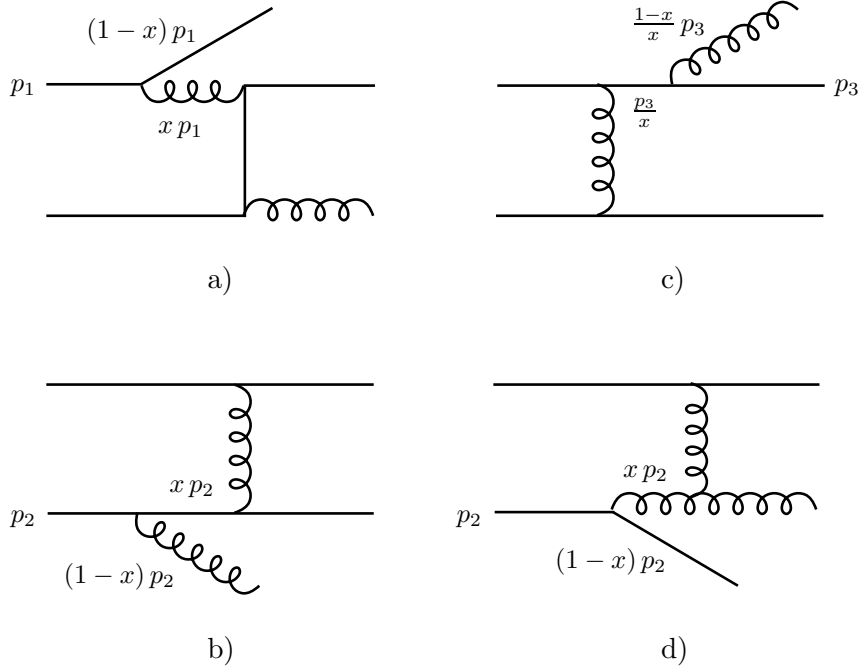


Figure 3.8: Various contributions to $qq \rightarrow qX$, which exhibit poles as a quark or gluon is emitted collinearly by one of the external legs: a) $q \rightarrow g$ transition in an initial state, followed by a $gq \rightarrow qq$ scattering; b) $q \rightarrow q$ transition with $qq \rightarrow qq$ scattering; c) $qq \rightarrow qq$ scattering with subsequent $q \rightarrow q$ splitting in the final state; d) $q \rightarrow g$ transition with $gq \rightarrow qq$ scattering. The labels denote the momenta of those partons which can become collinear to each other.

to the full partonic cross section $d\Delta\hat{\sigma}_{qq \rightarrow qX}/dvdw$. In a similar way, collinear emissions from the other parton legs, depicted in Fig. 3.8, are treated. We simply have to readjust the kinematics, Eq. (3.84), depending on which external parton undergoes the collinear splitting. Altogether, we obtain for this example

$$\begin{aligned}
\frac{1}{sv} \frac{d\Delta\hat{\sigma}^{counter}}{dvdw} = & -\frac{\alpha_s}{2\pi} \left\{ \int_0^1 dx \Delta H_{qq}(x, \mu_f) \frac{d\Delta\hat{\sigma}_{qq \rightarrow qq}}{dv}(xs, xt, u, \varepsilon) \delta(x[s+t] + u) \right. \\
& + \int_0^1 dx \Delta H_{gq}(x, \mu_f) \frac{d\Delta\hat{\sigma}_{gq \rightarrow qq}}{dv}(xs, xt, u, \varepsilon) \delta(x[s+t] + u) \\
& + \int_0^1 dx \Delta H_{qq}(x, \mu_f) \frac{d\Delta\hat{\sigma}_{qq \rightarrow qq}}{dv}(xs, t, xu, \varepsilon) \delta(x[s+u] + t) \\
& + \int_0^1 dx \Delta H_{gq}(x, \mu_f) \frac{d\Delta\hat{\sigma}_{gq \rightarrow qq}}{dv}(xs, t, xu, \varepsilon) \delta(x[s+u] + t) \\
& \left. + \int_0^1 dx H_{qq}(x, \mu'_f) \frac{d\Delta\hat{\sigma}_{qq \rightarrow qq}}{dv}\left(s, \frac{t}{x}, \frac{u}{x}, \varepsilon\right) \delta\left(s, \frac{1}{x}[t+u]\right) \right\}. \tag{3.88}
\end{aligned}$$

If we perform the x -integrals by explicitly making use of the delta functions for the respective contributions in Eq. (3.88) we arrive at

$$\begin{aligned} \frac{1}{sv} \frac{d\Delta\hat{\sigma}^{counter}}{dvdw} = & -\frac{\alpha_s}{2\pi} \left\{ \frac{1}{sv} \Delta H_{qq}(x=w, \mu_f) \frac{d\Delta\hat{\sigma}_{qq\rightarrow qq}}{dv} \right. \\ & + \frac{1}{sv} \Delta H_{gq}(x=w, \mu_f) \frac{d\Delta\hat{\sigma}_{gq\rightarrow qq}}{dv} \\ & + \frac{1}{s(1-vw)} \Delta H_{qq}(x=\frac{1-v}{1-vw}, \mu_f) \frac{d\Delta\hat{\sigma}_{qq\rightarrow qq}}{dv} \\ & + \frac{1}{s(1-vw)} \Delta H_{gq}(x=\frac{1-v}{1-vw}, \mu_f) \frac{d\Delta\hat{\sigma}_{gq\rightarrow qq}}{dv} \\ & \left. + \frac{1}{s(1-v+vw)} H_{qq}(x=1-v+vw, \mu'_f) \frac{d\Delta\hat{\sigma}_{qq\rightarrow qq}}{dv} \right\}, \quad (3.89) \end{aligned}$$

where for brevity we have omitted the arguments of the Born cross sections, which are to be taken at the x -values specified by the integration and can be found in App. B. The individual terms stem from gluon and quark emission from one of the incoming partons, and gluon emission from the quark in the final state, which subsequently fragments into the observed hadron (this parton is labeled by its momentum, p_3 , in Fig. 3.8). Collinear emissions from unobserved final state partons need not be considered here, as they have already been integrated out in the preceding phase space integration of the $2 \rightarrow 3$ matrix elements squared. Whenever the emitting parton is polarized, the spin-dependent ΔH_{ij} have to be applied, whereas contributions from unpolarized emissions require the spin-averaged H_{ij} . The factorization contribution $d\hat{\sigma}^{counter}$ for the unpolarized cross section $d\hat{\sigma}_{qq\rightarrow qX}$ can easily be obtained from the polarized one by replacing all spin-dependent quantities by their unpolarized counterparts, i.e., $d\Delta\hat{\sigma}_{ab\rightarrow cd} \rightarrow d\hat{\sigma}_{ab\rightarrow cd}$, and $\Delta H_{ij} \rightarrow H_{ij}$.

In a similar way factorization contributions for all partonic subprocesses $ab \rightarrow cX$ can be calculated. Adding them to the respective cross sections gives results which are completely finite such that the physical limit $\varepsilon \rightarrow 0$ can be taken. The resulting expressions can then be convoluted with the appropriate (dressed) parton densities and fragmentation functions for the external partons straightforwardly as specified in Eq. (3.2).

Part II

Phenomenological Applications and Results

Chapter 4

High- p_T Hadron Production in Longitudinally Polarized Proton-Proton Collisions Beyond the Leading Order

In this chapter we apply the methods introduced in the previous sections to hadron production in proton-proton collisions. As will be shown, the reaction

$$p(P_A) + p(P_B) \rightarrow H(P_H) + X, \quad (4.1)$$

is particularly sensitive to the gluon content of the proton, since subprocesses involving gluons in the initial state are present at Born level already and contribute a major fraction to the full differential cross section. That explains the considerable interest of spin physicists in single-inclusive hadron production, and the need for a reliable theoretical description of this reaction. With the NLO framework developed here, in principle the production of hadrons H of any type can be described. We will focus, however, on the experimentally most relevant case of single-inclusive pions in this thesis. It turns out that our results for spin-averaged pion production cross sections are in good agreement with recent data from RHIC [100, 101], giving confidence in the applicability of the perturbative framework used.

Along similar lines as in the unpolarized case we then investigate pion production with polarized proton beams, $\vec{p}\vec{p} \rightarrow \pi X$, which is currently studied at RHIC [29]. We put special emphasis on a critical discussion of the experimentally accessible spin asymmetry and its implications on the gluon polarization in the nucleon. These studies are of immediate relevance for a first determination of Δg from upcoming RHIC data and will therefore contribute to a better understanding of the spin structure of the proton.

4.1 Setting the Stage

A viable method for accessing the polarized parton distributions of the proton in experiment is the measurement of the double-spin asymmetry,

$$A_{LL}^\pi = \frac{d\Delta\sigma}{d\sigma} = \frac{d\sigma^{++} - d\sigma^{+-}}{d\sigma^{++} + d\sigma^{+-}}, \quad (4.2)$$

for the reaction (4.1). In the framework of pQCD A_{LL}^π is a complicated function of parton distributions, partonic cross sections, and fragmentation functions. However, due to the dominance of gluonic contributions to $d\Delta\sigma$ the spin asymmetry turns out to be very sensitive to Δg . This suggests that an analysis of A_{LL}^π may allow for an extraction of the spin-dependent gluon distribution in the proton, if theoretical uncertainties such as the dependence on unphysical renormalization and factorization scales are under control.

To NLO in α_s the polarized cross section for (4.1) is given by

$$\begin{aligned} E_\pi \frac{d\Delta\sigma}{d^3P_\pi} &= \frac{1}{\pi S} \sum_{a,b,c} \int_{z_0}^1 \frac{dz_c}{z_c^2} \int_{VW/z_c}^{1-(1-V)/z_c} \frac{dv}{v(1-v)} \int_{VW/vz_c}^1 \frac{dw}{w} \Delta a(x_a, \mu_f) \Delta b(x_b, \mu_f) \\ &\times \left[\frac{d\Delta\hat{\sigma}_{ab \rightarrow cX}^{(0)}(v)}{dv} \delta(1-w) + \frac{\alpha_s(\mu_r)}{\pi} \frac{d\Delta\hat{\sigma}_{ab \rightarrow cX}^{(1)}(s, v, w, \mu_r, \mu_f, \mu'_f)}{dv dw} \right] D_c^\pi(z_c, \mu'_f), \end{aligned} \quad (4.3)$$

including all contributing partonic channels $ab \rightarrow cX$ with a, b, c being either an (anti)quark or a gluon. In the following we will denote the momentum of parton i by p_i , with $i = a, b, c, \dots$. For simplicity we express the parton distributions introduced in Sec. 2.5, Δf_a^A and Δf_b^B , by Δa and Δb from now on. The unpolarized cross section is obtained by replacing all spin-dependent quantities by their unpolarized counterparts. The single-inclusive partonic cross sections $d\Delta\sigma_{ab \rightarrow cX}^{(n)}$ are summed over all possible configurations of the unobserved partons in the final state and integrated over the entire phase space of X . The superscript $n = 0(1)$ labels the Born (NLO) contributions to the partonic cross sections. As before, $\mu_f(\mu'_f)$ denotes the factorization scale for the initial (final) state, and μ_r the renormalization scale emerging as UV singularities are removed from the NLO $2 \rightarrow 2$ matrix elements. The lower limit of the z_c -integration is given by $z_0 = 1 - V + VW$. Similar to the partonic Mandelstams, defined in complete analogy to Eqs. (3.11), (3.50), and (3.65),

$$\begin{aligned} s &\equiv (p_a + p_b)^2, \quad t \equiv (p_a - p_c)^2, \quad u \equiv (p_b - p_c)^2, \\ v &\equiv 1 + \frac{t}{u}, \quad w \equiv \frac{-u}{s+t}, \end{aligned} \quad (4.4)$$

we introduce hadronic variables,

$$\begin{aligned} S &\equiv (P_A + P_B)^2, \quad T \equiv (P_A - P_\pi)^2, \quad U \equiv (P_B - P_\pi)^2, \\ V &\equiv 1 + \frac{T}{U}, \quad W \equiv \frac{-U}{S+T}, \end{aligned} \quad (4.5)$$

obeying the relations

$$\begin{aligned} s &= x_a x_b S, \quad t = \frac{x_a}{z_c} T, \quad u = \frac{x_b}{z_c} U, \\ x_a &= \frac{VW}{vwz_c}, \quad x_b = \frac{1-V}{z_c(1-v)}. \end{aligned} \quad (4.6)$$

At LO, only $2 \rightarrow 2$ amplitudes at tree level contribute to the partonic cross sections. The unobserved final state X then consists of a single parton only. Altogether, there are ten partonic channels,

$$\begin{aligned} qq' &\rightarrow qX \\ q\bar{q}' &\rightarrow qX \\ q\bar{q} &\rightarrow q'X \\ qq &\rightarrow qX \\ q\bar{q} &\rightarrow qX \\ q\bar{q} &\rightarrow gX \\ qg &\rightarrow qX \\ qg &\rightarrow gX \\ gg &\rightarrow gX \\ gg &\rightarrow qX. \end{aligned} \quad (4.7)$$

Beyond the leading order, the same $2 \rightarrow 2$ reactions have to be considered, now including virtual corrections. At $\mathcal{O}(\alpha_s^3)$, additionally processes with three partons in the final state contribute, giving rise to six further reactions,

$$\begin{aligned} qq' &\rightarrow gX \\ q\bar{q}' &\rightarrow gX \\ qq &\rightarrow gX \\ qg &\rightarrow q'X \\ qg &\rightarrow \bar{q}'X \\ qg &\rightarrow \bar{q}X. \end{aligned} \quad (4.8)$$

In contrast to the LO case, X consists of either one or two particles at NLO. E.g., the subprocess $qg \rightarrow qX$ contains then contributions from the $2 \rightarrow 2$ scattering $qg \rightarrow qg$, including virtual corrections, where $X = g$, and from real $2 \rightarrow 3$ processes with X being either gg , $q\bar{q}$, or $q'\bar{q}'$.

As mentioned in Sec. 3.1, the matrix elements for all $2 \rightarrow 2$ processes, sketched in Fig. 3.4, can be computed in two different ways, the diagrammatic and the helicity approach. We calculated the unpolarized and the polarized $2 \rightarrow 2$ matrix elements with both methods up to NLO and could thereby recover the results available in the literature [102] for the spin-averaged contributions. In the limit $\varepsilon \rightarrow 0$ the polarized matrix elements can be compared to the four-dimensional expressions in Ref. [103], and again we find complete agreement.

Next, the matrix elements have to be integrated over the entire phase space of the unobserved final state X . For the LO and NLO $2 \rightarrow 2$ subprocesses the phase space, differential in v and w , which can easily be obtained from Eq. (3.32),

$$\frac{dPS_2}{dvdw} = (4\pi)^{-1+\varepsilon} \frac{1}{2\Gamma(1-\varepsilon)} [sv(1-v)]^{-\varepsilon} \delta(1-w), \quad (4.9)$$

is trivial. It does not require any explicit integration, but simply multiplies the matrix elements with a prefactor depending on the variables s and v , and a delta function $\delta(1-w)$, reflecting the special Born kinematics with $s+t+u = sv(1-w) = 0$.

The phase space integration is more complicated for the $2 \rightarrow 3$ partonic channels with two unobserved particles in the final state as has been demonstrated in Sec. 3.4.1. In addition to a prefactor, now also depending on w , the $2 \rightarrow 3$ phase space given in Eq. (3.66) brings in extra integrations over the unobserved pair of partons. These integrations are performed term by term as outlined in Sec. 3.4.2, after a suitable parametrization of the corresponding matrix elements (cf. App. D). As expected, some of the integrals behave like $1/(1-w)$ and diverge for $w \rightarrow 1$. Such singularities can be traced back to a vanishing invariant mass $s_{23} = (p_d + p_e)^2 = sv(1-w)$ of the unobserved partons d and e . Together with the overall factor $(1-w)^{-\varepsilon}$ from the phase space they give rise to contributions of the form $(1-w)^{-1-\varepsilon}$, which are expressed in terms of plus distributions according to Eq. (3.74).

Some remarks are in order here. The plus-distributions introduced in Eq. (3.75) are defined in the context of an integral running from 0 to 1. However, the relevant w -integration in Eq. (4.3) always has a lower integration limit of $w_{min} = VW/vz_c \neq 0$. We thus need a prescription how to use plus distributions in integrals with arbitrary lower limits. Therefore a more general expression $[g(x)]_A$ is applied,

$$\int_A^1 dz f(z) [g(z)]_A \equiv \int_A^1 dz [f(z) - f(1)] g(z). \quad (4.10)$$

With this definition at hand, we can re-express the plus-distributions relevant for our calculation,

$$\begin{aligned} \frac{1}{(1-w)_+} &= \frac{1}{(1-w)_A} + \ln(1-A) \delta(1-w), \\ \left(\frac{\ln(1-w)}{1-w} \right)_+ &= \left(\frac{\ln(1-w)}{1-w} \right)_A + \frac{1}{2} \ln^2(1-A) \delta(1-w), \end{aligned} \quad (4.11)$$

with $A = w_{min}$ in our case. The same distributions emerge if the two incoming partons are exchanged. In terms of Mandelstams, this crossing amounts to a simple exchange of t and u , while s remains unaffected. Working with the dimensionless variables v and w instead, we have to transform these to v' and w' ,

$$v \rightarrow v' = 1 - vw, \quad w \rightarrow w' = \frac{1-v}{1-vw}. \quad (4.12)$$

In turn, also the $[g(w)]_+$ distributions are replaced by $[g(w')]_+$. All occurring distributions depending on the more complicated argument w' can then be re-expressed in terms of the basic $\delta(1-w)$, $1/(1-w)_+$, and $[\ln(1-w)/(1-w)]_+$ [104],

$$\begin{aligned}
\delta(1-w') &= \frac{1-v}{v} \delta(1-w), \\
\frac{1}{(1-w')_+} &= \frac{1-vw}{v} \frac{1}{(1-w)_+} + \frac{1-v}{v} \ln\left(\frac{v}{1-v}\right) \delta(1-w), \\
\left(\frac{\ln(1-w')}{1-w'}\right)_+ &= \frac{1-vw}{v} \left(\frac{\ln(1-w)}{1-w}\right)_+ + \frac{1-vw}{v} \ln\left(\frac{v}{1-vw}\right) \frac{1}{(1-w)_+} \\
&\quad + \frac{1-v}{2v} \ln^2\left(\frac{1-v}{v}\right) \delta(1-w),
\end{aligned} \tag{4.13}$$

where again $1/(1-w)_+$ and $(\ln(1-w)/(1-w))_+$ can be rewritten according to Eq. (4.11) if they emerge in integrals with arbitrary lower limits.

After performing the phase space integration of all matrix elements we have to take care of the remaining IR and collinear singularities. First we add up all $2 \rightarrow 2$ and $2 \rightarrow 3$ subprocesses contributing to a partonic channel. Infrared divergencies cancel after the combination of virtual and real NLO contributions as they should. The remaining collinear singularities are factorized into the parton distribution and fragmentation functions of hadrons associated with the external legs. As explained in some detail in Sec. 3.5 this can be done by adding an appropriate counter cross section to the NLO contributions for each partonic channel.

We have mentioned in Sec. 3.5 the delicate issue of implementing polarization in the context of the HVBM regularization scheme, in particular the subtleties related to helicity conservation at the quark-gluon vertex. As discussed in Sec. 3.5 the additional finite term Δh_{qq} in the factorization subtraction (3.83) is precisely designed [96, 97] to cure this shortcoming of the HVBM scheme. That finding can be tested on the basis of processes involving annihilation diagrams only, as, e.g., $q\bar{q} \rightarrow q'X$. In such reactions, the incoming parton and antiparton are always part of the same fermion line and are polarized in opposite directions. Keeping in mind the definitions (3.5), this helicity pattern implies that polarized annihilation cross sections are opposite in sign to their unpolarized counterparts, but equal in magnitude,

$$d\Delta\hat{\sigma}^{annih} = -d\hat{\sigma}^{annih}. \tag{4.14}$$

In the HVBM scheme, Eq. (4.14) holds only after the appropriate subtraction (3.83) has been performed. Checking this relation for all annihilation processes therefore provides a powerful check on the correctness of our calculation.

An additional observation can be made: Unlike the pure annihilation channel $q\bar{q} \rightarrow q'X$, the subprocess $q\bar{q} \rightarrow qX$ includes annihilation diagrams as well as other contributions which we have depicted in Fig. 4.1. Thus, (4.14) is not expected to apply to the latter reaction. However, we can make use of its substructure. The cross section for the process $q\bar{q} \rightarrow qX$ contains contributions from the same topologies as the reaction $q\bar{q}' \rightarrow qX$ as

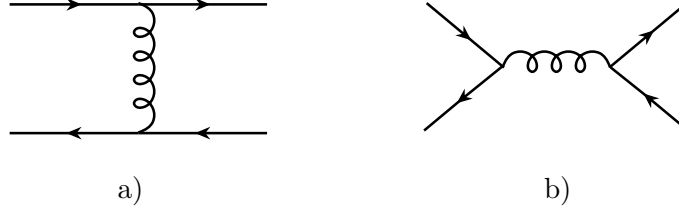


Figure 4.1: Generic contributions to the subprocess $q\bar{q} \rightarrow qX$: a) non-annihilation diagram as for $q\bar{q}' \rightarrow qX$; b) annihilation process as for $q\bar{q} \rightarrow q'X$.

well as the channel $q\bar{q} \rightarrow q'X$. Subtracting the non-annihilation contributions from the complete sum we should be left with terms stemming from the $q\bar{q} \rightarrow q'X$ like topology alone, which then have to fulfill Eq. (4.14), if nothing went wrong in the calculation of the subprocesses:

$$\left[d\Delta\hat{\sigma}_{q\bar{q} \rightarrow qX} - d\Delta\hat{\sigma}_{q\bar{q}' \rightarrow qX} \right] = - \left[d\hat{\sigma}_{q\bar{q} \rightarrow qX} - d\hat{\sigma}_{q\bar{q}' \rightarrow qX} \right]. \quad (4.15)$$

This relation has been verified for the $q\bar{q} \rightarrow qX$ cross sections as well as a similar equality for the reaction $q\bar{q} \rightarrow gX$.

Having removed all singularities from the phase space integrated matrix elements we arrive at the final results for the NLO partonic cross sections, which for each of the 16 subprocesses in Eqs. (4.7) and (4.8) can be cast into the form

$$\begin{aligned} s \frac{d\Delta\hat{\sigma}_{ab \rightarrow cX}^{(1)}(s, v, w, \mu_r, \mu_f, \mu_f')}{dv dw} &= \left(\frac{\alpha_s(\mu_r)}{\pi} \right)^2 \\ &\times \left\{ \left(A_0 \ln \frac{\mu_f^2}{s} + A_1 \ln \frac{\mu_f'^2}{s} + A_2 \ln \frac{\mu_r^2}{s} + A \right) \delta(1-w) \right. \\ &+ \left(B_0 \ln \frac{\mu_f^2}{s} + B_1 \ln \frac{\mu_f'^2}{s} + B \right) \frac{1}{(1-w)_+} + C \left(\frac{\ln(1-w)}{1-w} \right)_+ \\ &\left. + D_0 \ln \frac{\mu_f^2}{s} + D_1 \ln \frac{\mu_f'^2}{s} + D \right\}, \end{aligned} \quad (4.16)$$

and, analogously, for the unpolarized cross sections. Exchanging the two incoming partons a and b with each other yields cross sections of the same structure. However, the coefficients acquire a different form in this case. In the equation above, the coefficients A, A_i, B, B_i , and C are functions of v only, whereas D_0, D_1 , and D depend on v and w . Since some of these expressions are rather lengthy we refrain from quoting them here. They can be found in our computer codes, however.

The unpolarized cross sections for all partonic subprocesses are known for several years [104]. We have compared them *analytically* term by term to our corresponding results and found complete agreement.

With the partonic cross sections for all channels at hand, we are now in a position to compute the experimentally relevant quantities. Since the analytical results obtained so far are completely finite in the limit $\varepsilon \rightarrow 0$ they are amenable to a straightforward numerical convolution with the parton densities and fragmentation functions of the observed hadrons according to Eq. (4.3). The actual convolution is performed by means of a straightforward numerical integration routine [105], which allows for an accurate determination of the corresponding integrals.

We evaluate each of the 16 channels contributing to $pp \rightarrow \pi X$, as given in Eqs. (4.7) and (4.8), separately, keeping in mind that every process including quarks receives contributions from all flavors compatible with the corresponding reaction. E.g., in $qg \rightarrow qX$ the quark q can be of any flavor, but the flavors of incoming and outgoing quark are the same. We assume that the parton distributions of bottom and top quarks are negligible. Furthermore we have to account for the contributions coming from $\bar{q}g \rightarrow \bar{q}X$, which has not been considered as a separate channel, since the corresponding partonic cross sections are equal to their charge conjugated counterparts $qg \rightarrow qX$. Altogether, for a structure like $qg \rightarrow qX$, we end up with

$$\begin{aligned}
& \sum_{q=u,d,\dots} \Delta q(x_a) \otimes \Delta g(x_b) \otimes D_q^\pi(z_c) \otimes d\Delta\hat{\sigma}_{qg \rightarrow qX}(x_a P_A, x_b P_B, P_C/z_c) \\
&= \left[\Delta u(x_a) \otimes D_u^\pi(z_c) + \Delta d(x_a) \otimes D_d^\pi(z_c) + \Delta s(x_a) \otimes D_s^\pi(z_c) + \Delta c(x_a) \otimes D_c^\pi(z_c) \right. \\
&\quad \left. + \Delta \bar{u}(x_a) \otimes D_{\bar{u}}^\pi(z_c) + \Delta \bar{d}(x_a) \otimes D_{\bar{d}}^\pi(z_c) + \Delta \bar{s}(x_a) \otimes D_{\bar{s}}^\pi(z_c) + \Delta \bar{c}(x_a) \otimes D_{\bar{c}}^\pi(z_c) \right] \\
&\quad \otimes \Delta g(x_b) \otimes d\Delta\hat{\sigma}_{qg \rightarrow qX}(x_a P_A, x_b P_B, P_C/z_c) ,
\end{aligned} \tag{4.17}$$

where for brevity we have omitted all scale dependences in the arguments of partonic cross sections, parton distributions, and fragmentation functions and have written the $d\Delta\hat{\sigma}_{ab \rightarrow cX}$ as functions of the partonic momenta, $p_a = x_a P_A$, $p_b = x_b P_B$, and $p_c = P_C/z_c$. An additional subtlety arises since the partons participating in the hard scattering can emerge either from proton A or proton B . We thus also have to consider contributions with exchanged initial states,

$$\begin{aligned}
& \sum_{q=u,d,\dots} \Delta q(x_b) \otimes \Delta g(x_a) \otimes D_q^\pi(z_c) \otimes d\Delta\hat{\sigma}_{qg \rightarrow qX}(x_b P_B, x_a P_A, P_C/z_c) \\
&= \left[\Delta u(x_b) \otimes D_u^\pi(z_c) + \Delta d(x_b) \otimes D_d^\pi(z_c) + \Delta s(x_b) \otimes D_s^\pi(z_c) + \Delta c(x_b) \otimes D_c^\pi(z_c) \right. \\
&\quad \left. + \Delta \bar{u}(x_b) \otimes D_{\bar{u}}^\pi(z_c) + \Delta \bar{d}(x_b) \otimes D_{\bar{d}}^\pi(z_c) + \Delta \bar{s}(x_b) \otimes D_{\bar{s}}^\pi(z_c) + \Delta \bar{c}(x_b) \otimes D_{\bar{c}}^\pi(z_c) \right] \\
&\quad \otimes \Delta g(x_a) \otimes d\Delta\hat{\sigma}_{qg \rightarrow qX}(x_b P_B, x_a P_A, P_C/z_c) ,
\end{aligned} \tag{4.18}$$

where we have made use of the crossing relation

$$d\Delta\hat{\sigma}_{gq\rightarrow qX}(x_a P_A, x_b P_B, P_C/z_c) = d\Delta\hat{\sigma}_{qg\rightarrow qX}(x_b P_B, x_a P_A, P_C/z_c). \quad (4.19)$$

In terms of Mandelstams this exchange of p_a and p_b amounts to a replacement of v, w by v', w' as given in Eq. (4.12). A similar bookkeeping as in the case of $qg \rightarrow qX$ is necessary for all processes involving different incoming partons, whereas channels symmetric in the initial states as, e.g., $gg \rightarrow qX$, must not be double-counted. The numerical results we obtain after carefully sorting out and normalizing all contributions to the individual subprocesses are then added up to the pionproduction cross sections at the NLO of pQCD.

4.2 First Numerical Results and Discussion

Let us now turn to a phenomenological study of single-inclusive pionproduction in hadronic collisions. We organize our calculation such that it resembles the experimental conditions of the most recent measurements at RHIC as closely as possible. We choose a c.m.s. energy of $\sqrt{S} = 200$ GeV and consider pions which are scattered at an angle θ relative to one of the incoming proton beams with transverse momenta $p_T = |\vec{P}_\pi| \sin \theta$ in the range $2 \leq p_T \leq 13$ GeV. The pion's scattering angle is parametrized by its pseudorapidity

$$\eta = -\ln \tan \left(\frac{\theta}{2} \right). \quad (4.20)$$

η is particularly suitable for the description of high-energy scattering reactions since it is additive under Lorentz boosts and can therefore easily be adjusted to different kinematical situations and frames. If not specified otherwise, we will integrate over the range of pseudorapidities relevant for the PHENIX experiment at RHIC, $|\eta| \leq 0.38$. It is useful to express the (polarized) differential cross section in terms of p_T and η ,

$$E_\pi \frac{d^3(\Delta)\sigma}{d^3P_\pi} = \frac{d^3(\Delta)\sigma}{d\phi d\eta p_T dp_T}, \quad (4.21)$$

where the dependence on the azimuth is trivial. In the following, we will integrate over ϕ and η and consider only $d(\Delta)\sigma/dp_T$.

In order to test the importance of NLO corrections we will present results computed both at LO and NLO. All (N)LO calculations are performed using (N)LO parton distribution and fragmentation functions and taking α_s at (two) one loop(s). Unpolarized cross sections are evaluated with the CTEQ5 parton distributions [74], which include both a LO and an NLO parametrization. The spin structure of polarized protons is accounted for by the LO and NLO GRSV parton distributions [17]. Mostly, we will stick to their “standard” scenario with a moderately positive gluon polarization. To study the sensitivity of the relevant double spin asymmetries to Δg this choice will be contrasted to calculations with the “maximal gluon” scenario, which uses the maximal gluonic input at the starting point μ_0 of the evolution compatible with the positivity bound Eq. (2.47), i.e., $\Delta g(x, \mu_0) = g(x, \mu_0)$. If not stated otherwise we will apply the pion fragmentation functions proposed by Kramer, Kniehl, and Pötter [82], providing LO and NLO sets for neutral

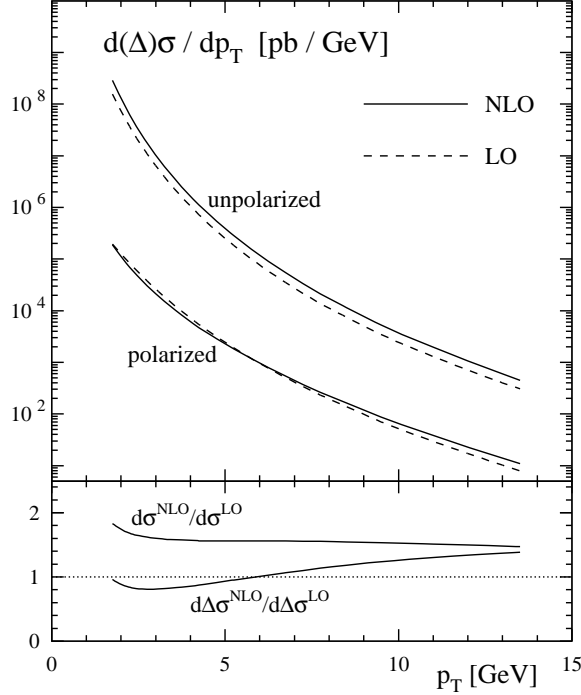


Figure 4.2: Unpolarized and polarized differential cross sections at LO (dashed) and NLO (solid) for the reaction $pp \rightarrow \pi^0 X$ at $\sqrt{S} = 200$ GeV. The lower panel shows the ratios of NLO and LO contributions.

and charged pions. This choice is supported by recent measurements of PHENIX [100], as will be discussed below. If the values of α_s differ for the parton distributions and fragmentation functions used, we will calculate cross sections with the strong coupling associated with the evolution of the parton densities.

In Fig. 4.2 our thereby obtained results are presented for the polarized and unpolarized differential cross sections $d(\Delta)\sigma/dp_T$ at LO and NLO. As stated before, the unphysical scales μ_r , μ_f , and μ'_f are only an artifact of a perturbative calculation and thus arbitrary. Here, for simplicity we have chosen all scales to coincide with the hard scale in the process, $p_T = \mu_r = \mu_f = \mu'_f$. The lower panel of the figure displays the so-called “ K -factor”, defined as the ratio of NLO to LO contributions,

$$K = \frac{d(\Delta)\sigma^{NLO}}{d(\Delta)\sigma^{LO}} . \quad (4.22)$$

The K -factor for the unpolarized cross sections is almost constant over the p_T -range considered. It increases only towards low values of the transverse momentum, where perturbative QCD is not supposed to be applicable. The functional behavior of K in

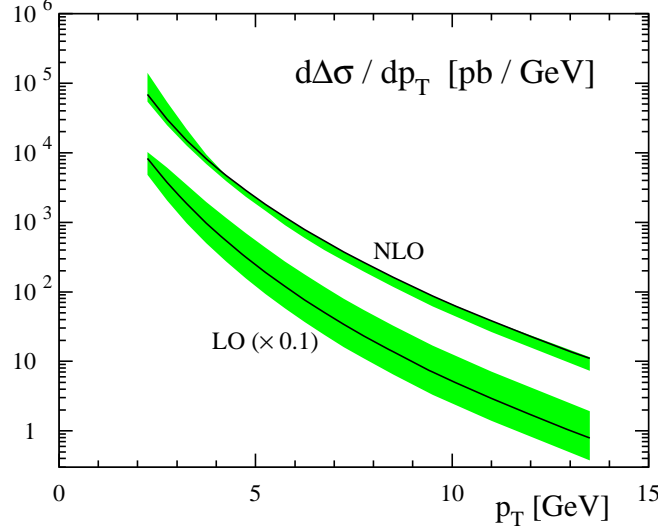


Figure 4.3: Scale dependence of the polarized cross section for $\vec{p}\vec{p} \rightarrow \pi^0 X$ at LO and NLO. All scales are varied in the range $p_T/2 \leq \mu_r = \mu_f = \mu'_f \leq 2p_T$. Solid lines correspond to the choice where all scales are set to p_T . The LO results have been rescaled by a factor 0.1 for a better legibility.

the polarized case with generally smaller NLO corrections can be traced back to large cancelations and zeroes of the corresponding cross sections. At larger p_T the K -factors for unpolarized and polarized cross sections approach each other. K is sometimes referred to as a “measure” for the importance of higher order corrections to hadronic processes. This proposition, however, has to be taken with some care. The K -factor depends strongly on the LO cross sections, which suffer from large scale uncertainties. In addition, new production mechanisms appearing for the first time at the NLO may lead to sizeable K -factors. However, similarly large corrections are not expected at higher orders.

A more reliable estimate on the impact of NLO corrections is provided by the improvement of scale dependence when extending a calculation from LO to NLO. We study this feature by a variation of the scales emerging in the computation, since setting all scales equal to p_T is a suggestive, but by no means mandatory choice. Figure 4.3 presents the results obtained for the polarized cross sections at LO and NLO when varying all scales simultaneously in the range $p_T/2 \leq \mu_r = \mu_f = \mu'_f \leq 2p_T$. Including NLO corrections to the cross sections reduces the scale uncertainty significantly, as expected from Eq. (2.12). Whereas the LO results exhibit a strong scale dependence over the whole p_T -range considered, the NLO predictions are by far better constrained and vary only slightly as the scales are modified. As discussed in Sec. 2.1, this feature is one of the main motivations for performing a QCD calculation at NLO accuracy, since scale uncertainties eventually translate into theoretical errors for the extraction of Δg . The inclusion of NLO corrections

leads to a reduction in theoretical uncertainties which are not sufficiently under control at the LO.

An excellent check for the reliability of our results is provided by a completely independent calculation of NLO corrections to single-inclusive pion production in pp -collisions in a Monte-Carlo approach by de Florian [106]. Rather than analytically phase space integrating all matrix elements in n dimensions as we did, a numerical Monte-Carlo integration has been performed in [106]. This technique makes use of the singularity structure of the $2 \rightarrow 3$ matrix elements, which allows for an explicit separation and cancelation of all poles by hand [93, 107]. The finite remainders are numerically phase space integrated in four dimensions, which is quite time-consuming and tedious, making the technique inappropriate for extracting parton densities in a global analysis of data, which will be discussed in Sec. 4.3. However, the Monte-Carlo approach has the advantage of a higher flexibility than our largely analytical method. Experimental cuts can easily be implemented, and an extension of the code to different observables such as jet production is relatively straightforward. The outcome of a comparison of our results to the ones of de Florian, however, was that both methods give the same answer.

Having ensured the reliability of our calculation in various ways, we are in a position to compare our results to experiment. In the following we set all scales to p_T by default. Figure 4.4 shows our predictions for the *unpolarized* π^0 -production cross section at NLO together with recent data from the PHENIX collaboration [100]. To get an estimate on the impact of different fragmentation functions we have performed the calculation with the KKP set as well as with Kretzer's parametrization [83]. The agreement of the data points with our theoretical prediction is encouraging, as it gives some confidence in the applicability of perturbation theory, down to rather low values of $p_T \simeq 1.5$ GeV. In particular, our results obtained with the KKP parametrization agree well with the measurement over almost the whole p_T -range considered. The calculation performed with Kretzer's set of fragmentation functions lies significantly below the data. This behavior can be traced back to a much smaller D_g^π in the latter set, which is not constrained by the e^+e^- data used for the extraction of the fragmentation functions [82, 83], as discussed in Sec. 2.5. Due to the dominance of gluonic channels at low-to-intermediate p_T , in this range the effects of a smaller D_g^π are particularly pronounced. Since the KKP parametrization gives a good description we will perform our further analyses using this set for describing pion fragmentation.

In Fig. 4.5 data from the STAR collaboration [101] are compared to our NLO calculation. Currently, the acceptance of the STAR detector is such that pions can only be detected at very small scattering angles, corresponding to rapidities up to $\eta \simeq 4$. Therefore, it allows, in principle, to access the parton distributions at smaller values of x than, e.g., the PHENIX experiment, where only events at central rapidity are detected, as can be seen from the definition of x_a and x_b in Eq. (4.6). Our calculation is performed at the RHIC c.m.s. energy of $\sqrt{S} = 200$ GeV and fixed $\eta = 3.8$. The results are displayed in terms of the pion's energy, $E_\pi = p_T \cosh \eta$, rather than its transverse momentum. Our predictions obtained with the KKP fragmentation functions [82] agree again rather well with the data over the whole E_π range considered. As before, using Kretzer's parametrization yields results lying somewhat below the data.

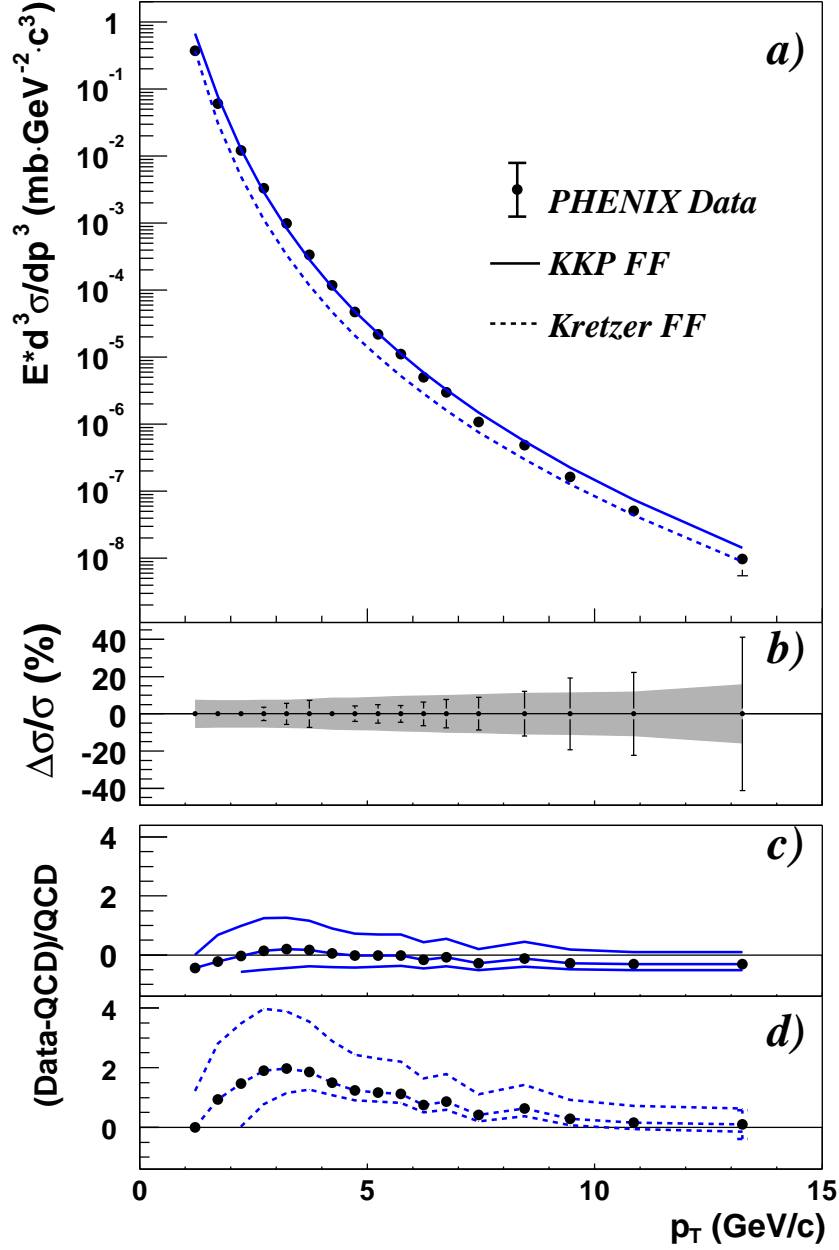


Figure 4.4: Unpolarized cross section $E_\pi (d^3 \sigma / d^3 P_\pi)$ for $pp \rightarrow \pi^0 X$ at $\sqrt{S} = 200$ GeV: a) Comparison of our NLO results obtained with the fragmentation functions of KKP [82] (solid line) and Kretzer [83] (dotted line) to the data from PHENIX [100]; b) Relative statistical errors (points) and systematic errors (bands) of data; c, d) Relative differences between data and the theoretical prediction with KKP and Kretzer, respectively. The figure has been taken from Ref. [100].

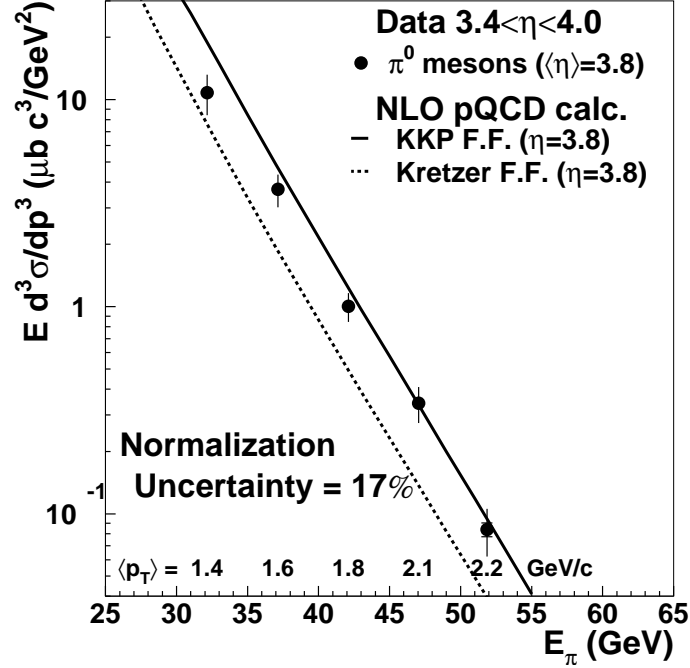


Figure 4.5: Data for the unpolarized cross section $E_\pi (d^3\sigma/d^3P_\pi)$ for $pp \rightarrow \pi^0 X$ at $\sqrt{S} = 200$ GeV from the STAR collaboration [101], compared to our NLO results using the KKP fragmentation functions [82]. The figure is taken from Ref. [101].

4.3 The Double-Spin Asymmetry A_{LL}^π

Having thus tested the reliability of our calculation we now turn to the actual quantity of interest in single-inclusive pionproduction – the double-spin asymmetry A_{LL}^π , defined in Eq. (4.2). A_{LL}^π is of particular importance since with the advent of new data from current and future measurements it could serve as a starting point for future analyses of the parton distributions of the proton with the major goal of constraining Δg .

In Fig. 4.6 we have plotted our expectations for A_{LL}^π in the mid-rapidity range relevant for PHENIX, i.e., integrated over $-0.38 \leq \eta \leq 0.38$, at LO and NLO for two sets of parton distributions [17] differing mainly in their gluon distributions. The NLO result with the GRSV standard scenario resembles the LO estimate, but its absolute value is somewhat smaller in size. This feature has already been indicated by the relative sizes of unpolarized and polarized K -factors in Fig. 4.2 and demonstrates the importance of including $\mathcal{O}(\alpha_s^3)$ contributions for an accurate determination of Δg from experiment. Much more pronounced than the effect of NLO corrections, however, is the difference of the two tested gluon scenarios. With a maximal gluon saturation one obtains asymmetries differing from those in the standard scenario by a considerable amount. In order to test, whether experiment might be able to discriminate between these two assumptions, we have also shown “error bars”, which give an estimate for the statistical accuracy [22] to be expected

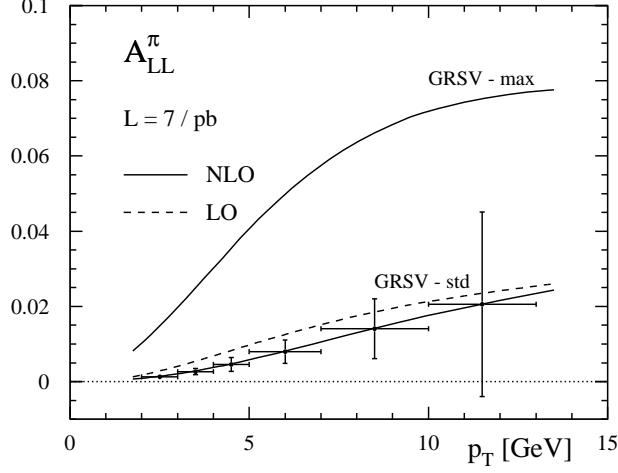


Figure 4.6: Double-spin asymmetry for $pp \rightarrow \pi^0 X$. The solid lines correspond to NLO results obtained with the GRSV standard and maximal gluon scenarios, respectively [17]. The dashed line shows a LO calculation with the GRSV standard parametrization. Also displayed is the expected statistical uncertainty in A_{LL}^π according to Eq. (4.23) assuming an integrated luminosity of $\mathcal{L} = 7 \text{ pb}^{-1}$.

from the PHENIX experiment at RHIC:

$$\delta A_{LL}^\pi \simeq \frac{1}{\mathcal{P}_p^2 \sqrt{\sigma_{bin} \mathcal{L}}} . \quad (4.23)$$

Here, \mathcal{P}_p stands for the polarization of the proton beams, \mathcal{L} for the integrated luminosity of the collisions, and σ_{bin} for the unpolarized cross section integrated over the p_T -bin for which the error is to be determined. In our estimate we have assumed $\mathcal{P}_p = 0.4$ for each proton beam, and $\mathcal{L} = 7/\text{pb}$, which are rather moderate values, as RHIC aims at a polarization of 70% and integrated luminosities up to 320 pb^{-1} at $\sqrt{S} = 200 \text{ GeV}$. We have taken into account that so far at PHENIX measurements can be performed only over half the azimuth angle ϕ . From the figure one may conclude that even data at low luminosities should clearly favor one of the gluon scenarios, thereby giving a first hint on the gluon decomposition of the polarized proton.

Thus, at first sight one is tempted to conclude, once data with reasonable statistical accuracy are available, Δg can be extracted from experiment straightforwardly. However, this assumption might be premature, and further, more thorough analyses are necessary to clarify whether an unambiguous determination of the proton spin structure will indeed be possible. We start with a presentation of additional predictions for A_{LL}^π , obtained with different assumptions about Δg in Fig. 4.7, where we also indicate first preliminary results from PHENIX [29]. Besides the curves already shown in Fig. 4.6, we have now also

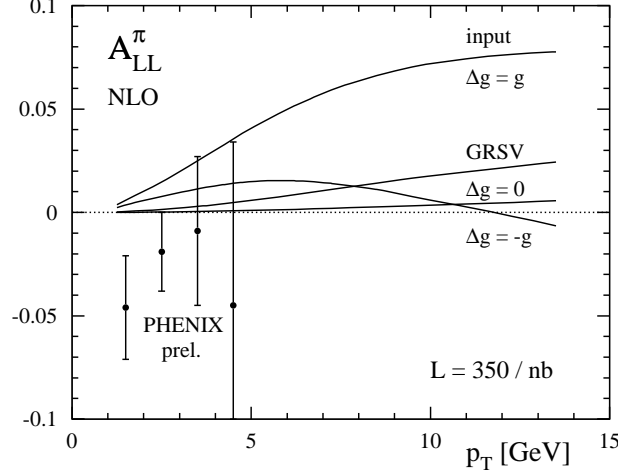


Figure 4.7: Double-spin asymmetry for $pp \rightarrow \pi^0 X$. Shown are NLO results obtained with different assumptions about Δg at the input scale of the evolution together with first preliminary results from PHENIX [29] based on an integrated luminosity of only $\mathcal{L} \simeq 350 \text{ nb}^{-1}$.

displayed double-spin asymmetries obtained with gluon distributions with a zero ($\Delta g = 0$) or maximally negative ($\Delta g = -g$) input for the evolution. First of all, it is interesting to observe that neither of the tested gluon distributions yields a negative A_{LL}^π in the range of small-to-moderate p_T , where preliminary data from PHENIX are available. Only the maximally negative Δg results in a spin asymmetry that eventually turns negative at $p_T \simeq 12 \text{ GeV}$ after exhibiting a maximum at $p_T \simeq 6 \text{ GeV}$. Below that value, however, the various parametrizations do not differ substantially. To clearly distinguish between different Δg , including their sign, data at higher values of p_T than currently available are necessary.

Before discussing possible implications of the preliminary PHENIX data, let us first turn to the general behavior of A_{LL}^π which can be readily understood by studying the weight of different partonic channels in $d\Delta\sigma$. To this end we have displayed the ratios of the dominant contributions, $gg \rightarrow cX$, $qg \rightarrow cX$, and $qq \rightarrow cX$, summed over all possible configurations of the final state, to the full cross section $d\Delta\sigma$ in Fig. 4.8. Here, the “ q ” denotes the sum of contributions from quarks and antiquarks of all flavors. The qq channels yield almost negligible contributions in all scenarios with non-vanishing gluonic input. The results for the gluon-induced reactions, qg and gg , on the other hand, depend rather strongly on the assumptions made on Δg , as expected. In the GRSV standard parametrization two-gluon processes are by far dominant up to $p_T \approx 8 \text{ GeV}$, where the qg channel takes over. A similar behavior can be observed in the maximal gluon scenario, where gg is even more pronounced at moderate p_T , and qg becomes equally important only above $p_T \gtrsim 12 \text{ GeV}$. Imposing a large negative gluon polarization causes strong

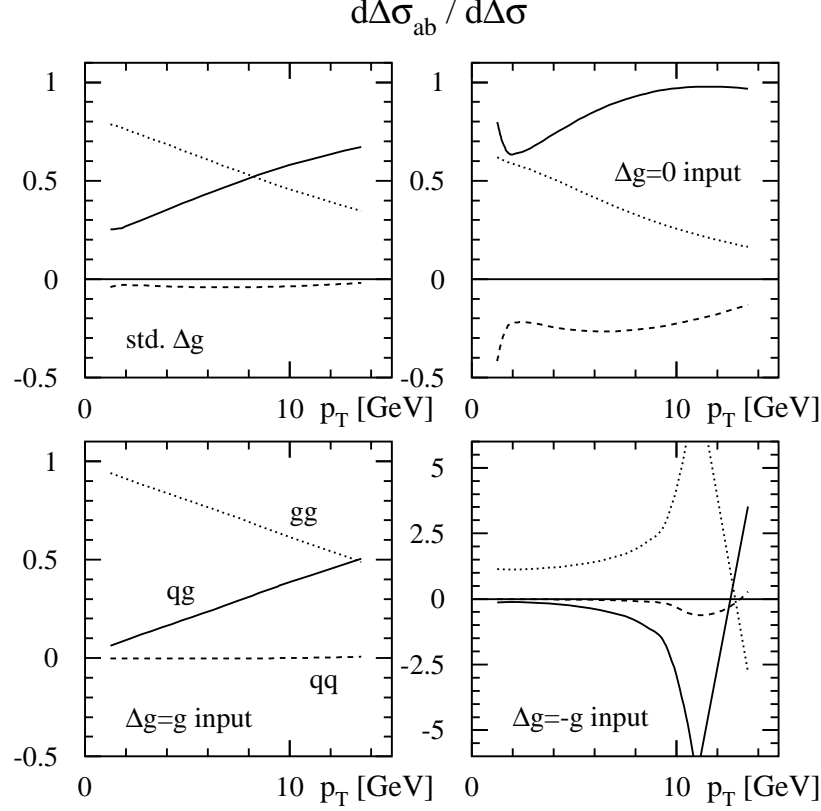


Figure 4.8: Relative contributions of different partonic scatterings $ab \rightarrow cX$ to the full differential cross section $d\Delta\sigma$ at NLO. Depicted are results for the channels qq (dashed), qg (solid), and gg (dotted) for the different gluon scenarios shown in Fig. 4.7.

cancellations between the gg and qg channels. The only scenario receiving more sizeable contributions from pure quark channels starts with a vanishing gluon distribution at the input scale. Since generally gluon-induced cross sections are numerically larger than quark contributions, the absolute value of $d\Delta\sigma$ in scenarios dominated by gg contributions is larger than in those which are to a large extent determined by other channels. This explains the large asymmetry in the maximal gluon scenario, where gg dominates over the whole p_T -range considered. On the other hand, a small A_{LL}^π results in the case of a vanishing gluonic input, where two-gluon channels are strongly suppressed and $d\Delta\sigma$ consists mainly of numerically small quark contributions. Only with a large negative gluonic input, a negative spin asymmetry is obtained once the qg channel becomes dominant. Intuitively, we suppose that an entirely negative Δg cannot cause a negative A_{LL}^π as long as it enters quasi quadratically as it does in two-gluon processes at PHENIX kinematics. At PHENIX,

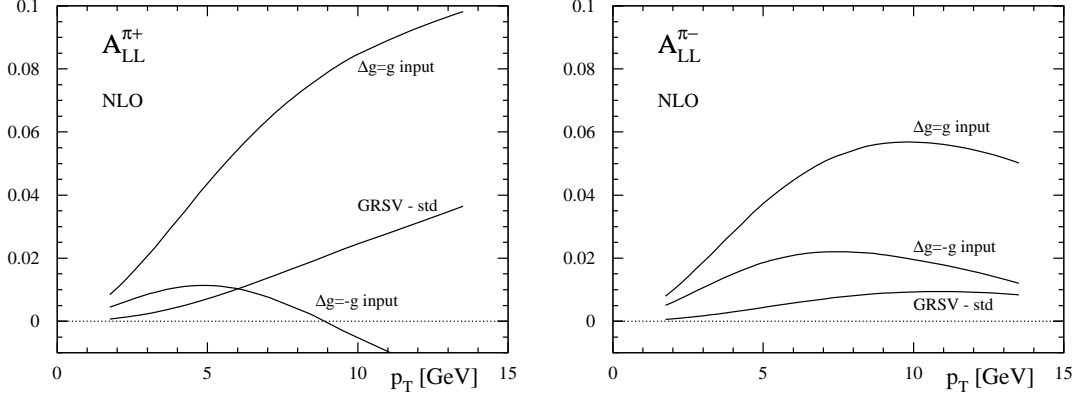


Figure 4.9: Double-spin asymmetry for hadroproduction of π^+ (l.h.s.) and π^- (r.h.s.), calculated at NLO for different assumptions about Δg at the starting point of the evolution.

only events in the central-rapidity range $-0.38 \lesssim \eta \lesssim 0.38$ are detected, where $x_a \simeq x_b$ and, therefore, $\Delta g(x_a, \mu) \simeq \Delta g(x_b, \mu)$. This explains the zero in the spin asymmetry which coincides with the p_T -range where qg channels start to dominate over the gg contributions.

From these considerations we conclude that from measurements of A_{LL}^π at central rapidities in the low- p_T -region alone it is not possible to determine the sign of Δg due to the dominance of the gg -induced subprocess. A clear distinction requires precision measurements at $p_T \gtrsim 10$ GeV. Here, additional information on the gluon polarization can be obtained by an extension of our analysis from neutral to charged pions [108]. Figure 4.9 indicates the behavior of the double-spin asymmetry for various gluon scenarios, if the detected π^0 is replaced by a π^+ or a π^- . In the following we denote the corresponding quantity for a neutral pion as before by A_{LL}^π , but we indicate the charge of the π^+, π^- explicitly in the spin asymmetry. We observe

$$\begin{aligned} \text{positive } \Delta g : \quad & A_{LL}^{\pi^+} > A_{LL}^\pi, \quad A_{LL}^{\pi^-} < A_{LL}^\pi, \\ \text{negative } \Delta g : \quad & A_{LL}^{\pi^+} < A_{LL}^\pi, \quad A_{LL}^{\pi^-} > A_{LL}^\pi. \end{aligned} \quad (4.24)$$

Whereas for positive gluon distributions $A_{LL}^{\pi^+}$ exceeds $A_{LL}^{\pi^0}$ and $A_{LL}^{\pi^-}$ at moderate-to-large p_T , the spin asymmetries for neutral and charged pions behave just oppositely if Δg is negative. This behavior is due to the dominance of the qg -channel at $p_T \gtrsim 10$ GeV. Since $D_u^{\pi^+} > D_u^{\pi^0}$, the absolute value of the cross section for the $ug \rightarrow uX$ subprocess is enhanced when the π^0 is replaced by a π^+ . The overall sign of this contribution, however, is determined by the sign of Δg , since the partonic cross section $d\hat{\sigma}_{qg \rightarrow qX}$ is entirely positive, see Fig. 4.10 below, and $\Delta u > 0$ [cf. Fig. 2.2]. In $pp \rightarrow \pi^+ X$, the dominant $ug \rightarrow uX$ channel enters thus with positive sign whenever $\Delta g > 0$. Then, the resulting spin asymmetry is enhanced as compared to the case of neutral pion production. If $\Delta g < 0$, $d\Delta\sigma_{ug \rightarrow uX}$ turns negative, and the polarized $pp \rightarrow \pi^+ X$ cross section is smaller

in size than $d\Delta\sigma_{pp\rightarrow\pi^0 X}$. Channels with a d -quark in the initial state do not affect this feature significantly, as $|\Delta d| \ll |\Delta u|$, and, therefore, $|d\Delta\sigma_{dg\rightarrow dX}| \ll |d\Delta\sigma_{ug\rightarrow uX}|$. On the other hand, $D_u^{\pi^-} < D_u^{\pi^0}$. Thus, the absolute value of $d\Delta\sigma_{ug\rightarrow uX}$ decreases, if the π^0 is replaced by a π^- rather than a π^+ . The thereby induced change in the spin asymmetry is just opposite to the case of π^+ -production. A comparison of the spin asymmetries for all types of pions at moderate-to-large values of p_T should therefore serve as an additional tool for constraining the sign of Δg , although its functional form cannot be determined from these considerations alone.

Having discussed how different assumptions for the spin-dependent parton distributions of the nucleon, in particular, for Δg , affect the double-spin asymmetry for single-inclusive pion production accessible at PHENIX, we turn now to a detailed outline of the methods required for an extraction of Δg from experiment. However, one should keep in mind that only a global analysis of data obtained in a variety of reactions will ultimately constrain the partonic structure of the polarized proton, while a determination of Δg on the basis of pion production alone will be difficult at $p_T \lesssim 10$ GeV. In the following we focus on the information contained in data on A_{LL}^π , taken in pp -collisions at RHIC. In particular, we will address the issue of a possible negative spin asymmetry in the range of low-to-medium p_T , perhaps indicated by first, preliminary data from PHENIX [29], cf. Fig. 4.7. Since we have not encountered a gluon distribution yielding negative values for A_{LL}^π at low p_T so far, some remarks are in order here.

We start from the p_T - and rapidity-dependent differential cross section for the reaction $\vec{p}\vec{p} \rightarrow \pi^0 X$ at NLO, Eq. (4.3), which can be cast into the form

$$\begin{aligned} \frac{d\Delta\sigma}{dp_T d\eta} &= \sum_{a,b,c} \int_{x_a^{\min}}^1 dx_a \Delta a(x_a, \mu_f) \int_{x_b^{\min}}^1 dx_b \Delta b(x_b, \mu_f) \\ &\times \int_{z_c^{\min}}^1 dz_c D_c^\pi(z_c, \mu_f') \frac{d\Delta\hat{\sigma}_{ab\rightarrow cX}}{dp_T d\eta}(p_T, \eta, x_a, x_b, z_c, \mu_r, \mu_f, \mu_f'). \end{aligned} \quad (4.25)$$

The further analysis is performed in Mellin- N moment rather than in Bjorken- x space, based on frequently used techniques in fitting procedures of parton distributions, see, e.g., [109]. This transformation is mainly motivated by the need for an efficient method to implement the rather complex and lengthy expressions for the partonic cross sections without any approximations in an NLO analysis. To this end, the parton densities are written in terms of their Mellin moments. For an arbitrary function ϕ , the N -th Mellin moment is defined as

$$\phi^N(\mu) \equiv \int_0^1 dx x^{N-1} \phi(x, \mu). \quad (4.26)$$

The solution of the differential evolution equations for the parton densities, Eqs. (2.46), becomes particularly simple in Mellin- N space and can be performed analytically, since there the cumbersome convolutions of the parton distributions with the evolution kernels factorize into ordinary products. After evolution to a specific scale μ in moment space the parton distributions in x -space are recovered via an inverse Mellin transform,

$$\phi(x, \mu) = \frac{1}{2\pi i} \int_{\Gamma_N} dN x^{-N} \phi^N(\mu). \quad (4.27)$$

The integration is to be performed along a suitable contour Γ_N in the complex N -plane to the right of all poles. Replacing the parton densities, $\Delta a(x_a, \mu_f)$ and $\Delta b(x_b, \mu_f)$, by their representations as inverse Mellin transforms, Eq. (4.27), the differential cross section, Eq. (4.25), acquires the form

$$\begin{aligned}
\frac{d\Delta\sigma}{dp_T d\eta} &= \frac{1}{(2\pi i)^2} \sum_{a,b,c} \int_{\Gamma_N} dN \int_{\Gamma_M} dM \Delta a^N(\mu_f) \Delta b^M(\mu_f) \\
&\quad \times \int_{x_a^{\min}}^1 dx_a \int_{x_b^{\min}}^1 dx_b \int_{z_c^{\min}}^1 dz_c x_a^{-N} x_b^{-M} D_c^\pi(z_c, \mu'_f) \\
&\quad \times \frac{d\Delta\hat{\sigma}_{ab \rightarrow cX}}{dp_T d\eta}(p_T, \eta, x_a, x_b, z_c, \mu_r, \mu_f, \mu'_f) \\
&= \sum_{a,b} \int_{\Gamma_N} dN \int_{\Gamma_M} dM \Delta a^N(\mu_f) \Delta b^M(\mu_f) \rho_{ab}^\pi(p_T, \eta, N, M, \mu_r, \mu_f, \mu'_f) .
\end{aligned} \tag{4.28}$$

In the last line all integrations over momentum fractions, the x_i^{-N} factors from the inverse Mellin transforms (4.27), the partonic cross sections, the summation over all final state particles c , and the integration over the fragmentation functions have been absorbed into the function ρ_{ab}^π . If the $D_c^\pi(z_c, \mu'_f)$ should be fitted to data along with the parton densities, they cannot be “absorbed” into the ρ_{ab}^π and an additional Mellin integration has to be performed. Assuming that the fragmentation functions are sufficiently constrained and using the analytically determined partonic cross sections, it is possible to calculate the functions ρ_{ab}^π , which contain known ingredients only, before the actual fitting procedure. The time-consuming integrations contained in ρ_{ab}^π are evaluated choosing the values of N, M on the contours Γ_N, Γ_M as supports of a numerical Gaussian integration. The subsequent inverse Mellin transformations linking the moments of the parton distributions with these quantities can then be performed extremely fast, allowing to access the spin-dependent parton distributions of the proton in reactions described by rather complex theoretical expressions at NLO without approximations. Of course, a global analysis of the polarized parton distributions will include not only data from pion production, but all experimental information on the polarized proton available.

We can now, in principle, make use of the preliminary data obtained by the PHENIX collaboration [29], which currently suggest negative spin asymmetries at low-to-moderate p_T [cf. Fig. 4.7], and try to find a gluon distribution accounting for these results by the fitting procedure sketched above. Before turning to this rather intricate full NLO analysis we wish, however, to discuss the dependence of the spin asymmetry on Δg on the basis of an instructive, largely analytical LO approach, and show how the structure of the contributions from the individual channels entering the polarized pion production cross section may set a lower bound on A_{LL}^π . Only afterwards we will aim to extend our analysis to NLO.

We base our discussion on the LO rapidity-integrated differential cross section

$$\begin{aligned} p_T^3 \frac{d\Delta\sigma}{dp_T} &= \sum_{a,b,c} \int_{x_T^2}^1 dx_a \Delta a(x_a, \mu_f) \int_{x_T^2/x_a}^1 dx_b \Delta b(x_b, \mu_f) \\ &\times \int_{x_T^2/\sqrt{x_a x_b}}^1 dz_c D_c^\pi(z_c, \mu_f') p_T^3 \frac{d\Delta\hat{\sigma}_{ab \rightarrow cX}}{dp_T}(\hat{x}_T^2, \mu_r, \mu_f, \mu_f') , \end{aligned} \quad (4.29)$$

as it is amenable to an analytical Mellin transform as we will outline below. In Eq. (4.29) we have introduced the dimensionless variables $x_T = 2p_T/\sqrt{S}$ and $\hat{x}_T^2 = x_T^2/z_c^2 x_a x_b$. At LO, all partonic cross sections occurring in Eq. (4.29) have been calculated analytically. We assume that the (anti)quark distributions are sufficiently well constrained to treat them as known. There is still room for improvement in our knowledge of, e.g., the flavor separation of the polarized sea in the nucleon, but this uncertainty does not affect A_{LL}^π in single-inclusive π^0 -production significantly: In the numerically most relevant subprocess including quarks in the initial state, $qg \rightarrow qg$ [cf. Fig. 4.8], the quark distributions enter only in the *sum*, $\Delta u + \Delta \bar{u} + \Delta d + \Delta \bar{d}$, since u and d quarks are equally likely to fragment into a π^0 .

Let us now investigate whether it is possible to obtain a negative A_{LL}^π and *how* negative it can be. As a first candidate for causing a negative spin asymmetry, negative spin-dependent partonic cross sections should be considered. They give rise to negative polarized hadronic cross sections when convoluted with positive parton densities and the always positive, spin-averaged fragmentation functions. At LO, ten partonic channels contribute to single-inclusive hadron production,

$$\begin{aligned} \text{(i)} \quad & gg \rightarrow gg , \\ \text{(ii)} \quad & gg \rightarrow q\bar{q} , \\ \text{(iii)} \quad & qg \rightarrow qg, q\bar{q} \rightarrow q\bar{q} , \\ \text{(iv)} \quad & q\bar{q} \rightarrow q\bar{q}, q\bar{q} \rightarrow gg, qq \rightarrow qq, \\ & qq' \rightarrow qq', q\bar{q} \rightarrow q'\bar{q}', q\bar{q}' \rightarrow q\bar{q}' , \end{aligned} \quad (4.30)$$

as discussed earlier, cf. Eq. (4.7). The partonic double-spin asymmetries \hat{a}_{LL} , defined in complete analogy to the hadronic A_{LL}^π , Eq. (4.2), by

$$\hat{a}_{LL} = \frac{d\Delta\hat{\sigma}}{d\hat{\sigma}} = \frac{d\hat{\sigma}^{++} - d\hat{\sigma}^{+-}}{d\hat{\sigma}^{++} + d\hat{\sigma}^{+-}} , \quad (4.31)$$

are depicted for some of the numerically important subprocesses in Fig. 4.10. The partonic channels $gg \rightarrow gg$, $qg \rightarrow qg$, $qq \rightarrow qq$, and $q\bar{q} \rightarrow q\bar{q}$ all exhibit positive asymmetries over the entire phase space and therefore cannot serve as a source for a negative hadronic A_{LL}^π when combined with positive parton densities. On the other hand, the reactions $gg \rightarrow q\bar{q}$ and $q\bar{q} \rightarrow gg$, and some other subprocesses of (iv) with $d\Delta\sigma_{ab \rightarrow cX} = -d\sigma_{ab \rightarrow cX}$ have $\hat{a}_{LL} = -1$ for all scattering angles due to helicity conservation at the quark-gluon vertex. However, as compared to the numerically by far dominant channel $gg \rightarrow gg$, the cross sections associated with these reactions are small. For example, the actual evaluation of

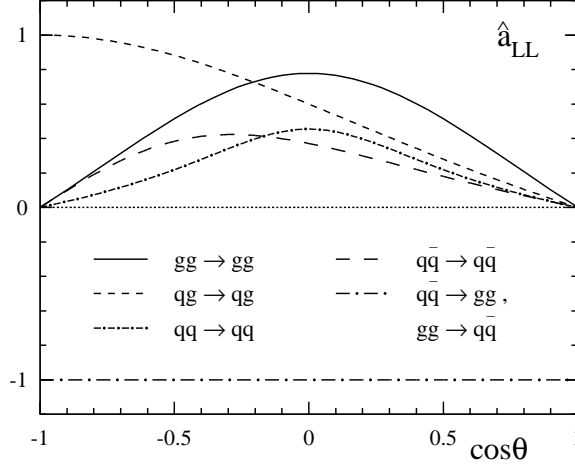


Figure 4.10: Partonic spin asymmetries \hat{a}_{LL} for various $2 \rightarrow 2$ scattering reactions at Born level, as a function of the scattering angle θ .

the partonic $gg \rightarrow q\bar{q}$ and $gg \rightarrow gg$ cross sections at $\theta = \pi/2$, i.e., mid-rapidity as for PHENIX, reveals a ratio of

$$\frac{d\Delta\hat{\sigma}_{gg \rightarrow q\bar{q}}}{d\Delta\hat{\sigma}_{gg \rightarrow gg}} \approx -\frac{1}{160} . \quad (4.32)$$

Even smaller results are obtained for the various quark-annihilation processes in (iv) of Eq. (4.30). They are negligible in comparison to all gluon-induced reactions as long as Δg does not vanish and p_T is not too large. Since A_{LL}^π is determined by the sum of all partonic cross sections, the small negative contribution from channel (ii) in Eq. (4.30) cannot cause a negative hadronic spin asymmetry A_{LL}^π , unless subprocess (i) is significantly suppressed, for instance, by a very small gluon-to-pion fragmentation function D_g^π , which is, however, very unlikely. Although our knowledge of the pion fragmentation functions is incomplete and certainly needs improvement, present data from $e^+e^- \rightarrow b\bar{b}$ jet reactions with subsequent hadronization of the jet into pions [110], put at least some lower bounds on D_g^π . They do not leave room for a much smaller than the currently assumed gluon fragmentation. Above that, a modification of D_g^π would strongly affect the differential cross section for unpolarized pion production in $pp \rightarrow \pi^0 X$, and would reduce it by about an order of magnitude at RHIC energies. This scenario is certainly disfavored by previous PHENIX measurements at $\sqrt{S} = 200$ GeV, which are fairly well described by our NLO analysis making use of the fragmentation functions proposed by [82], as discussed and illustrated in Fig. 4.4 above. We therefore conclude that subprocesses with negative partonic cross sections cannot be the main source for a negative A_{LL}^π .

Let us now turn our attention to the spin-dependent gluon density of the proton. It

emerges in all subprocesses with gluons in the initial state, i.e., in channel (iii) of Eq. (4.30) and, at central rapidities roughly quadratically, in $gg \rightarrow gg$ and $gg \rightarrow q\bar{q}$. Keeping in mind that the partonic cross section for the numerically dominant channel (i) is positive, it is obvious that a negative A_{LL}^π cannot easily be obtained within the perturbative framework we have applied so far.

However, so far we have not made use of the fact that the Δa and Δb in Eq. (4.29) are not necessarily probed at exactly $x_a = x_b$ (the arguments are equal only at $\eta = 0$), and that polarized parton distributions can exhibit a node, allowing for two alike parton densities to enter with different sign in the spin-dependent hadronic cross section. Before attempting to perform a thus inspired fit for an extraction of Δg from the data, we show how to derive an *explicit* lower bound on A_{LL}^π at the LO by a transformation of (4.29) to Mellin moment space. In contrast to the cumbersome numerical procedure required at NLO, outlined in Eq. (4.28), the simple structure of the Born cross sections makes $d\Delta\sigma/dp_T$ amenable to an analytical Mellin transform. Taking the Mellin moments with respect to x_T^2 ,

$$\Delta\sigma(N, \mu_r, \mu_f, \mu'_f) = \int_0^1 dx_T^2 (x_T^2)^{N-1} p_T^3 \frac{d\Delta\sigma}{dp_T}(\hat{x}_T^2, \mu_r, \mu_f, \mu'_f), \quad (4.33)$$

we obtain

$$\Delta\sigma(N) = \sum_{a,b,c} \Delta a^{N+1} \Delta b^{N+1} \Delta \hat{\sigma}_{ab}^{c,N} D_c^{\pi, 2N+3}, \quad (4.34)$$

where the $\Delta \hat{\sigma}_{ab}^{c,N}$ are the x_T^2 -moments of the partonic cross sections, defined in analogy to Eq. (4.26). The N -moments of the parton distribution and fragmentation functions have been introduced already in Eq. (4.26). Any dependence on the various scales is omitted from now on for simplicity. We can then rewrite Eq. (4.34) explicitly in terms of Δg^N ,

$$\begin{aligned} \Delta\sigma(N) = & (\Delta g^{N+1})^2 \left[\Delta \hat{\sigma}_{gg}^{g,N} D_g^{\pi, 2N+3} + \Delta \hat{\sigma}_{gg}^{q,N} \sum_{f=q,\bar{q}} D_f^{\pi, 2N+3} \right] \\ & + 2 \Delta g^{N+1} \Delta \hat{\sigma}_{qg}^{g,N} \sum_{f=q,\bar{q}} \Delta f^{N+1} [D_g^{\pi, 2N+3} + D_q^{\pi, 2N+3}] + \mathcal{C}^N. \end{aligned} \quad (4.35)$$

Here we have made use of the symmetry properties of the partonic cross sections at LO induced by the rapidity integration over a symmetric interval (in our case, $-\infty < \eta < \infty$). Exchanging the two final state partons in a $2 \rightarrow 2$ scattering process is generally equivalent to reversing the sign of rapidity. Integrating the partonic cross section for the generic reaction $ab \rightarrow cd$ over a rapidity interval $-\eta_0 \leq \eta \leq \eta_0$ therefore gives the same result as the corresponding integral for the reaction $ab \rightarrow dc$. This allows us, e.g., to express $\Delta \hat{\sigma}_{qg}^{q,N}$ in terms of $\Delta \hat{\sigma}_{qg}^{g,N}$. $\Delta\sigma(N)$ can then be cast into the compact form

$$\Delta\sigma(N) = (\Delta g^{N+1})^2 \mathcal{A}^N + 2 \Delta g^{N+1} \mathcal{B}^N + \mathcal{C}^N, \quad (4.36)$$

where \mathcal{A}^N includes all contributions from the processes with two gluons in the initial state, $gg \rightarrow gg$ and $gg \rightarrow q\bar{q}$. Likewise, \mathcal{B}^N represents the one-gluon channel $qg \rightarrow qg$, and \mathcal{C}^N ,

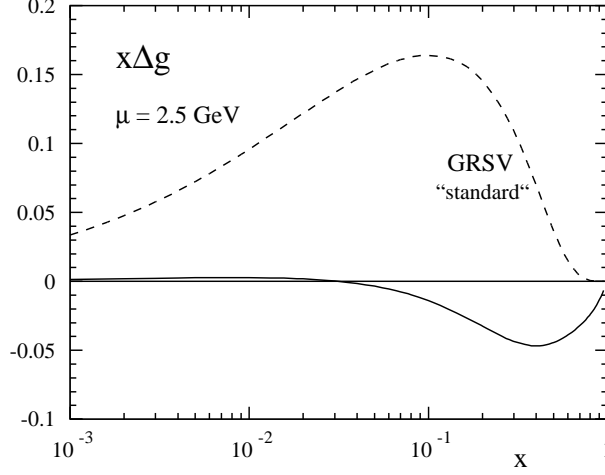


Figure 4.11: $\Delta g_{min}(x, \mu)$ resulting from the minimization condition Eq. (4.37) at a scale $\mu = 2.5$ GeV (solid), compared to the GRSV standard gluon density (dashed).

introduced already in Eq. (4.35), stands for all reactions without any incoming gluon. The quark densities, partonic cross sections and fragmentation functions of the respective processes are absorbed into the coefficients \mathcal{A}^N , \mathcal{B}^N , and \mathcal{C}^N , whose explicit form can be read off Eq. (4.35) easily.

Due to the dominance of the $gg \rightarrow gg$ channel with its positive partonic cross section over the negative contribution from the $gg \rightarrow q\bar{q}$ scattering, the latter can safely be neglected and \mathcal{A}^N is entirely positive. $\Delta\sigma(N)$ is then a quadratic form in the Mellin moment Δg^{N+1} with a minimum at

$$\Delta g^{N+1}|_{min} = -\frac{\mathcal{B}^N}{\mathcal{A}^N}. \quad (4.37)$$

The corresponding gluon density, $\Delta g_{min}(x, \mu)$, is straightforwardly obtained by an inverse Mellin transform (4.27). We depict Δg_{min} in Fig. 4.11, for comparison together with the gluon distribution of the GRSV standard set, which is larger and, by assumption, positive over the whole x -range considered. It can be seen that Δg_{min} almost vanishes in the small- x region, exhibits a node at intermediate x as expected, and turns to negative values at large x .

The node of Δg_{min} allows to probe the gluon densities in $gg \rightarrow gg$ at values of x_a and x_b where they have *different* sign. This can, in principle, be of particular importance for obtaining a sizeable negative spin asymmetry due to the dominance of the $gg \rightarrow gg$ channel in $pp \rightarrow \pi^0 X$. Using $\Delta g^{N+1}|_{min}$, the moments of the polarized pion production

cross section given in Eq. (4.36) take the form

$$\Delta\sigma(N)|_{min} = -\frac{(\mathcal{B}^N)^2}{\mathcal{A}^N} + \mathcal{C}^N, \quad (4.38)$$

which can be transformed to the hadronic cross section in p_T -space by an inverse Mellin transform,

$$p_T^3 \frac{d\Delta\sigma}{dp_T} \Big|_{min} = \frac{1}{2\pi i} \int_{\Gamma} dN (x_T^2)^{-N} \Delta\sigma(N)|_{min}. \quad (4.39)$$

We evaluate Eq. (4.39) with the (anti)quark distributions of the LO GRSV standard parametrization [17] and the fragmentation functions of Ref. [82]. The scales are fixed to the average transverse momentum of the data, $\mu_r = \mu_f = \mu'_f = \langle p_T \rangle \simeq 2.5$ GeV. In this way we obtain the *minimal* spin asymmetry $A_{LL}^{\pi,min}$ which is negative but does not exceed an absolute value of $\mathcal{O}(10^{-3})$ in the range $1 \lesssim p_T \lesssim 4$ GeV! Although our simplified LO analysis gives only an estimate for the double-spin asymmetry, it captures the main point we want to make: Since the spin-dependent hadronic cross section is a quadratic form in Δg , it is bounded from below and cannot acquire large negative values at moderate p_T and central rapidities. At higher transverse momentum sizeable (negative) results for A_{LL}^{π} are possible.

The largely analytical results we have obtained so far may slightly change in a more accurate analysis. However, the qualitative behavior of the spin asymmetry is not affected by the simplifying assumptions we have made. For example, to take the x_T^2 -moments analytically we had to integrate the hadronic cross section over all rapidities, whereas experiment is usually restricted to a certain range in η , e.g., PHENIX takes data only at $|\eta| \leq 0.38$. This approximation affects the x -ranges probed in the reaction. The larger the rapidity interval considered, the more likely collisions of partons with rather different momentum fractions $x_a \neq x_b$ become. This feature is illustrated by Fig. 4.12, where the polarized LO cross section is plotted at $\sqrt{S} = 200$ GeV and fixed $p_T = 2.5$ GeV versus the difference $|x_a - x_b|$ of the momentum fractions of the two incoming partons. The upper curve has been obtained by integrating over all η as in Eq. (4.29), whereas in the lower one rapidity has been restricted to $|\eta| \leq 0.38$. Obviously, allowing for a broader range of rapidities yields more events with $|x_a - x_b| > 0$ and – keeping the possibility of having a node for Δg in mind – more gg -reactions, where the two gluon distributions enter the hadronic cross section with different sign. Restricting our analysis to experimentally relevant rapidities, $|\eta| \leq 0.38$, thereby reduces the size of a negative A_{LL}^{π} even further. In addition, we have not adapted Δq and $\Delta \bar{q}$ to the new gluon scenario, but simply used the LO GRSV distributions throughout, although, in general, any change in Δg affects the (anti)quark distributions via evolution and thus requires in principle a refitting of Δq and $\Delta \bar{q}$. We have refrained therefrom assuming that the effects caused by this simplification will be negligible for our basic – and so far purely qualitative – estimate.

Regardless of the approximations made so far we think that we have illustrated clearly that a large negative double-spin asymmetry cannot be obtained within the framework of pQCD at low-to-moderate p_T -values. However, a thorough determination of Δg and, thereby, interpretation of a possibly large negative A_{LL}^{π} requires doubtlessly a global NLO

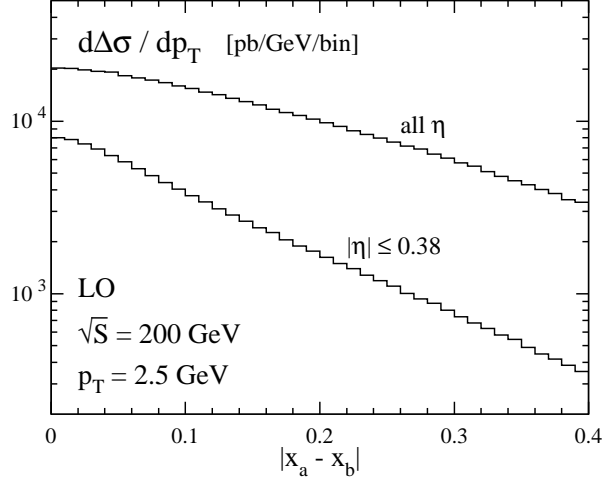


Figure 4.12: LO Rapidity-integrated pion production cross section $d\Delta\sigma/dp_T$ at $\sqrt{S} = 200$ GeV and $p_T = 2.5$ GeV, plotted in bins of $|x_a - x_b|$ for different ranges of the η integration.

analysis of all available data, which carefully takes into account all subtleties ignored so far. We have performed such an analysis including all data from polarized DIS along with the very recent (still preliminary) results from the PHENIX collaboration for $\vec{p}\vec{p} \rightarrow \pi^0 X$ [29] by means of the double Mellin transform technique sketched in Eq. (4.28). For this purpose, several ansätze have been tried for Δg , in particular, ones exhibiting a node. None of these fits allowed to reproduce a negative A_{LL}^π of approximately -2% in the region $1 \lesssim p_T \lesssim 4$ GeV. The utmost which could be achieved was a negative spin asymmetry with an absolute value of a few times 10^{-3} , consistent with the analytic bound derived above. Any such fit required gluon distributions having a node and violating positivity in certain ranges of x . We therefore conclude that even though it might be mathematically possible to find ways for reproducing large negative A_{LL}^π at $p_T \simeq 1 \div 4$ GeV, our full NLO analysis rules out physically acceptable solutions within the framework of pQCD. If future data should indeed confirm large negative spin asymmetries, we thus have to look for alternative ways of explanation. In the range of small-to-moderate p_T , power corrections, neglected in our analysis, could be of some importance. Although they do not seem to play a significant role in unpolarized pion production even at rather low transverse momenta, $p_T \approx 1.5$ GeV, they might affect the spin-dependent cross section more severely since $d\Delta\sigma$ is subject to strong cancelations among its various contributions. Such effects can, for instance, be modeled by taking into account the intrinsic transverse momentum k_T of the incoming partons. This would yield power corrections of the form $\langle k_T \rangle / p_T$, with $\langle k_T \rangle$ an average k_T , which possibly modify A_{LL}^π at $p_T \lesssim 5$ GeV, as, e.g., demonstrated in [111]. Above that, possibly further, so far unconsidered mechanisms might be instrumental in causing

a negative spin asymmetry, or a breakdown of pQCD could occur at low p_T . In any case, providing a satisfactory explanation for a large negative A_{LL}^π – should it indeed be confirmed experimentally – cannot be achieved within the standard framework of pQCD. It would require a deeper understanding of hadronic interactions and opens up new windows to a more comprehensive view of the nucleon’s structure.

4.4 Summary

In this chapter, we have presented a full NLO calculation of the spin-dependent partonic scattering cross sections relevant for single-inclusive pion production in longitudinally polarized hadron-hadron collisions. These calculations have been done in a fully analytical way. We then combined the partonic cross sections with parton distributions and fragmentation functions and performed a thorough analysis of the resulting single-inclusive pion cross sections. It turned out that NLO corrections to both, unpolarized and polarized LO cross sections are well under control, and that the dependence of these observables on unphysical scales is significantly reduced beyond the leading order, which ensures that our predictions are free of large theoretical uncertainties stemming from artifacts of the fixed order perturbative calculation. This was one of the main motivations for our NLO calculation, since only accurate results will allow for an extraction of information on the parton densities of the nucleon from experiment. Indeed, we have found that the unpolarized cross sections we obtained account well for recent measurements of the PHENIX and STAR collaborations at RHIC [100, 101], which gives us some confidence in the applicability of our approach, also for a future use in the polarized case. Next, we discussed the double-spin asymmetry in single-inclusive pion production, which turned out to be a promising tool for determining the gluon polarization of the nucleon. We found that A_{LL}^π is very sensitive to Δg even at low integrated luminosities, although the sign of Δg cannot be accessed in neutral pion production at the low-to-moderate values of p_T where data have already been taken [29]. This can only be achieved in measurements at higher p_T , or from additional studies of charged pion production which is, of course, feasible at RHIC in the future. We have outlined in some detail that a negative spin asymmetry at small-to-medium p_T can hardly be obtained within a leading power pQCD approach. Should the preliminary data from PHENIX, which indicate a sizeable negative A_{LL}^π , be confirmed, therefore an extension of the standard leading power perturbative calculation will become necessary. This opens up quite unexpected views on our present understanding of pQCD.

We stress that, in any case, our results allow for the first time for a quantitative comparison of theory with experiment in $\vec{p}\vec{p} \rightarrow \pi^0 X$, free of large theoretical uncertainties. New data from RHIC in the near future will provide us with excellent prospects for a determination of Δg , or, else, require us to extend the theoretical standard framework for the description of hard scattering processes – in either case a source for improving our knowledge on the strong interaction.

The methods developed in this chapter on the basis of single-inclusive pion production can straightforwardly be applied to processes involving other hadrons in the final state, and thereby serve as a source of information on fragmentation functions little explored so far.

A generalization to helicity transfer reactions, such as the production of lambda baryons, whose spin state is accessible in experiment via their self-analyzing decay distribution [81], is feasible, and could deepen our understanding of the mechanisms governing the formation of polarized hadrons.

In the next chapter we will, however, focus on single-inclusive jet production in pp -collisions, closely related to the case of pion production discussed above. The spin asymmetries encountered in jet production will turn out to be a particularly clean tool for gaining information on the parton distributions of the colliding hadrons, and, therefore, are invaluable for an extraction of Δg from experiment.

Chapter 5

High- p_T Single-Inclusive Jet Production in Polarized pp-Collisions at NLO QCD

Gaining a thorough understanding of hadronic spin structure requires a careful analysis of a broad variety of reactions sensitive to the parton content of the nucleon. In this context, processes which are not subject to uncertainties due to hadronization effects in the final state are particularly suitable. For this reason we will turn to the investigation of single-inclusive jet production in polarized proton-proton collisions at high- p_T [33],

$$p(P_A) + p(P_B) \rightarrow \text{jet}(P_J) + X. \quad (5.1)$$

Jets are abundantly produced in hadronic collisions at high energies, yielding sizeable cross sections even at rather low luminosities, and can therefore be studied extensively in the proton-proton mode at RHIC [22]. From the theoretical side, it is of particular importance to provide the necessary framework for an analysis of high- p_T jet production beyond the leading order, since the QCD structure of the jet starts to manifest itself only at NLO [112]. This is in contrast to the case of hadron production, since the hadronization process itself can be studied already at the LO. Above that, the inclusion of NLO corrections is expected to reduce the theoretical uncertainties, such as scale dependence, of the calculated jet cross sections. It should be noted that Monte-Carlo methods have been applied to single-inclusive jet production before [113]. We, however, focus on a largely analytical approach as in the previous chapter. Again, our results have the advantage of yielding much faster and more efficient computer codes.

5.1 Jet Definition

Jets are not intrinsically well-defined objects such as, e.g., hadrons. First introduced in the context of e^+e^- -annihilation by Sterman and Weinberg [114] in 1977, jets are now defined in different ways by different collaborations depending on the experimental conditions and

calculational techniques used [112, 115-120]. An attempt towards a standardization of jet definitions has been made by leading experts from experiment and theory at the Snowmass summer school 1990 [121], driven by the basic requirements that the definition must be simple to implement in an experimental analysis as well as in a theoretical calculation. The latter has to be meaningful at any order of perturbation theory and relatively insensitive to hadronization effects in the final state. These key issues, and the additional advantage of simple transformation properties under Lorentz boosts, are met by a standard jet definition in terms of cones in pseudorapidity η_J and azimuth ϕ_J . Within the Snowmass convention any parton i with coordinates (η_i, ϕ_i) inside a cone of radius

$$R \equiv \sqrt{(\eta_i - \eta_J)^2 + (\phi_i - \phi_J)^2} \quad (5.2)$$

around the jet axis (η_J, ϕ_J) is associated with the jet. Usually, R is chosen to lie in the range $0.4 \leq R \leq 1.0$. A jet composed of any number of partons is, in addition to η_J and ϕ_J , characterized by its transverse energy E_T . These quantities are defined as weighted sums of the corresponding partonic ones,

$$\begin{aligned} E_T &\equiv \sum_{i \in \text{cone}} E_{T_i} , \\ \eta_J &\equiv \frac{1}{E_T} \sum_{i \in \text{cone}} E_{T_i} \eta_i , \\ \phi_J &\equiv \frac{1}{E_T} \sum_{i \in \text{cone}} E_{T_i} \phi_i , \end{aligned} \quad (5.3)$$

where only partons inside the cone are considered.

The Snowmass jet convention can only be implemented numerically [113, 118, 120]. An analytical approach requires a simplified criterion. In the jet definition first adopted by Furman [115] and later also used by Aversa et al. [104, 122] for the calculation of unpolarized jet cross sections, the direction of the jet axis \vec{P}_J is fixed by the condition

$$\vec{P}_J \equiv \sum_{i \in \text{cone}} \vec{p}_i , \quad (5.4)$$

which in the limit of vanishing jet invariant mass, $M_J^2 = P_J^2 = (\sum_i E_i)^2 - (\sum_i \vec{p}_i)^2 \approx 0$, equals the covariant version of Ref. [116]

$$P_J^\mu \equiv \sum_{i \in \text{cone}} p_i^\mu , \quad (5.5)$$

rather than Eqs. (5.3) [116]. The jet itself is now supposed to be a deposit of transverse energy in a cone with semi-aperture δ around the jet axis, cf. Fig. 5.1. The scattering angle of the jet with respect to the incoming hadron beam, θ_J , is related to the jet's pseudorapidity as usual, $\eta_J = -\ln(\tan \theta_J/2)$, and δ can straightforwardly be identified with the cone radius (5.2) via $R = \delta \cosh \eta_J + \mathcal{O}(\delta^2)$. In the so-called ‘‘small cone approximation’’ (SCA) of Refs. [115, 104, 122], only small cone openings are considered, and

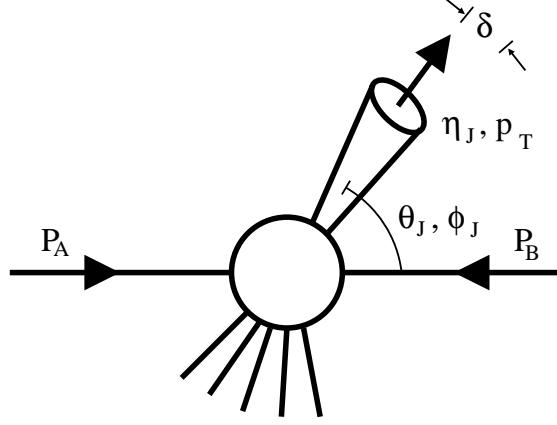


Figure 5.1: Sketch of single-inclusive jet production in $p(P_A) + p(P_B) \rightarrow \text{jet}(P_J) + X$.

terms of $\mathcal{O}(\delta^2)$ can safely be neglected. The partonic jet cross section is then of the form $\mathcal{A} + \mathcal{B} \ln \delta$, and the coefficients \mathcal{A} and \mathcal{B} can be determined at an analytical level. The validity of this assumption has been demonstrated by a comparison of unpolarized jet cross sections, calculated in the SCA, to a computation where finite cone sizes have numerically been taken into account [123, 116], which showed that the SCA works well for cone sizes up to $R \simeq 0.7$. We will confirm this finding below. In the range where $\delta \cosh \eta_J \approx R \ll 1$, i.e., where the SCA is supposed to be reliable, the jet axis chosen according to Eq. (5.5) coincides with the corresponding direction of the Snowmass definition (5.3) [124]. For this reason and, as we will show below, because corrections of $\mathcal{O}(\delta^2)$ to observables computed in the SCA are indeed small also in the polarized case, it is sensible to perform largely analytical calculations making use of the jet definition (5.5) as we will do in the following.

Different jet finding algorithms differ not only in the definition of the jet axis, but also in what they actually count as “one-jet event” [112, 117]. Within the SCA [115, 104, 122], any configuration with at least one jet in the final state is considered when single-inclusive jet cross sections are calculated. More specifically, this means that, e.g., two-jet events are counted twice as either of the two jets can be detected. This is to be contrasted to algorithms which count only the most energetic jet in an event. Both types of algorithm are sensible as they respect all requirements put on a reasonable jet convention. However, they yield different results. When presenting predictions or data for jet observables it is therefore crucial to specify the explicit convention they refer to.

5.2 Analytical Calculation of Jet Cross Sections

In complete analogy to hadroproduction of inclusive pions, discussed in Chap. 4, the spin-dependent high- p_T jet cross section for the reaction $p(P_A) + p(P_B) \rightarrow \text{jet}(P_J) + X$ is given

by the convolution of the parton densities of the proton with the partonic cross sections,

$$\begin{aligned} \frac{d\Delta\sigma}{dp_T d\eta_J} &= \frac{2p_T}{S} \sum_{a,b} \int_{VW}^V \frac{dv}{v(1-v)} \int_{VW/v}^1 \frac{dw}{w} \Delta a(x_a, \mu_f) \Delta b(x_b, \mu_f) \\ &\times \left[\frac{d\Delta\hat{\sigma}_{ab \rightarrow jet X}^{(0)}(s, v)}{dv} \delta(1-w) + \frac{\alpha_s(\mu_r)}{\pi} \frac{d\Delta\hat{\sigma}_{ab \rightarrow jet X}^{(1)}(s, v, w, \mu_f, \mu_r)}{dv dw} \right]. \end{aligned} \quad (5.6)$$

It is important to note that, although the initial state is handled in exactly the same way as in the case of single-inclusive pion production, jet cross sections differ significantly in the treatment of the final state. They do not contain parton-to-hadron fragmentation functions describing the hadronization process. As a consequence, jet observables are free of any dependence on a final state factorization scale μ'_f , since singularities in the partonic cross sections need not be factorized into fragmentation functions at some scale, but cancel in the sum of all contributions to a well-defined jet quantity. As we will see below, this feature makes jet cross sections a very clean tool for gaining a better knowledge of the parton distributions of the proton, in particular Δg . Of course, divergencies in the initial state still have to be factorized into the parton densities, thereby introducing a dependence on the factorization scale μ_f . As before, through the renormalization of the strong running coupling α_s a renormalization scale μ_r enters into the cross section.

In Eq. (5.6), η_J and p_T refer to the pseudorapidity and the transverse component of the jet momentum P_J , which is given by the sum of partonic momenta according to the jet definition Eq. (5.5). It is convenient to express all quantities in terms of the dimensionless variables V and W ,

$$V = 1 - \frac{p_T}{\sqrt{S}} e^{\eta_J} \quad \text{and} \quad W = \frac{p_T^2}{SV(1-V)}, \quad (5.7)$$

with $S = (P_A + P_B)^2$ being the available c.m.s. energy squared, as usual. The related parton-level variables read, in analogy to Eq. (4.4),

$$\begin{aligned} v &\equiv 1 + \frac{t}{s}, \quad w \equiv \frac{-u}{s+t}, \\ s &\equiv (p_a + p_b)^2, \quad t \equiv (p_a - P_J)^2, \quad u \equiv (p_b - P_J)^2, \end{aligned} \quad (5.8)$$

and the momentum fractions of the hadrons' momenta carried by the respective partons are given by

$$x_a = \frac{VW}{vw} \quad \text{and} \quad x_b = \frac{1-V}{1-v}, \quad (5.9)$$

similar to the corresponding expressions for hadron-production reactions in Eq. (4.6).

Contrary to the case of single-inclusive hadron production, discussed in Chap. 4, where different final-state partons have to be weighted with different fragmentation functions,

leading to the ten separate LO channels of Eq. (4.7) and six additional NLO processes, specified in Eq. (4.8), in a jet cross section no distinction is made between different partons, i.e., gluons and quarks or antiquarks of different flavors, producing the jet. All processes with the same initial-state partons have to be summed appropriately. This ultimately leads to the cancelation of final-state singularities at higher orders. There are only six basic processes $a + b \rightarrow \text{jet} + X$ which contribute to single inclusive jet production at LO and NLO,

$$\begin{aligned}
qq' &\rightarrow \text{jet } X \\
q\bar{q}' &\rightarrow \text{jet } X \\
qq &\rightarrow \text{jet } X \\
q\bar{q} &\rightarrow \text{jet } X \\
qg &\rightarrow \text{jet } X \\
gg &\rightarrow \text{jet } X .
\end{aligned} \tag{5.10}$$

At LO, two partons in the final state recoil off each other in opposite directions. The observed jet consists then only of a single parton, a scenario barely encountered in experiment. Above that, a calculation relying on the assumption that a jet is formed by a single parton does not offer any chance to study the internal structure of a realistic jet event [112]. Therefore, at least, $\mathcal{O}(\alpha_s^3)$ contributions have to be considered, which account for jets consisting of more than one parton. At this order of perturbation theory, in addition to the $2 \rightarrow 2$ processes present already at LO, new $2 \rightarrow 3$ partonic scattering reactions emerge, and the partons in such a final state can combine in many possible ways. Again, there is the possibility that only one of the outgoing partons forms a jet, leaving the remaining two as unobserved by-products of the reaction, but then also any pair of partons can produce the jet *together*. Only the sum of all these reactions yields finite jet cross sections which are free of any singularities in the final state.

To economize the analytical calculation of all partonic matrix elements it is desirable to make as much use as possible of the single-inclusive parton cross sections already encountered in Chap. 4. Of course, the treatment of the final state, in particular of the singularities which have been shifted to the bare fragmentation functions in the case of hadron production, has to be modified. New contributions stemming from configurations where two outgoing partons form a jet together must be included. These amendments are most easily performed in the context of the SCA, which relies on the dominance of mostly collinear jet “constituents”.

As proposed by Furman [115], it is convenient to split the full partonic jet cross sections into separate contributions, depending on which partons serve to form the jet. We have sketched these configurations in Fig. 5.2 for the partonic $2 \rightarrow 3$ reaction $ab \rightarrow jkl \rightarrow \text{jet} X$. In the first case, only parton j forms the jet. Partons k and l are anywhere, but, of course, not in the jet cone. Such configurations are included already in the single-inclusive parton cross section for the reaction $ab \rightarrow jX$, which we denote by $d\Delta\hat{\sigma}_j$ from now on. However, this cross section contains also unwanted terms from configurations where another parton is in the cone, although it does not contribute to the jet. We thus have to subtract such

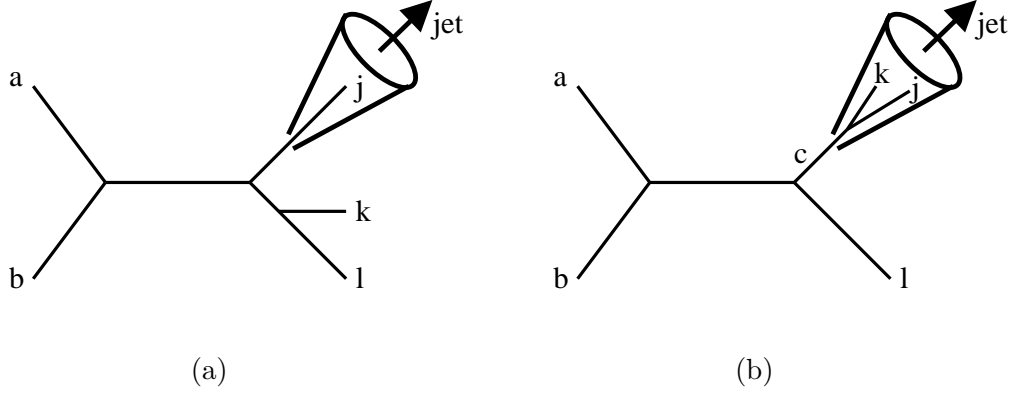


Figure 5.2: Contributions to single-inclusive jet production from partonic reactions where only one parton forms the jet (a), and where two essentially collinear partons are inside the cone associated with the jet (b).

terms from $d\Delta\hat{\sigma}_j$. In the following we will call the cross section for the reaction $ab \rightarrow jkX$, where j and k are in the cone, but only j produces the jet, $d\Delta\hat{\sigma}_{j(k)}$. Finally, certainly also two essentially collinear partons, e.g., j and k , can form the jet together, giving rise to a type of cross section, labeled $d\Delta\hat{\sigma}_{jk}$, that has not been present in the case of single-inclusive parton production of Chap. 4. Of course, in the same way as j any of the partons k or l can form the jet. Taking all these pieces together we end up with the full parton-to-jet cross section for the reaction $ab \rightarrow \text{jet}X$:

$$\begin{aligned}
 d\Delta\hat{\sigma}_{ab \rightarrow \text{jet}X} = & \left[d\Delta\hat{\sigma}_j - d\Delta\hat{\sigma}_{j(k)} - d\Delta\hat{\sigma}_{j(l)} \right] + \left[d\Delta\hat{\sigma}_k - d\Delta\hat{\sigma}_{k(j)} - d\Delta\hat{\sigma}_{k(l)} \right] \\
 & + \left[d\Delta\hat{\sigma}_l - d\Delta\hat{\sigma}_{l(j)} - d\Delta\hat{\sigma}_{l(k)} \right] + d\Delta\hat{\sigma}_{jk} + d\Delta\hat{\sigma}_{jl} + d\Delta\hat{\sigma}_{kl} . \quad (5.11)
 \end{aligned}$$

The actual calculation of the various contributions to Eq. (5.11) requires some care. We are therefore going to discuss the steps required for the computation of the $d\Delta\hat{\sigma}_{j(k)}$ and $d\Delta\hat{\sigma}_{jk}$ more in detail, putting special emphasis on the proper treatment of the singularities emerging in intermediate steps of the calculation.

5.2.1 The One-Parton-to-Jet Cross Section $d\Delta\hat{\sigma}_{j(k)}$

We start with the computation of contributions to the jet cross section stemming from configurations where one parton, j , produces the jet, but a second parton, k , is also in the cone. Within the SCA such contributions only arise when partons j and k are essentially parallel to each other, emerging from a collinear splitting of an intermediate state c as illustrated in Fig. 5.2 (b). The spin-dependent matrix element squared $\Delta|\mathcal{M}|_{ab \rightarrow jkl}^2$ for

the reaction $ab \rightarrow cl \rightarrow jkl$ takes then the form

$$\Delta|\mathcal{M}|_{ab \rightarrow jkl}^2(s, v, w) = \frac{c_m}{2p_j \cdot p_k} \Delta|\mathcal{M}|_{ab \rightarrow cl}^2\left(s, v' = \frac{vw}{1-v+vw}\right) P_{jc}^<(z = 1-v+vw) , \quad (5.12)$$

with some constant of proportionality c_m . The LO matrix element $\mathcal{M}_{ab \rightarrow cl}$ accounts for the $2 \rightarrow 2$ scattering which precedes the collinear splitting of the intermediate state c into partons j and k . Since c is not a free state but undergoes a further interaction the argument of the Born matrix element is shifted from the v of an ordinary tree level diagram to $v' = vw/(1-v+vw)$. The propagation of the intermediate state is accounted for by a denominator of the form $1/p_j \cdot p_k$. It can be shown to yield

$$2p_j \cdot p_k = 2E_j^2 \frac{v(1-w)}{1-v+vw} (1 - \cos \theta_{jk}) , \quad (5.13)$$

where θ_{jk} is the angle between partons j and k , and E_j refers to the energy of particle j . In Eq. (5.12) all quantities are understood in n dimensions and $P_{jc}^<(z)$ denotes a collinear $c \rightarrow j$ splitting with $z < 1$ which, in contrast to the full splitting function $P_{jc}(z)$, does not contain a $\delta(1-z)$ contribution if $c = j$.

For the phase space integration of $\Delta|\mathcal{M}|_{ab \rightarrow jkl}^2$ in Eq. (5.12) we impose that parton j serves to form the jet,

$$\begin{aligned} \int dPS_3 \Delta|\mathcal{M}|_{ab \rightarrow jkl}^2 &= (2\pi)^{3-2n} \int \frac{d^{n-1}p_j}{2E_j} d^n p_k d^n p_l \delta(p_k^2) \delta(p_l^2) \\ &\times \frac{d^{n-1}P_J}{2E_J} 2E_J \delta^{(n-1)}(P_J - p_j) \delta^{(n)}(p_a + p_b - p_j - p_k - p_l) \Delta|\mathcal{M}|_{ab \rightarrow jkl}^2 , \end{aligned} \quad (5.14)$$

where $\delta^{(n-1)}(P_J - p_j)$ ensures that the jet criterion (5.5) is fulfilled. After rewriting all quantities in terms of v , v' , and w , the $2 \rightarrow 3$ phase space integration gives

$$\begin{aligned} \int \frac{dPS_3}{dv dw} \Delta|\mathcal{M}|_{ab \rightarrow jkl}^2 &= \left[\frac{1}{8\pi} \left(\frac{4\pi}{s} \right)^\varepsilon \frac{1}{\Gamma(1-\varepsilon)} [v'(1-v')]^{-\varepsilon} \right] \frac{1}{8\pi^2} \left(\frac{4\pi}{s} \right)^\varepsilon \\ &\times \frac{1}{\Gamma(1-\varepsilon)} \frac{v}{1-v+vw} \left[\frac{E_j^2 v^2 (1-w)^2}{s} \right]^{-\varepsilon} c_m \Delta|\mathcal{M}|_{ab \rightarrow cl}^2(s, v') P_{jc}^<(z) \int_0^\delta d\theta_{jk} \frac{\sin^{1-2\varepsilon} \theta_{jk}}{1 - \cos \theta_{jk}} . \end{aligned} \quad (5.15)$$

The factor in square brackets in the first line of (5.15) is the usual $2 \rightarrow 2$ phase space in n dimensions of Eq. (4.9) with v being replaced by v' . Here, we have already made use of the simple structure of $\Delta|\mathcal{M}|_{ab \rightarrow jkl}^2$, whose only dependence on θ_{jk} stems from the propagator denominator $1/p_j \cdot p_k$. To evaluate the angular integral in (5.15) we perform

a series expansion in θ_{jk} , which is allowed as long as the angle is small as assumed in the SCA. Thereby we obtain

$$\int_0^\delta d\theta_{jk} \frac{\sin^{1-2\varepsilon} \theta_{jk}}{1 - \cos \theta_{jk}} = -\frac{\delta^{-2\varepsilon}}{\varepsilon} + \mathcal{O}(\delta^2) . \quad (5.16)$$

With this integral at hand we can compute the corresponding n -dimensional partonic cross section,

$$\begin{aligned} \frac{d\Delta\hat{\sigma}_{ab \rightarrow jkl}}{dvdw} &= \frac{d\Delta\hat{\sigma}_{ab \rightarrow cl}}{dv} \left(v' = \frac{vw}{1-v+vw} \right) P_{jc}^<(z = 1-v+vw) \\ &\times \frac{\alpha_s}{2\pi} \left(-\frac{1}{\varepsilon} \right) \frac{1}{\Gamma(1-\varepsilon)} \frac{v}{1-v+vw} \left[\frac{E_j^2 \delta^2 v^2 (1-w)^2}{s} \right]^{-\varepsilon} , \end{aligned} \quad (5.17)$$

where $d\Delta\hat{\sigma}_{ab \rightarrow cl}$ stands for the Born cross section for the scattering $a+b \rightarrow c+l$ preceding the final state collinear splitting.

If the $P_{jc}^<(z)$ corresponds to a non-diagonal splitting, i.e., $j \neq c$, the further computation of $d\Delta\hat{\sigma}_{j(k)}$ is straightforward. In that case, the full splitting function $P_{jc}(z)$ is regular at $z = 1$, and Eq. (5.17) can safely be expanded in ε . The remaining pole in ε was also present in the single-parton inclusive cross section $d\Delta\hat{\sigma}_j$. However, there it has been subtracted by a final state factorization into the bare parton-to-pion fragmentation functions at a scale μ'_f . Obviously, such a factorization is no longer possible in the case of jet production, and any dependence on the final state factorization scale μ'_f has to drop out in the sum Eq. (5.11). Since we still want to use the $d\Delta\hat{\sigma}_j$ of Chap. 4 we have to compensate for the final state factorization by applying the same subtraction $d\Delta\hat{\sigma}_{fact}$ to the $d\Delta\hat{\sigma}_{j(k)}$,

$$\begin{aligned} \frac{d\Delta\hat{\sigma}_{fact}}{dvdw} &= -\frac{\alpha_s}{2\pi} \frac{d\Delta\hat{\sigma}_{ab \rightarrow cl}}{dv} \left(v' = \frac{vw}{1-v+vw} \right) P_{jc}^{(4)}(z = 1-v+vw) \\ &\times \left(-\frac{1}{\varepsilon} \right) \frac{v}{1-v+vw} \left(\frac{\mu_f'^2}{s} \right)^{-\varepsilon} . \end{aligned} \quad (5.18)$$

As usual, $P_{jc}^{(4)}(z)$ denotes the four-dimensional splitting function for a collinear $c \rightarrow j$ splitting. It is related to the full n -dimensional splitting function via

$$P_{jc}(z) = P_{jc}^{(4)}(z) + \varepsilon P_{jc}^{(\varepsilon)}(z) . \quad (5.19)$$

In QCD, the n -dimensional unpolarized LO-splitting functions are given by [65]

$$P_{qq}(z) = C_F \left[\frac{1+z^2}{(1-z)_+} + \frac{3}{2} \delta(1-z) - \varepsilon(1-z) + \frac{\varepsilon}{2} \delta(1-z) \right], \quad (5.20)$$

$$P_{qg}(z) = \frac{1}{2} \left[z^2 + (1-z)^2 - 2\varepsilon z(1-z) \right], \quad (5.21)$$

$$P_{gq}(z) = C_F \left[\frac{1+(1-z)^2}{z} - \varepsilon z \right], \quad (5.22)$$

$$P_{gg}(z) = 2C_A \left[\frac{z}{(1-z)_+} + \frac{1-z}{z} + z(1-z) + \frac{\varepsilon}{12} \delta(1-z) \right] + \left(\frac{11}{6} C_A - \frac{N_f}{3} \right) \delta(1-z). \quad (5.23)$$

Adding up Eqs. (5.17) and (5.18) we obtain the final (and finite) result for $d\Delta\hat{\sigma}_{j(k)}$ for $j \neq c$:

$$\begin{aligned} \frac{d\Delta\hat{\sigma}_{j(k)}}{dvdw} &= \frac{\alpha_s}{2\pi} \frac{v}{1-v+vw} \frac{d\Delta\hat{\sigma}_{ab \rightarrow cl}^{n=4}}{dv} \left(v' = \frac{vw}{1-v+vw} \right) \\ &\times \left[P_{jc}^{(4)}(z=1-v+vw) \ln \left(\frac{E_j^2 \delta^2 v^2 (1-w)^2}{\mu_f'^2} \right) - P_{jc}^{(\varepsilon)}(z=1-v+vw) \right], \end{aligned} \quad (5.24)$$

with $d\Delta\hat{\sigma}_{ab \rightarrow cl}^{n=4}$ denoting the four-dimensional LO cross section for the reaction $a+b \rightarrow c+l$.

Some care has to be taken in the treatment of matrix elements including a diagonal splitting, since the $P_{jc}(z)$ emerging in the $d\Delta\hat{\sigma}_{j(k)}$ exhibit an infrared singularity at $z=1$, if $j=c$. This divergence is regularized by the factor $(1-w)^{-2\varepsilon}$ from the phase space, cf. Eq. (5.17). It thereby gives rise to a $1/\varepsilon^2$ pole which is canceled by a corresponding singularity in the $d\Delta\hat{\sigma}_{jk}$. Since the results for the $d\Delta\hat{\sigma}_{j(k)}$ in the diagonal case are rather lengthy we do not list them here, but first turn to the discussion of those configurations where two partons form a jet and show afterwards how to combine them with the corresponding one-parton contributions to obtain finite expressions.

5.2.2 The Two-Parton-to-Jet Cross Section $d\Delta\hat{\sigma}_{jk}$

If two quasi-collinear partons j and k produce a jet together, Eq. (5.5) yields $P_J = p_j + p_k$. The corresponding $2 \rightarrow 3$ phase space takes then the form

$$\begin{aligned} dPS_3 &= (2\pi)^{3-2n} \frac{d^{n-1}p_k}{2E_k} d^n p_j d^n p_l \delta(p_j^2) \delta(p_l^2) \frac{d^{n-1}P_J}{2E_J} 2E_J \\ &\times \delta^{(n-1)}(P_J - p_j - p_k) \delta^{(n)}(p_a + p_b - p_j - p_k - p_l). \end{aligned} \quad (5.25)$$

After performing the p_k - and p_l -integrations one ends up with

$$2E_J \frac{dPS_3}{d^{n-1}P_J} = (2\pi)^{3-2n} \int d^n p_j \delta(p_j^2) \frac{E_J}{E_k} \delta([p_a + p_b - P_J]^2) , \quad (5.26)$$

where E_J is the jet's energy, $E_J = E_j + E_k$. In the collinear approximation, where $P_J^2 \approx 0$, the delta function $\delta([p_a + p_b - P_J]^2)$ can be rewritten as

$$\delta([p_a + p_b - P_J]^2) \approx \delta(s + t + u) = \frac{1}{sv} \delta(1 - w) , \quad (5.27)$$

stating that the $d\Delta\hat{\sigma}_{jk}$ contribute only for $w = 1$. For the phase space integral of the relevant matrix elements, which are of the form (5.12), we obtain then

$$\begin{aligned} \int \frac{dPS_3}{dv dw} \Delta|\mathcal{M}|_{ab \rightarrow jkl}^2 &= \left[\frac{1}{8\pi} \left(\frac{4\pi}{s} \right)^\varepsilon \frac{1}{\Gamma(1-\varepsilon)} [v(1-v)]^{-\varepsilon} \right] \frac{1}{8\pi^2} \left(\frac{4\pi}{s} \right)^\varepsilon \delta(1-w) \\ &\times \frac{1}{\Gamma(1-\varepsilon)} c_m \Delta|\mathcal{M}|_{ab \rightarrow cl}^2(s, v) \int_0^{E_{\text{jet}}} dE_j \frac{E_J}{E_k^2} \left(\frac{E_j^2}{s} \right)^{-\varepsilon} P_{jc}^< \left(\frac{E_j}{E_J} \right) \int_0^{\theta_{\text{max}}} d\theta_j \frac{\sin^{1-2\varepsilon} \theta_j}{1 - \cos \theta_{jk}} , \end{aligned} \quad (5.28)$$

with θ_i denoting the angle between the direction of parton i and the jet axis, whereas θ_{jk} is, as before, the angle between partons j and k . The argument of the underlying $2 \rightarrow 2$ cross section, $\Delta|\mathcal{M}|_{ab \rightarrow cl}^2(s, v)$, is v rather than v' due to the Born kinematics of the $d\Delta\hat{\sigma}_{jk}$ enforced by the $\delta(1-w)$ distribution from the phase space integration. It is crucial to note that the argument, z , of the splitting function emerging in the matrix element Eq. (5.12) is no longer fixed to $z = 1 - v + vw$ as in the case of $d\Delta\hat{\sigma}_{j(k)}$. Rather, it has to be integrated over since the phase space (5.28) depends explicitly on E_j , which is related to the momentum fraction carried by parton j via $z = E_j/E_J$, when both partons emerging from the splitting form the jet together.

As the next step, we need to express θ_j in terms of θ_{jk} . To this end, we write

$$\cos \theta_{jk} = \frac{\vec{p}_j \cdot \vec{p}_k}{|\vec{p}_j| |\vec{p}_k|} = \frac{\vec{p}_j \cdot (\vec{P}_J - \vec{p}_j)}{E_j (E_J - E_j)} = \frac{|\vec{P}_J| \cos \theta_j - E_j}{E_J - E_j} , \quad (5.29)$$

and then use

$$\vec{P}_J^2 = (\vec{p}_j + \vec{p}_k)^2 = E_j^2 + (E_J - E_j)^2 + 2E_j(E_J - E_j) \cos \theta_{jk} , \quad (5.30)$$

to find in the collinear approximation

$$\theta_j \approx \frac{E_J - E_j}{E_J} \theta_{jk} \quad \text{and} \quad \theta_k \approx \frac{E_j}{E_J} \theta_{jk} . \quad (5.31)$$

Since neither of the two partons producing the jet is allowed to be outside the cone, the upper limit of the angular integration, θ_{max} , is found to be

$$\begin{aligned} E_k > E_j &: \quad \theta_{max} = \delta, \\ E_j > E_k &: \quad \theta_{max} = \frac{E_k}{E_j} \delta, \end{aligned} \quad (5.32)$$

depending on the distribution of energy between partons j and k .

We are now in a position to perform the angular integral in (5.28), and obtain, after a transformation of the integration variable E_j to $\xi = E_j/E_J$,

$$\begin{aligned} \int \frac{dPS_3}{dvdw} \Delta |\mathcal{M}|_{ab \rightarrow jkl}^2 &= \left[\frac{1}{8\pi} \left(\frac{4\pi}{s} \right)^\varepsilon \frac{1}{\Gamma(1-\varepsilon)} [v(1-v)]^{-\varepsilon} \right] \frac{1}{8\pi^2} \left(\frac{4\pi}{s} \right)^\varepsilon \\ &\times \frac{1}{\Gamma(1-\varepsilon)} \left(-\frac{1}{\varepsilon} \right) \left(\frac{E_J^2 \delta^2}{s} \right)^{-\varepsilon} \delta(1-w) c_m \Delta |\mathcal{M}|_{ab \rightarrow cl}^2(s, v) \\ &\times \int_0^1 d\xi \left[\xi^{-2\varepsilon} \Theta\left(\frac{1}{2} - \xi\right) + (1-\xi)^{-2\varepsilon} \Theta\left(\xi - \frac{1}{2}\right) \right] P_{jc}^<(\xi). \end{aligned} \quad (5.33)$$

For the ξ -integral we write

$$I_{mn} \equiv \int_0^1 d\xi \left[\xi^{-2\varepsilon} \Theta\left(\frac{1}{2} - \xi\right) + (1-\xi)^{-2\varepsilon} \Theta\left(\xi - \frac{1}{2}\right) \right] P_{mn}^<(\xi). \quad (5.34)$$

Computing I_{mn} for all relevant splitting functions yields

$$\begin{aligned} I_{qq} &= C_F \left[-\frac{1}{\varepsilon} - \frac{3}{2} + \varepsilon \left(-\frac{7}{2} + \frac{\pi^2}{3} - 3 \ln(2) \right) \right] = I_{gq}, \\ I_{qg} &= \frac{1}{2} \left[\frac{2}{3} + \varepsilon \left(\frac{23}{18} + \frac{4}{3} \ln(2) \right) \right], \\ I_{gg} &= 2C_A \left[-\frac{1}{\varepsilon} - \frac{11}{6} + \varepsilon \left(-\frac{137}{36} + \frac{\pi^2}{3} - \frac{11}{3} \ln(2) \right) \right]. \end{aligned} \quad (5.35)$$

Obviously, the $1/\varepsilon$ pole terms in Eqs. (5.35) give rise to double poles when they are combined with the overall $1/\varepsilon$ singularity in Eq. (5.33). Such divergencies in the $d\Delta\hat{\sigma}_{jk}$ have already been anticipated when a similar pole structure occurred in the calculation of the $d\Delta\hat{\sigma}_{j(k)}$ in the previous section. We will show in the following how to combine the individual parts contributing to the full partonic jet cross sections such that all singularities associated with the final state cancel explicitly.

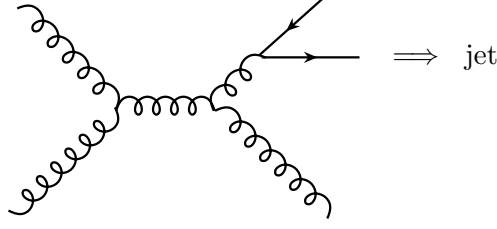


Figure 5.3: Sample diagram for the process $gg \rightarrow gg \rightarrow q\bar{q}g \rightarrow \text{jet}X$, where the quark produces a jet and gives rise to the one-parton-to-jet cross section $d\Delta\hat{\sigma}_{q(\bar{q})}$.

5.2.3 Cancellation of Final State Singularities

The cancelation of final state singularities by the appropriate combination of individual contributions to observable jet cross sections as given in Eq. (5.11) is most clearly illustrated by an example. Let us therefore resort to the reaction $gg \rightarrow \text{jet}X$. The generalization to other channels will then be straightforward.

We have elaborated in some detail in Sec. 5.2.1 that those $d\Delta\hat{\sigma}_{j(k)}$, which stem from a non-diagonal splitting, are finite by themselves. In the example $gg \rightarrow \text{jet}X$, such a contribution arises from a $gg \rightarrow gg$ scattering, followed by a gluon-to-quark splitting, which we have sketched in Fig. 5.3. The corresponding cross section $d\Delta\hat{\sigma}_{q(\bar{q})}$ can easily be computed from Eq. (5.24) by inserting the appropriate expressions for the $d\Delta\hat{\sigma}_{ab \rightarrow cl}(v')$ and $P_{jc}(z)$,

$$\frac{d\Delta\hat{\sigma}_{q(\bar{q})}}{dvdw} = \frac{\alpha_s}{2\pi} \frac{v}{1-v+vw} \frac{d\Delta\hat{\sigma}_{gg \rightarrow gg}^{n=4}(v')}{dv} \left[P_{qg}^{(4)}(z) \ln \left(\frac{E_j^2 \delta^2 v^2 (1-w)^2}{\mu_f'^2} \right) - P_{qg}^{(\varepsilon)}(z) \right]. \quad (5.36)$$

Since all pieces entering this expression are finite by themselves, $d\Delta\hat{\sigma}_{q(\bar{q})}$ is free of singularities as well. The same result is obtained for $d\Delta\hat{\sigma}_{\bar{q}(q)}$.

Things become more involved for the a priori divergent one-parton-to-jet contributions, which include a diagonal splitting function. They have to be combined with appropriate two-parton-to-jet cross sections to cancel unphysical poles. Let us study this procedure in more detail for our example $gg \rightarrow \text{jet}X$. Here, divergencies arise, when the incoming gluons first produce a $q\bar{q}$ -pair, followed by a subsequent diagonal splitting of the quark into another quark and a gluon. We have illustrated this “configuration” in Fig. 5.4. The contribution $d\Delta\hat{\sigma}_{g(q)}$, which includes a quark-to-gluon splitting with an additional (unobserved) quark, is finite due to the non-singular structure of the P_{qg} , cf. Eq. (5.22). If, on the other hand, the quark rather than the gluon forms the jet we encounter the cross section $d\Delta\hat{\sigma}_{q(g)}$. This expression exhibits a double pole stemming from the distributions in $P_{qq}(z)$ at $z = 1$, cf. Eq. (5.20). As indicated before, such poles can only be canceled by corresponding singularities in the related $d\Delta\hat{\sigma}_{gg}$. Clearly, whenever there are a quark and

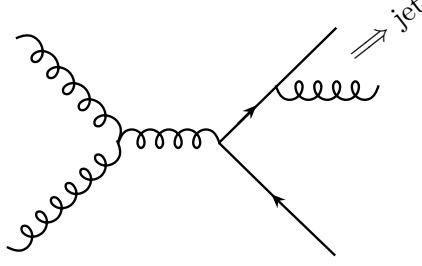


Figure 5.4: Sample diagram for the process $gg \rightarrow q\bar{q} \rightarrow q\bar{q}g \rightarrow \text{jet}X$, where either the gluon alone, the quark alone, or the quark and the gluon together form a jet, yielding $d\Delta\hat{\sigma}_{g(g)}$, $d\Delta\hat{\sigma}_{q(g)}$, and $d\Delta\hat{\sigma}_{qg}$, respectively.

a gluon in the final state of a partonic reaction, a jet can be produced by either of them individually, leaving the other parton unobserved, or by both partons, thereby giving rise to a two-parton-to-jet cross section. Any contribution $d\Delta\hat{\sigma}_{q(g)}$ will thus be accompanied by a corresponding $d\Delta\hat{\sigma}_{qg}$. These two pieces add up with different sign and give

$$d\Delta\hat{\sigma}_{q(g)} - d\Delta\hat{\sigma}_{qg}$$

$$\begin{aligned} & \propto \frac{\alpha_s}{2\pi} C_F \left\{ \delta(1-w) \left[\left(2\ln v + \frac{3}{2} \right) \ln \left(\frac{\delta^2 E_J^2}{\mu_f'^2} \right) + 2\ln^2 v - \frac{7}{2} + \frac{\pi^2}{3} - 3\ln(2) \right] \right. \\ & + \frac{2}{(1-w)_+} \left[2\ln v + \ln \left(\frac{\delta^2 E_J^2}{\mu_f'^2} \right) \right] + 4 \left[\frac{\ln(1-w)}{1-w} \right]_+ \\ & \left. + \frac{v^2(1-w)}{1-v+vw} \left[1 + \ln \left(\frac{\delta^2 E_J^2 v^2 (1-w)^2}{\mu_f'^2} \right) \right] \right\}. \end{aligned} \quad (5.37)$$

To account for the $2 \rightarrow 2$ scattering preceding the collinear splitting, the expression on the r.h.s. of Eq. (5.37) has to be multiplied with the appropriate Born cross section: $d\Delta\hat{\sigma}_{gg \rightarrow q\bar{q}}$ in the case of $gg \rightarrow \text{jet}X$.

Finally, we have to deal with the contribution $d\Delta\hat{\sigma}_{q\bar{q}}$. The singularity in this quantity is not canceled, if we add the corresponding $d\Delta\hat{\sigma}_{q(\bar{q})}$. Nonetheless, we have to remove the poles to get a reasonable result for the full partonic jet cross section $d\Delta\hat{\sigma}_{gg \rightarrow \text{jet}X}$. This can be achieved by including the other partonic subprocesses contributing to $gg \rightarrow \text{jet}X$, which we have not considered so far. Besides the $gg \rightarrow q\bar{q}g$ scattering encountered before, also an underlying $gg \rightarrow ggg$ reaction has to be taken into account. The splitting of the intermediate gluon yields then a gg -pair, giving rise to the contributions $d\Delta\hat{\sigma}_{gg}$ and $d\Delta\hat{\sigma}_{g(g)}$. We have depicted both, the quark and the gluon configurations in Fig. 5.5. Combining the singular pieces of $d\Delta\hat{\sigma}_{q\bar{q}}$ and $d\Delta\hat{\sigma}_{gg}$, which are caused by the $1/3$ and $(-11C_A/3)$ terms in the I_{qg} and I_{gg} of Eq. (5.35), respectively, with the appropriate

explicitly, we obtain for our example $gg \rightarrow \text{jet}X$:

$$\begin{aligned}
d\Delta\hat{\sigma}_{gg \rightarrow \text{jet}X} &= d\Delta\hat{\sigma}_g + 2N_f d\Delta\hat{\sigma}_q - 2N_f (d\Delta\hat{\sigma}_{g(q)} + d\Delta\hat{\sigma}_{q(\bar{q})}) \\
&+ 2N_f (d\Delta\hat{\sigma}_{qg} - d\Delta\hat{\sigma}_{q(g)}) + (d\Delta\hat{\sigma}_{gg} + 2N_f d\Delta\hat{\sigma}_{q\bar{q}} - 2d\Delta\hat{\sigma}_{g(g)}) ,
\end{aligned}
\tag{5.39}$$

where we have used that all subprocesses including antiquarks can be accounted for by taking the corresponding quark cross sections twice.

In a similar manner one obtains the parton-to-jet cross sections for the remaining five subprocesses $ab \rightarrow \text{jet}X$ listed in Eq. (5.10). Since they are rather lengthy we refrain from quoting them here. They can be found, however, in a FORTRAN code available upon request. We wish to emphasize that all of these cross sections have to be free of any dependence on the final state factorization scale μ'_f , which is present in all intermediate steps of our calculation as an artifact of the separation of the full jet cross section into various parts associated with different jet configurations. Verifying that the physical cross section does not depend on μ'_f therefore provides a powerful check for the correctness of our calculation. Above that, we have re-calculated the unpolarized cross sections as well. The treatment of the final state, of course, does not depend on the polarization of the initial state particles. Replacing the polarized LO $2 \rightarrow 2$ cross sections underlying the $2 \rightarrow 3$ reactions with collinear parton-to-parton splittings in the final state by their unpolarized counterparts yields the spin-averaged results for the various jet cross sections. We fully agree at an analytical level with the results of [104], which can be retrieved from their FORTRAN code, after an appropriate transformation to the $\overline{\text{MS}}$ factorization scheme.

5.3 Numerical Results and Discussion

We are now in a position to perform a detailed phenomenological study of jet production observables focusing on quantities of immediate interest for current and future experiments at BNL-RHIC. We will carry out our calculations in the kinematical range relevant for the STAR experiment at RHIC, where jet events in the pseudorapidity range $-1 \leq \eta_J \leq 1$ can be detected, and choose c.m.s. energies of $\sqrt{S} = 200$ GeV and $\sqrt{S} = 500$ GeV, which are relevant for the current and long-term spin program at RHIC, respectively. We are going to present our predictions in terms of p_T , and will therefore integrate the differential cross section (5.6) over the accessible rapidity range, if not stated otherwise. For an NLO (LO) computation of cross sections we always apply NLO (LO) parton distribution functions and the two-loop (one-loop) expression for α_s . We use the CTEQ6M (CTEQ6L) [4] set of unpolarized parton densities throughout. In the polarized case we will mostly employ the NLO (LO) “standard” set of GRSV [17]. Like in Sec. 4.2, when studying the sensitivity of the double-spin asymmetry to Δg , we will, however, apply also other sets of GRSV distributions, differing from the standard scenario mainly in the gluon polarization.

Before turning to the observables most relevant for experiment, we have to clarify how accurate our results obtained within the SCA are in cases of practical relevance. As

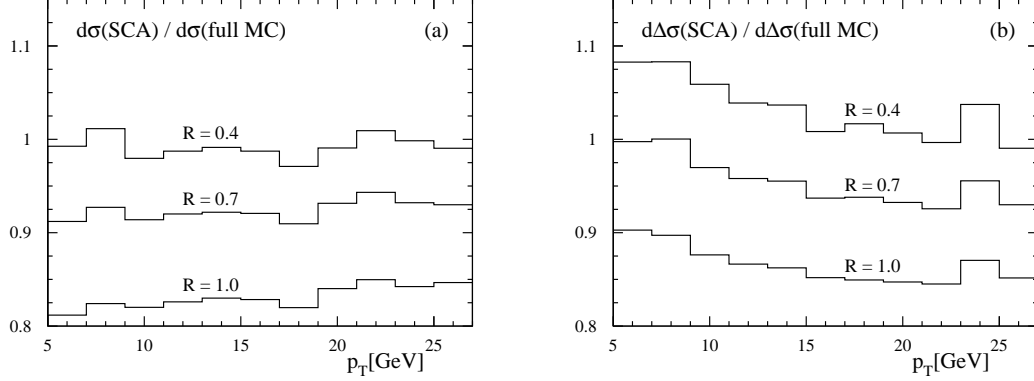


Figure 5.6: Ratio of the unpolarized (a) and polarized (b) single inclusive jet cross sections in the SCA and within the full Monte-Carlo approach of [113] at $\sqrt{S} = 200$ GeV for three different cone sizes R .

mentioned in Sec. 5.1, it has been shown (see, e.g., [125]) that most generally a jet cross section can be parametrized in terms of the cone size R as

$$d\sigma(R) = \mathcal{A} + \mathcal{B} \ln R + \mathcal{C} R^2, \quad (5.40)$$

with three “parameters” \mathcal{A} , \mathcal{B} , and \mathcal{C} . A similar relation applies in the polarized case. Within the SCA all terms of $\mathcal{O}(\delta^2)$, and thus $\mathcal{O}(R^2)$, are neglected, whereas contributions logarithmic in R or free of any dependence on the cone size are fully taken into account. At first sight, one would assume that this approximation works well only if $\delta \ll 1$. However, it has been demonstrated by an explicit calculation [123, 116] that in the case of unpolarized single-inclusive jet cross sections corrections to the SCA of $\mathcal{O}(\delta^2)$ are practically negligible up to $\delta \approx 0.7$. By numerically integrating the contributions to $d\sigma$ which are not covered by the SCA it has been found that the resulting corrections amount to less than 5% for cone openings as large as $\delta \approx 0.7$. For $\delta < 0.7$ the corrections are even smaller. The SCA is thus applicable in the analysis of spin-averaged jet observables as long as $\delta \lesssim 0.7$.

Although we expect a similar behavior of the polarized jet cross section, we have to make sure that the SCA is not spoiled by any effects suppressed or absent in the unpolarized case, such as possible cancelations between the two helicity configurations entering the spin-dependent cross section, cf. Eqs. (3.3) and (3.4). For that reason, in Fig. 5.6 we compare the results of a Monte-Carlo based NLO calculation [113], which takes $\mathcal{O}(R^2)$ contributions to $d(\Delta)\sigma$ fully into account, to the unpolarized and polarized cross sections we have obtained within the SCA for three different cone sizes. In the unpolarized case, we encounter only small finite cone-size corrections indeed, thereby confirming the statement of Refs. [123, 116]. Qualitatively similar results are obtained in the polarized case. For a rather large cone radius of $R = 0.7$ the SCA gives cross sections still within ten percent or less of the full Monte-Carlo calculation. When R approaches even larger values, corrections

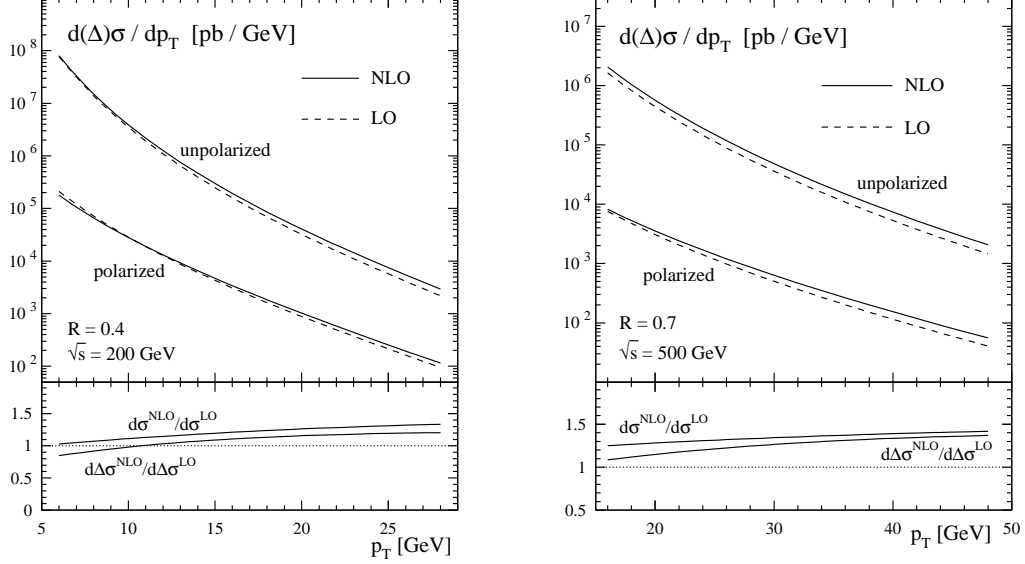


Figure 5.7: Unpolarized and polarized differential cross sections at LO (dashed) and NLO (solid) for the reaction $pp \rightarrow \text{jet}X$ at $\sqrt{S} = 200$ GeV (l.h.s.) and $\sqrt{S} = 500$ GeV (r.h.s.) with cone sizes of $R = 0.4$ and $R = 0.7$, respectively. Also shown are the ratios of NLO and LO contributions.

of $\mathcal{O}(R^2)$ become sizeable, and the SCA starts to break down. It is expected, however, that a cone size of $0.4 \lesssim R \lesssim 0.7$ will be chosen by the STAR collaboration at RHIC in their forthcoming analysis. Due to the limited angular acceptance of the detector larger cone sizes are not really practical.

These observations lead us to the conclusion that the SCA we have applied is reliable for cone sizes up to $R \approx 0.7$. The strength of the approach we have chosen is its largely analytical implementation of partonic matrix elements. This makes our FORTRAN codes, similar to those used in the analysis of single-inclusive hadron production in Sec. 4.2, extremely fast and efficient, and opens up opportunities for a future global analysis of forthcoming jet data. That feature of our codes is a clear advantage over a Monte-Carlo code with its considerable numerical complexity, which yields results with rather large numerical fluctuations (still visible in Fig. 5.6) even after hours of running. Numerically stable results are obtained with our computer code in a matter of minutes.

Having made sure that our results agree well with the full Monte-Carlo calculation of [113], we turn now to a phenomenological study of single-inclusive jet production in the kinematical range relevant for the STAR experiment. Figure 5.7 shows our predictions for the unpolarized and polarized single inclusive jet cross sections for the reaction $pp \rightarrow \text{jet}X$, differential in p_T , at c.m.s. energies of $\sqrt{S} = 200$ GeV and $\sqrt{S} = 500$ GeV with cone sizes of $R = 0.4$ and $R = 0.7$, respectively. The scales are set to $\mu_r = \mu_f = p_T$. It can be seen that the NLO corrections to the Born results are small over the whole p_T -range considered.

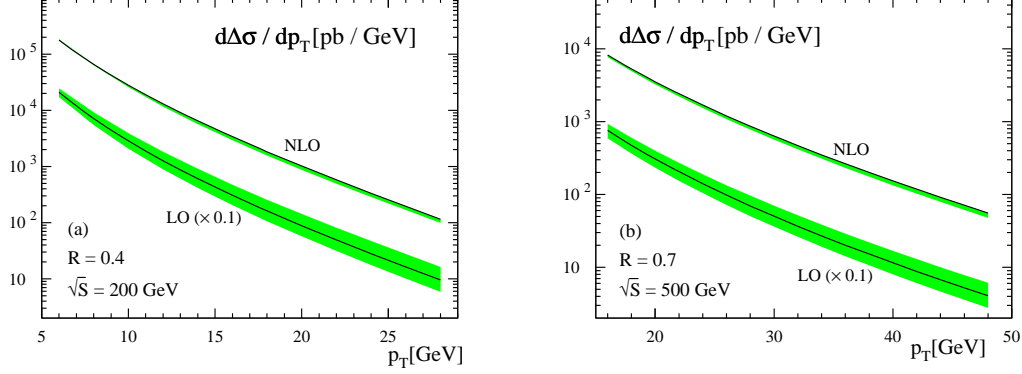


Figure 5.8: Scale dependence of the spin-dependent cross sections for $pp \rightarrow \text{jet}X$ at LO and NLO in the range $p_T/2 \leq \mu_r = \mu_f \leq 2p_T$ for c.m.s. energies of $\sqrt{S} = 200$ GeV (a) and $\sqrt{S} = 500$ GeV (b). The solid lines correspond to the choice where all scales are set to p_T . The LO results have been rescaled by a factor 0.1 for a better readability.

This feature manifests itself in the behavior of the respective K -factors, defined according to Eq. (4.22), which are found to be well under control for high- p_T -jet production. As we have mentioned in Sec. 4.2, some care has to be taken in the interpretation of the K -factors due to the large scale uncertainties associated with the LO cross sections entering in their denominators.

A better “measure” for the impact of higher order corrections is the reduction of scale dependence when going to higher orders of the perturbative calculation. To get an estimate for the scale dependence of single-inclusive jet cross sections we have varied the scales in our calculation in the range $p_T/2 \leq \mu_r = \mu_f \leq 2p_T$. Our results are depicted in Fig. 5.8. It can be seen that the improvement in scale dependence when extending the calculation from LO to NLO is indeed significant. At NLO, the scale uncertainty of the single-inclusive jet cross sections is almost negligible irrespective of the c.m.s. energy and cone size used in the calculation. This feature is even more pronounced in jet production than in single-inclusive hadron production, cf. Fig. 4.3 – a behavior that can perhaps be traced back to the absence of a final state factorization scale in jet observables, which constitutes an additional source of scale dependence in reactions involving hadrons in the final state.

Of particular interest for gaining information on the gluon polarization in the nucleon is again the experimentally accessible double-spin asymmetry A_{LL}^{jet} , defined in analogy to the corresponding observable in hadron-production reactions, Eq. (4.2), as

$$A_{LL}^{\text{jet}} \equiv \frac{d\Delta\sigma}{d\sigma}. \quad (5.41)$$

As we have mentioned before, being free of uncertainties from hadronization mechanisms in the final state and depending very slightly on unphysical scales, single-inclusive jet ob-

servables provide an outstandingly clean probe for the proton's spin structure in general and – the quark polarization being fairly well constrained by DIS data already – Δg in particular. To study the sensitivity of the spin asymmetry to Δg , we have calculated A_{LL}^{jet} with several sets of parton distributions which differ mainly in their gluon polarization. Figure 5.9 shows A_{LL}^{jet} at NLO in two different kinematic ranges as obtained with the GRSV “standard” parton distributions [17], and three other parametrizations of the same set, relying on the assumption that the gluon polarization at the input scale of the evolution, μ_0 , obeys either $\Delta g = g$, $\Delta g = 0$, or $\Delta g = -g$. All of these scenarios account for the presently available polarized DIS data. To give an estimate of how well future measurements of STAR may constrain A_{LL}^{jet} , we also indicate the expected statistical errors,

$$\delta A_{LL}^{\text{jet}} \simeq \frac{1}{\mathcal{P}_p^2 \sqrt{\mathcal{L} \sigma_{\text{bin}}}} , \quad (5.42)$$

assuming a proton beam polarization of $\mathcal{P}_p = 40\%$. For the c.m.s. energy used at present, $\sqrt{S} = 200$ GeV, we take an integrated luminosity of only $\mathcal{L} = 3 \text{ pb}^{-1}$ which is the target for the next RHIC spin run and well below the design value of $\mathcal{L} = 320 \text{ pb}^{-1}$. In this estimate we furthermore take into account that the calorimeter so far covers only half of the angular range by integrating over the available range in pseudorapidity $0 \leq \eta_J \leq 1$. For $\sqrt{S} = 500$ GeV we assume $\mathcal{L} = 20 \text{ pb}^{-1}$ and $-1 \leq \eta_J \leq 1$. Figure 5.9 illustrates very clearly that different gluon scenarios for the nucleon result in well-distinct spin asymmetries for single-inclusive jet production. Assuming a large and positive gluonic input yields relatively large A_{LL}^{jet} , whereas a moderate or vanishing Δg gives sizeably smaller results. With a large negative input the spin asymmetries change sign as p_T increases. The statistical accuracy expected for measurements in the near future should allow to distinguish between these gluon scenarios, in particular at moderate values of p_T , where the error bars are small.

It is important to note that A_{LL}^{jet} behaves very similarly to the double-spin asymmetry encountered in hadroproduction of inclusive pions, discussed in Sec. 4.3. Within pQCD, A_{LL}^{jet} seems bound to be positive in the moderate p_T -range, irrespective of the initial conditions imposed on Δg . Due to the dominance of the partonic $gg \rightarrow \text{jet}X$ subprocess which probes the parton distributions of two gluons, $\Delta g(x_a, \mu)$ and $\Delta g(x_b, \mu)$, at mid-rapidities at very similar momentum fractions, i.e., $x_a \simeq x_b$, and the positive value of the corresponding partonic cross section, one expects a positive A_{LL}^{jet} in this range. At larger transverse momenta, the $qg \rightarrow \text{jet}X$ process gradually takes over, resulting in a sensitivity of A_{LL}^{jet} to the sign of Δg . It is interesting to note, however, that the onset of the qg dominance depends on the c.m.s. energy of the reaction, since the spin asymmetry scales roughly with $2p_T/\sqrt{S}$.

These properties of the partonic scatterings are illustrated by Fig. 5.10. There, the solid lines show the relative contributions $d\Delta\sigma_{ab}/d\Delta\sigma$ of the gg , qg , and qq channels to the full polarized NLO jet cross section for the standard set of [17] at $\sqrt{S} = 200$ GeV. Here, the “ q ” denotes the sum of contributions from quarks and antiquarks of all flavors, such that all three curves add up to unity for every p_T . For comparison, we also show the corresponding results for inclusive π^0 production, discussed in Chap. 4, at mid-pseudorapidities. It can be seen that the results for jets and pions almost coincide, if we rescale the axis for p_T^π by a factor of 2. This is due to the fragmentation process which governs the formation of

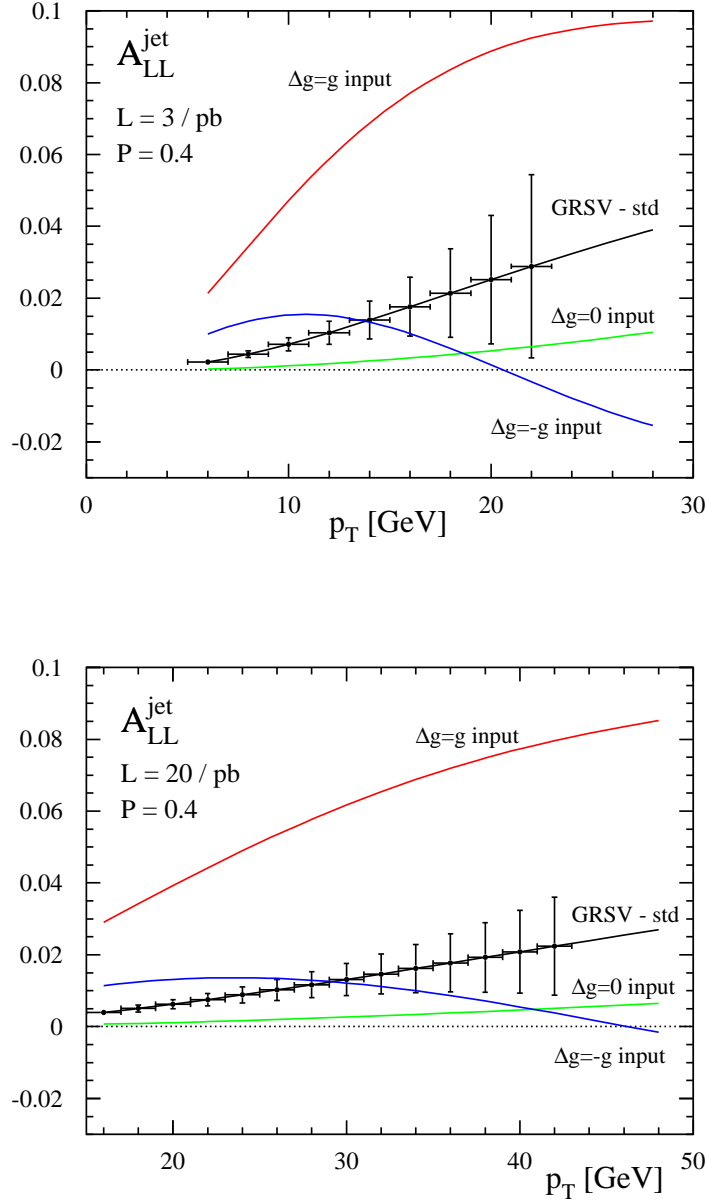


Figure 5.9: Double-spin asymmetry for $pp \rightarrow \text{jet}X$ at $\sqrt{S} = 200 \text{ GeV}$ (upper plot) and $\sqrt{S} = 500 \text{ GeV}$ (lower plot) using cone sizes of $R = 0.4$ and $R = 0.7$, respectively, and sets of parton distributions with different gluon polarizations (see text) [17]. The error bars indicate the expected statistical accuracy $\delta A_{LL}^{\text{jet}}$ for a beam polarization of 40%, and integrated luminosities of 3 pb^{-1} and 20 pb^{-1} , respectively.

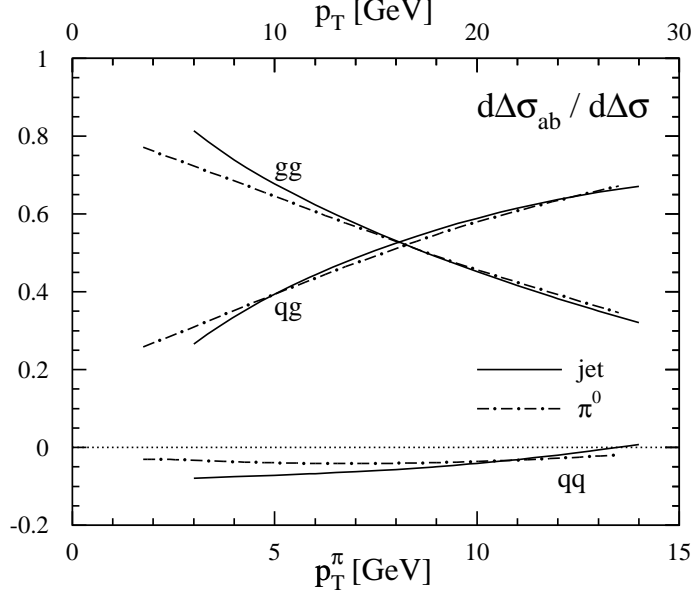


Figure 5.10: Relative contributions from gg , qg , and qq scatterings to the NLO polarized cross section with the standard set of GRSV [17] for jet and π^0 production at mid-pseudorapidities. Note that we use two separate coordinate axes for the two cases. p_T refers to the jet, whereas p_T^π stands for the transverse momentum of the pion.

pions carrying a momentum fraction z of the final-state parton. At RHIC-energies, one finds for mid-pseudorapidities an average z of about 0.5. Thus, e.g., a pion of $p_T^\pi = 5$ GeV results in average from a scattering with a final-state parton of 10 GeV. In jet production, on the other hand, the same parton would produce a jet with $p_T = 10$ GeV. This explains the pattern seen in Fig. 5.10, as well as a similar behavior of the spin asymmetries A_{LL}^{jet} and A_{LL}^π . The encountered relationship between hadron and jet observables can be used to cross-check results, and – more importantly – to gain a better understanding of the dynamics governing the formation of final states in high- p_T reactions.

We close our study of jet production with an explicit analysis of the cone-size dependence of the polarized and unpolarized jet cross sections and the double-spin asymmetry, illustrated by Fig. 5.11. There we have depicted the various observables as functions of the cone size R for different values of p_T as obtained in the SCA. Since the LO jet cross sections are free of any dependence on the jet parameters such as R , investigating the cone size dependence of jet observables allows to access NLO corrections directly. We recall from Eq. (5.40) that for R not too large, the dependence of $d(\Delta)\sigma$ on R is logarithmic. Obviously, at least in the unpolarized case, the cross section has to rise with increasing R . At larger R , deviations from our curves would be expected due to the terms $\propto R^2$ becoming important. The R -dependence of A_{LL}^{jet} turns out to be rather mild, especially for moderate p_T , which indicates a cancelation between polarized and unpolarized contributions.

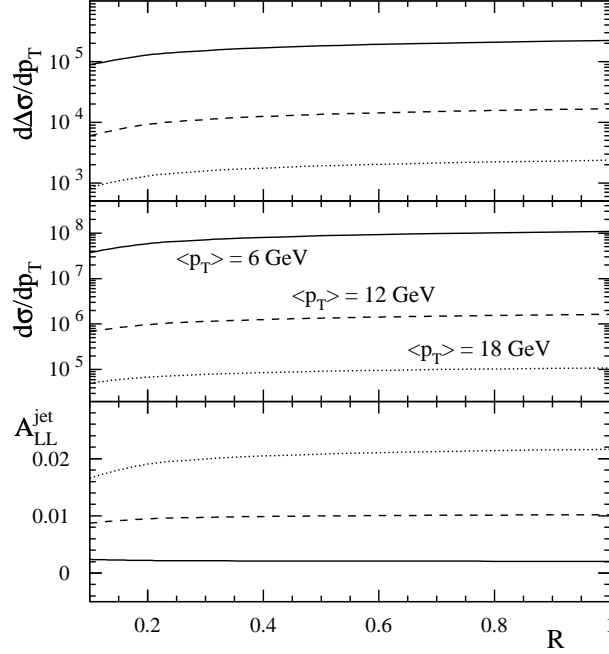


Figure 5.11: Cone size dependence of the polarized and unpolarized cross sections, given in [pb/GeV], and the corresponding spin asymmetry for the reaction $pp \rightarrow \text{jet}X$ at NLO for $\sqrt{S} = 200$ GeV. We have depicted the results obtained within the SCA for three different values of p_T .

5.4 Summary and Conclusions

In this chapter, we have presented an NLO calculation of single-inclusive jet production in longitudinally polarized proton-proton collisions. We have shown in some detail how to compute jet cross sections on a largely analytical level within the framework of the small-cone approximation, making use as much as possible of the previously calculated single-inclusive hadron production cross sections discussed in Chap. 4. By a comparison to the results of the Monte-Carlo jet code of [113] it has been demonstrated that this approximation is applicable for jet cone sizes up to $R \simeq 0.7$. Details of the algorithm used to define the jet do not affect the experimentally relevant spin asymmetries significantly. Our code has the advantage of being numerically stable, fast, and extremely efficient, since the use of the SCA allowed us to perform the phase space integration of all partonic cross sections analytically and to cancel poles associated with collinear configurations in the final state explicitly. Singularities stemming from the initial state as well as ultraviolet and infrared divergencies of the partonic matrix elements are treated in complete analogy to the case of single-inclusive hadron production, discussed in Chap. 4, by a factorization

and a renormalization procedure, respectively. They give rise to a residual dependence of the hadronic cross sections on unphysical scales. We have shown, however, that this source of theoretical uncertainty is significantly reduced when including NLO corrections to the Born cross sections. In addition to the mild scale dependence, single-inclusive jet observables are insensitive to final state hadronization mechanisms and thus provide a particularly clean tool for studying the spin structure of the nucleon in polarized pp -collisions.

We have demonstrated that the double-spin asymmetries for large- p_T jet production at RHIC are sensitive to Δg even for rather moderate beam polarizations and integrated luminosities. Therefore, first data on jet production, which are expected to be released soon by the STAR collaboration, will shed some light on the gluon polarization Δg . On the long run, single-inclusive jet production will contribute invaluable information to a quantitative determination of the spin-dependent parton distributions of the nucleon.

Chapter 6

NLO Corrections to Longitudinally Polarized Photoproduction of Inclusive Hadrons

In the foregoing chapters we have studied single-inclusive hadron and jet production in polarized proton-proton collisions as a tool for gaining information on the spin structure of the proton. Alternatively, the parton content of the nucleon can be accessed in photoproduction of inclusive hadrons – either on a fixed target, as in the already running COMPASS experiment at CERN [27], or at a future lepton-hadron collider, for instance the planned eRHIC facility at BNL [28]. It was found in a first exploratory LO analysis [126] that investigating photoproduction reactions in polarized electron-proton collisions additionally allows studying the inner (spin) structure of real photons which is completely unknown so far. Motivated by these twofold prospects, in this chapter we will focus on the process

$$l(P_l) + p(P_p) \rightarrow l'(P'_l) + \pi(P_\pi) + X , \quad (6.1)$$

where a lepton scatters elastically off a proton via the exchange of a (quasi-) real photon to produce a hadron in the final state. The by-products X emerging from the reaction are not detected and will not be of any concern to us.

Throughout this chapter we will put special emphasis on aspects of photoproduction reactions we have not encountered in hadroproduction processes, since these have been discussed in some detail in Chap. 4. After a brief discussion of our current knowledge of the photon structure we will start with the calculation of the partonic matrix elements relevant for the various channels contributing to (6.1). It is vital to take into account that the photon can interact either directly as an elementary particle, or resolve into partonic constituents which in turn interact with the partons of the proton. We adopt the partonic matrix elements of Chap. 4 and Ref. [31] for the resolved contributions. The direct components are known for some time in the polarized [127] and unpolarized case [128, 129], but we recalculate them both. Again, we aim to perform the entire calculation on a largely

analytical level and implement the partonic matrix elements in a fast computer code. The numerical results we thereby obtain will show sensitivity to the parton distributions of the photon as well as the gluon polarization of the proton.

6.1 The Parton Structure of the Photon

What makes the photon special in comparison to all other kinds of hadrons and partons is its two-fold occurrence as an elementary particle and also as a hadron-like conglomerate of quarks, antiquarks and gluons. Whereas the parton distributions of the structureless “direct” photon are trivial,

$$(\Delta)\gamma^\gamma(x, \mu) \sim \delta(1 - x) , \quad (6.2)$$

in the polarized case the parton content of the “resolved” photon, Δf^γ with $f = q, \bar{q}, g$, is completely unknown. The spin-averaged f^γ have been determined from data of DIS off a quasi-real photon target in e^+e^- collisions [130]. The evolution of the spin-dependent – and likewise the unpolarized – parton densities is governed by inhomogeneous integro-differential equations [131-133],

$$\begin{aligned} \mu \frac{d\Delta q^\gamma(x, \mu)}{d \ln \mu} &= \frac{\alpha_s}{2\pi} \left\{ \Delta k_q(x, \mu) + [\Delta P_{qq} \otimes \Delta q^\gamma + \Delta P_{qg} \otimes \Delta g^\gamma] \right\} , \\ \mu \frac{d\Delta g^\gamma(x, \mu)}{d \ln \mu} &= \frac{\alpha_s}{2\pi} \left\{ \Delta k_g(x, \mu) + \Delta P_{gq} \otimes [\Delta q^\gamma + \Delta \bar{q}^\gamma] + \Delta P_{gg} \otimes \Delta g^\gamma \right\} , \end{aligned} \quad (6.3)$$

where we have denoted the convolution of the parton distributions with appropriately defined splitting functions by

$$\Delta P_{ij} \otimes \Delta f^\gamma = \int_x^1 \frac{dy}{y} \Delta P_{ij} \left(\frac{x}{y}, \mu \right) \Delta f^\gamma(y, \mu) . \quad (6.4)$$

The spin-dependent parton-to-parton ΔP_{ij} and photon-to-parton splitting functions Δk_i and their unpolarized counterparts can be calculated perturbatively and are known up to two loops, i.e., NLO accuracy [67-70, 131, 133],

$$\begin{aligned} \Delta k_i(x, \mu) &= \frac{\alpha_{em}}{2\pi} \Delta k_i^{(0)}(x) + \frac{\alpha_{em} \alpha_s(\mu)}{(2\pi)^2} \Delta k_i^{(1)}(x) , \\ \Delta P_{ij}(x, \mu) &= \frac{\alpha_s(\mu)}{2\pi} \Delta P_{ij}^{(0)}(x) + \left(\frac{\alpha_s(\mu)}{2\pi} \right)^2 \Delta P_{ij}^{(1)}(x) . \end{aligned} \quad (6.5)$$

Altogether, the $(\Delta)f^\gamma$ are of order α_{em}/α_s . In contrast to the homogeneous DGLAP equations (2.46), describing the scale dependence of the parton densities of the proton, Eqs. (6.3) contain inhomogeneous terms which account for a photon-to-parton splitting. They give rise to a so-called “pointlike” solution Δf_{pl}^γ in addition to the homogeneous, hadronic contribution Δf_{had}^γ ,

$$\Delta f^\gamma(x, \mu) = \Delta f_{pl}^\gamma(x, \mu) + \Delta f_{had}^\gamma(x, \mu) . \quad (6.6)$$

The pointlike part can be calculated perturbatively. It depends only on the boundary conditions, but not on the non-perturbative input, which resides solely in the Δf_{had}^γ and has to be extracted from experiment. In the absence of any data the latter is fixed by vector meson dominance (VMD) like assumptions, stating that the photon tends to fluctuate into states of identical quantum numbers.

Beyond the leading order in α_s the decomposition of the parton densities into pointlike and hadronic components depends on the factorization scheme chosen. In the analysis of unpolarized e^+e^- data two factorization schemes have been used. Contrary to the conventional $\overline{\text{MS}}$ factorization, the so-called DIS_γ scheme [132] absorbs the NLO $\gamma^*\gamma \rightarrow q\bar{q}$ coefficient function C_γ in F_2^γ , which diverges as $x \rightarrow 1$, into the definition of the photonic parton densities. This allows for choosing very similar, VMD-inspired, inputs in LO and NLO analyses. A similar scheme has been proposed in the polarized case [133]. Technically, the $\overline{\text{MS}}$ and the DIS_γ scheme are related via a simple factorization scheme transformation, which will be discussed in Sec. 6.2.

Since the polarized parton densities Δf^γ are completely unknown, usually two extreme scenarios are employed to study the sensitivity of physical observables to the spin-dependent parton content of the photon. Figure 6.1. shows Δu^γ and Δg^γ at a scale $\mu = \sqrt{10}$ GeV at LO and NLO, determined in the DIS_γ scheme for these parametrizations. Whereas for the “minimal” set a vanishing hadronic input is imposed,

$$\Delta f_{had}^{\gamma,min}(x, \mu_0) = 0, \quad (6.7)$$

in the “maximal” scenario the maximal hadronic input compatible with the positivity bound $|\Delta f^\gamma(x, \mu)| \leq f^\gamma(x, \mu)$ is used,

$$\Delta f_{had}^{\gamma,max}(x, \mu_0) = f_{had}^\gamma(x, \mu_0), \quad (6.8)$$

with the unpolarized parton densities f^γ of Ref. [130]. The pointlike contribution is chosen to vanish at the input scale μ_0 . Note that Eq. (6.7) yields non-vanishing parton densities for $\mu > \mu_0$ due to the inhomogeneous nature of the evolution equations (6.3), in contrast to the homogeneous evolution of hadronic parton densities, Eq. (2.46). From Fig. 6.1 it can also be seen that the quark distributions exhibit a characteristic bump as $x \rightarrow 1$, which is caused by the pointlike part of the solution (6.6). As we will see in Sec. 6.3, in experiments probing large values of x the Δf_{had}^γ can therefore be hardly accessed.

Of course, the parametrizations (6.7) and (6.8) illustrate only the extreme scenarios for the parton distributions of the photon, derived solely on the basis of physically motivated model assumptions. Definite knowledge of the hadronic components of the photon can only be obtained by an analysis of data from future experiments, for instance, at eRHIC [28]. However, the very concept of photonic quark and gluon densities has firmly been established by extensive studies at the unpolarized HERA and LEP colliders [134], which revealed that resolved contributions to photoproduction cross sections are sizeable in certain kinematic regions. Above that, it has been shown that spin-averaged e^+e^- and ep data can simultaneously be described by the same set of photonic parton densities, which marks an important test for their universality and therefore success of the concept of a composite photon.

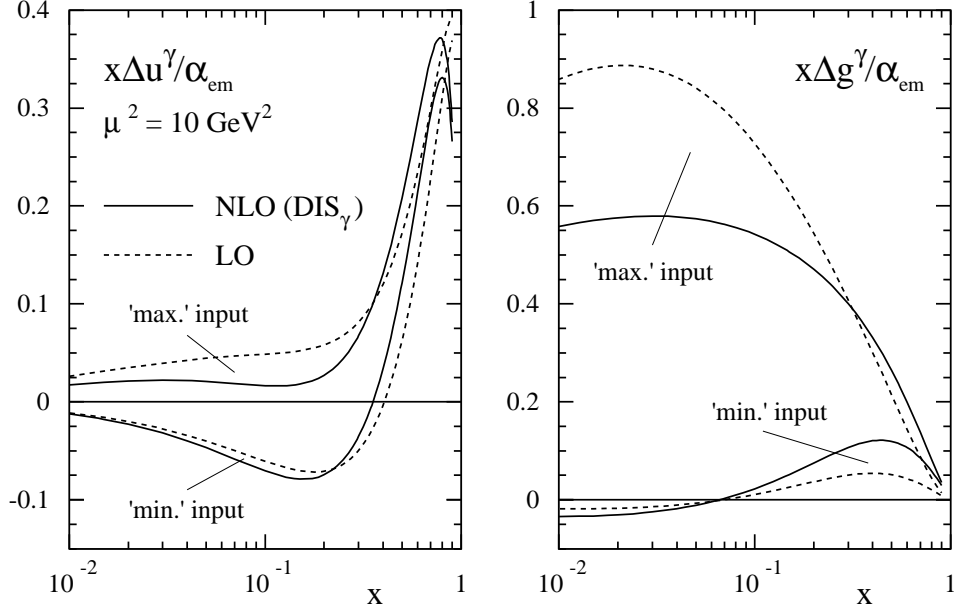


Figure 6.1: Spin-dependent parton densities of the u -quark (left) and the gluon (right) in the photon as obtained by Ref. [133]. Dashed lines correspond to LO results whereas NLO predictions in the DIS $_\gamma$ factorization scheme are depicted by solid lines for the two extreme scenarios of maximal and minimal hadronic input at the starting point of the evolution. The figure has been adapted from Ref. [133].

To provide a reliable framework for a similar extraction of the spin-dependent photon densities from future photoproduction experiments in polarized lepton-hadron collisions NLO results for a variety of processes sensitive to Δf^γ are required. In the following we therefore present a full NLO calculation for the experimentally relatively easily accessible photoproduction of single-inclusive hadrons, which additionally could yield information on the gluon polarization of the nucleon, complementary to what can be learned from hadronic collisions.

6.2 Some Technicalities

Contrary to single-inclusive pion production in proton-proton collisions, the cross section for $lp \rightarrow l'\pi X$ receives two types of contributions, sketched in Fig. 6.2. First, the photon can interact as an elementary particle and couple directly to the partons of the proton. Contributions stemming from this process are called “direct”. It is expected [135] that they dominate the photoproduction cross section at the low energies which are available,

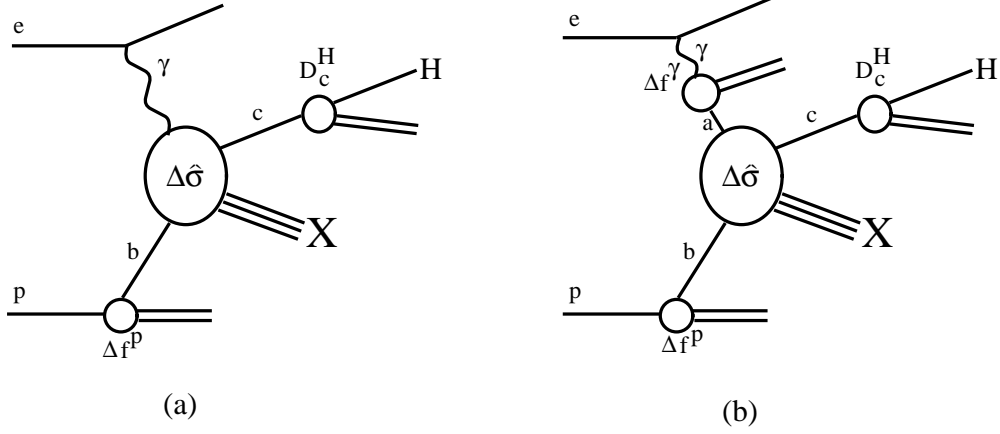


Figure 6.2: Direct (a) and resolved (b) contributions to $ep \rightarrow e'\pi X$.

e.g., in fixed-target experiments. On the other hand, the photon can resolve into its hadronic constituents which in turn may undergo scattering reactions. These processes are referred to as “resolved”. Since the parton distributions accounting for the hadronic structure of the photon are of $\mathcal{O}(\alpha_{em}/\alpha_s)$ as mentioned in Sec. 6.1, in combination with a pure QCD hard scattering they contribute at the same order as the direct channels, where the photon scatters off the protonic constituents itself. It is generally believed that the resolved components start to compete with the direct contributions only at collider energies. The full differential cross section for photoproduction reactions is then the sum of direct and resolved components. Both of these contributions take the form

$$\begin{aligned} \frac{d\Delta\sigma}{dp_T d\eta} &= \frac{2p_T}{S} \sum_{a,b,c} \int_{1-V+VW}^1 \frac{dz}{z^2} \int_{VW/z}^{1-(1-V)/z} \frac{dv}{v(1-v)} \int_{VW/vz}^1 \frac{dw}{w} \Delta a^l(x_l, \mu_f) \Delta b^p(x_p, \mu_f) \\ &\times \left[\frac{d\Delta\hat{\sigma}_{ab \rightarrow cX}^{(0)}(v)}{dv} \delta(1-w) + \frac{\alpha_s(\mu_r)}{\pi} \frac{d\Delta\hat{\sigma}_{ab \rightarrow cX}^{(1)}(s, v, w, \mu_r, \mu_f, \mu'_f)}{dv dw} \right] D_c^\pi(z, \mu'_f). \end{aligned} \quad (6.9)$$

The unpolarized cross section is obtained by replacing all spin-dependent quantities, as usual indicated by a “ Δ ”, with their unpolarized counterparts. In Eq. (6.9) the hadronic variable $S = (P_l + P_p)^2$ is the c.m.s. energy squared and V, W can be expressed in terms of the transverse momentum p_T of the observed pion and its pseudorapidity η in the c.m.s. system according to Eq. (5.7). Positive rapidity is counted in the forward direction of the proton. The corresponding parton-level variables are given by

$$s = (p_a + p_b)^2 = x_l x_p S, \quad x_l = \frac{VW}{vwz}, \quad x_p = \frac{1-V}{z(1-v)}. \quad (6.10)$$

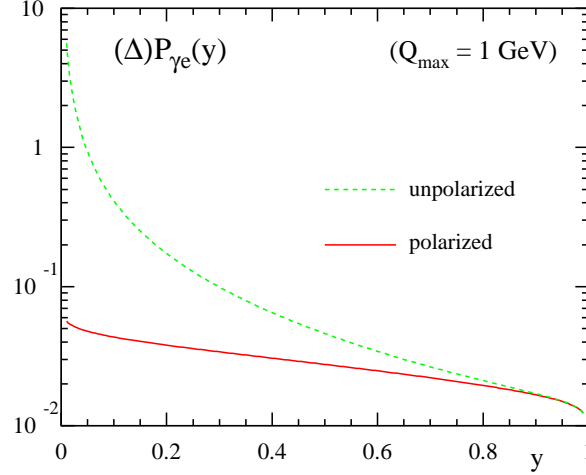


Figure 6.3: Unpolarized (dashed) and polarized (solid) equivalent photon spectrum $(\Delta)P_{\gamma e}(y)$ for an electron beam with $Q_{max}^2 = 1 \text{ GeV}^2$.

In complete analogy to Eq. (4.3) the sum in (6.9) runs over all partonic channels $ab \rightarrow cX$ contributing to pion photoproduction up to $\mathcal{O}(\alpha_{em}\alpha_s^2)$ with the corresponding partonic cross sections $\Delta\hat{\sigma}_{ab \rightarrow cX}^{(0,1)}$ at LO and NLO. Since they are universal quantities independent of the foregoing reaction, the fragmentation functions $D_c^\pi(z, \mu_f')$ are the same as those used to describe pion fragmentation in hadroproduction processes. The $\Delta b^p(x_p, \mu_f)$ stands for the distribution of parton b in the proton at a scale μ_f with a momentum $p_b = x_p P_p$. Similarly, the $\Delta a^l(x_l, \mu_f)$ is an effective density describing parton a emerging from the lepton with a momentum $p_a = x_l P_l$. It is given by the convolution

$$\Delta a(x_l, \mu_f) = \int_{x_l}^1 \frac{dy}{y} \Delta P_{\gamma l}(y) \Delta a^\gamma \left(x_\gamma = \frac{x_l}{y}, \mu_f \right) \quad (6.11)$$

of the spin-dependent Weizsäcker-Williams “equivalent photon” spectrum $\Delta P_{\gamma l}$ and the parton distributions Δa^γ of the circularly polarized photon, where x_γ is the fraction of the photon’s momentum carried by parton a . The Weizsäcker-Williams spectrum reads [136]

$$\Delta P_{\gamma l}(y) = \frac{\alpha_{em}}{2\pi} \left\{ \left[\frac{1 - (1-y)^2}{y} \right] \ln \frac{Q_{max}^2(1-y)}{m_l^2 y^2} + 2m_l^2 y^2 \left(\frac{1}{Q_{max}^2} - \frac{1-y}{m_l^2 y^2} \right) \right\}. \quad (6.12)$$

It describes the radiation of a photon with a momentum fraction y and a virtuality lower than Q_{max} by a lepton of mass m_l . We have depicted $(\Delta)P_{\gamma l}$ for an electron in Fig. 6.3.

The explicit form of Δa^γ differs for direct and resolved cases. As mentioned above, in direct photoproduction reactions the photon emitted from the lepton interacts itself with

parton b from the proton. Since it does not emit any other particles before undergoing the scattering it does not lose momentum and $x_\gamma = x_l$. The corresponding distribution function therefore takes the form

$$\Delta a^\gamma(x_\gamma, \mu_f) \rightarrow \delta(1 - x_\gamma) . \quad (6.13)$$

In the resolved case, the photon splits into its hadronic constituents. One of these partons, denoted by a , subsequently scatters off the proton. Here, the Δa^γ denote the so far unknown spin-dependent quark, antiquark and gluon distributions of the photon. Generally, $x_\gamma < 1$ in this case, as the photon's momentum is shared between the scattering parton a and other constituents which do not participate in the hard reaction.

With these definitions at hand, direct and resolved photoproduction cross sections can be calculated. The partonic cross sections $d(\Delta)\hat{\sigma}_{ab \rightarrow cX}$ contributing to the resolved part are the same as those already calculated for hadroproduction of pions, $pp \rightarrow \pi X$, in Chap. 4 [31], the only difference being that parton a now is emerging from a photon instead of a proton. This, however, is accounted for by the convolution with the proper parton distribution functions and does not affect the hard scattering itself. The partonic cross sections for the direct contributions $\gamma b \rightarrow cX$ have been published in the unpolarized [128, 129] and polarized case [127], but we will recalculate both. To this end, we consider the subprocesses

$$\begin{aligned} \gamma q &\rightarrow q'X \\ \gamma q &\rightarrow \bar{q}X \\ \gamma q &\rightarrow qX \\ \gamma q &\rightarrow gX \\ \gamma g &\rightarrow qX \\ \gamma g &\rightarrow gX . \end{aligned} \quad (6.14)$$

In the calculation of the respective partonic cross sections some care has to be taken when the electromagnetic coupling of the photon to a quark is to be considered. In contrast to the quark-gluon coupling which is of equal strength for quarks of any flavor, the electromagnetic interaction differentiates between quarks of different charges. For instance, in the reaction $\gamma q \rightarrow q'\bar{q}'q$ the photon can couple to quark q as well as to q' or \bar{q}' , as illustrated by Fig. 6.4. Depending on the actual coupling the corresponding scattering amplitudes acquire a charge factor of e_q or $e_{q'}$, respectively. If the matrix elements are squared one thus encounters contributions being proportional to e_q^2 , $e_{q'}^2$, and $e_q e_{q'}$. To simplify the subsequent convolution with parton densities and summation over quarks of different flavor and charge, we have re-organized the partonic subprocesses involving different types of quarks in terms of charge factors,

$$d\Delta\hat{\sigma}_{ab \rightarrow cX} = e_q^2 d\Delta\hat{\sigma}_{ab \rightarrow cX}^I + e_q e_{q'} d\Delta\hat{\sigma}_{ab \rightarrow cX}^{II} + e_{q'}^2 d\Delta\hat{\sigma}_{ab \rightarrow cX}^{III} . \quad (6.15)$$

Apart from this book-keeping exercise the partonic cross sections contributing to direct photoproduction are calculated in complete analogy to the resolved case. Singularities are

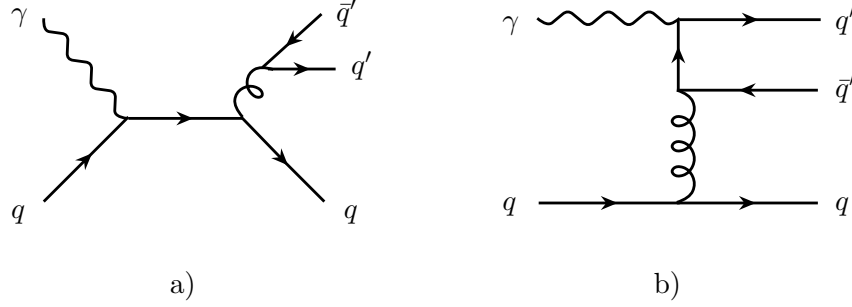


Figure 6.4: Generic Feynman diagrams contributing to the $2 \rightarrow 3$ process $\gamma q \rightarrow q' \bar{q}' q$, where the photon couples either to quark q (a) or q' (b), thereby giving rise to different charge factors, e_q or $e_{q'}$.

made manifest as poles in ε by evaluating all diagrams in $n = 4 - 2\varepsilon$ dimensions. The renormalization of UV divergencies emerging in $2 \rightarrow 2$ processes with selfenergy and vertex corrections is performed in the $\overline{\text{MS}}$ scheme by using the tabulated insertions of Ref. [88] as discussed in Chap. 2. The result given there for the quark-gluon coupling can be converted to the corresponding correction for a quark-photon vertex by disregarding terms stemming from gluonic self-interactions and replacing color factors and strong coupling constant,

$$ig_s \frac{\alpha_s}{4\pi} \left\{ \left(C_F - \frac{C_A}{2} \right) \Lambda_1^\mu + \frac{C_A}{2} \Lambda_2^\mu \right\} \rightarrow ig_e \frac{\alpha_s}{4\pi} C_F \Lambda_1^\mu. \quad (6.16)$$

Selfenergy corrections of photon legs are of higher order in α_{em} and thus need not be considered here. Box diagrams are calculated from the scratch adopting an appropriate Passarino-Veltman decomposition of the emerging loop integrals. The computation of the real $2 \rightarrow 3$ scattering diagrams is straightforward. After the phase space integration of the squared matrix elements the sum of all contributions to a subprocess is free of infrared singularities. The remaining collinear divergencies are then factored into the bare parton distributions and fragmentation functions of the external legs. We thereby obtain finite results for the direct contributions to the photoproduction cross section, which fully agree with [127]. In the unpolarized case, we found some minor mistakes in [128].

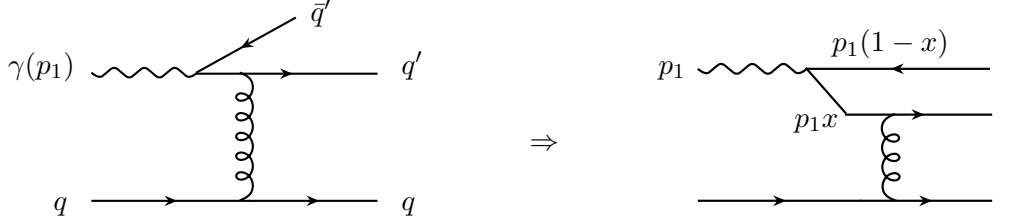
It has to be stressed at this point that neither the direct ($d\Delta\sigma_{dir}$) nor the resolved ($d\Delta\sigma_{res}$) hadronic cross sections are physical quantities individually. Only their sum,

$$d\Delta\sigma = d\Delta\sigma_{dir} + d\Delta\sigma_{res}, \quad (6.17)$$

is a meaningful observable which can be measured in experiment. From the theoretical point of view this entanglement arises from the factorization of initial state collinear divergencies. The singular configuration where the direct photon entering the hard scattering splits collinearly into a quark-antiquark pair cannot be absorbed into corresponding photonic parton densities, since the direct photon acts as an elementary particle. The divergence stemming from a direct contribution therefore has to be moved into the pointlike part of the hadronic photon densities and thus into the resolved component. A priori

arbitrary finite pieces can be subtracted along with the poles, which gives rise to a factorization scheme dependence. However, the sum of direct and resolved contributions has to be independent of this choice.

Let us illustrate this feature on the basis of the reaction $\gamma q \rightarrow q' X$. Here, an initial state singularity arises, if the photon emits a collinear quark-antiquark pair,



Subtracting this divergence requires, as usual, adding an appropriate counter term to the partonic cross sections,

$$d\Delta\hat{\sigma}_{\gamma q \rightarrow q' X}^{counter} \sim -\frac{\alpha_{em}}{2\pi} \Delta H_{q\gamma} \otimes d\Delta\hat{\sigma}_{q' q \rightarrow q' q}, \quad (6.18)$$

with $d\Delta\hat{\sigma}_{q' q \rightarrow q' q}$ denoting the polarized Born cross section for the reaction $q' q \rightarrow q' q$ which has to be convoluted with

$$\Delta H_{q\gamma}(x, \mu_f) = \left(-\frac{1}{\varepsilon} + \gamma_E - \ln 4\pi \right) \Delta P_{q\gamma}^{(4)}(x) \left(\frac{s}{\mu_f} \right)^\varepsilon + \Delta h_{q\gamma}(x). \quad (6.19)$$

Although this counter term is subtracted from a direct contribution to the photoproduction cross section it has to be factored into the hadronic parton distributions of the photon, and is thereby “shifted” to the resolved cross section. This makes immediately clear that considering the direct cross section alone is meaningless. Also the separation between direct and resolved components is *not* unique. In Eq. (6.19) this freedom in the choice of the factorization scheme is reflected by the *arbitrary* finite piece $\Delta h_{q\gamma}$ which is to be subtracted along with the pole terms. Whereas the singularities always emerge in a universal way in the form of a LO splitting function combined with a LO Born cross section, the further finite subtractions vary depending on the factorization scheme chosen, as discussed in Sec. 3.5. In the $\overline{\text{MS}}$ convention, $\Delta h_{q\gamma}(x) = 0$. Alternatively, we are going to use the DIS_γ scheme [132], introduced in Sec. 6.1. The photonic parton densities in the DIS_γ and $\overline{\text{MS}}$ scheme are related to each other via

$$\Delta a^{\gamma, \overline{\text{MS}}}(x, \mu) = \Delta a^{\gamma, \text{DIS}}(x, \mu) + \delta \Delta a^\gamma(x), \quad (6.20)$$

where $a = q, \bar{q}, g$ and

$$\begin{aligned} \delta \Delta q^\gamma(x) &= \delta \Delta \bar{q}^\gamma(x) \\ &= -2C_A e_q^2 \frac{\alpha_{em}}{4\pi} \left[(2x-1) \left(\ln \frac{1-x}{x} - 1 \right) + 2(1-x) \right], \\ \delta \Delta g^\gamma(x) &= 0. \end{aligned} \quad (6.21)$$

Having calculated partonic cross sections in the $\overline{\text{MS}}$ scheme they can straightforwardly be converted to their DIS_γ counterparts by demanding that the sum of direct and resolved contributions to the hadronic cross sections be independent of the factorization convention chosen,

$$d\Delta\sigma = d\Delta\sigma^{\overline{\text{MS}}} = d\Delta\sigma^{\text{DIS}}, \quad (6.22)$$

at least up to the order in perturbation theory considered here. Schematically, denoting convolutions again by the symbol \otimes , we can write $d\Delta\sigma$ as the sum

$$\begin{aligned} d\Delta\sigma &= \underbrace{\sum_{b,c} \Delta b^p \otimes d\Delta\hat{\sigma}_{\gamma b \rightarrow cX}^{\overline{\text{MS}}} \otimes D_c^\pi}_{\text{direct}} + \underbrace{\sum_{b,c} \sum_a \Delta b^p \otimes \Delta a^{\gamma, \overline{\text{MS}}} \otimes d\Delta\hat{\sigma}_{ab \rightarrow cX} \otimes D_c^\pi}_{\text{resolved}} \\ &= \sum_{b,c} \Delta b^p \otimes \left[d\Delta\hat{\sigma}_{\gamma b \rightarrow cX}^{\text{DIS}} - \sum_a \delta a^\gamma \otimes d\Delta\hat{\sigma}_{ab \rightarrow cX}^{(0)} \right] \otimes D_c^\pi \\ &\quad + \sum_{b,c} \sum_a \Delta b^p \otimes \left[\Delta a^{\gamma, \text{DIS}} \otimes d\Delta\hat{\sigma}_{ab \rightarrow cX} + \delta \Delta a^\gamma \otimes d\Delta\hat{\sigma}_{ab \rightarrow cX}^{(0)} \right] \otimes D_c^\pi \\ &= \underbrace{\sum_{b,c} \Delta b^p \otimes d\Delta\hat{\sigma}_{\gamma b \rightarrow cX}^{\text{DIS}} \otimes D_c^\pi}_{\text{direct}} + \underbrace{\sum_{b,c} \sum_a \Delta b^p \otimes \Delta a^{\gamma, \text{DIS}} \otimes d\Delta\hat{\sigma}_{ab \rightarrow cX} \otimes D_c^\pi}_{\text{resolved}}, \end{aligned} \quad (6.23)$$

where we have used Eq. (6.20) to express the photonic parton densities in the $\overline{\text{MS}}$ scheme in terms of $\Delta a^{\gamma, \text{DIS}}$ and $\delta \Delta a^\gamma$. Inserting

$$d\Delta\hat{\sigma}_{\gamma b \rightarrow cX}^{\text{DIS}} = d\Delta\hat{\sigma}_{\gamma b \rightarrow cX}^{\overline{\text{MS}}} + \sum_a \delta \Delta a^\gamma \otimes d\Delta\hat{\sigma}_{ab \rightarrow cX}^{(0)} \quad (6.24)$$

ensures that the physical observable $d\Delta\sigma$ remains invariant under factorization scheme transformations up to $\mathcal{O}(\alpha_{em}\alpha_s^2)$. Since the $\delta \Delta a^\gamma$ bring an additional factor of α_{em} , contributions to (6.24) stemming from $\sum \delta \Delta a^\gamma \otimes d\Delta\hat{\sigma}_{ab \rightarrow cX}^{(1)}$ are disregarded as they are beyond the order in α_{em} considered here.

It is important to note that the purely hadronic quantities Δb^p , D_c^π and the resolved partonic cross sections $\Delta\hat{\sigma}_{ab \rightarrow cX}$ are not affected by this scheme transformation. Only the photonic parton densities and the direct contributions to the partonic cross sections have to be modified according to Eqs. (6.20), (6.24) *simultaneously*, if results in the $\overline{\text{MS}}$ scheme are to be expressed in the DIS_γ scheme. The sum of direct and resolved contributions is then independent of the factorization prescription chosen as required. We will demonstrate this numerically in the following section.

6.3 Numerical Results

6.3.1 Single-Inclusive Pionproduction at an Electron-Proton Collider

Having specified how meaningful predictions for photoproduction cross sections can be obtained, we are now in a position to discuss some phenomenological implications and results. Our aim is, first to demonstrate the importance of NLO corrections to hadronic cross sections and their independence of purely theoretical scheme conventions. We are then going to estimate observables which are accessible in experiment and show how they can serve for gaining insight into the spin structure of the photon. In passing, we will also stress the possibility to further study the gluon polarization of the nucleon.

Our calculations are intended to resemble the kinematics of the considered polarized electron-proton collider eRHIC at BNL [28]. eRHIC would add an electron beam with an energy of 10 GeV to the existing RHIC proton beam. For a proton energy of 250 GeV this amounts to a c.m.s. energy of $\sqrt{S} = 100$ GeV. As usual, NLO (LO) partonic cross sections are combined with NLO (LO) parton distribution and fragmentation functions and the two-loop (one-loop) expression for the strong coupling constant α_s . The value of α_s is always taken as demanded by the corresponding parton densities of the proton, for which we have chosen the CTEQ5 set [74] in the unpolarized case and the GRSV distributions [17] in the polarized one. To ensure that indeed photoproduction cross sections are probed rather than electroproduction reactions including the exchange of highly virtual photons the maximally allowed virtuality in the equivalent photon spectrum (6.12) is restricted to be $Q_{max}^2 = 1 \text{ GeV}^2$. This parameter eventually has to be adjusted to future machine requirements. It does not significantly affect the results to be discussed below, however. We note that photoproduction was successfully studied by H1 and ZEUS in unpolarized ep collisions at about $\sqrt{S} = 300$ GeV. We closely follow the cuts applied there and require the momentum fraction of the photon to be in the range $0.2 \leq y \leq 0.85$.

It has been mentioned before that the parton distributions of the polarized photon are unknown so far. In the description of the spin-dependent parton content of the photon we therefore have to rely solely on model assumptions and estimate the uncertainty caused by our ignorance of the Δf^γ . To this end, we consider the two extreme scenarios (6.7), and (6.8) introduced above for the photon structure: Adopting the GRV parton distributions f^γ [130] for the unpolarized photon according to [137] we assume maximal [$\Delta f^\gamma(x, \mu_0) = f^\gamma(x, \mu_0)$] and minimal [$\Delta f^\gamma(x, \mu_0) = 0$] saturation of the positivity bound, $|\Delta f^\gamma(x, \mu)| \leq f^\gamma(x, \mu)$, at the input scale of the perturbative evolution. Both extreme sets are used with appropriate LO [137] and NLO [133, 138] boundary conditions and evolution equations. If not stated otherwise, use of the maximal scenario is implicitly understood. For the pion fragmentation functions, D_c^π , the set proposed by Kramer, Kniehl, and Pötter [82] is adopted throughout our analysis, as in Chap. 4.

In order to study photonic parton densities in photoproduction reactions, rapidity-dependent differential cross sections are particularly suitable, as pointed out in [126]. Since the momentum fraction of the parton emerging from the photon, x_γ , is closely related to rapidity, different ranges of x_γ can be probed as η is varied. From the definition of the momentum fractions x_p and x_l in the protonic and photonic parton distributions in

terms of rapidity [cf. Eqs. (5.7), (6.10)], it follows that large negative values of η correspond to large $x_\gamma \rightarrow 1$. At $x_\gamma = 1$ the photon interacts solely as an elementary particle meaning that the photoproduction cross section in this kinematic range is mainly determined by the direct contribution. Furthermore, as $x_\gamma \rightarrow 1$, the pointlike part of the parton distributions, Δf_{pl}^γ , dominates over the hadronic one. Since Δf_{pl}^γ is free of any model assumptions on the photonic structure this region does not contain information on the non-perturbative hadronic components of the photon, but gives access to the gluon polarization of the proton, as we will show below. At large and positive rapidities corresponding to small values of x_γ , however, the hadronic part of the resolved cross section becomes dominant, and the effects of different hadronic input distributions for the photon are especially pronounced. These features of photoproduction reactions have been observed in the unpolarized case by H1 and ZEUS.

In the following we will present results in terms of the experimentally relevant pseudorapidity in the laboratory frame, η_{lab} , rather than the so far used c.m.s. rapidity η . As demonstrated in App. E, these two quantities are related to each other via

$$\eta_{lab} = \eta + \frac{1}{2} \ln \frac{E_p}{E_l}, \quad (6.25)$$

where E_p, E_l are the energies of the colliding protons and leptons. The simple relation between rapidities in different frames is due to the additivity of η under Lorentz boosts, which is the reason for favoring formulations in terms of rapidities rather than scattering angles. Boosting a rapidity-dependent cross section from one frame to another will only cause a simple shift whereas its shape remains unaffected.

In Fig. 6.5 we present our results for unpolarized and polarized photoproduction cross sections, $d(\Delta)\sigma/d\eta_{lab}$, in electron-proton collisions, including both direct and resolved contributions. The calculations are performed at a c.m.s. energy of $\sqrt{S} = 100$ GeV, with $E_p = 250$ GeV and $E_e = 10$ GeV. The transverse momentum of the produced pion has been integrated out, demanding $p_T \geq 4$ GeV, as p_T sets the hard scale for the perturbative calculation. All scales are chosen to be equal, $\mu_r = \mu_f = \mu'_f = p_T$. It can be seen that in the unpolarized case the NLO corrections to the cross section are sizeable and thus indispensable in a thorough analysis of photoproduction reactions. This effect is much less pronounced in the polarized cross sections, where the NLO predictions seem to almost coincide with the LO ones, as is transparently illustrated by the respective K -factors, defined in Eq. (4.22). Only at negative rapidities, where the spin-dependent cross section changes sign, the NLO corrections to $d\Delta\sigma$ are large. At positive η_{lab} they become negligible for the chosen values of the various scales. Contrary to the polarized case, in the unpolarized cross sections these corrections are roughly constant over the rapidity range considered here and amount to almost $60 \div 80\%$. This implies that A_{LL}^π is reduced in NLO.

A better indicator for the necessity of NLO corrections to hadronic cross sections is their dependence on unphysical scales, as discussed in Chap. 4. Therefore, we have studied the variation of $d\Delta\sigma/d\eta_{lab}$ with the scale parameters. For simplicity, again we set all scales equal and varied them in the typical range $p_T/2 \leq \mu_r = \mu_f = \mu'_f \leq 2p_T$. Our predictions are depicted in Fig. 6.6. The uncertainty of the LO cross section due to

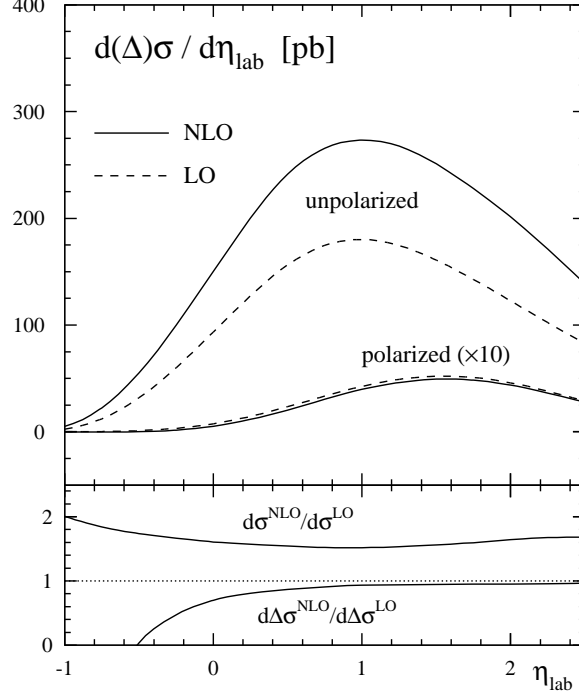


Figure 6.5: Unpolarized and polarized differential cross sections at LO (dashed) and NLO (solid) for the reaction $ep \rightarrow e'\pi^0 X$ at $\sqrt{S} = 100$ GeV. The polarized cross sections have been multiplied by a factor of 10 for a better readability. The lower panel shows the ratios of NLO and LO contributions.

the unconstrained scale parameters, in the plot indicated by a yellow band, is huge and spoils any predictive power of the Born approximation. This deficiency is widely cured by extending the perturbative calculation to the NLO in α_s . Modifying the scales no longer affects the results for the polarized cross sections considerably, if NLO effects are taken into account in the evaluation of $d\Delta\sigma/d\eta_{lab}$. This feature again illustrates the relevance of higher order corrections in the perturbative description of photoproduction reactions, if not only qualitative estimates but quantitative predictions are required.

It has been outlined in some detail before that neither direct nor resolved contributions to photoproduction cross sections are physically observable quantities themselves. Individually, each of them depends on the factorization scheme chosen for the subtraction of collinear divergencies from the partonic cross sections into the photonic parton densities. To illustrate this “ambiguity” we have plotted the resolved and direct contributions to $d\Delta\sigma/d\eta_{lab}$ separately in Fig. 6.7 in the $\overline{\text{MS}}$ and DIS_γ factorization schemes. According to

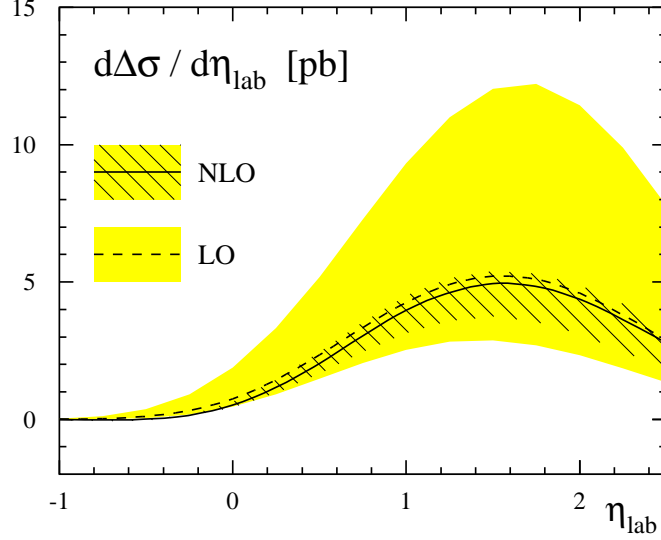


Figure 6.6: Scale dependence of the polarized rapidity-differential cross section in $\vec{e}\vec{p} \rightarrow e'\pi^0 X$ in the range $p_T/2 \leq \mu_r = \mu_f = \mu'_f \leq 2p_T$. The solid (NLO) and dashed (LO) curves correspond to the choice where $\mu_r = \mu_f = \mu'_f = p_T$. The yellow band indicates the scale uncertainty at LO, whereas the shaded area corresponds to the NLO result.

Eq. (6.23) they are given by

$$\begin{aligned}
 d\Delta\sigma_{dir}^{\overline{\text{MS}}/\text{DIS}} &= \sum_{b,c} \Delta b^p \otimes d\Delta\hat{\sigma}_{\gamma b \rightarrow cX}^{\overline{\text{MS}}/\text{DIS}} \otimes D_c^\pi, \\
 d\Delta\sigma_{res}^{\overline{\text{MS}}/\text{DIS}} &= \sum_{a,b,c} \Delta a^{\gamma, \overline{\text{MS}}/\text{DIS}} \otimes \Delta b^p \otimes d\Delta\hat{\sigma}_{ab \rightarrow cX} \otimes D_c^\pi.
 \end{aligned} \tag{6.26}$$

The figure shows that each of these contributions varies as the factorization scheme is modified. However, the sum of direct and resolved contributions, $d\Delta\sigma = d\Delta\sigma_{res}^{\overline{\text{MS}}/\text{DIS}} + d\Delta\sigma_{dir}^{\overline{\text{MS}}/\text{DIS}}$, is independent of the factorization prescription used, as it should.

Having thus ensured that theoretical artifacts are strongly reduced at the NLO, we are now in a position to investigate the polarized cross section more thoroughly. In Fig. 6.8 we have plotted the ratios $d\Delta\sigma_{ab}/d\Delta\sigma_{res}$ of the dominant channels contributing to resolved photoproduction. Here, $d\Delta\sigma_{ab}$ stands for the partonic cross sections $ab \rightarrow cX$, summed over all final state channels c and convoluted with the corresponding parton distribution and fragmentation functions,

$$d\Delta\sigma_{ab} = \sum_c \Delta a^l \otimes \Delta b^p \otimes d\Delta\hat{\sigma}_{ab \rightarrow cX} \otimes D_c^\pi. \tag{6.27}$$

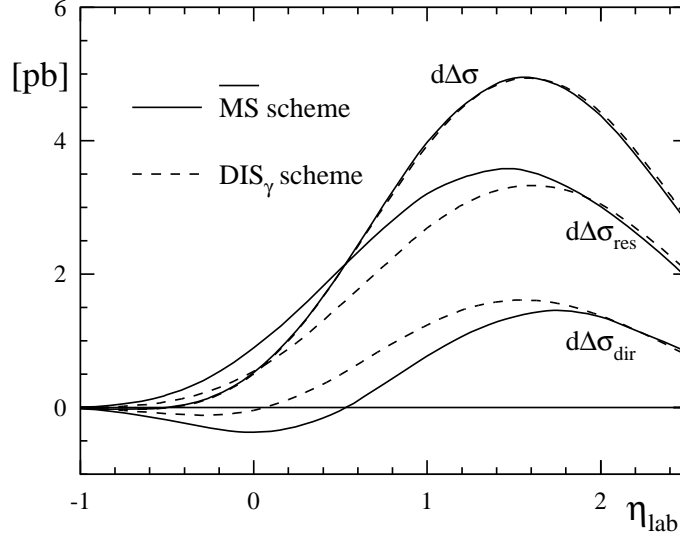


Figure 6.7: Direct and resolved contributions to $d\Delta\sigma/d\eta_{lab}$ in the $\overline{\text{MS}}$ (solid) and DIS_γ (dashed) factorization schemes at NLO. Also shown is their sum, which is independent of theoretical conventions used in the perturbative calculation.

As usual, a and b denote the partons emerging from the photon and proton, respectively. For the parton distributions of the resolved photon, we employ the maximal scenario. Whereas at large and negative rapidities the qg -channel is by far dominant, at positive values of η_{lab} the subprocesses gq and gg become equally important and even exceed qg in magnitude at the upper end of the η_{lab} -range considered. This reflects the rise in the gluonic component of the photon's parton densities, Δg^γ , at small values of x_γ which correspond to large and positive rapidities. On the other hand, the gluon density in the photon is strongly suppressed as $x_\gamma \rightarrow 1$ and thus $\eta_{lab} \ll 0$, whereas the quark distributions are peaked near $x_\gamma \rightarrow 1$. The strong suppression of the pure quark channels is due to the moderate quark densities in the proton and the small absolute value of the partonic qq -scattering cross sections which has already been discussed in Chap. 4.

It is interesting to note that the actual distribution of all of these ratios depends on the explicit form of the Weizsäcker-Williams spectrum used to describe the splitting of a photon from an electron. So far, we have used the expression given in Eq. (6.12). However, in the literature the nonlogarithmic term in Eq. (6.12) is often neglected. It is argued that disregarding the nonlogarithmic terms in $\Delta P_{\gamma l}$ modifies the full results only marginally. To study the effect of this assumption in detail, we have calculated the ratios of the various subprocesses also with this modified Weizsäcker-Williams spectrum. Figure 6.9 shows that the corresponding results differ – at large positive η_{lab} significantly – from the ratios depicted in Fig. 6.8. However, the sum of all channels is practically independent of the

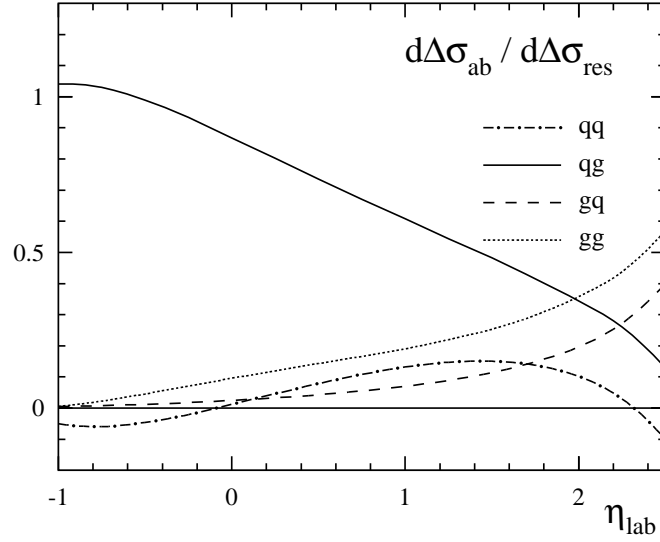


Figure 6.8: Relative contributions of the partonic channels $ab \rightarrow cX$, summed over all final states c , to the resolved part of the polarized cross section for $\vec{e}\vec{p} \rightarrow e'\pi^0 X$. The electron-photon splitting is described by the full Weizsäcker-Williams spectrum (6.12).

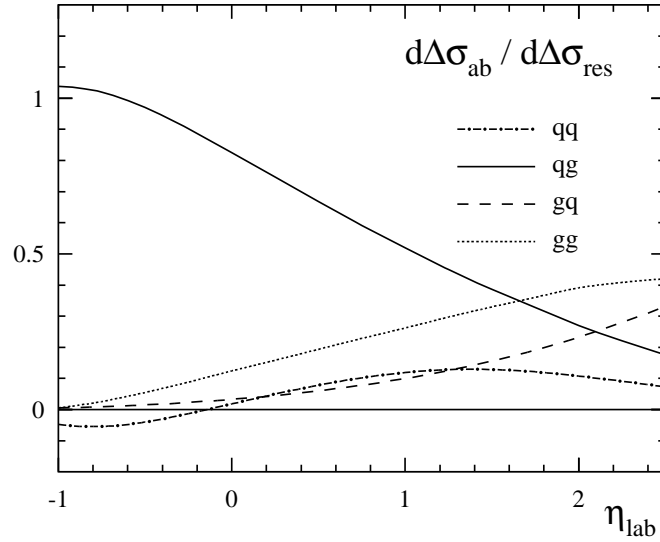


Figure 6.9: Ratios of partonic channels to the full polarized cross section like in Fig. 6.8, but now without the logarithmic terms in $\Delta P_{\gamma l}$.

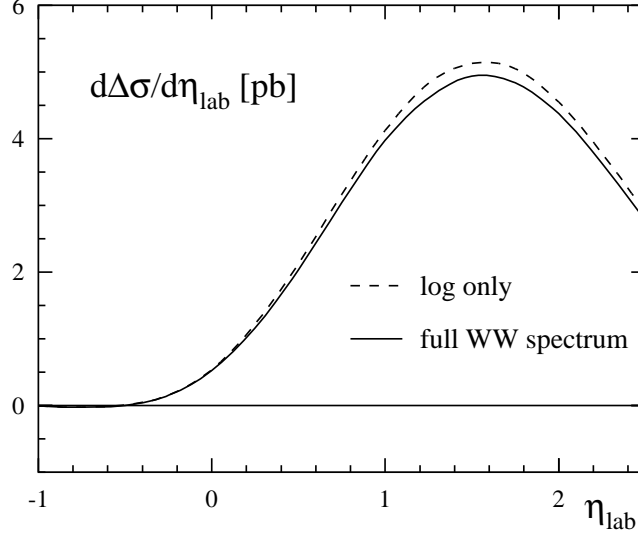


Figure 6.10: Spin-dependent differential NLO cross section for the reaction $\bar{e}\vec{p} \rightarrow e'\pi^0 X$. The splitting of the photon from the electron is described by the full Weizsäcker-Williams spectrum (6.12) (solid line) and the equivalent photon spectrum without the nonlogarithmic terms (dashed line), respectively.

nonlogarithmic terms, as illustrated by Fig. 6.10. Although disregarding the nonlogarithmic terms in the equivalent photon spectrum affects the full photoproduction cross section only slightly, we will use the full Weizsäcker-Williams spectrum throughout our analysis.

So far, we have presented our results for single-inclusive π^0 -production cross sections in electron-proton collisions and studied their perturbative stability and dependence on calculational artifacts. In particular, we have shown that a NLO calculation provides a considerable reduction of the theoretical uncertainties arising in any perturbative approach as compared to a mere LO analysis. With these pre-requisites at hand we are now in a position to compute the actual quantity of interest: the longitudinal double-spin asymmetry A_{LL}^π , which, in complete analogy to the spin asymmetry in pion hadroproduction, Eq. (4.2), is defined by the ratio of the polarized to the unpolarized cross section.

$$A_{LL}^\pi \equiv \frac{d\Delta\sigma}{d\sigma} = \frac{d\sigma^{++} - d\sigma^{+-}}{d\sigma^{++} + d\sigma^{+-}}. \quad (6.28)$$

We employ the rapidity-differential cross sections integrated over all $p_T \geq 4$ GeV as discussed before to obtain predictions for A_{LL}^π as functions of η_{lab} . Our results are depicted in Fig. 6.11. To get an estimate for the sensitivity of the spin asymmetry to the parton content of the photon we have calculated A_{LL}^π with the two extreme scenarios for the Δf^γ discussed in Sec. 6.1. We furthermore make sure that the information we wish to

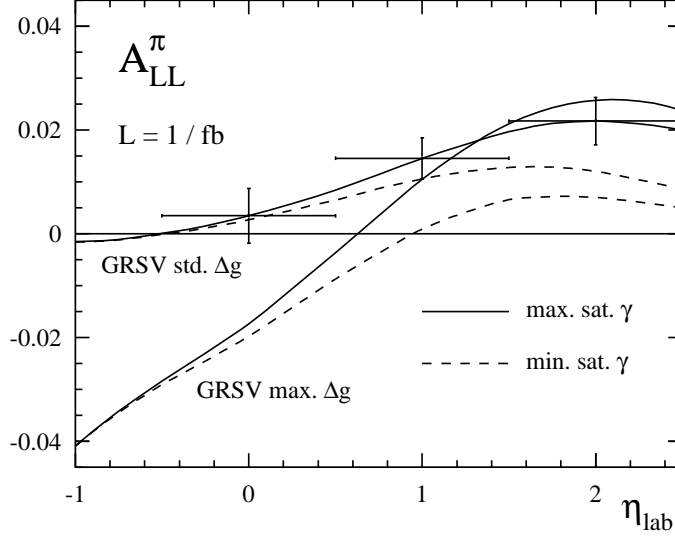


Figure 6.11: Double-spin asymmetry for the reaction $ep \rightarrow e'\pi^0 X$, evaluated to NLO in α_s with two different choices for the parton distributions of the proton and the two extreme scenarios for the polarized photon densities. Also shown are the error bars expected for future measurements at eRHIC at an integrated luminosity of 1 fb^{-1} .

gain on the photon structure is not obscured by our ignorance of the gluon distribution in the proton by imposing different assumptions on Δg and show results obtained with the standard and “maximal Δg ” sets of Ref. [17]. The error bars in the diagram indicate the expected statistical errors of a future experiment at eRHIC:

$$\delta A_{LL}^{\pi} \simeq \frac{1}{\mathcal{P}_e \mathcal{P}_p \sqrt{\sigma_{bin} \mathcal{L}}} . \quad (6.29)$$

Here, \mathcal{P}_e and \mathcal{P}_p denote the polarization of the electron and proton beam, respectively, \mathcal{L} the integrated luminosity and σ_{bin} the unpolarized cross section, integrated over the relevant bin in η_{lab} . For our estimate we have assumed $\mathcal{P}_e = \mathcal{P}_p = 0.7$, and $\mathcal{L} = 1 \text{ fb}^{-1}$. Such a luminosity could be achieved at eRHIC after only a few weeks of running time so that the actual statistical accuracy might eventually be much better than indicated in Fig. 6.11.

Figure 6.11 shows that at large and positive rapidities the double-spin asymmetries obtained with the two extreme photon scenarios show indeed a pronounced difference irrespective of the gluon distribution in the scattering proton. A maximal saturation of the polarized photon distributions yields larger results for A_{LL}^{π} than a minimal one for any Δg in the proton over the whole η_{lab} -range considered. At the high η_{lab} -end the difference between these scenarios is large enough to favor either of them in a future measurement at

eRHIC with the statistical accuracy estimated above. At negative η_{lab} , where the resolved photoproduction cross section is small, A_{LL}^π is insensitive to the parton content of the photon. In this region the spin asymmetry would be a valuable source of information on the gluon polarization of the proton, as it clearly distinguishes between different gluonic scenarios. We expect, however, that by the time A_{LL}^π will be measured at a new electron-proton collider facility, Δg will be known to a much greater extent than now, for instance, from the measurements discussed in Chaps. 4 and 5, and the parton distributions of the photon can be extracted from future data on photoproduction of single-inclusive pions. Nevertheless, a measurement of Δg in photoproduction reactions would be an excellent opportunity to further test the universality of the parton distributions in a completely different environment than in pp -collisions at RHIC.

6.3.2 Single-Inclusive Pionproduction in Fixed-Target Experiments

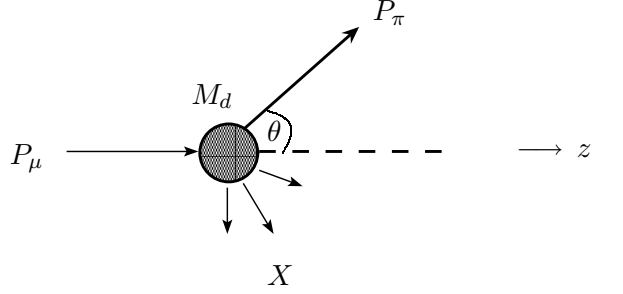
So far, we have considered photoproduction of inclusive pions at an electron-proton collider such as the planned eRHIC facility at BNL. Alternatively, single-inclusive pionproduction can be studied in currently operating fixed-target experiments where a polarized lepton beam scatters off a target at rest. From the experimentalist's point of view such measurements have the advantage that the target can be polarized more easily than, e.g., a proton beam, whose polarization is rather hard to maintain in collider experiments. However, the c.m.s. energies that can be achieved in a fixed-target setup with typical lepton beam energies are much lower than in comparable lepton-proton colliders, therefore giving access to rather small transverse momentum pions only. In this kinematic range, the applicability of pQCD is a priori not guaranteed. To study the capability of fixed-target experiments in more detail we concentrate on the reaction

$$\mu(P_l) + N(P_N) \rightarrow \mu'(P_l') + \pi^0(P_\pi) + X, \quad (6.30)$$

with a polarized muon beam and target N , which can be measured, for instance, by the COMPASS collaboration at CERN [27], on which we focus in the following, as the c.m.s. energies accessible there are higher than at the – otherwise comparable – HERMES experiment at DESY [139].

The COMPASS experiment is currently running with a ^6LiD target which – apart from nuclear corrections – can be viewed as a deuteron sample. The deuteron, d , is defined as the average of its proton and neutron components, $d = (p + n)/2$. Isospin symmetry requires the up-quark content of the proton to be equal to the down-quark distribution of the neutron and vice versa. The strange, charm, and gluon components of proton and neutron are supposed to be identical. Therefore, the parton densities of the deuteron are directly related to those of the proton, and, e.g., Δg can be determined from reactions with deuterons or protons alike. The main goal of the spin program at COMPASS is a determination of Δg from photoproduction of hadron pairs. However, no NLO calculation for polarized dihadron production has been performed so far. In the following we therefore restrict ourselves to single-inclusive hadron production on a fixed target, which can be accessed at COMPASS as well.

Let us first specify the kinematics of the COMPASS experiment: In the target rest frame the deuteron's four momentum takes the form $P_N = P_d = (M_d, 0, 0, 0)$, depending on its mass $M_d = (M_p + M_n)/2$ only. Kinematics becomes particularly simple, if the z -axis is chosen to coincide with the muon beam direction,



The incoming muon's four momentum is then given by $P_\mu = (E_\mu, 0, 0, P_\mu)$, and P_π can be parametrized in terms of its azimuth ϕ and pseudorapidity η , related to the scattering angle θ as usual, $\eta = -\ln \tan(\theta/2)$, yielding $P_\pi = (p_T \cosh \eta, p_T \cos \phi, p_T \sin \phi, p_T \sinh \eta)$. Currently muons with an energy of $E_\mu = 160$ GeV are used, which for fixed-target kinematics corresponds to a c.m.s. energy of approximately $\sqrt{S} \simeq 18$ GeV, where $S = (P_\mu + P_d)^2 = m_\mu^2 + M_d^2 + 2E_\mu M_d$. In the experimental setup only pions with a transverse momentum $p_T > 0.1$ GeV are detected. The photons emerging from the muons are described by a Weizsäcker-Williams spectrum in complete analogy to the equivalent photon spectrum in the electron, Eq. (6.12), with the electron's mass replaced by the muon's and the maximally allowed photon virtuality given by $Q_{max}^2 = 0.5$ GeV². Furthermore the photon momentum fraction y is restricted to lie in the range $0.2 \leq y \leq 0.9$. Note that the muon beam produces a much smaller amount of photons than an electron beam due to the larger lepton mass entering the corresponding Weizsäcker-Williams spectrum (6.12) in this case. With the present setup, events with scattering angles up to $\theta_{max} = 70$ mrad can be detected, corresponding to a minimal rapidity in the laboratory (rest) frame of $\eta_{lab}^{min} \simeq 3.35$. Whereas all measurements are done in the target-rest system, calculations are most easily performed in the c.m.s. frame of the muon-deuteron system. Therefore, the rest-system rapidity η_{lab} has to be transformed to η_{cms} via a Lorentz boost (cf. App. E),

$$\eta_{cms} = \eta_{lab} - \frac{1}{2} \ln \frac{2E_\mu}{M_d}. \quad (6.31)$$

The minimal c.m.s. rapidity is then given by $\eta_{cms}^{min} \simeq 0.44$. In the c.m.s. frame the maximal value of the energy of the produced pion, $E_\pi = p_T \cosh \eta_{cms}$, is given by $E_\pi^{max} = \sqrt{S}/2$. Putting these relations together we obtain

$$\eta_{cms}^{max} = \cosh^{-1} \frac{\sqrt{S}}{2p_T}. \quad (6.32)$$

Having specified the kinematics relevant for COMPASS we are now in a position to calculate pion production cross sections with the same “master formula”, Eq. (6.9), we have

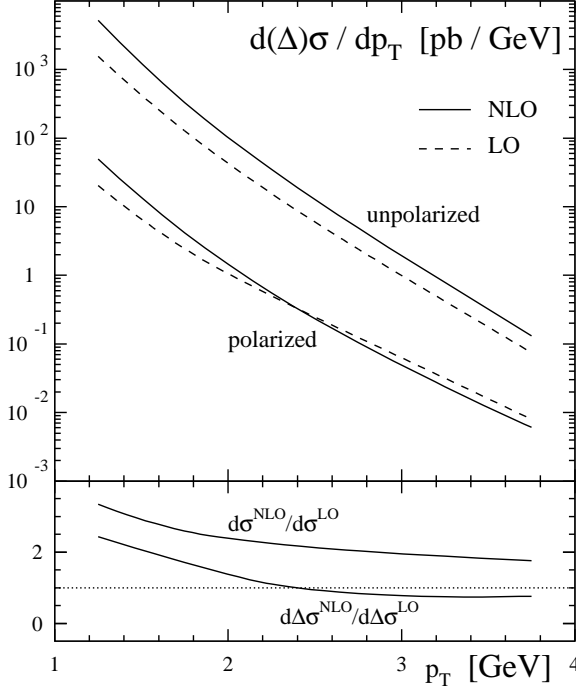


Figure 6.12: Unpolarized and polarized differential cross sections at LO (dashed) and NLO (solid) for the reaction $\mu d \rightarrow \mu' \pi^0 X$ at $\sqrt{S} = 18$ GeV. The lower panel shows the ratios of NLO and LO contributions.

applied before to the computation of single-inclusive pion observables in ep -collisions. Again, we adopt the CTEQ5 [74] and GRVS [17] parton distributions for unpolarized and polarized nucleons, respectively, and the fragmentation functions of Ref. [82]. We will present our results as functions of p_T , integrated over the accessible rapidity range,

$$\eta_{cms}^{min} = 0.44 \leq \eta_{cms} \leq \cosh^{-1} \left[\frac{\sqrt{S}}{2p_T} \right] = \eta_{cms}^{max}. \quad (6.33)$$

Figure 6.12 displays the differential cross sections $d(\Delta)\sigma/dp_T$ for single-inclusive pion production on a deuteron target at LO and NLO in the p_T -range accessible for the COMPASS experiment. Due to the small c.m.s. energy available, p_T is restricted to values less than 9 GeV. However, at $p_T \gtrsim 4$ GeV the production rate is already so low that we have refrained from plotting the corresponding cross sections in this region. Although data are taken down to $p_T \simeq 0.1$ GeV, we do not extend our analysis to $p_T \lesssim 1$ GeV, since a fixed order perturbative calculation is not supposed to yield reliable predictions in the absence of the hard scale. The figure shows clearly – similar to the case of pion photoproduction

at a collider facility – the importance of NLO corrections to the unpolarized cross section which are sizeable over the whole p_T -range considered, in contrast to the polarized NLO contributions which are much less pronounced. This finding is emphasized by the respective K -factors, Eq. (4.22), being well above unity, in particular for the unpolarized cross sections. At $p_T \lesssim 1.5$ GeV both, polarized and unpolarized K -factors, are large, reflecting the breakdown of the perturbative expansion at low p_T . As further indicator for the importance of the NLO corrections we have studied the dependence of the cross sections on the unphysical scales μ_r , μ_f , and μ'_f in Figs. 6.13. Whereas the scale dependence of the polarized cross section improves beyond the leading order with increasing values of p_T , the unpolarized cross section remains strongly scale dependent even at NLO, which illustrates the delicacy of a perturbative calculation in the low-energy range associated with fixed-target experiments.

In order to estimate the sensitivity of the polarized hadronic cross sections to the spin-dependent parton distributions of the proton, in particular Δg , and the resolved photon, it is necessary to analyze the weight of the various subprocesses contributing to pion production at COMPASS kinematics. It turns out that in this energy domain large values of x_l are probed where at first sight the direct part of the cross section is expected to dominate over the resolved one. However, displaying the ratios of direct and resolved contributions to the total polarized cross section in Fig. 6.14 gives a different picture. The sum of all resolved contributions, $d\Delta\sigma_{res}$, even exceeds the direct components, $d\Delta\sigma_{dir}$, in magnitude. Only towards larger p_T -values the direct part gains in size. This behavior can be understood by a closer look onto the relative weights of the individual subprocesses, shown in Fig. 6.15. Indeed, the cross sections for the direct channels, γg and γq , are much larger in magnitude than any of the resolved subprocesses, gg , qg , gq , and qq , but they differ in sign, which causes drastic cancelations between the direct contributions. Thus the channel where the photon resolves into a quark and subsequently scatters off a gluon out of the deuteron becomes effectively dominant at low p_T . This is due to the large value of $\Delta q^\gamma(x, \mu)$ at large x , where $\Delta g^\gamma(x, \mu)$ is quite small and, therefore, subprocesses with a gluon emerging from the photon are suppressed. It has to be stressed, however, that at large x , the quark polarization Δq^γ is governed by its pointlike part Δq_{pl}^γ , which is not sensitive to the hadronic structure of the photon, but purely perturbative, cf. Fig. 6.1.

Having studied the decomposition of the full polarized cross section we are now in a position to analyze the double-spin asymmetry $A_{LL}^{\pi,d}$ encountered in $\mu d \rightarrow \mu' \pi^0 X$, which we have depicted for different sets of parton distributions for the deuteron in Fig. 6.16 together with the estimated statistical error

$$\delta A_{LL}^{\pi,d} \simeq \frac{1}{\mathcal{P}_b \mathcal{P}_N \sqrt{\sigma_{bin} \mathcal{L}}}, \quad (6.34)$$

where σ_{bin} denotes the unpolarized cross section integrated over the p_T -bin considered. We have assumed a beam polarization of $\mathcal{P}_b = 76\%$, and a target polarization of $\mathcal{P}_N = 50\%$ with an integrated luminosity of 1 fb^{-1} . All scales are set equal, $\mu_r = \mu_f = \mu'_f = p_T$. Due to the significance of NLO corrections to the unpolarized cross section the LO result differs substantially from the NLO predictions. We will therefore refrain from discussing the spin asymmetry at Born level any further. To test the sensitivity of $A_{LL}^{\pi,d}$ to the

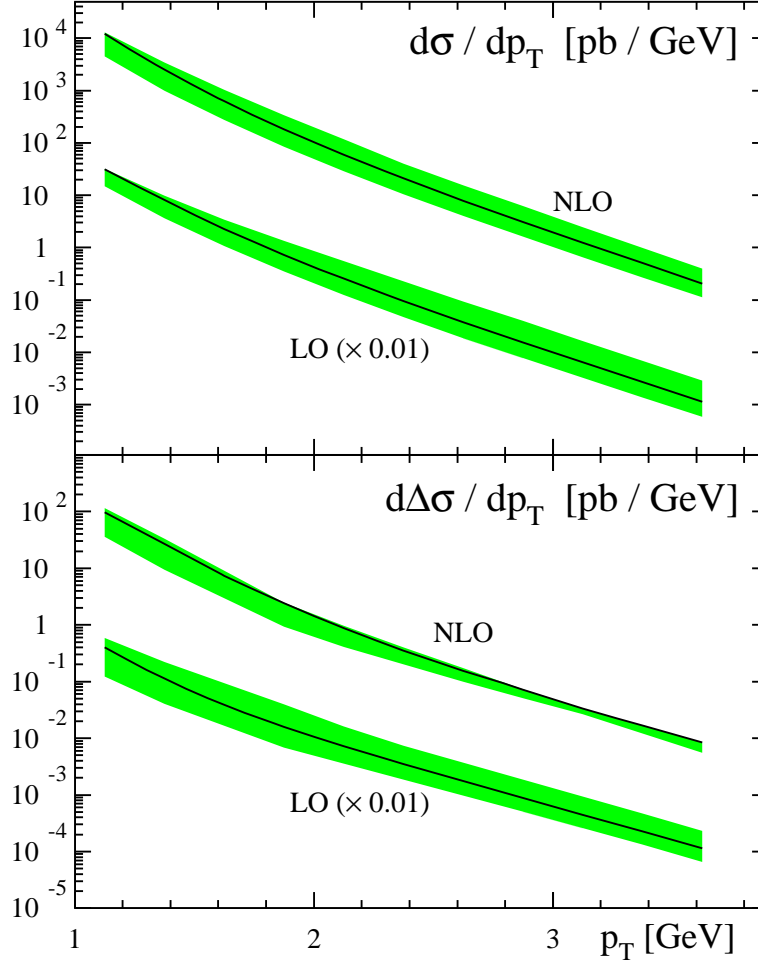


Figure 6.13: Scale dependence of the LO and NLO unpolarized (upper panel) and polarized (lower panel) cross sections for $\mu d \rightarrow \mu' \pi^0 X$ at COMPASS kinematics. All scales are varied in the range $p_T/2 \leq \mu_r = \mu_f = \mu'_f \leq 2p_T$. Solid lines correspond to the choice where all scales are set to p_T . The LO results have been rescaled by a factor 0.1 for a better legibility.

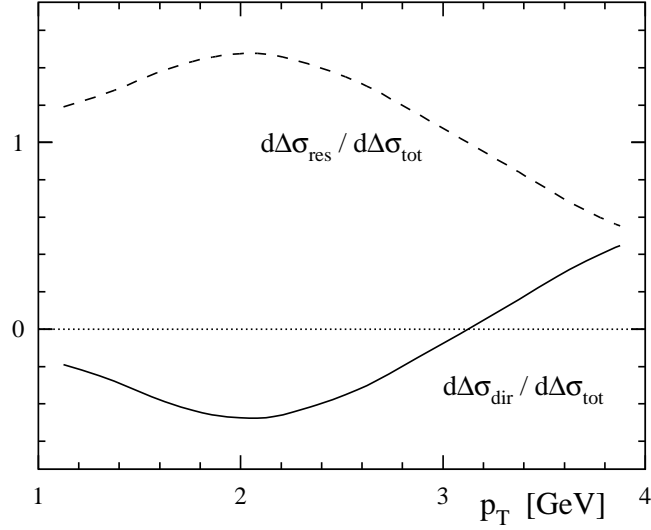


Figure 6.14: Relative contributions of the direct and resolved cross sections at NLO to polarized photoproduction of inclusive pions at COMPASS kinematics obtained with the GRSV standard set for the parton distributions of the deuteron and the maximal scenario for the polarized photon densities.

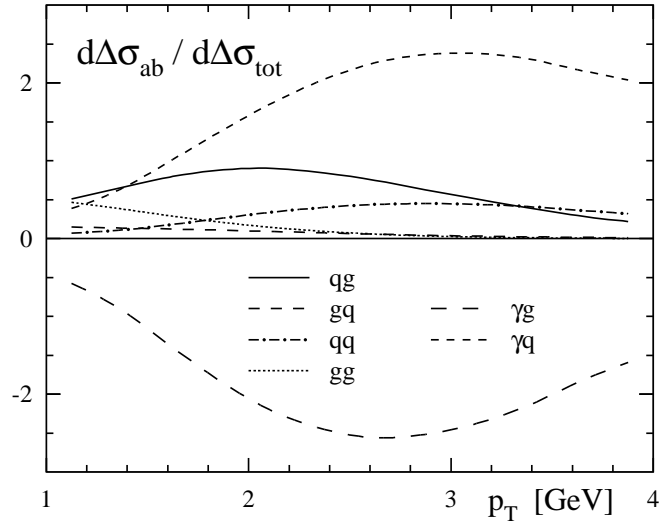


Figure 6.15: Relative contributions of different partonic channels $ab \rightarrow cX$, summed over all final states c , to the full polarized cross section at COMPASS.

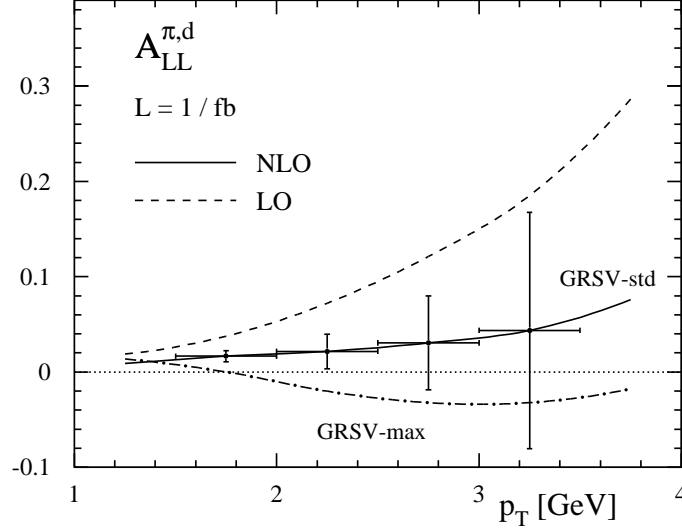


Figure 6.16: Double-spin asymmetry for $\mu d \rightarrow \mu' \pi^0 X$ at fixed-target kinematics with $\sqrt{S} = 18$ GeV. The dashed line shows the LO result, whereas the NLO predictions are represented by a solid (GRSV-std) and a dash-dotted (GRSV-max) curve. The error bars indicate the estimated statistical uncertainty for the COMPASS experiment at an integrated luminosity of 1 fb^{-1} .

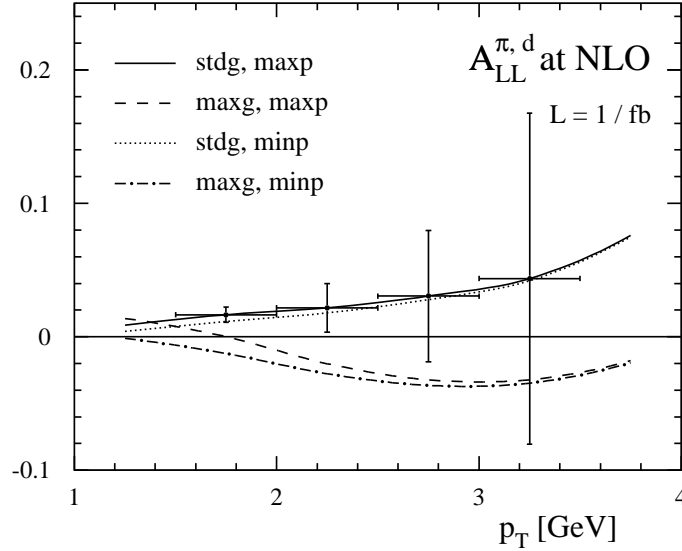


Figure 6.17: Double-spin asymmetry for pion photoproduction at COMPASS. The curves show our results for two choices of the parton distributions of the deuteron (GRSV-stdg and GRSV-maxg), and minimal or maximal saturation of the polarized photon densities, respectively. The error bars indicate the estimated statistical uncertainty for COMPASS at an integrated luminosity of 1 fb^{-1} .

gluon polarization of the deuteron target we have calculated it using the standard and the maximal gluon scenarios of the GRSV parton distributions. Over the whole p_T -range considered the asymmetry obtained with the standard set exceeds the corresponding curve with the maximal gluonic input. This behavior can be traced back to the large magnitude of the only subprocess which yields negative contributions to the polarized cross section, γg . Increasing Δg necessarily enhances the absolute value of $d\Delta\sigma_{\gamma g}$, and therefore causes a decrease of $A_{LL}^{\pi,d}$. This feature is not overshadowed by the uncertainty on the structure of the resolved photon, as illustrated by Fig. 6.17. The difference between curves obtained with the GRSV standard or maximal gluon sets for the polarized proton is much more pronounced than the slight variation of the results associated with the change of the photon densities from minimal to maximal saturation at the input scale. This effect is due to the dominance of the pointlike parts of the quark distributions at the large x_l probed at COMPASS kinematics, whereas the hadronic components of the photon densities are strongly suppressed as $x_l \rightarrow 1$.

Measuring $A_{LL}^{\pi,d}$ at COMPASS is thus suitable for gaining knowledge on Δg , but does not give access to the non-perturbative structure of the resolved photon, in contrast to the eRHIC collider facility discussed above, which probes the spin-dependent gluon density of the proton as well as the parton distributions of the photon in different rapidity ranges. We furthermore note that due to the small value of the cross section the statistical error of the COMPASS experiment becomes so large at $p_T \gtrsim 3$ GeV that the two gluon scenarios cannot be distinguished any longer. In this respect, collider measurements are certainly advantageous since they achieve a by far higher statistical accuracy than fixed-target experiments with comparable polarizations and luminosities in the p_T -range where perturbative calculations are supposed to yield reliable predictions. For COMPASS kinematics the scale dependence of the unpolarized cross section casts serious doubts on the applicability of pQCD at small p_T and low \sqrt{S} . It is thus mandatory to analyze not only spin asymmetries, but first check whether the perturbative calculation can, at least, reproduce the unpolarized cross sections encountered in experiment within the theoretical uncertainties, similar as it has been done in the case of single-inclusive pion production at RHIC, cf. Fig. 4.4.

To somewhat improve on the poor statistics of the fixed-target experiment, a higher production rate at large p_T could be achieved by increasing the angular acceptance covered by the COMPASS detector. The planned upgrade from $\theta_{max} = 70$ mrad to $\theta_{max} = 180$ mrad would cause a rise in the unpolarized and polarized pion photoproduction cross sections by approximately half an order of magnitude over the whole p_T -range accessible, as shown in Fig. 6.18. This improvement leaves the associated K -factors almost unaffected, but reduces the statistical errors $\delta A_{LL}^{\pi,d}$ in the double-spin asymmetry. However, as illustrated by Fig. 6.19, simultaneously with the decrease of the statistical uncertainty the sensitivity to the gluon polarization in the deuteron becomes less pronounced. Improving statistics by enlarging the acceptance of the COMPASS detector thus will not necessarily simplify the analysis of $A_{LL}^{\pi,d}$ in terms of Δg .

Qualitatively similar cross sections are obtained, if the deuteron target of the COMPASS experiment is replaced by a proton target. It is interesting to note that the in-

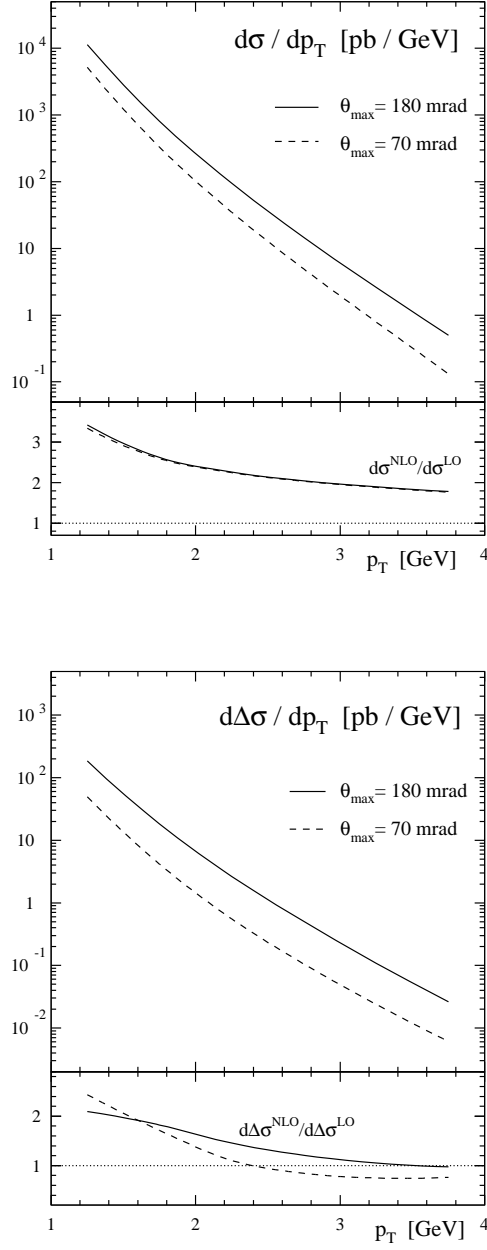


Figure 6.18: Unpolarized (upper plot) and polarized (lower plot) differential cross sections at NLO for the reaction $\mu d \rightarrow \mu' \pi^0 X$ at $\sqrt{S} = 18$ GeV, counting events at angles smaller than $\theta_{\max} = 180$ mrad (solid) and $\theta_{\max} = 70$ mrad (dashed). Also shown are the ratios of NLO and LO contributions.

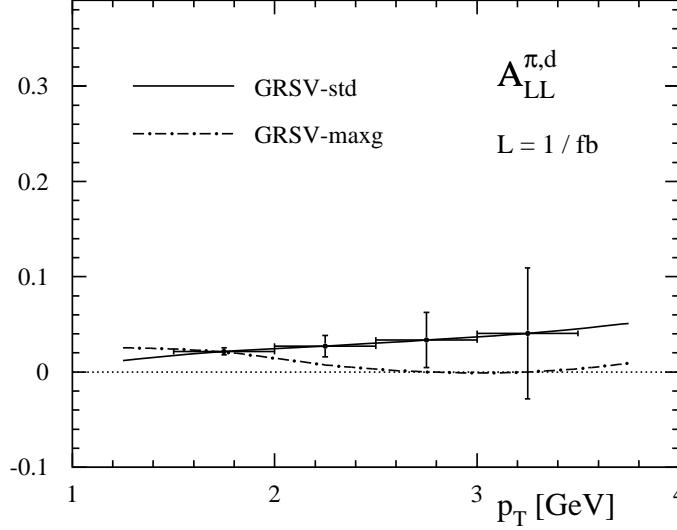


Figure 6.19: Double-spin asymmetry for pion photoproduction at COMPASS kinematics with $\theta_{max} = 180$ mrad. The two curves show predictions obtained with the GRSV standard and maximal gluon scenarios for the spin-dependent parton distributions of the deuteron, respectively, assuming maximal saturation of the polarized photon densities. The error bars indicate the estimated statistical uncertainty for COMPASS at an integrated luminosity of 1 fb^{-1} .

dividual direct and resolved subprocesses gain now different weights due to the replacement of the deuteron's parton distributions with the ones of the proton, as depicted in Figs. 6.20 and 6.21. However, the sum of all contributions is barely affected by this modification and the spin asymmetries $A_{LL}^{\pi,p}$ associated with photoproduction on a proton target, which we depict in Figs. 6.22, 6.23 for completeness, are very reminiscent of the corresponding $A_{LL}^{\pi,d}$ discussed above.

6.4 Summary and Conclusions

In this chapter we have studied single-inclusive pion photoproduction at lepton-hadron colliders and in fixed-target experiments beyond the leading order. These processes are of particular interest, since they give access to the so far completely unknown parton densities of the circularly polarized photon and, above that, can serve to deepen our understanding of the spin structure of the nucleon.

We have given a short overview on the present knowledge of the hadronic structure of the photon, which is to be contrasted to the elementary gauge boson of the electromagnetic interaction. Next we have shown how to extend the NLO calculation for inclusive pion

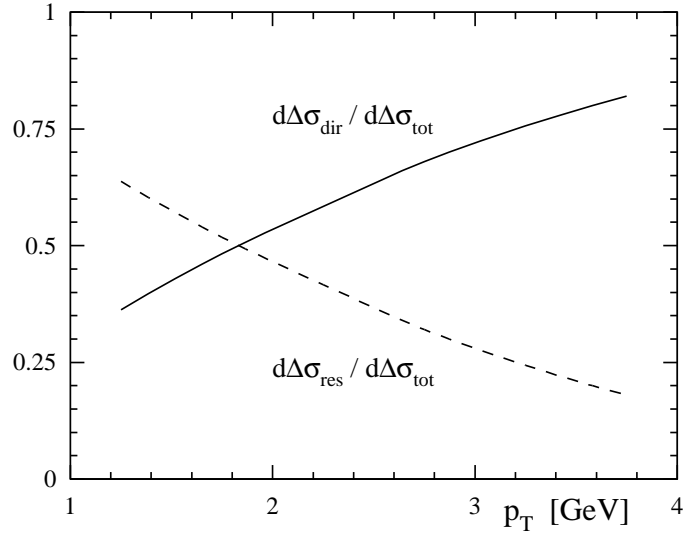


Figure 6.20: As in Fig. 6.14, but now for a proton target.

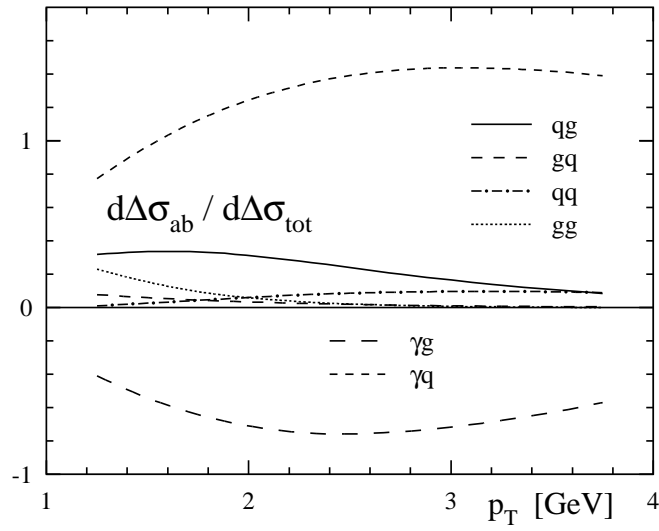


Figure 6.21: As in Fig. 6.15, but now for $\mu p \rightarrow \mu' \pi^0 X$.

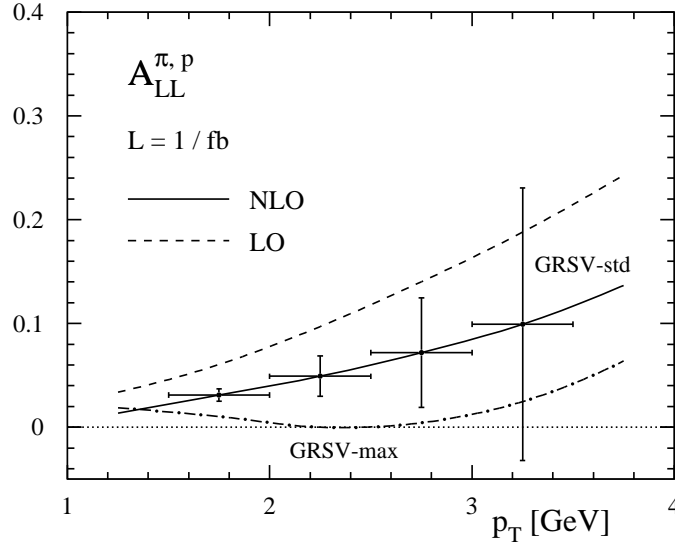


Figure 6.22: As in Fig. 6.16, but now for $\mu p \rightarrow \mu' \pi^0 X$.

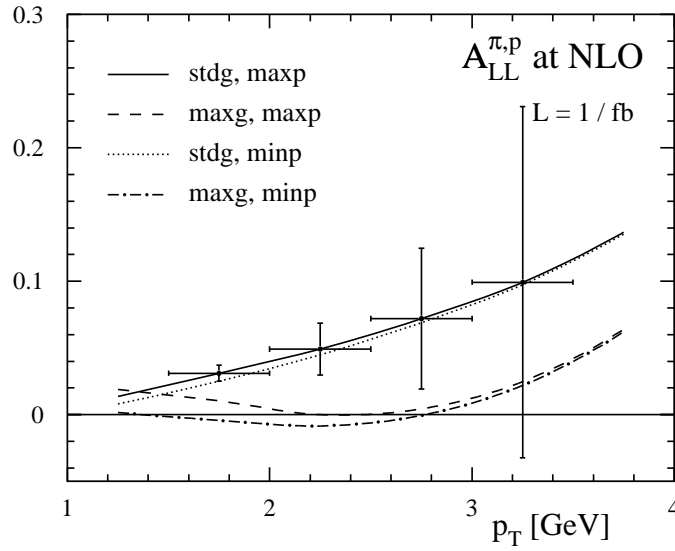


Figure 6.23: As in Fig. 6.17, but now for a proton target.

production cross sections of Chap. 4 to reactions including resolved photons. In passing, we demonstrated how results in different factorization schemes are related to each other, thereby ensuring the independence of physical observables on theoretical conventions. In a numerical analysis we studied the relevance of NLO corrections and their dependence on unphysical scales. It turned out that double-spin asymmetries for single-inclusive photoproduction in ep -collisions, e.g., at a future facility such as eRHIC, are indeed sensitive to the parton content of the photon, and provide therefore an excellent tool for a first determination of the parton distributions of circularly polarized photons. In addition, such measurements can deepen our knowledge on Δg and establish the universality of the polarized parton distributions of the nucleon.

Before the advent of a high-energy polarized ep -collider we are restricted to data from fixed-target experiments, however. We have therefore also studied pion photoproduction at the COMPASS experiment, which yields data in the lowest p_T -range accessible with perturbative methods. In contrast to a collider experiment, at COMPASS the double-spin asymmetry is probed in a domain where it is completely insensitive to the non-perturbative structure of the photon, but rather capable to yield information on the gluon polarization of the nucleon. A determination of Δg is the main goal of COMPASS. With the statistics available at present, it is difficult, however, to distinguish between different gluon scenarios in the target hadron towards higher p_T , where pQCD can safely be applied.

We therefore conclude that a polarized lepton-proton collider is essential for gaining insight into the hadronic spin structure of the photon. Combined with additional data from other photoproduction processes such as jet or heavy flavor production, information from single-inclusive pion production experiments at an ep -collider facility could serve as important input for a global QCD analysis to ultimately constrain the spin-dependent parton distributions of the photon.

Chapter 7

Summary and Conclusions

The ultimate goal of this work was to provide a reliable theoretical framework in the context of pQCD for gaining a better understanding of hadronic spin-structure from polarized scattering experiments. We performed a detailed NLO QCD study of single-inclusive hadron and jet production processes. Both turned out to be particularly sensitive to the so far only insufficiently known gluon polarization in the nucleon. In addition, we explored the possibility of accessing the completely unknown spin-dependent parton distributions of the circularly polarized photon in present and future experiments from photoproduction reactions.

We started with a general introduction to the methods of pQCD and showed explicitly how to calculate partonic cross sections beyond the leading order in a fully analytical approach. These results were then implemented in a phenomenological analysis of experimentally relevant processes. The predictions we obtained for single-inclusive pion production in *unpolarized* high-energy pp -collisions turned out to be in complete agreement with recent data from the PHENIX and STAR collaborations at RHIC down to unexpectedly small values of transverse momentum. Such a comparison is vital for two reasons: Firstly, it demonstrates the applicability of the theoretical framework used and, secondly, it boosts confidence in similar measurements in longitudinally *polarized* collisions. Of special interest is the longitudinal double spin asymmetry associated with pion production due to its sensitivity to the gluon polarization in the nucleon, as shown in Chap. 4. We also found that at low-to-moderate p_T sizeable negative spin asymmetries can hardly be obtained within the standard framework of a leading power perturbative calculation. This result is of particular relevance in the context of first experimental indications for a negative spin asymmetry in that p_T -range. If preliminary data should indeed be confirmed by future measurements, it would open up quite unexpected windows on the structure of the nucleon.

Next we turned to single-inclusive jet production at high transverse momenta in longitudinally polarized hadronic collisions. As expected, we found that this reaction is a very clean tool for accessing the gluon polarization in the nucleon, since it is free of final-state hadronization effects. Like in the case of hadron production, including the NLO corrections to the polarized and unpolarized cross sections leads to a sizeable reduction of their

dependence on unphysical scales, thereby strongly reducing theoretical uncertainties. This is mandatory for a reliable and meaningful extraction of information about the spin structure of the nucleon from experiment. In addition, we checked that the analytical results we obtained in the small cone approximation do not receive large corrections from finite cone size effects and are roughly equivalent to the outcome of a previous Monte-Carlo calculation. The spin asymmetries turned out to be sensitive to Δg even for rather moderate integrated luminosities and beam polarizations. Hence they are particularly suitable for a first determination of the gluon polarization with the STAR experiment at RHIC.

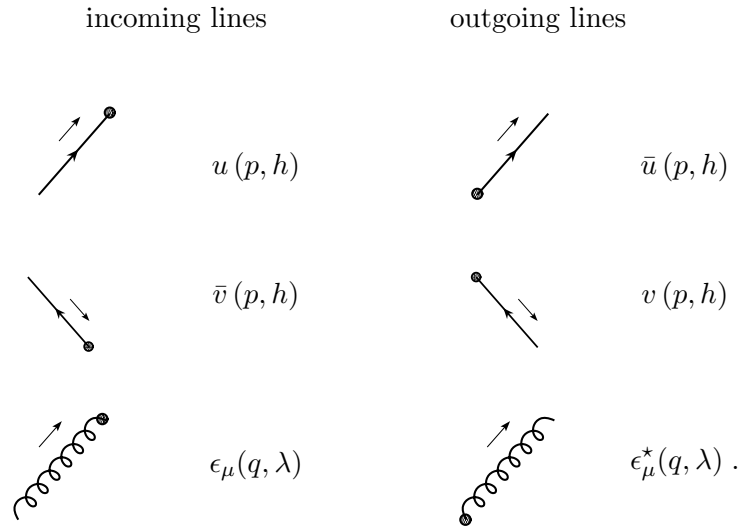
The remaining part of this work was devoted to photoproduction of inclusive pions in spin-dependent lepton-proton collisions beyond the LO of QCD. Our results show that photoproduction reactions at a future polarized collider, such as the planned eRHIC facility at BNL, would be very useful for constraining the spin-dependent parton distributions of the circularly polarized photon for the first time. Above that, the corresponding double-spin asymmetry at eRHIC kinematics is sensitive to the gluon polarization in the nucleon as well. It could therefore yield additional information on the spin structure of the proton. For pion photoproduction in a fixed-target experiment like COMPASS at CERN we encountered a completely different behavior of the corresponding observables due to the rather low energies available there. The large theoretical uncertainties in the limited p_T -range accessible demonstrate that the outcome of a pQCD analysis of photoproduction data from a fixed-target experiment has to be taken with a grain of salt. Nonetheless, the double-spin asymmetries measured in such a reaction are sensitive to the gluon polarization of the nucleon, and could therefore also help to improve our knowledge of Δg .

We conclude by stressing that a careful analysis of spin-dependent processes in the kinematic domain accessible with perturbative methods opens up unequaled possibilities for a thorough understanding of hadronic structure. Soon our results will be challenged by first data from the RHIC experiment. They will indicate whether a fixed-order perturbative calculation is indeed capable of a reliable description of spin-dependent observables in QCD, or if aspects of hadronic structure little explored so far are more important than expected. With the advent of precision data in the near future there is certainly an exciting time ahead of us, providing new insight into the spin-structure of hadrons and thereby extending our understanding of the microscopic world.

Appendix A

Feynman Rules

In the following we list the Feynman rules of QCD necessary for the computation of any physical amplitude $i\mathcal{M}$. Quarks, gluons, and ghosts are represented by solid, curly, and dashed lines, respectively. The small arrows next to the lines indicate the direction of momentum flow. Lorentz indices are denoted by Greek letters $(\mu, \nu, \rho, \sigma, \dots)$, whereas color indices are indicated by a, b, c, d for gluons and ghosts, and i, j for quarks. Flavor and spinor indices for quarks are implicitly understood and not shown. For external quark, antiquark, and gluon legs we have



Here $u(p, h)$ and $v(p, h)$ denote the spinor of a quark or antiquark, respectively, with momentum p and helicity h . $\epsilon_\mu(q, \lambda)$ is the polarization vector of a gluon with momentum q and helicity λ .

Quark, gluon, and ghost propagators are given by

$$i \xrightarrow{k} j \quad i \delta_{ij} \frac{(\not{k} + m)}{k^2 - m^2 + i\epsilon}$$

$$\begin{array}{c} a \\ \mu \end{array} \xrightarrow[k]{\quad} \begin{array}{c} b \\ \nu \end{array} \quad \frac{-i \delta_{ab}}{k^2 + i\epsilon} \left[g_{\mu\nu} - (1 - \eta) \frac{k_\mu k_\nu}{k^2} \right]$$

$$a \xrightarrow[k]{\quad} b \quad \frac{-i \delta_{ab}}{k^2 + i\epsilon},$$

where k is the momentum of the respective particles and \not{k} is short for $k_\mu \gamma^\mu$. The $i\epsilon$ in the denominators of the propagators can be neglected in all our calculations. The parameter η in the gluon propagator depends on the gauge. Our actual calculations are performed in Feynman gauge where $\eta = 1$. Final results, however, are independent of η .

Quark-gluon, three-gluon, ghost-gluon, and four-gluon vertex read as follows:

$$\begin{array}{c} i \\ \nearrow \\ a \\ \mu \end{array} \quad \begin{array}{c} \searrow \\ j \end{array} \quad -ig_s \gamma_\mu T_{ij}^a$$

$$\begin{array}{c} c \\ \nearrow \\ a \\ \rho \end{array} \quad \begin{array}{c} p \\ \leftarrow \\ q \end{array} \quad \begin{array}{c} \searrow \\ r \\ b \\ \mu \end{array} \quad -g_s f^{abc} [(p-q)_\nu g_{\rho\mu} + (q-r)_\rho g_{\mu\nu} + (r-p)_\mu g_{\nu\rho}]$$

$$\begin{array}{c} p \\ \nearrow \\ b \\ \mu \end{array} \quad \begin{array}{c} \searrow \\ a \\ c \end{array} \quad g_s f^{abc} p_\mu \text{ (} p_\mu \text{ outgoing)}$$

$$\begin{array}{c} \rho \\ a \end{array} \quad \begin{array}{c} \sigma \\ d \end{array} \quad \begin{array}{c} \mu \\ b \end{array} \quad \begin{array}{c} \nu \\ c \end{array} \quad \begin{aligned} &-ig_s^2 f^{abe} f^{cde} (g_{\rho\nu} g_{\mu\sigma} - g_{\rho\sigma} g_{\mu\nu}) \\ &-ig_s^2 f^{ace} f^{bde} (g_{\rho\mu} g_{\nu\sigma} - g_{\rho\sigma} g_{\mu\nu}) \\ &-ig_s^2 f^{ade} f^{cbe} (g_{\rho\nu} g_{\mu\sigma} - g_{\rho\mu} g_{\sigma\nu}) \end{aligned}$$

Four-momentum conservation is fulfilled on each vertex.

For processes involving a photon, its propagator and the fermion-photon vertex are needed:



The image shows two Feynman diagrams. The top diagram is a photon propagator, represented by a horizontal wavy line with an arrow pointing to the right, labeled with momentum k above it. The ends of the wavy line are labeled μ on the left and ν on the right. The bottom diagram is a fermion-photon vertex, represented by a wavy line (photon) on the left meeting a vertex from which two straight lines (fermions) emerge at an angle. The wavy line is labeled μ on the left. To the right of each diagram is its corresponding mathematical expression.

$$\frac{-i g_{\mu\nu}}{k^2 + i\epsilon}$$

$$-ig_e \gamma_\mu$$

The coupling of a fermion to a photon is proportional to g_e rather than g_s , where g_e is the electric charge of the respective fermion. External photon legs acquire a polarization vector $\epsilon_\mu(p, \lambda)$ like external gluons.

In addition to the rules given above one has to

- integrate over the loop momentum k in n dimensions for each closed loop with a measure

$$\int \frac{d^n k}{(2\pi)^n},$$

- multiply with a factor of (-1) for each closed quark or ghost loop,
- include a symmetry factor which takes care of possible permutations of fields in a diagram, if necessary.

It is common to rewrite g_s in terms of the strong coupling constant α_s via $\alpha_s = g_s^2/4\pi$. The electric coupling can be expressed accordingly in terms of $\alpha_{em} = g_e^2/4\pi$.

Using these prescriptions one can immediately write down $i\mathcal{M}$ for processes involving quarks, gluons, ghosts, and photons. For the computation of cross sections, however, $\mathcal{M}\mathcal{M}^*$ is required. In such products projection operators for (anti)quarks and massless bosons of definite helicities will show up which are given by:

$$u(p, h) \bar{u}(p, h) = \frac{1}{2}(\not{p} + m) [1 - \gamma_5 h], \quad (\text{A.1})$$

$$v(p, h) \bar{v}(p, h) = \frac{1}{2}(\not{p} - m) [1 + \gamma_5 h], \quad (\text{A.2})$$

$$\epsilon^\mu(q, \lambda) \epsilon^{\nu*}(q, \lambda) = \frac{1}{2} \left[-g^{\mu\nu} + \frac{q^\mu r^\nu + q^\nu r^\mu}{q \cdot r} + i\lambda \epsilon^{\mu\nu\sigma\kappa} \frac{q_\sigma r_\kappa}{q \cdot r} \right], \quad (\text{A.3})$$

where r is an arbitrary momentum fulfilling $r^2 = 0$ and $q \cdot r \neq 0$.

Appendix B

Leading Order $2 \rightarrow 2$ Scattering Cross Sections in n dimensions

Here, we list the n -dimensional unpolarized and polarized LO cross sections for the $2 \rightarrow 2$ scattering reactions $\gamma + b \rightarrow c + d$ and $a + b \rightarrow c + d$ with $a, b, c, d = q, \bar{q}, g$, as obtained in the HVBM regularization scheme. Writing

$$\begin{aligned}\tilde{\mathcal{N}} &= \alpha_s \alpha_e \mu_d^{4\varepsilon} \frac{\pi}{s} \frac{1}{\Gamma(1-\varepsilon)} \left[\frac{4\pi}{sv(1-v)} \right]^\varepsilon, \\ \mathcal{N} &= \alpha_s^2 \mu_d^{4\varepsilon} \frac{\pi}{s} \frac{1}{\Gamma(1-\varepsilon)} \left[\frac{4\pi}{sv(1-v)} \right]^\varepsilon,\end{aligned}\tag{B.1}$$

where v is given in Eq. (4.4), $\varepsilon = (4-n)/2$, and μ_d denotes the mass scale introduced by dimensional regularization according to Eq. (2.16), the unpolarized scattering cross sections take the form

$$\begin{aligned}\frac{d\hat{\sigma}_{\gamma q \rightarrow gq}}{dv} &= -\tilde{\mathcal{N}} e_q^2 \frac{2C_F}{v} \left[-1 + \varepsilon - 2\varepsilon v - v^2 + \varepsilon v^2 \right], \\ \frac{d\hat{\sigma}_{\gamma g \rightarrow q\bar{q}}}{dv} &= -\tilde{\mathcal{N}} e_q^2 \frac{1}{(1-\varepsilon)} \frac{2(-1 + \varepsilon + 2v - 2v^2)}{v(1-v)},\end{aligned}$$

$$\begin{aligned}
\frac{d\hat{\sigma}_{qq' \rightarrow qq'}}{dv} &= \mathcal{N} \frac{C_F}{C_A} \left[\frac{1+v^2}{(1-v)^2} - \varepsilon \right], \\
\frac{d\hat{\sigma}_{q\bar{q} \rightarrow q' \bar{q}'}}{dv} &= \mathcal{N} \frac{C_F}{C_A} \left[(1-v)^2 + v^2 - \varepsilon \right], \\
\frac{d\hat{\sigma}_{q\bar{q} \rightarrow q\bar{q}}}{dv} &= \mathcal{N} \frac{C_F}{C_A} \left\{ \frac{1+v^2}{(1-v)^2} - \varepsilon + v^2 + (1-v)^2 - \varepsilon - \frac{2}{C_A} (1-\varepsilon) \left[-\frac{v^2}{(1-v)} + \varepsilon \right] \right\}, \\
\frac{d\hat{\sigma}_{qq \rightarrow qq}}{dv} &= \mathcal{N} \frac{C_F}{C_A} \left\{ \frac{1+v^2}{(1-v)^2} - \varepsilon + \frac{1+(1-v)^2}{v^2} - \varepsilon - \frac{2}{C_A} (1-\varepsilon) \left[\frac{1}{v(1-v)} + \varepsilon \right] \right\}, \\
\frac{d\hat{\sigma}_{q\bar{q} \rightarrow gg}}{dv} &= \mathcal{N} \frac{2C_F}{C_A} (1-\varepsilon) \left[\frac{C_F}{v(1-v)} - C_A \right] \left\{ (1-\varepsilon) [v^2 + (1-v)^2] - 2\varepsilon v(1-v) \right\}, \\
\frac{d\hat{\sigma}_{gg \rightarrow q\bar{q}}}{dv} &= \mathcal{N} \frac{1}{2C_F C_A (1-\varepsilon)} \left[\frac{C_F}{v(1-v)} - C_A \right] \left\{ [(1-v)^2 + v^2] (1-\varepsilon) - 2\varepsilon v(1-v) \right\}, \\
\frac{d\hat{\sigma}_{gg \rightarrow qq}}{dv} &= \mathcal{N} \frac{1}{C_A} \left[\frac{C_A}{(1-v)^2} + \frac{C_F}{v} \right] \left\{ (1+v^2)(1-\varepsilon) + 2\varepsilon v \right\}, \\
\frac{d\hat{\sigma}_{gg \rightarrow gg}}{dv} &= \mathcal{N} \frac{2C_A}{C_F} \frac{1}{v^2 (1-v)^2} \left[(1-v)^2 + v(1-v) + v^2 \right]^3.
\end{aligned} \tag{B.2}$$

Similarly, for the scattering of two polarized particles in the initial state we obtain:

$$\begin{aligned}
\frac{d\Delta\hat{\sigma}_{\gamma q \rightarrow gq}}{dv} &= -\tilde{\mathcal{N}} e_q^2 2C_F \frac{(1-v)}{v} \left[-1 - \varepsilon - v + \varepsilon v \right], \\
\frac{d\Delta\hat{\sigma}_{\gamma g \rightarrow q\bar{q}}}{dv} &= -\tilde{\mathcal{N}} e_q^2 \frac{2(1-2v+2v^2)}{v(1-v)},
\end{aligned}$$

$$\begin{aligned}
\frac{d\Delta\hat{\sigma}_{qq' \rightarrow qq'}}{dv} &= \mathcal{N} \frac{C_F}{C_A} \frac{1-v^2}{(1-v)^2}, \\
\frac{d\Delta\hat{\sigma}_{q\bar{q} \rightarrow q'\bar{q}'}}{dv} &= -\mathcal{N} \frac{C_F}{C_A} \left[\varepsilon + (1-v)^2 + v^2 \right], \\
\frac{d\Delta\hat{\sigma}_{q\bar{q} \rightarrow q\bar{q}}}{dv} &= \mathcal{N} \frac{C_F}{C_A} \left\{ \frac{1-v^2}{(1-v)^2} - \varepsilon - v^2 - (1-v)^2 \right. \\
&\quad \left. + \frac{2}{C_A} \left[-(1+\varepsilon) \frac{v^2}{(1-v)} - \varepsilon (2v-1-\varepsilon) \right] \right\}, \\
\frac{d\Delta\hat{\sigma}_{qq \rightarrow qq}}{dv} &= \mathcal{N} \frac{C_F}{C_A} \left\{ \frac{1-v^2}{(1-v)^2} + \frac{1-(1-v)^2}{v^2} - \frac{2}{C_A} \left[\frac{(1+\varepsilon)}{v(1-v)} - \varepsilon(3+\varepsilon) \right] \right\}, \\
\frac{d\Delta\hat{\sigma}_{q\bar{q} \rightarrow gg}}{dv} &= -\mathcal{N} \frac{2C_F}{C_A} \left[\frac{C_F}{v(1-v)} - C_A \right] \left\{ (1+\varepsilon)^2 [v^2 + (1-v)^2] + (6\varepsilon + 2\varepsilon^2) v(1-v) \right\}, \\
\frac{d\Delta\hat{\sigma}_{gg \rightarrow q\bar{q}}}{dv} &= -\mathcal{N} \frac{1}{2C_A C_F} \left[\frac{C_F}{v(1-v)} - C_A \right] \left[(1-v)^2 + v^2 \right], \\
\frac{d\Delta\hat{\sigma}_{gg \rightarrow qq}}{dv} &= \mathcal{N} \frac{1}{C_A} \left[\frac{C_A}{(1-v)^2} + \frac{C_F}{v} \right] \left[1 - v^2 + \varepsilon(1-v)^2 \right], \\
\frac{d\Delta\hat{\sigma}_{gg \rightarrow gg}}{dv} &= \mathcal{N} \frac{2C_A}{C_F} \frac{1}{v(1-v)} \left[(1-v)^2 + v(1-v) + v^2 \right] \\
&\quad \times \left[2(1-v)^2 + (3+\varepsilon) v(1-v) + 2v^2 \right].
\end{aligned}
\tag{B.3}$$

Appendix C

Passarino-Veltman Decomposition

Here, we discuss the reduction of a general loop structure into a set of scalar integrals, needed for the evaluation of box diagrams, as outlined in Chap. 2. Tensor integrals of the form

$$B^{\{0,\mu,\mu\nu\}}(q_1) \equiv \int \frac{d^n q}{(2\pi)^n} \frac{\{1, q^\mu, q^\mu q^\nu\}}{L_1 L_2}, \quad (\text{C.1})$$

$$C^{\{0,\mu,\mu\nu,\mu\nu\rho\}}(q_1, q_2) \equiv \int \frac{d^n q}{(2\pi)^n} \frac{\{1, q^\mu, q^\mu q^\nu, q^\mu q^\nu q^\rho\}}{L_1 L_2 L_3}, \quad (\text{C.2})$$

$$D^{\{0,\mu,\mu\nu,\mu\nu\rho\}}(q_1, q_2, q_3) \equiv \int \frac{d^n q}{(2\pi)^n} \frac{\{1, q^\mu, q^\mu q^\nu, q^\mu q^\nu q^\rho\}}{L_1 L_2 L_3 L_4}, \quad (\text{C.3})$$

with $L_1 = q^2$, $L_2 = (q+q_1)^2$, $L_3 = (q+q_1+q_2)^2$, and $L_4 = (q+q_1+q_2+q_3)^2$, are most easily evaluated by means of a Passarino-Veltman decomposition [89]. This procedure relies on the fact that the Lorentz structure of a tensor integral is determined by the “external” momenta which are not integrated over and the metric tensor $g^{\mu\nu}$. Then the most general form of the integrals (C.1), (C.2), and (C.3) can be expressed as

$$\begin{aligned} B^\mu &= q_1^\mu B_1, \\ B^{\mu\nu} &= q_1^\mu q_1^\nu B_{21} + g^{\mu\nu} B_{22}, \end{aligned} \quad (\text{C.4})$$

$$\begin{aligned} C^\mu &= q_1^\mu C_{11} + q_2^\mu C_{12}, \\ C^{\mu\nu} &= q_1^\mu q_1^\nu C_{21} + q_2^\mu q_2^\nu C_{22} + \{q_1 q_2\}^{\mu\nu} C_{23} + g^{\mu\nu} C_{24}, \\ C^{\mu\nu\rho} &= q_1^\mu q_1^\nu q_1^\rho C_{31} + q_2^\mu q_2^\nu q_2^\rho C_{32} + \{q_1 q_1 q_2\}^{\mu\nu\rho} C_{33} \\ &\quad + \{q_1 q_2 q_2\}^{\mu\nu\rho} C_{34} + \{q_1 g\}^{\mu\nu\rho} C_{35} + \{q_2 g\} C_{36}, \end{aligned} \quad (\text{C.5})$$

$$\begin{aligned}
D^\mu &= q_1^\mu D_{11} + q_2^\mu D_{12} + q_3^\mu D_{13} , \\
D^{\mu\nu} &= q_1^\mu q_1^\nu D_{21} + q_2^\mu q_2^\nu D_{22} + q_3^\mu q_3^\nu D_{23} + \{q_1 q_2\}^{\mu\nu} D_{24} \\
&\quad + \{q_1 q_3\}^{\mu\nu} D_{25} + \{q_2 q_3\}^{\mu\nu} D_{26} + g_{\mu\nu} D_{27} , \\
D^{\mu\nu\rho} &= q_1^\mu q_1^\nu q_1^\rho D_{31} + q_2^\mu q_2^\nu q_2^\rho D_{32} + q_3^\mu q_3^\nu q_3^\rho D_{33} + \{q_1 q_1 q_2\}^{\mu\nu\rho} D_{34} \\
&\quad + \{q_1 q_1 q_3\}^{\mu\nu\rho} D_{35} + \{q_1 q_2 q_2\}^{\mu\nu\rho} D_{36} + \{q_1 q_3 q_3\}^{\mu\nu\rho} D_{37} \\
&\quad + \{q_2 q_2 q_3\}^{\mu\nu\rho} D_{38} + \{q_2 q_3 q_3\}^{\mu\nu\rho} D_{39} + \{q_1 q_2 q_3\}^{\mu\nu\rho} D_{310} \\
&\quad + \{q_1 g\}^{\mu\nu\rho} D_{311} + \{q_2 g\}^{\mu\nu\rho} D_{312} + \{q_3 g\}^{\mu\nu\rho} D_{313} ,
\end{aligned} \tag{C.6}$$

where we have omitted the arguments q_1 , q_2 , and q_3 of the integrals and the coefficients, B_i , C_i , and D_i , for brevity. The B_i , C_i , and D_i furthermore depend on the scalar integrals B^0 , C^0 , and D^0 . The latter are tabulated and can be found in the literature [88, 140, 141]. The brackets $\{\dots\}^{\mu\nu\dots}$ in Eqs. (C.5) and (C.6) denote the sum of all possible different permutations of Lorentz indices. For instance, $\{q_1 q_1 q_2\}^{\mu\nu\rho} = q_1^\mu q_1^\nu q_2^\rho + q_1^\nu q_1^\rho q_2^\mu + q_1^\rho q_1^\mu q_2^\nu$, and $\{q_1 g\}^{\mu\nu\rho} = q_1^\mu g^{\nu\rho} + q_1^\nu g^{\rho\mu} + q_1^\rho g^{\mu\nu}$.

Tensor integrals containing an additional factor of q^2 in the numerator, e.g.,

$$\tilde{D}^\mu(q_1, q_2, q_3) = \int \frac{d^n q}{(2\pi)^n} \frac{q^2 q^\mu}{L_1 L_2 L_3 L_4} = \int \frac{d^n q}{(2\pi)^n} \frac{q^\mu}{L_2 L_3 L_4} , \tag{C.7}$$

can be reduced to known integrals by a simple shift. In (C.7), replacing $q \rightarrow q' = q + q_1$ yields

$$\begin{aligned}
\tilde{D}^\mu(q_1, q_2, q_3) &= \int \frac{d^n q'}{(2\pi)^n} \frac{q'^\mu}{L'_1 L'_2 L'_3} - \int \frac{d^n q'}{(2\pi)^n} \frac{q_1^\mu}{L'_1 L'_2 L'_3} \\
&= C^\mu(q_2, q_3) - q_1^\mu C^0(q_2, q_3) .
\end{aligned} \tag{C.8}$$

With these decompositions any loop integral arising in the calculation of $\mathcal{O}(\alpha_s)$ corrections to $2 \rightarrow 2$ scattering processes can be evaluated.

Appendix D

Parametrization of Momenta

For a single-inclusive $2 \rightarrow 3$ scattering reaction

$$a(p_1) + b(p_2) \rightarrow c(p_3) + d(p_4) + e(p_5) \quad (\text{D.1})$$

the parametrization of momenta in the corresponding matrix elements can be performed in the rest frame of the two *unobserved* partons $p_4 + p_5$,

$$\begin{aligned} p_4 &= (p_0, p_0 \sin \theta_1 \cos \theta_2, p_y, p_0 \cos \theta_1, \hat{p}) , \\ p_5 &= (p_0, -p_0 \sin \theta_1 \cos \theta_2, -p_y, -p_0 \cos \theta_1, -\hat{p}) , \end{aligned} \quad (\text{D.2})$$

where $p_0 = \sqrt{s_{23}}/2$ and p_y is arbitrary, by using one of the following sets [142]:

$$\begin{aligned} \text{Set 1:} \quad p_1 &= p_1^0 (1, 0, 0, 1, 0, \dots) , \\ p_2 &= p_2^0 (1, -\sin \psi'', 0, \cos \psi'', 0, \dots) , \\ p_3 &= p_3^0 (1, -\sin \psi, 0, \cos \psi, 0, \dots) . \end{aligned} \quad (\text{D.3})$$

$$\begin{aligned} \text{Set 2:} \quad p_1 &= p_1^0 (1, \sin \psi'', 0, \cos \psi'', 0, \dots) , \\ p_2 &= p_2^0 (1, 0, 0, 1, 0, \dots) , \\ p_3 &= p_3^0 (1, \sin \psi', 0, \cos \psi', 0, \dots) . \end{aligned} \quad (\text{D.4})$$

$$\begin{aligned} \text{Set 3:} \quad p_1 &= p_1^0 (1, \sin \psi, 0, \cos \psi, 0, \dots) . \\ p_2 &= p_2^0 (1, -\sin \psi', 0, \cos \psi', 0, \dots) . \\ p_3 &= p_3^0 (1, 0, 0, 1, 0, \dots) . \end{aligned} \quad (\text{D.5})$$

Sets 1-3 above depend on which momentum is chosen to point into the z -direction. All hat-momenta \hat{p}_1 , \hat{p}_2 , and \hat{p}_3 have to vanish. One finds

$$p_1^0 = \frac{sv}{2\sqrt{s_{23}}} , \quad p_2^0 = \frac{s(1-vw)}{2\sqrt{s_{23}}} , \quad p_3^0 = \frac{s(1-v+vw)}{2\sqrt{s_{23}}} . \quad (\text{D.6})$$

For the parameters ψ , ψ' , and ψ'' we have

$$\begin{aligned}
\sin \psi &= \frac{2\sqrt{w(1-v)(1-w)}}{1-v+vw}, & \cos \psi &= \frac{-1+v+2w-vw}{1-v+vw}, \\
\sin \psi' &= \frac{2v\sqrt{w(1-v)(1-w)}}{(1-vw)(1-v+vw)}, & \cos \psi' &= \frac{1-v-v^2w+v^2w^2}{(1-vw)(1-v+vw)}, \\
\sin \psi'' &= \frac{2\sqrt{w(1-v)(1-w)}}{1-vw}, & \cos \psi'' &= \frac{-1-vw+2w}{1-vw}.
\end{aligned} \tag{D.7}$$

The Mandelstam variables defined in Eq.(3.50) then take the form

Set 1:	$ \begin{aligned} s_{12} &= \frac{s}{2}(1-v+vw)[1 + \sin \psi \sin \theta_1 \cos \theta_2 - \cos \psi \cos \theta_1] \\ s_{13} &= \frac{s}{2}(1-v+vw)[1 - \sin \psi \sin \theta_1 \cos \theta_2 + \cos \psi \cos \theta_1] \\ t_2 &= -\frac{sv}{2}[1 - \cos \theta_1] \\ t_3 &= -\frac{sv}{2}[1 + \cos \theta_1] \\ u_2 &= -\frac{s}{2}(1-vw)[1 + \sin \psi'' \sin \theta_1 \cos \theta_2 - \cos \psi'' \cos \theta_1] \\ u_3 &= -\frac{s}{2}(1-vw)[1 - \sin \psi'' \sin \theta_1 \cos \theta_2 + \cos \psi'' \cos \theta_1] \end{aligned} \tag{D.8} $
Set 2:	$ \begin{aligned} s_{12} &= \frac{s}{2}(1-v+vw)[1 - \sin \psi' \sin \theta_1 \cos \theta_2 - \cos \psi' \cos \theta_1] \\ s_{13} &= \frac{s}{2}(1-v+vw)[1 + \sin \psi' \sin \theta_1 \cos \theta_2 + \cos \psi' \cos \theta_1] \\ t_2 &= -\frac{sv}{2}[1 - \sin \psi'' \sin \theta_1 \cos \theta_2 - \cos \psi'' \cos \theta_1] \\ t_3 &= -\frac{sv}{2}[1 + \sin \psi'' \sin \theta_1 \cos \theta_2 + \cos \psi'' \cos \theta_1] \\ u_2 &= -\frac{s}{2}(1-vw)[1 - \cos \theta_1] \\ u_3 &= -\frac{s}{2}(1-vw)[1 + \cos \theta_1] \end{aligned} \tag{D.9} $
Set 3:	$ \begin{aligned} s_{12} &= \frac{s}{2}(1-v+vw)[1 - \cos \theta_1] \\ s_{13} &= \frac{s}{2}(1-v+vw)[1 + \cos \theta_1] \\ t_2 &= -\frac{sv}{2}[1 - \sin \psi \sin \theta_1 \cos \theta_2 - \cos \psi \cos \theta_1] \\ t_3 &= -\frac{sv}{2}[1 + \sin \psi \sin \theta_1 \cos \theta_2 + \cos \psi \cos \theta_1] \\ u_2 &= -\frac{s}{2}(1-vw)[1 + \sin \psi' \sin \theta_1 \cos \theta_2 - \cos \psi' \cos \theta_1] \\ u_3 &= -\frac{s}{2}(1-vw)[1 - \sin \psi' \sin \theta_1 \cos \theta_2 + \cos \psi' \cos \theta_1] \end{aligned} \tag{D.10} $

The other variables,

$$t = -s(1 - v) \, , \quad u = -svw \, , \quad s_{23} = sv(1 - w) \, , \quad (\text{D.11})$$

are independent of the parametrization of the momenta.

Appendix E

Lorentz Boosts

Most generally, a momentum (E, \vec{p}) in any coordinate system is seen as a different momentum (E', \vec{p}') in another system, which moves with a velocity β relative to the original one. The boosted momentum is given by [64]

$$\begin{pmatrix} E' \\ p'_{\parallel} \end{pmatrix} = \begin{pmatrix} \gamma & -\gamma\beta \\ -\gamma\beta & \gamma \end{pmatrix} \begin{pmatrix} E \\ p_{\parallel} \end{pmatrix}. \quad (\text{E.1})$$

Here, $\gamma = (1 - \beta^2)^{-1/2}$, and p_{\parallel} is the component of \vec{p} parallel to the boost direction. The transverse momentum components are not affected by the boost: $p_T = p'_T$. From the definition of rapidity,

$$y \equiv \frac{1}{2} \ln \left[\frac{E + p_z}{E - p_z} \right], \quad (\text{E.2})$$

we can easily see that under a boost β in z -direction y transforms as

$$y' = \frac{1}{2} \ln \left[\frac{E' + p'_z}{E' - p'_z} \right] = y - \tanh^{-1} \beta = y - \frac{1}{2} \ln \left[\frac{1 + \beta}{1 - \beta} \right]. \quad (\text{E.3})$$

Thus a boost changes the value of y just by a constant, which makes rapidity particularly suitable for the description of high-energy reactions. In the massless case, the rapidity equals the pseudorapidity, which is defined by

$$\eta \equiv -\ln \tan \left(\frac{\theta}{2} \right), \quad (\text{E.4})$$

where $\cos \theta = p_z / |\vec{p}|$.

A boost from the c.m.s. system of two massless particles to a system with arbitrary momenta $\vec{p}_1' \neq \vec{p}_2'$ along their direction of motion is described by a velocity

$$\beta = -\frac{|\vec{p}_1'| + |\vec{p}_2'|}{E'_1 + E'_2}, \quad (\text{E.5})$$

and causes a shift in rapidity,

$$\eta_{lab} = \eta_{cms} - \frac{1}{2} \ln \frac{E'_2}{E'_1} . \quad (\text{E.6})$$

Eqs. (E.5), and (E.6) are needed, e.g., in the case of electron-proton collisions with different beam energies $E_p \neq E_e$.

Similarly, one obtains for the boost of a frame, where a massless particle with four-momentum $p_1 = (E_1, \vec{p}_1)$ moves towards a particle of mass M_2 at rest, to the c.m.s. system of these two particles

$$\beta = \frac{|\vec{p}_1|}{E_1 + M_2} , \quad (\text{E.7})$$

and

$$\eta_{cms} = \eta_{rest} - \frac{1}{2} \ln \frac{2E_1}{M_2} . \quad (\text{E.8})$$

These relations are useful for the transformation of quantities calculated in the c.m.s. system to the laboratory frame of fixed-target experiments where measurements are performed.

Acknowledgements

The work presented in this thesis would not have been possible without the help of many – teachers and collaborators, friends and colleagues. I owe sincere thanks to all of them:

First, to Prof. Dr. Andreas Schäfer, who gave me the possibility to perform my PhD studies in a motivating environment. I am particularly grateful for his advice, his interest in my work, and for support in many respects.

Very special thanks go to Marco Stratmann. He patiently introduced me into the mysteries of pQCD with grand expertise, never getting tired of solving all kinds of puzzles, and made NLO calculations real fun. In very much the same way I would like to thank Werner Vogelsang for a great collaboration, and for always sharing his broad experience and deep physical insight with me. It was – and still is – a continuous pleasure and a big challenge to learn from and work with Marco and Werner.

To my colleagues, Axel Kirchner, Tim Oppermann, and Wolfgang Söldner, for the cheerful atmosphere in our office, and to all the other members of our group for their company in innumerable coffee breaks – and assistance in many issues of daily research life. To our secretary, Monika Maschek, for her help in everything surrounding physics.

To the many teachers, in particular my diploma advisor, Wolfgang Schweiger, who made me familiar with the basic concepts of science, thereby awakening my interest in physics.

During the various steps of my PhD studies I have been supported by the European ESOP network, the Bundesministerium für Bildung und Forschung (BMBF), and the Deutsche Forschungsgemeinschaft (DFG). I am grateful to Brookhaven National Laboratory and the RIKEN-BNL Research Center for generous hospitality making possible two fruitful research visits at BNL, where important parts of the work presented here have been completed.

Bibliography

- [1] D. J. Gross and F. Wilczek, Phys. Rev. **D9**, 980 (1974).
- [2] S. B. Libby and G. Sterman, Phys. Rev. **D18**, 3252 (1978);
R. K. Ellis, H. Georgi, M. Machacek, H. D. Politzer, and G. G. Ross, Phys. Lett. **78B**, 281 (1978); Nucl. Phys. **B152**, 285 (1979);
D. Amati, R. Petronzio, and G. Veneziano, Nucl. Phys. **B140**, 54 (1980); Nucl. Phys. **B146**, 29 (1978);
G. Curci, W. Furmanski, and R. Petronzio, Nucl. Phys. **B175**, 27 (1980);
J. C. Collins, D. E. Soper, and G. Sterman, Phys. Lett. **B134**, 263 (1984); Nucl. Phys. **B261**, 104 (1985);
J. C. Collins, Nucl. Phys. **B394**, 169 (1993).
- [3] M. Beneke, Phys. Rept. **317**, 1 (1999).
- [4] CTEQ Collaboration, J. Pumplin *et al.*, JHEP **0207**, 012 (2002).
- [5] D. Stump *et al.*, Phys. Rev. **D65**, 014012 (2002);
J. Pumplin *et al.*, Phys. Rev. **D65**, 014013 (2002).
- [6] M. Glück, E. Reya, and A. Vogt, Eur. Phys. J. **C5**, 461 (1998).
- [7] A. Martin *et al.*, Eur. Phys. J. **C28**, 455 (2003).
- [8] For a recent review of pol. DIS data see, e.g.: E. W. Hughes, R. Voss, Ann. Rev. Nucl. Part. Sci. **49**, 303 (1999).
- [9] European Muon Collaboration (EMC), J. Ashman *et al.*, Phys. Lett. **B206**, 364 (1988); Nucl. Phys. **B328**, 1 (1989).
- [10] X.-D. Ji, Phys. Rev. Lett **78**, 610 (1997); J. Phys. **G24**, 1181 (1998);
P. Hoodbhoy, X.-D. Ji, and W. Lu, Phys. Rev. **D59**, 074010 (1999); Phys. Rev. **D59**, 014013 (1999).
- [11] R. L. Jaffe and A. Manohar, Nucl. Phys. **B337**, 509 (1990);
R. L. Jaffe, Phil. Trans. Roy. Soc. Lond. **A359**, 391 (2001).
- [12] I. Balitsky and X.-D. Ji, Phys. Rev. Lett. **79**, 1225 (1997).

- [13] X.-D. Ji, Phys. Rev. **D55**, 7114 (1997).
- [14] N. Mathur *et al.*, Phys. Rev. **D62**, 114504 (2000).
- [15] M. Göckeler *et al.*, Phys. Rev. Lett. **92**, 042002 (2004).
- [16] P. Hägler *et al.*, Phys. Rev. **D68**, 034505 (2003).
- [17] M. Glück, E. Reya, M. Stratmann, and W. Vogelsang, Phys. Rev. **D63**, 094005 (2001).
- [18] J. Blümlein and H. Böttcher, Nucl. Phys. **B636**, 225 (2002).
- [19] Asymmetry Analysis Collaboration, Y. Goto *et al.*, Phys. Rev. **D62**, 034017 (2000).
- [20] M. Glück, E. Reya, M. Stratmann, and W. Vogelsang, Phys. Rev. **D53**, 4775 (1996).
- [21] G. Altarelli, R. D. Ball, S. Forte, and G. Ridolfi, Nucl. Phys. **B496**, 337 (1997);
Acta Phys. Polon. **B29**, 1145 (1998);
T. Gehrmann and W. J. Stirling, Phys. Rev. **D53**, 6100 (1996);
SM Collaboration (SMC), D. Adams *et al.*, Phys. Rev. **D56**, 5330 (1997); SMC,
B. Adeva *et al.*, Phys. Rev. **D58**, 112002 (1998);
D. de Florian, O. A. Sampayo, and R. Sassot, Phys. Rev. **D57**, 5803 (1998);
D. de Florian and R. Sassot, Phys. Rev. **D62**, 094025 (2000);
E. Leader, A. V. Sidorov, and D. Stamenov, Eur. Phys. J. **C23**, 479 (2002).
- [22] See, for example: G. Bunce, N. Saito, J. Soffer, and W. Vogelsang, Annu. Rev. Nucl. Part. Sci. **50**, 525 (2000).
- [23] A. P. Contogouris, B. Kamal, Z. Merebashvili, and F. V. Tkachov, Phys. Lett. **B304**, 329 (1993); Phys. Rev. **D48**, 4092 (1993);
A. P. Contogouris and Z. Merebashvili, Phys. Rev. **D55**, 2718 (1997).
- [24] L. E. Gordon and W. Vogelsang, Phys. Rev. **D48**, 3136 (1993); Phys. Rev. **D49**, 170 (1994).
- [25] S. Frixione and W. Vogelsang, Nucl. Phys. **B568**, 60 (2000).
- [26] I. Bojak and M. Stratmann, Phys. Lett. **B433**, 411 (1998); Phys. Rev. **D67**, 034010 (2003).
- [27] COMPASS Collaboration, G. Baum *et al.*, CERN/SPSLC-96-14 (1996).
- [28] See <http://www.bnl.gov/eic> for information concerning the eRHIC/EIC project, including the Whitepaper.
- [29] A. Bazilevsky, talk presented at the “Xth Workshop on High Energy Spin Physics (Spin-03)”, Dubna, Russia, 2003.
- [30] B. Jäger, M. Stratmann, and W. Vogelsang, Phys. Rev. **D68**, 114018 (2003).

- [31] B. Jäger, A. Schäfer, M. Stratmann, and W. Vogelsang, Phys. Rev. **D67**, 054005 (2003).
- [32] B. Jäger, M. Stratmann, S. Kretzer, and W. Vogelsang, Phys. Rev. Lett. **92**, 121803 (2004).
- [33] B. Jäger, M. Stratmann, and W. Vogelsang, hep-ph/0404057 (submitted for publication to Phys. Rev. D).
- [34] T. Muta, *Foundations of Quantum Chromodynamics*, World Scientific (1987).
- [35] G. Sterman, *Introduction to Quantum Field Theory*, Cambridge University Press (1993).
- [36] R. K. Ellis, W. J. Stirling, and B. R. Webber, *QCD and Collider Physics*, Cambridge University Press (1996).
- [37] J. C. Collins, *Renormalization*, Cambridge University Press (1984).
- [38] P. Pascual and R. Tarrach, *QCD: Renormalization for the Practitioner*, Springer (1984).
- [39] J. D. Bjorken and S. D. Drell, *Relativistic Quantum Fields*, McGraw Hill (1964).
- [40] L. Faddeev and V. N. Popov, Phys. Lett. **B25**, 29 (1967).
- [41] For a recent review see, e.g.: T. DeGrand, hep-lat/0312241.
- [42] J. Gasser and H. Leutwyler, Ann. Phys. **158**, 142 (1984).
- [43] A. Chodos *et al.*, Phys. Rev. **D9**, 3471 (1974).
- [44] L. Y. Glozman, W. Plessas, K. Varga, and R. F. Wagenbrunn, Phys. Rev. **D58**, 094030 (1998).
- [45] M. Anselmino, P. Kroll, and B. Pire, Z. Phys. **C36**, 89 (1987).
- [46] D. I. Diakonov *et al.*, Nucl. Phys. **B480**, 341 (1996).
- [47] For a detailed review see, e.g.: T. Schäfer and E. V. Shuryak, Rev. Mod. Phys. **70**, 323 (1998).
- [48] *Large Order Behavior Of Perturbation Theory*, eds. J. C. Le Guillou and J. Zinn-Justin, North-Holland (1990).
- [49] For a detailed discussion see, e.g.: C. F. Berger, *Soft Gluon Exponentiation and Resummation*, Ph.D. thesis, State University of New York at Stony Brook (2003).
- [50] S. Frixione and W. Vogelsang, Nucl. Phys. **B568**, 60 (2000).

- [51] T. Kinoshita, J. Math. Phys. **3**, 650 (1962);
T. D. Lee and M. Nauenberg, Phys. Rev. **B133**, 1549 (1964).
- [52] F. Bloch and A. Nordsieck, Phys. Rev. **52**, 54 (1937).
- [53] G. 't Hooft and M. Veltman, Nucl. Phys. **B44**, 189 (1972).
- [54] E. R. Speer, J. Math. Phys. **15**, 1 (1974).
- [55] C. G. Bollini and J. J. Giambiagi, Phys. Lett. **40B**, 566 (1972); Nuovo Cim. **12B**, 20 (1972);
J. F. Ashmore, Lett. Nuovo Cim. **4**, 289 (1972);
G. M. Cicuta and E. Montaldi, Lett. Nuovo Cim. **4**, 329 (1972).
- [56] P. Breitenlohner and D. Maison, Commun. Math. Phys. **52**, 11 (1977).
- [57] M. Jamin and M. E. Lautenbacher, Comput. Phys. Commun. **74**, 265 (1993).
- [58] J. C. Taylor, Nucl. Phys. **B33**, 436 (1971).
- [59] A. A. Slavnov, Teor. Mat. Fiz. **10**, 153 (1972).
- [60] G. 't Hooft, Nucl. Phys. **B61**, 455 (1973).
- [61] W. A. Bardeen, A. J. Buras, D. W. Duke, and T. Muta, Phys. Rev. **D18**, 3998 (1978).
- [62] E. Zijlstra, *Second order QCD corrections to deep inelastic processes*, Ph.D Thesis, University of Leiden (1993).
- [63] E. C. G. Stückelberg and A. Petermann, Helv. Phys. Acta **26**, 499 (1953);
M. Gell-Mann and F. E. Low, Phys. Rev. **95**, 1300 (1954);
L. V. Ovsyannikov, Dokl. Acad. Nauk SSSR **109**, 1112 (1956);
K. Symanzik, Comm. Math. Phys. **18**, 227 (1970);
C. G. Callan, Jr., Phys. Rev. **D2**, 1541 (1970);
S. Weinberg, Phys. Rev. **D8**, 3497 (1973).
- [64] Particle Data Group, K. Hagiwara *et al.*, Phys. Rev. **D66**, 010001 (2002).
- [65] G. Altarelli and G. Parisi, Nucl. Phys. **B126**, 298 (1977).
- [66] L. N. Lipatov, Sov. J. Nucl. Phys. **20**, 95 (1975);
V. N. Gribov and L. N. Lipatov, Sov. J. Nucl. Phys. **15**, 438 (1972);
Yu. L. Dokshitzer, Sov. Phys. JTEP **46**, 641 (1977).
- [67] E. G. Floratos, D. A. Ross, and C. T. Sachrajda, Nucl. Phys. **B129**, 66 (1977);
B139, 545 (1978); Nucl. Phys. **B152**, 493 (1979);
see also: A. Gonzales-Arroyo, C. Lopez, and F. J. Yndurain, Nucl. Phys. **B153**, 161 (1979);

- A. Gonzales-Arroyo and C. Lopez, Nucl. Phys. **B166**, 429 (1980);
E. G. Floratos, C. Kounnas, and R. Lacaze, Phys. Lett. **98B** 89,285 (1981); Nucl. Phys. **B192**, 417 (1981).
- [68] G. Curci, W. Furmanski, and R. Petronzio, Nucl. Phys. **B175**, 27 (1980);
W. Furmanski and R. Petronzio, Phys. Lett. **97B**, 437 (1980).
- [69] W. Vogelsang, Phys. Rev. **D54**, 2023 (1996); Nucl. Phys. **B475**, 47 (1996).
- [70] R. Mertig and W. L. van Neerven, Z. Phys. **C70**, 637 (1996).
- [71] C. F. Berger, Phys. Rev. **D66**, 116002 (2002);
S. Moch, J. A. M. Vermaseren, and A. Vogt, Nucl. Phys. **B646**, 181 (2002).
- [72] S. Moch, J. A. M. Vermaseren, and A. Vogt, [hep-ph/0403192](#).
- [73] S. Moch, J. A. M. Vermaseren, and A. Vogt, [hep-ph/0404111](#).
- [74] CTEQ Collaboration, H.-L. Lai *et al.*, Eur. Phys. J. **C12**, 375 (2000).
- [75] A. Martin *et al.*, Eur. Phys. J. **C23**, 73 (2002).
- [76] J. Huston *et al.*, Phys. Rev. **D58**, 114034 (1998);
A. D. Martin *et al.*, Eur. Phys. J. **C14**, 133 (2000).
- [77] M. Glück, E. Reya, and A. Vogt, Z. Phys. **C48**, 471 (1990).
- [78] P. J. Rijken and W. L. van Neerven, Nucl. Phys. **B487**, 233 (1997).
- [79] M. Glück, E. Reya, and A. Vogt, Phys. Rev. **D48**, 116 (1993); **D51**, 1427 (1995) (E).
- [80] M. Stratmann and W. Vogelsang, Nucl. Phys. **B496**, 41 (1997).
- [81] See, for example: D. H. Perkins, *Introduction to High Energy Physics*, Addison-Wesley (1982).
- [82] B.A. Kniehl, G. Kramer, and B. Pötter, Nucl. Phys. **B582**, 514 (2000).
- [83] S. Kretzer, Phys. Rev. **D62**, 054001 (2000).
- [84] D. de Florian, M. Stratmann, and W. Vogelsang, Phys. Rev. **D57**, 5811 (1998).
- [85] S. Wolfram, Mathematica; see also: www.wri.com.
- [86] J. Küblböck, M. Böhm, and A. Denner, Comput. Phys. Commun. **60**, 165 (1990);
for a documentation of the latest version by R. Mertig, see: www.feyncalc.org.
- [87] See, for example: J. Babcock, E. Monsay, and D. Sivers, Phys. Rev. Lett. **40**, 1161 (1978); Phys. Rev. **D19**, 1483 (1979).

- [88] M.A. Nowak, M. Praszalowicz, and W. Slominski, *Ann. Phys.* **166**, 443 (1986).
- [89] G. Passarino and M. J. G. Veltman, *Nucl. Phys.* **B160**, 151 (1979).
- [90] Z. Xu, D. Zhang, and L. Chang, *Nucl. Phys.* **B291**, 392 (1987);
R. Kleiss and W. J. Stirling, *Nucl. Phys.* **B262**, 235 (1985).
- [91] J. Gunion and Z. Kunszt, *Phys. Lett.* **B161**, 333 (1985).
- [92] Z. Kunszt, A. Signer, and Z. Trocsanyi, *Nucl. Phys.* **B411**, 397 (1994).
- [93] Z. Kunszt and D. E. Soper, *Phys. Rev.* **D46**, 192 (1992).
- [94] W. L. van Neerven, *Nucl. Phys.* **B268**, 453 (1986).
- [95] W. Beenakker, H. Kuijf, and W. L. van Neerven, *Phys. Rev.* **D40**, 54 (1989).
- [96] R. Mertig and W. L. van Neerven, *Z. Phys.* **C70**, 637 (1996).
- [97] W. Vogelsang, *Phys. Rev.* **D54**, 2023 (1996); *Nucl. Phys.* **B475**, 47 (1996).
- [98] M. Stratmann, W. Vogelsang, and A. Weber, *Phys. Rev.* **D53**, 138 (1996).
- [99] Y. Matiounine, J. Smith, W. L. van Neerven, *Phys. Rev.* **D58**, 076002 (1998).
- [100] PHENIX Collaboration, S. S. Adler *et al.*, *Phys. Rev. Lett.* **91**, 241803 (2003).
- [101] STAR Collaboration, J. Adams *et al.*, [hep-ex/0310058](#).
- [102] R. K. Ellis and J. C. Sexton, *Nucl. Phys.* **B269**, 445 (1986).
- [103] R. Gastmans and T. T. Wu, *The ubiquitous photon*, Oxford Science Publications (1990).
- [104] F. Aversa, P. Chiappetta, M. Greco, and J.-Ph. Guillet, *Nucl. Phys.* **B327**, 105 (1989).
- [105] G. P. Lepage, *J. Comp. Phys.* **27**, 192 (1978); G. P. Lepage, Cornell Preprint, CLNS-80/447 (1980).
- [106] D. de Florian, *Phys. Rev.* **D67**, 054004 (2003).
- [107] W. T. Giele and E. W. N. Glover, *Phys. Rev.* **D46**, 1980 (1992);
W. T. Giele, E. W. N. Glover, and D. A. Kosower, *Nucl. Phys.* **B403**, 633 (1993);
S. Frixione, Z. Kunszt, and A. Signer, *Nucl. Phys.* **B467**, 399 (1996);
S. Catani and M. Seymour, *Nucl. Phys.* **B485**, 291 (1997), Erratum **B510**, 503 (1998);
S. Frixione, *Nucl. Phys.* **B507**, 295 (1997).
- [108] N. Saito, private communication.

- [109] M. Stratmann and W. Vogelsang, Phys. Rev. **D64**, 114007 (2001).
- [110] See, e.g.: DELPHI Collab., P. Abreu *et al.*, Eur. Phys. J. **C13**, 573 (2000), and references therein.
- [111] W. Vogelsang and A. Weber, Phys. Rev. **D45**, 4069 (1992).
- [112] See, e.g.: M. H. Seymour, Nucl. Phys. **B513**, 269 (1998); Proceedings of the “8th International Workshop on Deep Inelastic Scattering and QCD (DIS 2000)”, Liverpool, England, World Scientific, 27 (2001).
- [113] D. de Florian, S. Frixione, A. Signer, and W. Vogelsang, Nucl. Phys. **B539**, 455 (1999).
- [114] G. Sterman and S. Weinberg, Phys. Rev. Lett. **39**, 1436 (1977).
- [115] M.A. Furman, Nucl. Phys. **B197**, 413 (1982).
- [116] J.-Ph. Guillet, Z. Phys. **C51**, 587 (1991).
- [117] See also the discussions about jet definitions and algorithms in, e.g.: W. B. Kilgore and W. T. Giele, Phys. Rev. **D55**, 7183 (1997).
- [118] S. D. Ellis, Z. Kunszt, and D. E. Soper, Phys. Rev. Lett. **62**, 726 (1989); Phys. Rev. **D 40**, 2188 (1989); Phys. Rev. Lett. **64**, 2121 (1990).
- [119] UA2 Collaboration, J. Alitti *et al.*, Phys. Lett. **B257**, 232 (1991); CDF Collaboration, F. Abe *et al.*, Phys. Rev. **D45**, 1448 (1992); D0 Collaboration, S. Abachi *et al.* Phys. Rev. **D53**, 6000 (1996).
- [120] S. Catani, Yu. L. Dokshitzer, M. H. Seymour, and B. R. Webber, Nucl. Phys. **B406**, 187 (1993); S. D. Ellis and D. E. Soper, Phys. Rev. **D48**, 3160 (1993).
- [121] J. E. Huth *et al.*, published in the proceedings of the 1990 DPF “Summer Study on High Energy Physics: Research Directions for the Decade”, Snowmass, CO, USA, World Scientific, 134 (1992).
- [122] F. Aversa, P. Chiappetta, M. Greco, and J.-Ph. Guillet, Z. Phys. **C46**, 253 (1990).
- [123] F. Aversa, P. Chiappetta, M. Greco, and J.-Ph. Guillet, Phys. Rev. Lett. **65**, 401 (1990); F. Aversa *et al.*, Z. Phys. **C49**, 459 (1991).
- [124] S. G. Salesch, *Photoproduktion von Jets bei HERA mit aufgelösten Photonen bis zur Ordnung $\mathcal{O}(\alpha \alpha_S^2)$* , Ph.D. thesis, University of Hamburg (1993).
- [125] S.D. Ellis, Z. Kunszt, and D.E. Soper, Phys. Rev. Lett. **69**, 3613 (1992).

- [126] M. Stratmann and W. Vogelsang, Z. Phys. **C74**, 641 (1997);
J.M. Butterworth, N. Goodman, M. Stratmann, and W. Vogelsang, in proceedings of the workshop on “Physics with Polarized Protons at HERA”, Hamburg, Germany, 120 (1997) [[hep-ph/9711250](#)].
- [127] D. de Florian and W. Vogelsang, Phys. Rev. **D57**, 4376 (1998).
- [128] L. E. Gordon, Phys. Rev. **D50**, 6753 (1994).
- [129] P. Aurenche *et al.*, Nucl. Phys. **B286**, 553 (1987).
- [130] M. Glück, E. Reya, and A. Vogt, Phys. Rev. **D46**, 1973 (1992).
- [131] M. Glück and E. Reya, Phys. Rev. **D28**, 2749 (1983);
M. Fontannaz and E. Pilon, Phys. Rev. **D45**, 382 (1992).
- [132] M. Glück, E. Reya, and A. Vogt, Phys. Rev. **D45**, 3986 (1992).
- [133] M. Stratmann and W. Vogelsang, Phys. Lett. **B386**, 370 (1996).
- [134] A recent review can be found, e.g., in: M. Klasen, Rev. Mod. Phys. **74**, 1221 (2002).
- [135] See discussions in: J. F. Owens, Phys. Rev. **D21**, 54 (1980);
M. Drees and R. M. Godbole, Phys. Rev. Lett. **61**, 682 (1988); Phys. Rev. **D39**, 169 (1989).
- [136] D. de Florian and S. Frixione, Phys. Lett. **B457**, 236 (1999).
- [137] M. Glück and W. Vogelsang, Z. Phys. **C55**, 353 (1992); **C57**, 309 (1993);
M. Glück, M. Stratmann, and W. Vogelsang, Phys. Lett. **B337**, 373 (1994).
- [138] M. Glück, E. Reya, and C. Sieg, Phys. Lett. **B503**, 285 (2001).
- [139] HERMES Collaboration, *The HERMES Physics Program & Plans for 2001-2006*, DESY-PRC (2000).
- [140] W. J. P. Beenakker, *Electroweak Corrections: Techniques and Applications*, Ph.D. thesis, University of Leiden (1989).
- [141] I. Bojak, *NLO QCD Corrections to the Polarized Photo- and Hadroproduction of Heavy Quarks*, Ph.D. thesis, University of Dortmund (2000).
- [142] W. Vogelsang, *Tests and Signatures of Spin-Dependent Parton Distributions in Leading and Next-to-Leading Order of QCD*, Ph.D. thesis, University of Dortmund (1993).